# Woods Hole Oceanographic Institution

Massachusetts Institute of Technology
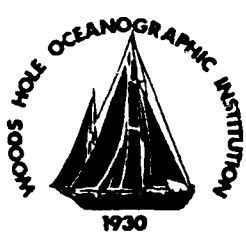
Joint Program
in Oceanography
and
Oceanographic
Engineering
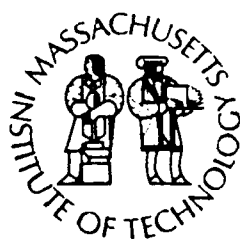
DOCTORAL DISSERTATION

Acoustic Scattering from Elastic Ice:
A Finite Difference Solution

by

J. Robert Fricke

June 1991

APR 0 3 1992
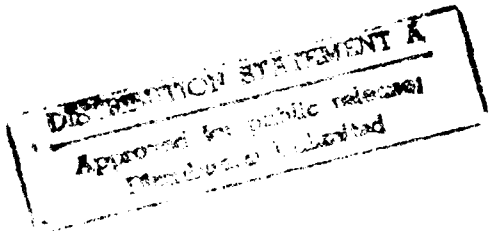
92-08386

92 4 02 045

WHOI-91-10

Acoustic Scattering from Elastic Ice:
A Finite Difference Solution

by

J. Robert Fricke

Woods Hole Oceanographic Institution
Woods Hole, Massachusetts 02543

and

The Massachusetts Institute of Technology
Cambridge, Massachusetts 02139

June 1991

DOCTORAL DISSERTATION

Approved for Distribution:

Albert J. Williams 3rd, Chairman
Department of Applied Ocean Physics & Engineering

John W. Farrington
Dean of Graduate Studies

ACOUSTIC SCATTERING FROM ELASTIC ICE:

A FINITE DIFFERENCE SOLUTION

by

J. Robert Fricke

B. S. Biomedical Engineering, Vanderbilt University, 1974

M. S. Electrical Engineering, Vanderbilt University, 1977

Submitted in partial fulfillment
of the requirements for the degree of

DOCTOR OF PHILOSOPHY

at the
Massachusetts Institute of Technology
and the
Woods Hole Oceanographic Institution
June, 1991

Signature of Author_____.
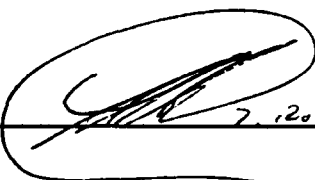
MIT/WHOI Joint Program in
Oceanographic Engineering

Certified by_____.

Arthur B. Baggeroer, Thesis Co-Supervisor
Professor, Departments of Electrical
and Ocean Engineering, MIT

Certified by_____.
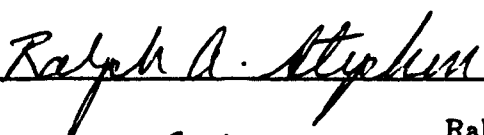
Ralph A. Stephen, Thesis Co-Supervisor
Senior Scientist, WHOI

Accepted by_____.

W. Kendall Melville
Chairman, Joint Committee for Oceanographic Engineering

Acoustic scattering from elastic ice:
A finite difference solution

by
J. Robert Fricke

Abstract

In this thesis I consider acoustic scattering from rough Arctic ice. Many scattering studies using the method of small perturbations (MSP) have been done; none are able to explain the low frequency scattering loss observed in long-range propagation experiments. Neither the magnitude nor the frequency dependence of the loss are properly modeled. Roughness and slope are required to be small if the MSP is to yield valid solutions. While the average roughness of the ice in the Arctic satisfies the smallness criterion, both of the restrictions are violated by discrete, large pressure ridges for the important frequency band of 10-100 Hz. An empirical fit to the observed loss has been derived and may be written $L_e = 3f^{\frac{3}{2}} dB/Km$, where f is frequency in kilohertz.

Reasoning that a full-wave solution holds the key to the scattering phenomenon, I use the finite difference method to solve the elastodynamic equations numerically. In contrast to the MSP, this technique allows arbitrary roughness, unrestricted in slope, displacement, or radius of curvature. Because of this feature, finite difference solutions provide direct, physical insight into the scattering mechanism of rough sea ice. The underlying analytic formulation treats the air-ice-water complex as a heterogeneous continuum in three dimensions. A plane strain approximation reduces the formulation to two dimensions. This, in turn, limits the computational burden when computing the finite difference solution, while permitting the salient features of the scattering process to be studied.

Numerical experiments involving scatter from individual roughness elements are conducted. A broadband source excites the numerical grid and the interplay of acoustic and elastic energy is observed during the course of the experiment. Two classes of roughness elements are considered: pressure ridge formations, of various shapes and sizes, and an ice edge. The specular loss from an ice edge is too low to explain the observed scattering loss in the central Arctic. Newly formed pressure ridges in the Arctic are loose aggregations of ice blocks with free flooding interstitial voids. These ridges cannot support shear strain and are modeled as fluid structures connected to elastic ice plates. Multi-year ridges, in contrast, are completely frozen and are better modeled as elastic structures.

Specular energy loss is affected by three identified phenomena: mass loading, excitation of plate waves, and a material dependent power law. The first two phenomena affect the magnitude of the specular loss, while the last affects the frequency dependence.

- Specular energy loss is proportional to ridge cross sectional area for both fluid and elastic ridges, and for a fixed ice density, area is proportional to mass per unit length.

- For a $3\,m$ ice plate surrounding an elastic ridge, the excitation of plate waves roughly doubles the specular loss relative to the loss of an identical ridge floating free. Loss from fluid ridges is unaffected by the presence or absence of a surrounding ice plate.

- Fluid ridges produce a dipolar diffraction pattern with a specular loss power law of $\sim f^{\frac{2}{3}}$, while elastic ridges produce a quadrupolar pattern and a power law of $\sim f^{\frac{9}{3}}$.

These results are used to argue that scatter from relatively young, large pressure ridges is the dominant scattering mechanism in long-range acoustic propagation. Future work with scale models at ultrasonic frequencies and full-scale field experiments are required before this hypothesis can be fully tested.

Thesis Co-Supervisor: Arthur B. Baggeroer
Professor, Departments of Electrical and Ocean Engineering, MIT

Thesis Co-Supervisor: Ralph A. Stephen
Senior Scientist, WHOI

3

... the sea is a mighty soul...

We can never pierce its infinite mystery – we may only

wand'er, awed and spellbound, on the outer fringe of it.

— L. M. MONTGOMERY,

ANNE'S HOUSE OF DREAMS (1915)

Acknowledgements

Writing is not hard for me. I spin words out quickly and smith them into shape with a certain ease. An acknowledgement of thanks, however, is another matter. The difficulty is not in forgetting names, which must perforce happen, but rather in boring readers for whom the names are flat and shapeless. Nevertheless, I am compelled to give thanks to certain individuals who have been instrumental in making the path to Ph.D. an enlightening and generally pleasant sojourn.

In matters of money, one must eat, have a place to sleep, pay tuition, and deal with other earthly things. It is to Tom Curtin and Bob Obrochta that I give thanks for the means to the end. Their financial support through the Office of Naval Research and the Arctic Acoustics Program was gratefully received.

In matters of intellect, the sure and steady minds of my thesis advisors Art Baggeroer and Ralph Stephen guided me through the rough waters along the way. In addition, dealings with Nick Trefethen and Henrik Schmidt were beyond value. Nick, in particular, led me through the early stages of my work and never swayed in his diligence to keep me on the right path.

In matters of technology, the finished document you now hold was composed and typeset on a computing machine, the workings of which I only vaguely understand. Eddie Scheer and Nan Galbraith managed to keep it all tied together and operating, even in the occasional last minute crunch. I thank them for their commitment.

In matters of spirit, many friends and acquaintances have reached out to me over the years. I'll not name them all. My soul, however, cries out to name a few. During the Arctic experiment, CEAREX '89, Keith von der Heydt and Neal McPhee provided companionship and ears seemingly interested in my musings on acoustic scattering – not to mention the comradery of escapades under the midnight sun on Nansen sleds at breakneck speeds. What fun!

My graduate student colleagues, some of whom have now crossed to the other side of Ph.D., kept things light but challenging, taking nothing for granted, always bringing me down to the core of my understanding. Peter Dahl, Dan Diperna, and D.J. Tang all helped mold my thinking.

Finally, there is a familiar quote concerning great women being the pillar of support for great men. While I don't claim to be a great man, my wife, Marianne, has been the keystone of my life. She has moved with me from home to home like an academic nomad, raised two magnificent kids, managed our finances, and reigned over another hundred sundry activities. All the while, she claims to have actually enjoyed my graduate school years. It is to Marianne that I dedicate this thesis, for it serves as a proxy of my life; you see, it is really I who am dedicated to her.

5

Contents

Chapter 1

Introduction

1.1 History and context

From the earliest observations during the International Geophysical Year in 1957-8, the cause of low frequency acoustic scattering loss in the Arctic Ocean has eluded complete scientific understanding. The practical consequences are many. Only low frequency sound, meaning 10-100 Hz, propagates over long distances in the Arctic. After traveling hundreds of kilometers, the sound arrives with strong amplitude and phase distortions that affect many fields of ocean acoustics such as the study of marine mammal vocalizations, seismic exploration, and long-range submarine detection.

The first long-range propagation experiments revealed that the Arctic sound channel transforms short, impulsive source signatures into long, dispersive chirps [31,45]. In addition, estimates of attenuation were found to be surprisingly large relative to similar estimates made in open oceans. These two phenomena were respectively attributed to multipath and rough surface scattering within the sound channel.

Ray tracing calculations soon described the multipath component of propagation. With a knowledge of the sound speed profile, it was possible to compute ray paths between

9
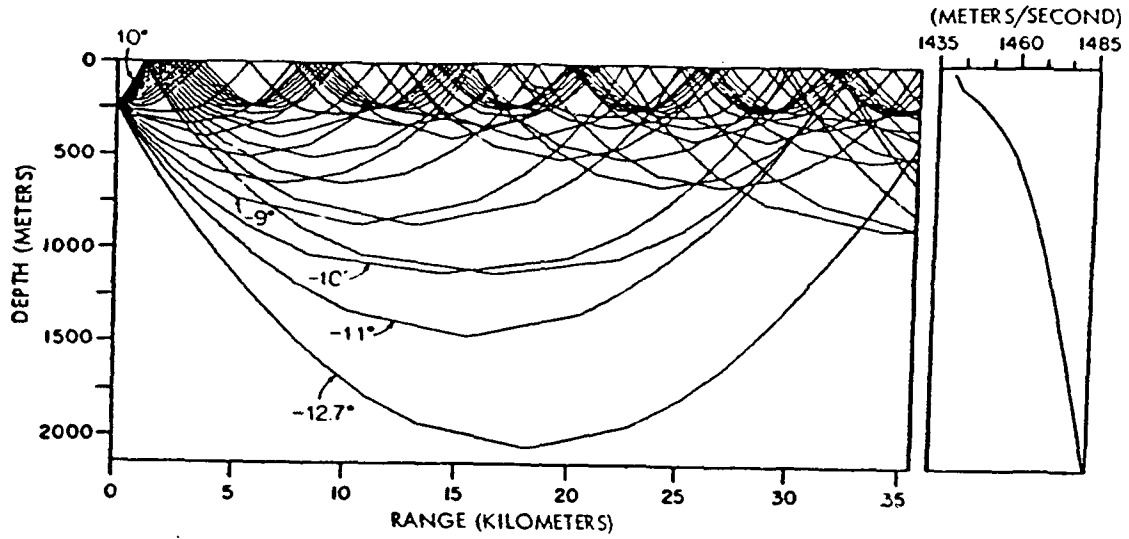
Figure 1.1: Sound speed profile and corresponding ray diagram. The Arctic sound channel has a large gradient of $g \simeq 0.06\,s^{-1}$ from the surface down to about $300\,m$ then a smaller gradient of $g \simeq 0.016\,s^{-1}$ from $300\,m$ on down. This sound speed profile causes the upward refraction of rays as seen in. (This figure was taken from Diachok [12].)

a source and receiver. An example is shown in Figure 1.1 of the results of a ray tracing calculation for the typical sound speed profile shown. The sound channel is said to be upward refracting. This effect is caused by a monotonically increasing sound speed profile, which, in turn, is caused by monotonically increasing pressure in an isothermal water column. Due to the upward refracting sound speed profile in the Arctic, rays bounce repeatedly along the undersurface of the ice as the sound propagates horizontally. For a given source and receiver location, many rays, known as the eigenrays, connect the two points. The eigenray ensemble forms a multipath complex that causes dispersive arrivals and may be thought of in terms of normal-modes [9,29]. In stark contrast to the known cause and effect relationship between multipath and dispersion, the relationship between rough surface scattering and attenuation is not clear.

By virtue of the ray-mode equivalence theorem, every long-range propagation mode comprises an infinite number of rays. Imagine following an acoustic energy packet along any

10

particular ray as it propagates down the channel. In all cases the energy packet encounters the ice time and again. The ice encounters are interleaved with curved paths through the water. At low frequencies the absorption and volume scattering loss in the water is negligible and cannot explain the attenuation observed in experiments [67, p. 102]. The excess attenuation must be due to the local scatter that occurs at each ice encounter. Thus, the local scattering process associated with a single ice encounter is a fundamental component of acoustic loss over long distances.

Many theories have attempted to describe the scattering losses. These theories have roots in the classical scattering literature that dates to Lord Rayleigh's investigation of scatter from a corrugated surface [59, V.II, Art. 272]. Due to analytical complexities, the theories have been developed for simple scattering problems with features such as "fluid" ice [13], small roughness [30], single scatter [41,42], rough pressure release interfaces [13], and ensembles of identical scatterers [66]. To date, none of the theories can completely account for the observed loss, which has a frequency dependence of $\simeq f^{1.5}$ as seen in Figure 1.2. Buck and Greene [6] derived an empirical fit to the data and described the excess loss due to rough surface scattering. Early analytic solutions, assuming a rough free surface, led to a loss function with the correct frequency dependence, $\simeq f^{1.5}$, but the magnitude was too small [46]. Later work with an "improved" model, based on the impedance of the ice, gave worse results; the frequency dependence was $\simeq f^3$ and the magnitude was much too low [46]. Hence, the best predictions of scattering loss in units of dB/Km are much lower than the observed loss, as shown in Figure 1.2, and have the wrong frequency dependence [44].

Since, as described above, the unexplained long-range propagation loss is attributed to numerous local encounters with the ice, in this thesis I study ice scattering from a local, short-range perspective. Specifically, I focus on individual scattering events and watch the interplay of acoustic and elastic energy during the passage of a sound pulse. My primary
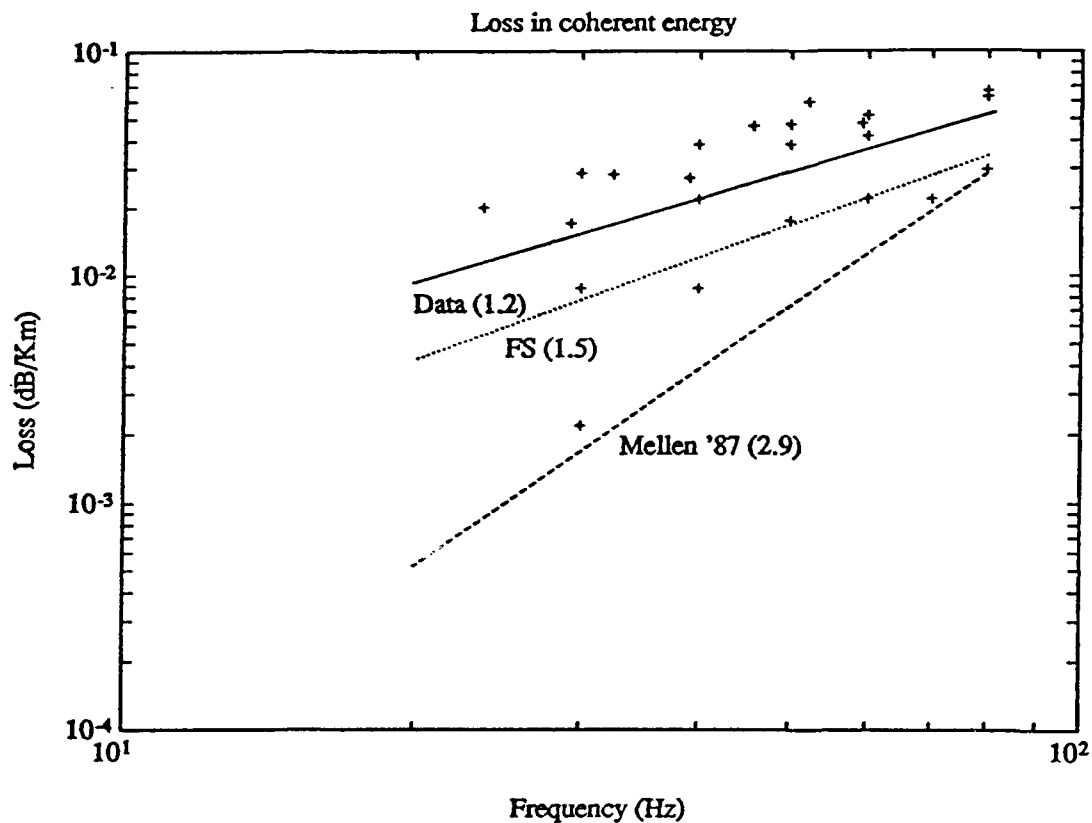
Figure 1.2: Observed specular energy loss from field data compared to analytic predictions. The measured data has a frequency dependence of $\simeq f^{1.5}$. The analytic solutions are based on the method of small perturbations. The curve marked "FS" assumes a rough free surface. This prediction has the correct slope but does not consider the mass loading effect of the ice. The curve marked "Mellen '87" is based on an impedance formulation, which in this frequency range is dominated by mass loading [46]. Here the slope is wrong and the magnitude is very low. The "improved" impedance solution is worse than the earlier free surface solution.

12

goal is to develop a better understanding of the local ice scattering process. I want to understand the physical mechanism of the scattering process and to quantify the acoustic and elastic energy partitioning as a function of ice geometry and propagation angle. My original hypothesis was that the unexplained loss would be accounted for by conversion of acoustic energy in the water into flexural energy in the ice. This process permanently extracts energy from the coherent forward propagating signal. As my research proceeded, it became clear that this hypothesis was too simple. The scattering loss is increased by the excitation of plate waves, as originally conjectured, but the frequency dependence of the loss is still wrong. As I show later, the frequency dependence can be explained by an appropriate choice of material properties for the ice.

1.2 The problem

The scattered field for a given acoustic excitation is determined by the geometry and material composition of the ice and the surrounding fluid media.

The geometric aspects of this problem are discussed first. At low frequency two elemental scattering structures are important in the Arctic: pressure ridges and leads. Ridges are piles of disoriented ice blocks, formed by compressive forces acting on more or less flat sheets of ice. The ice sheets are forced together to the point of failure during the ridge building process. The process is illustrated in Figure 1.3(a). Leads, by contrast, are formed by tensile forces pulling an ice sheet apart to the point of failure and producing an open water gap ranging in size from virtually zero to tens of kilometers [28]. This process is illustrated in Figure 1.3(b).

The roughness of the Arctic ice has length scales ranging from sub-crystalline dendrites at $O(10^{-3}\,m)$ to pressure ridges and keels at $O(10\,m)$ to tabular ice islands at $O(10^3\,m)$ [17,38,60]. I focus on the midrange of the roughness spectrum, where ridge size is matched to the wa-

13
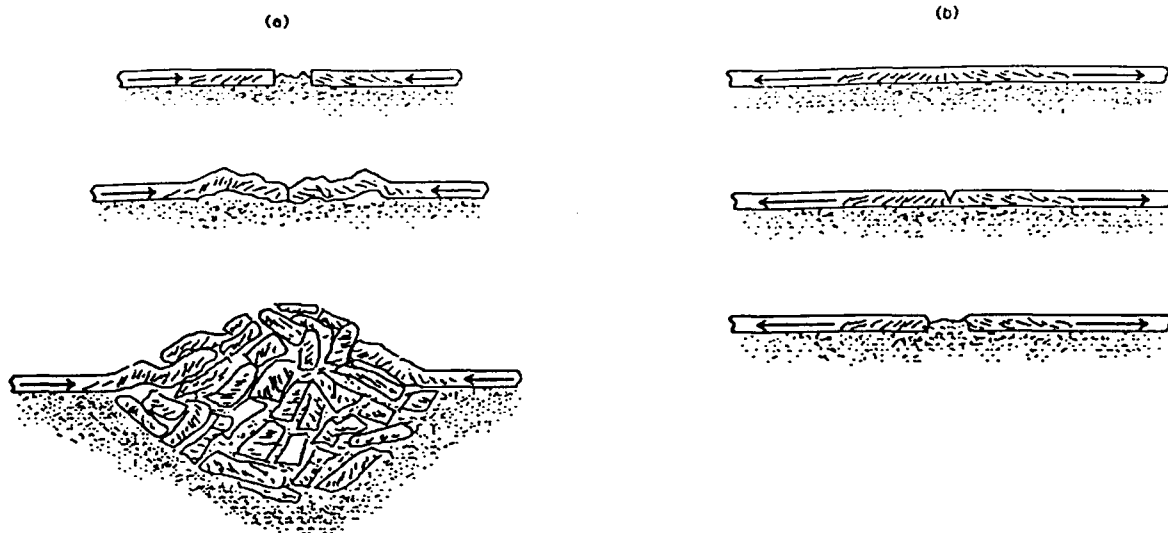
Figure 1.3: Ridge and lead formation. (a) Pressure ridges are formed when two sheets of ice of comparable thickness are forced together. The ridge builds by breaking blocks of ice from the surrounding sheets and piling them into the sail and keel of the ridge. (b) Leads are formed by the opposite mechanism; tensile forces pull the ice apart forming open water gaps.

ter wavelength at low frequency, $\lambda = O(10\,m)$. At this length scale, scattering effects are complicated [12]. Furthermore, field observations show that ridge keel size and spatial frequency, that is number of keels per kilometer, are proportional [21,70]. Thus, if keels occur in the sound path, the scattering effect of a large keel is aggravated by the tendency of large keels to group together.

Now consider leads. They occur over the entire Arctic ocean but are the dominant roughness feature in the marginal ice zone, which is the sometimes large transition region between the central Arctic and the open ocean [11,71].

The elastic nature of the ice canopy adds complexity to the problem. Not only are reflections and scatter seen in the water below the ice but plate waves are excited in the ice sheet as well [24]. Two types of plate waves exist in thin ice. One type is a bending wave called the flexural or anti-symmetric Lamb wave, and the other type is a compressional

14

air: $\rho = 1.2 \ Kg/m^3, C_p = 340 \ m/s, C_s = 0$

ice: $\rho = 910 \ Kg/m^3, C_p = 3500 \ m/s, C_s = 1600 \ m/s$

water: $\rho = 1000 \ Kg/m^3, C_p = 1500 \ m/s, C_s = 0$
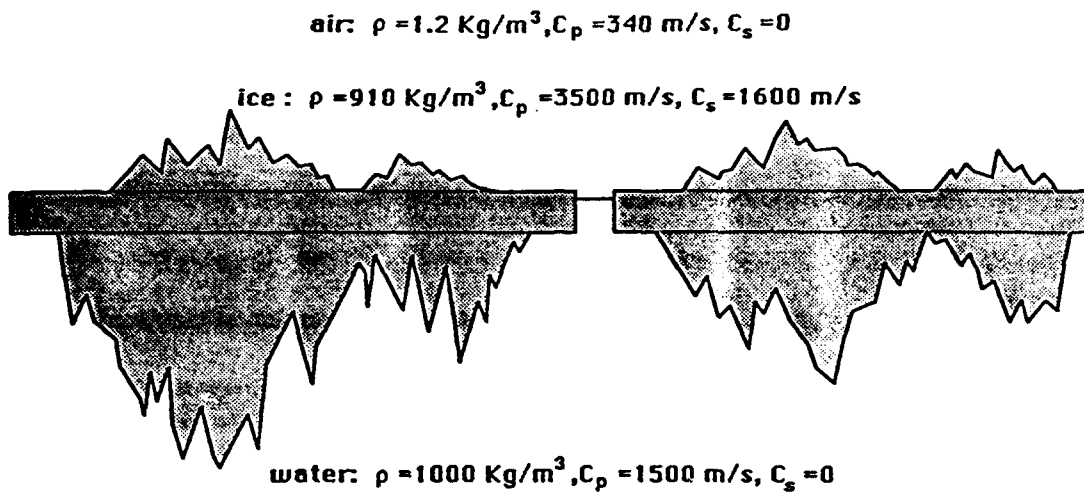
Figure 1.4: Idealized rough ice model. Abrupt transitions are assumed between air, ice, and water with the indicated material properties changing across the boundary.

wave called the longitudinal or symmetric Lamb wave. If ice were a fluid, the flexural wave could not exist. In this case, the longitudinal wave would propagate like the compressional energy in a Pekeris waveguide, but the waveguide would have rough boundaries. Thus, for real ice the scattering process is composed of a number of distinct parts: reflection and diffraction, which are primarily geometric effects, and mode conversion between acoustic and elastic energy, which is an elastic material effect.

An idealized air-ice-water model is characterized by large, abrupt changes in material property as shown in Figure 1.4. Each material is completely described by three properties: density, bulk compressional velocity, and shear velocity. The contrast in density between ice and water is modest, but between ice and water or air it is enormous: three orders of magnitude. For bulk compressional velocity, the contrast is never more than about one order of magnitude. Ice is the only material in this model which has a shear velocity. The transition between materials is almost infinitely sharp; a more precise description of the transition is deferred to Chapter 2. The ice-air or ice-water interface is a true material boundary, not a pressure-release surface. The high-contrast discontinuity between air and

15

ice or water acts like a stationary shock, which is important in the development of the modeling algorithm. In nature, the ice-water boundary is sharp in some locations [25] and not sharp in others [33]. When the boundary is not sharp, the transition region is typically a few centimeters thick, and therin the ice is slushy [33]. This slush ice behaves more like a visco-elastic material than like an elastic material. However, since the region is thin with respect to the acoustic wavelength, I ignore the visco-elastic effect and model the ice as an isotropic elastic material.

1.3   The approach

Scattering investigations may be grouped into four broad categories: field experiments, scale model experiments, analytical solutions, and numerical solutions. Each of these approaches has its strengths and weaknesses, which must be weighed in light of achieving my research objective. In choosing a method to study ice scattering the most important aspects of the problem must be identified and isolated, thereby simplifying the analysis and interpretation of the results. By isolating individual aspects of the problem, say the effect of ice heterogeneity from geometry, it is possible to build a comprehensive picture of the scattering process as a whole. This is the synthesis approach and the approach I seek.

Field data obviously contains the truest scattering information. Data collection in the field, however, is plagued by lack of observations that are important for meaningful data interpretation. Even if it were possible to measure everything affecting the data, which it never is, problems would still exist. Principally, no simplifications can be made. If, as suggested above, one wishes to study of effects of ice geometry versus material heterogeneity, this cannot be done. Analysis of field data is exactly the opposite of the desired approach; the whole must be analyzed to reveal its constituents rather than the other way around.

Having eliminated field experimentation, one might consider scale model experiments,

which provide a measure of control impossible in the field; materials can be made homogeneous, geometries can be prescribed and machined exactly, and sources and receivers can be placed precisely [43]. Building the models and instrumenting the experiment, however, is a tedious, time-consuming process. This aspect of the scale model approach tends to discourage its use if many different models are to be considered. Furthermore, it is difficult to visualize the acoustic and elastic fields as the scattering process evolves. Because of this, a measurement and analysis problem nearly as complicated as that for field data remains.

For a number of reasons, the ice scattering problem is not easily solved analytically. In particular, it is not possible to develop analytic solutions for the field scattered from realistic structures. While some statistically formulated problems can be solved analytically, they place restrictions on the form of the roughness such as small heights, small gradients, or large curvatures. Solutions that exist for simple problems do not explain the observed scattering loss seen in long-range propagation experiments. Furthermore, analytic solutions are often farfield solutions and do not provide the physical insight necessary to investigate the scattering mechanism at the fluid-solid boundary.

On the other hand, analytic solutions are powerful tools for gaining insight into the character of the scattered field from simple canonical objects like fluid and elastic cylinders. To the extent that the ice scattering problem can be decomposed into canonical parts, analytic solutions contribute to a better understanding of rough surface scattering. Although I do not solve the ice scattering problem analytically, I do use analytic solutions as a guide to understanding the character of certain scattering phenomenon.

Numerical methods are the remaining option. They provide solutions to otherwise intractable problems. Specifically, finite difference solutions to the elastodynamic equations of motion are considered here. This method permits arbitrary specification of geometries and material properties, limited only by the coarseness of the grid. The acoustic and elastic

fields are trivial to visualize since these are the computed fields and the solution can be sampled any place or time. With this visualization capability, the scattering process can be observed in detail as acoustic energy encounters a roughness element in the elastic plate. The finite difference method is not perfect, of course; the computed solutions are not exact. In this study the geometry is limited to two dimensional scatter from one dimensional rough surfaces. Furthermore, roughness with a length scale smaller than the spatial sampling interval is ignored. The limitation to a two dimensional solution renders it insensitive to any scattering process involving transverse motion. These processes include out of plane scatter due to oblique azimuthal incidence on linear features and to two dimensionally rough surfaces. Energy scattered into horizontal shear (SH) motion by such processes is not computed in the two dimensional solutions. These weaknesses, however, are outweighed by the strengths that bear on the scattering problem. For this reason, I have chosen finite difference modeling as the best method for gaining insight into the local scattering phenomenon.

1.4   Preliminary effort

In seismology, plane strain linear elastodynamics are used to study wave propagation through two-dimensional heterogeneous media [63]. The plane strain approximation models the cross section of an infinitely long slab extending in and out of the observation plane. For the ice scattering problem it is desirable to use a heterogeneous continuum formulation to avoid explicitly matching boundary conditions between different materials. The latter approach is especially odious for spatially varying boundaries. In that case, at each point along the boundary the algorithm must compute the local normal, rotate the coordinate system, match the boundary conditions, then rotate back. Either custom coding for each model or some kind of boundary tracker is required to implement this technique. In con-

trast, the heterogeneous formulation handles the boundaries between materials as internal boundaries of a single spatially varying continuum. Using this approach, arbitrary models can be specified with no recoding.

The apparent price to pay for ease of coding is two fold: an increased operation count for elastic versus fluid materials and an increased number of grid points due to the small spatial increment dictated by the low sound speed of air. For the ice scattering problem, neither of these actually affect the efficiency of the implementation very much. The operation count is kept low in fluid regions by checking for zero shear modulus; in which case, it is known that the two normal stresses, σ_{11} and σ_{22}, are equal and the shear stress, σ_{12}, is zero. With this knowledge, the operation count can be reduced nearly to the level of a pure fluid code. Thus, the heterogeneous formulation provides a convenient framework within which to compute the field in a fluid or an elastic material without loss of generality and without over-computation.

The spatial discretization for the ice scattering problem is actually limited by the relative thinness of the ice and not the low sound speed in air. Further, for simplicity, I take the spatial increment to be uniform throughout the computational domain. Consequently, it makes no difference, in terms of the spatial increment, whether or not air is included in the model. This, obviously, is a special feature of the ice scattering problem and does not generalize to other rough surface studies.

The plane strain approximation of the linear elastodynamic equations for smooth heterogeneous materials undergoing infinitesimal strain can be written[†]

$$v_{1,t} = b(\sigma_{11,1} + \sigma_{12,2}),$$

$$v_{2,t} = b(\sigma_{12,1} + \sigma_{22,2}),$$

[†]The notation $(1.1)^{1,2}$ indicates equations 1 and 2 of the system labeled as Equation (1.1). Similar notation is used throughout.

19
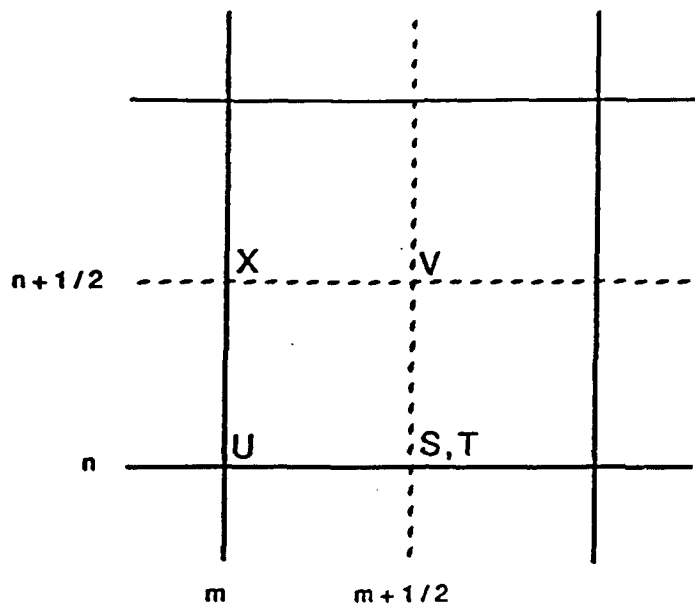
Figure 1.5: Virieux staggered grid. Stresses and velocities are placed such that central differences can be computed with a compact stencil. The time step size is $k = \Delta t$, and the time step index is l.

$$\sigma_{11,t} = (\lambda + 2\mu)v_{1,1} + \lambda v_{2,2},$$

$$\sigma_{22,t} = \lambda v_{1,1} + (\lambda + 2\mu)v_{2,2},$$

$$\sigma_{12,t} = \mu(v_{2,1} + v_{1,2}), \tag{1.1}$$

where v_1 and v_2 are the particle velocities in the horizontal and vertical directions and σ_{ij} is the symmetric stress tensor with normal stresses σ_{11} and σ_{22} and shear stress σ_{12} [19, Appendix A] [48, p. 120]. Partial differentiation with respect to time is indicated by $(\cdot)_{,t}$, while differentiation with respect to the x_i spatial coordinate is indicated by $(\cdot)_{,i}$. Finally, λ and μ are Lamé parameters, and $b = \rho^{-1}$ is buoyancy or inverse density. The first two equations of (1.1) are statements of Newton's second law, $F = ma$. The last three equations are Hooke's law, $F = kx$.

20
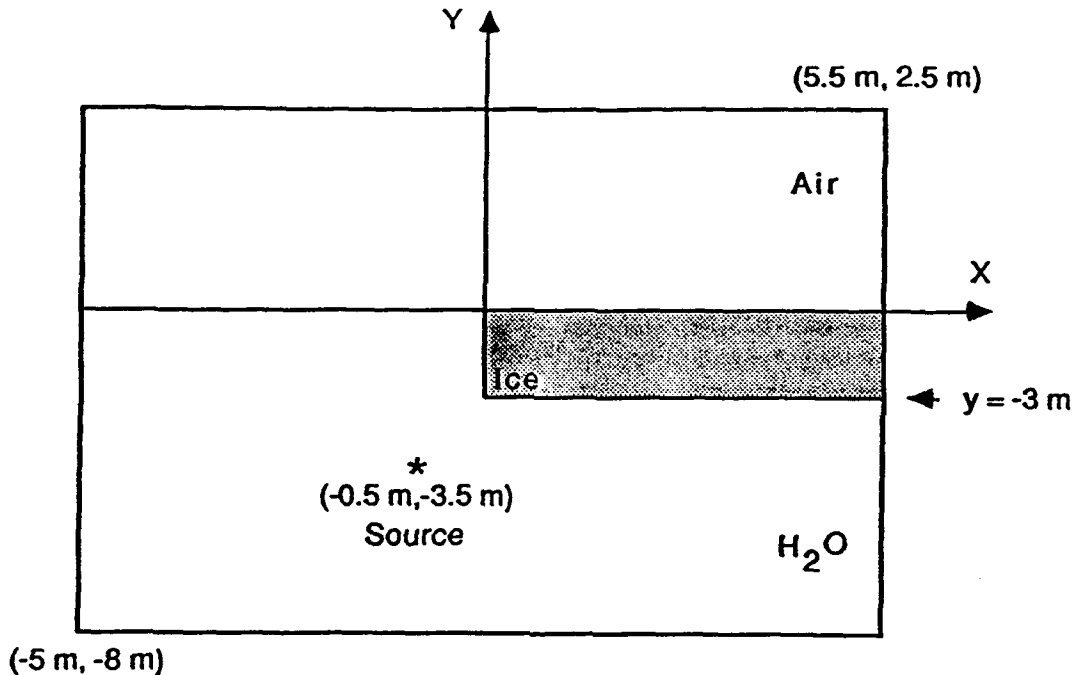
Figure 1.6: *Ice edge model. Scattering experiments from this model are unstable using the Virieux scheme.* The material properties are as follows: for air, $C_p = 340\,m/s$ and $\rho = 1.2\,Kg/m^3$; for ice, $C_p = 3500\,m/s$, $C_s = 1600\,m/s$, and $\rho = 910\,Kg/m^3$; and for water, $C_p = 1500\,m/s$ and $\rho = 1000\,Kg/m^3$. The ice is $3\,m$ thick and the center frequency of the source is $55\,Hz$.

These equations, or their second order equivalent, have been solved using many finite differences schemes for the computation of synthetic seismograms [3,14,26,40,69]. Stephen has written an excellent review on the use of finite difference solutions to elastic wave propagation in heterogeneous media [63]. To my knowledge, finite differences have never been used to study the ice scattering problem.

Virieux [69] discretized these equations on a staggered grid in both space and time as shown in Figure 1.5. His correspondence between continuous and discrete field variables is

$$(v_1, v_2, \sigma_{11}, \sigma_{22}, \sigma_{12})^T \Leftrightarrow (U, V, S, T, X)^T. \tag{1.2}$$

Virieux's analysis indicates his system of difference equations is applicable to arbitrary,

heterogeneous models containing both solids and liquids. Encouraged by the success of Virieux and the others referenced above, I attempted to run the ice edge model shown in Figure 1.6. One might find such a feature at a lead or between floes in the marginal ice zone. To my dismay the computation is unstable and results in floating point overflows. The unstable point is in the air just above the three-phase corner, where air, ice, and water come together. It is clear that Virieux's heterogeneous formulation is not sufficiently general to handle the ice scattering problem. Furthermore, several other finite difference schemes are also unstable. Evidently, the analytic system of equations do not adequately describe the elastodynamic motion associated with the high-contrast air-ice-water interface.

1.5   The approach, revisited

Since the heterogeneous linear elastodynamic formulation is unstable for the ice scatter-ing problem, an improved modeling algorithm is required. I derive a set of quasi-linear elastodynamic equations for heterogeneous, not necessarily smooth materials undergoing infinitesimal strain. I also demonstrate why a quasi-linear system of equations is needed for a problem that, intuition would say, requires only a linear system. All terms in the quasi-linear system are analyzed for the magnitude of their contribution in the presence of a high-contrast discontinuity. Further, since the large, abrupt changes in material proper-ties behave like stationary shocks, a differencing scheme able to handle these shocks and remain stable is selected. The development of an improved modeling algorithm, then, is the secondary goal of my research.

1.6 Overview of thesis

In correspondence to my research goals, namely, one, the elucidation of the local scattering process and two, the development of an improved modeling algorithm, there are two parts to this thesis. Since the improved algorithm must come first, Chapters 2 and 3 address its development. Chapter 4 is a transition chapter, which describes the data analysis approach used to reduce the experimental data. Chapters 5 and 6 describe the numerical experiments and analysis conducted to elucidate the local scattering process.

Specifically, in Chapter 6 I argue, based on the experimental results of Chapter 5, that the excess scattering loss observed in long-range propagation experiments can be explained by scatter from "fluid" ridges connected to elastic ice sheets. A fluid ridge models a newly formed pressure ridge, which is weak in shear and behaves acoustically like a fluid object. Justification for this argument is given in Chapter 5, Section 5.2.1.

Finally, Chapter 7 provides an executive summary of the significant contributions of this thesis and some implications and directions for future research.

Chapter 2

Analytic development

2.1 Overview

In this chapter I derive the quasi-linear elastodynamic equations of motion needed to solve the rough ice scattering problem. The system comprises two conservation equations, mass and linear momentum, and a constitutive equation relating stress to momentum.

Usually the elastodynamic equations in Eulerian coordinates are linearized and have one equation for momentum, or equivalently velocity, and one constitutive equation. I show that the linear system is ill-posed if a sufficiently large density gradient exists. Detailed arguments are given in the section on dimensional analysis, Section 2.5, and in the discussion of Section 2.6.

2.2 Physical assumptions

Equations of motion are derived by first making a priori assumptions about the physical effects that are important in the problem to be studied. For the ice scattering problem I derive the equations in conservation law form for heterogeneous material undergoing in-

finitesimal strain in Eulerian coordinates. I ignore viscosity since viscous boundary layers are small for acoustic waves in water and air [4, p. 308], [15, p. 15]. Recall, in Section 1.2 I described the ice-water boundary as being occasionally a thin, slushy, visco-elastic transition between fluid water and elastic ice. I ignore the effects of this transition region in this thesis, thus eliminating consideration of viscous losses altogether. Gravity is ignored since it only provides static stability to the heterogeneous model and plays no part in the wave propagation process. Intrinsic attenuation, the irreversible conversion of mechanical energy to heat, in air, ice, and water is assumed negligible since the experiments model only short ranges at low frequency. Finally, the scattering process is assumed to be adiabatic, which means energy can be computed from the mechanical field variables, and there is no need for a separate energy equation [47, p. 264, 355].

I use a phenomenological model for the ice which is assumed to be a simple material described by constant Lamé parameters, λ, μ, and ρ. This is in contrast to a more complete composite material model which comprehends the heterogeneous, porous nature of sea ice. Since the exact composite material of ice is not known and varies from point to point, it is more appropriate to use a simple material model. Furthermore, even though ice is known to be anisotropic, for simplicity I take it to be isotropic.

The intent of this study is to capture the phenomenological character of the ice scattering process by separating the effects of geometry from those of the material. Simple material descriptions and simple geometries provide leading order insight into the scattering process. Future studies can be done using refined definitions of geometric complexity and material property to extend the understanding.

2.3 Conservation equations

When computing a numerical solution using finite differences, it is essential to have a set of well-posed analytic equations or else convergence to a stable solution is never reliable. Since the linear system of Equations (1.1) produces unstable results using Virieux's scheme (and many others, not shown), development of the equations of motion from first principles is prescribed. Specifically, the conservation equations for mass and momentum are derived with the help of the kinematic transport theorem. This theorem relates the total rate of change of a conserved field quantity, also known as the total or material derivative, to fluxes and partial time derivatives of the conserved quantity.

There are two ways to view the total derivative. The first is to consider the region $\mathcal{D}$, which always contains a fixed amount of material as shown in Figure 2.1. The volume deforms under the action of surface forces but no material crosses into or out of the defined region; it behaves like a pinched balloon. In this case, the total derivative of the conserved quantity is computed as

$$\frac{d}{dt} \int_{\mathcal{D}} \Theta dV, \tag{2.1}$$

where Θ is a field quantity per unit volume. The total time derivative operates on the entire integral including the rate of change of the region boundary, $\partial \mathcal{D}$. This is a Lagrangian point of view, where individual particles of material are tagged and followed as they move. If one wishes to actually track the location of a particular packet of material, this formulation is the one to choose. But for the infinitesimal and oscillatory particle motion associated with acoustic and elastic wave propagation, the Lagrangian approach is unnecessary.

The other way to view the total derivative is to consider a region, $\mathcal{D}$, enclosed by a surface, $\partial \mathcal{D}$, fixed in an arbitrary reference frame. The total derivative of the conserved quantity, Θ, is the integral of the partial time derivative of Θ in $\mathcal{D}$ plus the integral of the flux of Θ across $\partial \mathcal{D}$. In this case the volume acts like a screen box immersed in a moving
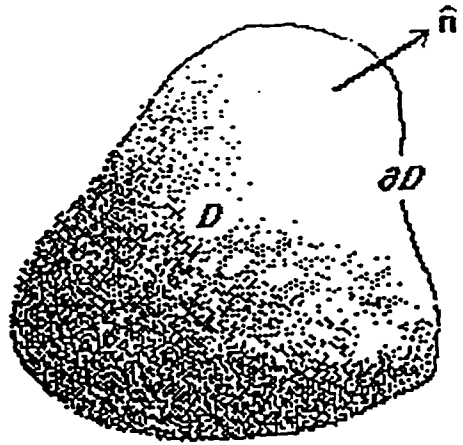
Figure 2.1: Material volume for derivation of kinematic transport theorem. The volume is denoted as D with the boundary ∂D with an outward pointing normal. The material contained in D must be a continuum but may have high gradients of the material properties.

fluid. This is the Eulerian point of view and the total derivative is computed as

$$\int_D \Theta_{,t} dV + \int_{\partial D} \Theta v_i n_i dS, \tag{2.2}$$

where v_i are the material velocities and n_i are the direction cosines at the region boundary. Since there is no need to track individual packets of material to describe infinitesimal wave propagation, the Eulerian approach is sufficient. In addition, an Eulerian formulation is more convenient to implement than a Lagrangian formulation. For these reasons I use an Eulerian formulation for the equations of motion.

Now, the kinematic transport theorem is stated by explicitly noting the equivalence of Equation (2.1) and (2.2). Batchelor [4, p. 131] derives the theorem more formally and states the result in two ways. For an arbitrary region, D, bounded by the surface, ∂D, with outward pointing normal pictured in Figure 2.1, there are two transport identities. For a material property per unit volume, Θ,

$$\frac{d}{dt} \int_D \Theta dV = \int_D \Theta_{,t} + (\Theta v_i)_{,i} dV \tag{2.3}$$

27

and for a material property per unit mass, F,

$$\frac{d}{dt} \int_D \rho F dV = \int_D \rho \frac{dF}{dt} dV, \tag{2.4}$$

where the operator $\frac{d}{dt} = \frac{\partial}{\partial t} + v_i \frac{\partial}{\partial x_i}$. On the left side of both equations the amount of material is arbitrary but fixed, while on the right volume is arbitrary but fixed.

The equation for conservation of mass is derived by letting Θ be mass per unit volume, or density, ρ, and using the kinematic transport theorem Equation (2.3). Since mass is conserved and the region D is arbitrary,

$$
\begin{aligned}
\rho_{,t} &= -(\rho v_i)_{,i}, \\
&= -\nu_{i,i}, \tag{2.5}
\end{aligned}
$$

where $\nu_i \equiv \rho v_i$ is the linear momentum in the i direction.

The equation for conservation of linear momentum is derived by recognizing that the total derivative of momentum in D must be balanced by the traction, T_i, applied on the surface of the region, ∂D. Mathematically the balance is expressed

$$\frac{d}{dt} \int_D \nu_i dV = \int_{\partial D} T_i dS. \tag{2.6}$$

Using the kinematic transport theorem, Equation (2.3), on the left and the traction stress relation, $T_i = \sigma_{ij} n_j$, and the divergence theorem on the right we find for an arbitrary region

$$\nu_{i,t} = -\left(\frac{\nu_i \nu_j}{\rho}\right)_{,j} + \sigma_{ij,j}. \tag{2.7}$$

28

These conservation equations differ from the usual elastodynamic equations in two ways. First, I have retained the mass equation, and second, I have kept the quasi-linear convective term in the momentum equation. Later I show under what circumstances these extra terms may be dropped and the system reduced to the more common linear system.

2.4 Constitutive equation

The constitutive equation is fundamentally different from the conservation equations developed in the last section. It is an equation of state relating stress, σ_{ij}, to the conserved quantities ρ and ν_i and provides closure to the system of equations. For infinitesimal, adiabatic particle motion stress is only due to the current state of deformation or strain. In particular, Graff [19, Appendix A] shows that stress is related to strain energy (or potential energy), W, by

$$\sigma_{ij} = \frac{\partial W}{\partial \epsilon_{ij}}, \tag{2.8}$$

where $\epsilon_{ij} = \frac{1}{2}(v_{i,j} + v_{j,i})$ is strain. For infinitesimal strains the Taylor expansion of strain energy is valid and may be written

$$
\begin{aligned}
W(\epsilon_{ij}) &= W_o + \frac{\partial W_o}{\partial \epsilon_{ij}}\epsilon_{ij} + \frac{1}{2}\frac{\partial^2 W_o}{\partial \epsilon_{ij}\partial \epsilon_{kl}}\epsilon_{ij}\epsilon_{kl} + O(\epsilon_{ij}^3) \\
&\equiv W_o + \overset{\circ}{\sigma}_{ij}\,\epsilon_{ij} + \frac{1}{2}C_{ijkl}\epsilon_{ij}\epsilon_{kl} + O(\epsilon_{ij}^3),
\end{aligned} \tag{2.9}
$$

where

$$W_o \equiv W(\epsilon_{ij})\,|_{\epsilon_{ij}=0} \tag{2.10}$$

is the arbitrary strain energy datum, $\overset{\circ}{\sigma}_{ij}$ is residual stress at zero strain, and C_{ijkl} are elastic constants. Setting the residual stress to zero for convenience and differentiating Equation (2.9) with respect to strain yields the linear stress-strain relation

$$\sigma_{ij} = C_{ijkl}\epsilon_{kl}. \tag{2.11}$$

29

Consider the validity of this relation in the vicinity of a contact discontinuity in the idealized air-ice-water model. I stated in Chapter 1 that the transition between materials is almost infinitely sharp. The description of the material transition must be made more precise in light of two comments about the stress-strain relation.

First, the strain energy, W, is assumed to be a differentiable function of strain, ϵ_{ij}, which itself, must be spatially differentiable. This is a problem at a fluid-solid contact discontinuity if the material transition is truly infinitely sharp. In this case some of the strain components are discontinuous and hence are non-differentiable. One way around this dilemma is to use one-sided derivatives and match boundary conditions at the discontinuity. But this is exactly what I am trying to avoid in going to a heterogeneous continuum formulation. Another way to handle this problem is to restrict the idealized model in such a way that material transitions occur very quickly over a finite but small region and have well defined spatial gradients. If the material properties are spatially differentiably then the field variables are differentiable and the problem is well posed [23]. For low frequency approximations the distinction between the two models, an infinitesimal transition width versus a finite but small transition width, is negligible if the transition width is small enough in the latter case. The finite difference solution discussed in the next chapter makes an implicit, but unknown and irrelevant, assumption about the transition model as shown in Figure 2.2.

The second comment has to do with the elastic constants. The stress-strain relation is linear since only the quadratic terms in the Taylor expansion are retained. Thus the C_{ijkl} are constants with respect to strains, that is

$$\frac{\partial C_{ijkl}}{\partial \epsilon_{mn}} \equiv 0. \tag{2.12}$$

This is not to say the elastic properties are constants with respect to the spatial coordinates.
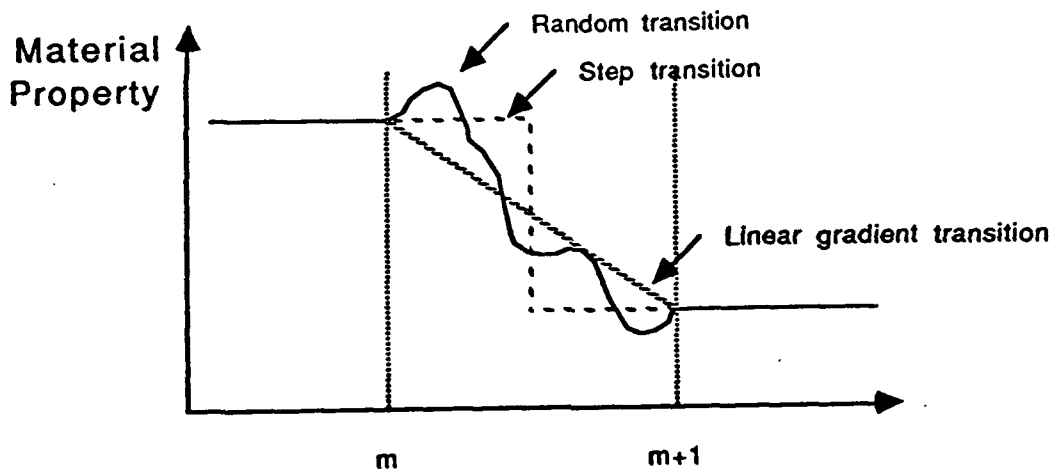
Figure 2.2: Material property transition model between grid points in the finite difference scheme. The transition model is never defined, only the material property values at the grid points, m and $m+1$, in this case. I have suggested three models out of an infinite set that are possible with the material specification at only two points. In choosing the spatial increment, $h = \Delta x$, one is saying that the details of the model and the details of the solution for smaller lengths scales are not important to the problem.

In particular, I certainly admit the possibility that

$$\frac{\partial C_{ijkl}}{\partial x_m} \neq 0. \tag{2.13}$$

For an isotropic, but possibly heterogeneous, material the elastic constants reduce to

$$C_{ijkl} = \lambda \delta_{ij}\delta_{kl} + \mu(\delta_{ik}\delta_{jl} + \delta_{il}\delta_{jk}), \tag{2.14}$$

where λ and μ are Lamé constants that may be spatially varying. Using this in the general stress-strain relation, Equation (2.11), and differentiating with respect to time yields the isotropic stress-strain relation

$$\sigma_{ij,t} = \lambda \epsilon_{kk,t} \delta_{ij} + 2\mu \epsilon_{ij,t},$$

$$= \lambda v_{k,k} \delta_{ij} + \mu(v_{i,j} + v_{j,i}),$$

$$= \lambda \left(\frac{\nu_k}{\rho}\right)_{,k} \delta_{ij} + \mu \left[\left(\frac{\nu_i}{\rho}\right)_{,j} + \left(\frac{\nu_j}{\rho}\right)_{,i}\right]. \tag{2.15}$$

This is the time derivative of the usual isotropic stress-strain relation written in terms of momentum and density instead of velocity.

In going from Equation $(2.15)^1$ to $(2.15)^2$ I have used the linearized equation of strain

$$\epsilon_{ij} = \frac{1}{2}(u_{i,j} + u_{j,i}), \tag{2.16}$$

where u is particle displacement. A more complete description of strain includes quadratic terms in the displacement and may be written [32, p. 2]

$$\epsilon_{ij} = \frac{1}{2}(u_{i,j} + u_{j,i} + u_{k,i}u_{k,j}). \tag{2.17}$$

In the next section on dimensional analysis I show that the quadratic terms can always be dropped for the finite difference solution and need be considered no further.

2.5 Dimensional analysis

The quasi-linear elastodynamic equations comprise the conservative and constitutive equations, which are written in an Eulerian reference frame as

$$
\begin{aligned}
\rho_{,t} &= -\nu_{i,i}, \\
\nu_{i,t} &= -\left(\frac{\nu_i \nu_j}{\rho}\right)_{,j} + \sigma_{ij,j}, \\
\sigma_{ij,t} &= \lambda \left(\frac{\nu_k}{\rho}\right)_{,k} \delta_{ij} + \mu \left[\left(\frac{\nu_i}{\rho}\right)_{,j} + \left(\frac{\nu_j}{\rho}\right)_{,i}\right].
\end{aligned} \tag{2.18}
$$

When can the quasi-linear momentum term and the mass equation be dropped to yield the linear elastodynamic equations? To answer this question I use dimensional analysis to find the relative size of the various terms. Nothing is lost by reducing the system to one dimension (1-D),

$$
\begin{aligned}
\rho_{,t} &= -(\rho v)_{,x}, \\
\nu_{,t} &= -(\rho v^2)_{,x} + \sigma_{,x}, \\
\sigma_{,t} &= \mathcal{L} v_{,x},
\end{aligned} \tag{2.19}
$$

where $v \equiv (\nu_1/\rho)$, $\sigma \equiv \sigma_{11}$, and $\mathcal{L} = \lambda + 2\mu$. My primary concern is what happens at material boundaries since the solution in smooth regions is well understood [23]. Velocity and stress are used on the right side of Equation (2.19) since their continuity conditions are known at boundaries.

Perturbations of density are usually considered small and the mass equation is usually dropped. Consider the size of these perturbations in the neighborhood of a boundary to see when this is a legitimate approximation. Define density as

$$
\rho = \rho_o + \rho_\delta, \tag{2.20}
$$

where $\rho_o = \rho_o(x)$ is locally constant, $\rho_\delta = \rho_\delta(x, t)$ is the density perturbation, and $\rho = \rho(x, t)$ is the total density. Only ρ_o is independent of time. Using this definition in the conservation

33

of mass equation (2.19)[1] yields

$$\rho_{\delta,t} = -\rho_{,x}v - \rho v_{,x}.$$ (2.21)

In dimensional analysis one normally takes a term like $\rho_{,x}v$ and brings the magnitude and dimension out as a leading coefficient multiplying a term of $O(1)$. Specifically, one defines something like

$$\rho_{,x}v = \frac{RV}{L}\rho_{,x^*}^* v^*,$$ (2.22)

where the * quantities are dimensionless and of $O(1)$, and R, V, and L, are respectively, a characteristic density, velocity, and length. This approach works well for smooth models but breaks down where the characteristic density is different on two sides of a boundary. In this case, I define a characteristic density difference, R_Δ, such that

$$\rho_\Delta \equiv \rho(x_o + \epsilon) - \rho(x_o - \epsilon) = [R(x_o + \epsilon) - R(x_o - \epsilon)]\rho^* \equiv R_\Delta \rho^*,$$ (2.23)

where the material transition occurs at $x = x_o$, as shown in Figure 2.3(b). Note that the characteristic density R is a function of x so that an evaluation of the quantity R_Δ/R depends on which side of the interface x is taken. For example, say $R_\Delta = R_+ - R_-$ with $R_+ \gg R_-$. Then $R_\Delta \simeq R_+$ and $R_\Delta/R \sim O(1)$ to the right of the interface and $\gg 1$ to the left.

Now to continue, define a similar difference for velocity, $v_\Delta = V_\Delta v^*$. Also define a characteristic density perturbation, $\rho_\delta = \mathcal{R}\rho_\delta^*$. Using these definitions in the conservation of mass equation (2.21), normalizing the left side, and dropping the *'s yields

$$\rho_{\delta,t} = -\frac{R_\Delta V T}{\mathcal{R}L}\rho_{,x}v - \frac{R V_\Delta T}{\mathcal{R}L}\rho v_{,x}.$$ (2.24)

Using the same procedure on the horizontal momentum and the stress equations (2.19)[2,3] yields the dimensionless system

$$\rho_{\delta,t} = -\frac{R_\Delta V T}{\mathcal{R}L}\rho_{,x}v - \frac{R V_\Delta T}{\mathcal{R}L}\rho v_{,x},$$

$$\nu_{,t} = -\frac{V^2 R_\Delta T}{RVL}\rho_{,x}v^2 - \frac{V_\Delta T}{L}2\rho v v_{,x} + \frac{P_\Delta T}{RVL}\sigma_{,x},$$

$$\sigma_{,t} = \frac{\Lambda V_\Delta T}{PL}\mathcal{L}v_{,x}, \tag{2.25}$$

where I used $\nu = RV\nu^*$, $\sigma = P\sigma^*$, and $\mathcal{L} = \Lambda\mathcal{L}^*$ before dropping the $*$'s. To determine the relative size of each term use the order of magnitude relations

$$\frac{L}{T} \sim C, \text{ numerical grid velocity if } L = \Delta x \text{ and } T = \Delta t,$$

$$P \sim RCV, \text{ pressure,}$$

$$\Lambda \sim RC^2, \text{ local Lamé constant,}$$

$$V_\Delta \sim V, \text{ since normal velocity is continuous across an interface,}$$

$$P_\Delta \sim P, \text{ since normal stress is continuous across an interface,}$$

$$\frac{V}{C} \sim M \equiv \text{ Mach number} \ll 1. \tag{2.26}$$

Using these relations in the dimensionless equations (2.25) and replacing leading coefficients of $O(1)$ with unity yields

$$\rho_{\delta,t} = -\left[\frac{R_\Delta M}{R}\right]\rho_{,x}v - \left[\frac{RM}{R}\right]\rho v_{,x},$$

$$\nu_{,t} = -\left[\frac{R_\Delta M}{R}\right]\rho_{,x}v^2 - [M]\,2\rho v v_{,x} + \sigma_{,x},$$

$$\sigma_{,t} = v_{,x}. \tag{2.27}$$

It is obvious the stress equation, $\sigma_{,t} = v_{,x}$, and the stress term of the momentum equation, $\nu_{,t} = \cdots \sigma_{,x}$, must be retained since they are always leading order. The second quasi-linear term of the momentum equation is $O(M)$ and can always be dropped. But what about the other terms?

Suppose the density distribution is smooth as shown in Figure 2.3(a) with $R_\Delta \ll R$; then the first term of the density equation (2.27)[1] and the remaining quasi-linear term of the momentum equation (2.27)[2] drop out. Since the leading coefficient of the second term
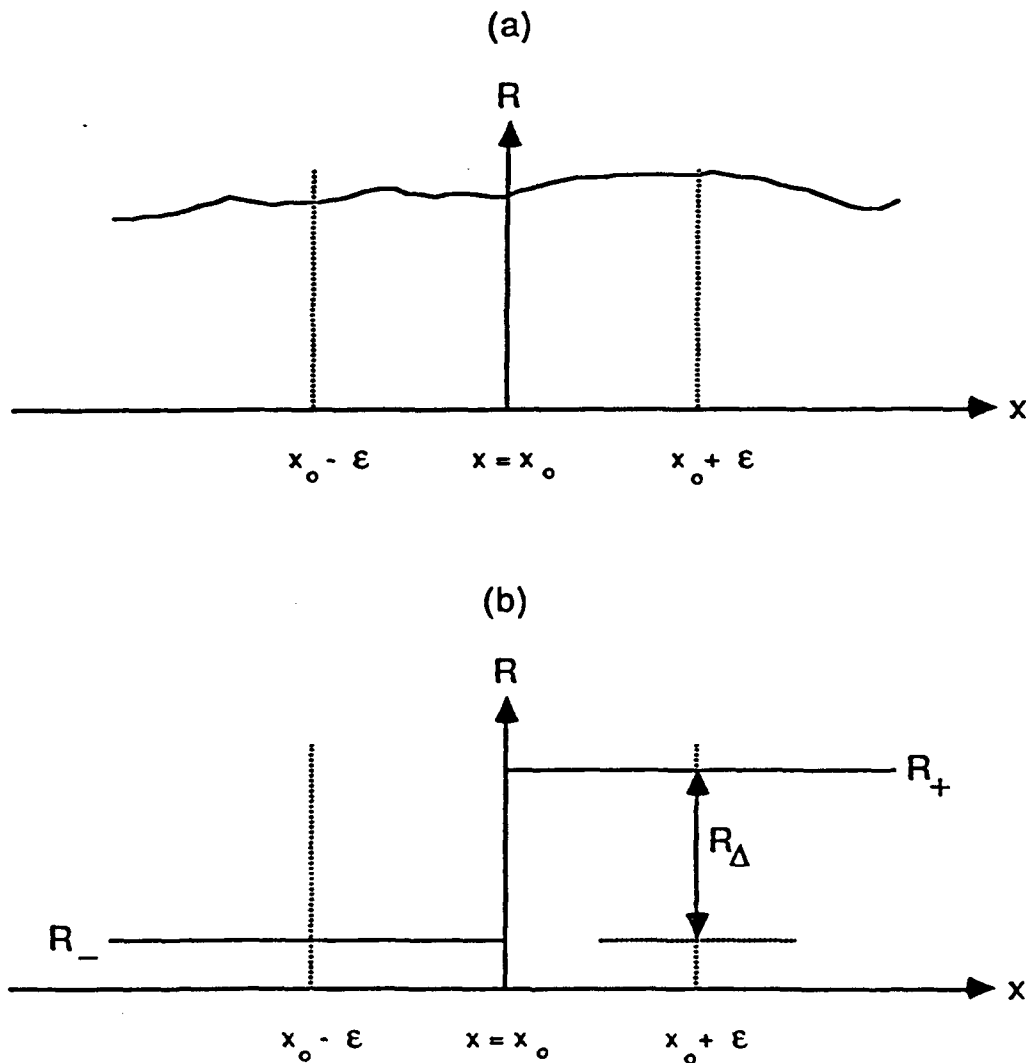
Figure 2.3: Low-contrast and high-contrast density interface. (a) The density contrast is low across the "interface" at $x = x_o$ with a small gradient. The quantity R_Δ/R is always $\ll 1$, no matter which side of the interface it is evaluated. (b) The density contrast is high across the interface, and the value of R_Δ/R is sensitive to the local value of R. To the right, $R_\Delta/R \sim O(1)$, while to the left, $R_\Delta/R \gg 1$.

of the density equation must be $O(1)$ the density perturbation is $\mathcal{R} \simeq RM \ll R$ and the density equation drops out entirely since it decouples from the other equations. The reduced system in this case is

$$\nu_{,t} = \sigma_{,x},$$
$$\sigma_{,t} = \nu_{,x} \qquad (2.28)$$

which is the same as the usual linear elastodynamic equation with normalized material properties. Hence, if the density distribution is smooth then the linear equations can be used.

For the next two examples, consider a high-contrast density discontinuity, where $R(x_o + \varepsilon) \gg R(x_o - \varepsilon)$ as shown in Figure 2.3(b). First, consider a point on the high density side of the density discontinuity, where $R_\Delta \simeq R$. The first quasi-linear term of the momentum equation $(2.27)^2$ drops but both terms of the mass equation $(2.27)^1$ must be kept. In this case, however, the mass equation again decouples from the others since $\mathcal{R} \simeq RM \ll R$, i.e., the local density perturbation is much less than the local density. Again, the linear system can be used.

Next, consider a point on the low density side of the density discontinuity shown in Figure 2.3(b), where $R_\Delta/R \gg 1$, say $R_\Delta M \simeq R$. In this case, the quasi-linear term in the momentum equation $(2.27)^2$ must be retained along with the first term of the mass equation $(2.27)^1$. The mass equation does not decouple in this case since $\mathcal{R} \simeq R_\Delta M \simeq R$. In other words, the local density perturbation is the same size as the local density. This situation arises near high-contrast boundaries and is due to the interface moving with respect to the fixed Eulerian coordinates. If a dense material, say ice, moves even slightly into a very light material, say air, it dramatically changes the average density of the material in a fixed grid cell. Thus, to honor conservation of mass, the entire quasi-linear elastodynamic system Equation (2.19), or more generally Equation (2.18), must be used.

Recall I mentioned in the previous section that the quadratic terms in the strain equation (2.17) could always be dropped. Using dimensional analysis, I now show why this is so. Writing the equation in dimensionless form yields

$$\frac{U_\Delta}{L}\epsilon_{ij}^* = \frac{1}{2}(\frac{U_\Delta}{L}u_{i,j}^* + \frac{U_\Delta}{L}u_{j,i}^* + \frac{U_\Delta^2}{L^2}u_{k,i}^*u_{k,j}^*), \tag{2.29}$$

where U_Δ is the characteristic displacement difference and L is the characteristic length as above. Normalizing the left hand side and dropping the stars, the dimensionless equation is written

$$\epsilon_{ij} = \frac{1}{2}(u_{i,j}^* + u_{j,i}^* + \frac{U_\Delta}{L}u_{k,i}^*u_{k,j}^*). \tag{2.30}$$

I define the ratio $N \equiv U/L$ and call it the *Mach displacement* due to its similarity to the Mach number, $M = V/C$. The characteristic length, L, is set to the spatial increment for the finite difference scheme. Because this is a study in infinitesimal strain elastic wave propagation, $U_\Delta \sim O(U)$ and the Mach displacement is always small, even near boundaries. Non-linear effects such as acoustic streaming, which would produce large Mach displacements, are not considered here. Since the Mach displacement is always small, the quadratic term in the strain equation may always be dropped, leaving a linear strain equation and, thus, a linear constitutive equation.

2.6 Discussion

Generally, the measure of R_Δ is made meaningful only when the characteristic length L_o over which the density difference occurs is defined. Two cases exist: either the material transition is spatially differentiable or it is not. For analytically differentiable transitions, regardless of the gradient magnitude, Hughes shows that only the linear elastodynamic equations are needed and the equations are well posed [23]. This is consistent with my analysis since the characteristic length of the differencing interval, ∂x and the like, approaches zero and

the ratio R_Δ/R is always small. Hence, the quasi-linear terms and the mass equation are unnecessary.

If the transition is not differentiable, Hughes' theory breaks down. If the density step is small,

$$\frac{R_\Delta}{R} \sim O(M), \tag{2.31}$$

where

$$R = \frac{R_+ + R_-}{2} \tag{2.32}$$

is the average density, then there is no problem and my analysis shows that the linear system can be used. On the other hand, if the density step is large,

$$\frac{R_\Delta}{R} \sim O(1) \tag{2.33}$$

with

$$\frac{R_\Delta}{R_-} \sim O(M^{-1}), \tag{2.34}$$

then no matter how small the differencing interval, the ratio R_Δ/R is never small on the low density side of the discontinuity. The full quasi-linear system is needed to handle this situation.

In contrast to the vanishing characteristic length implied by analytic analysis, the finite difference method, to be introduced in the next chapter, has a fixed characteristic length, namely the spatial sampling interval. If the sampling interval is larger than the transition width between materials, then it does not matter whether the transition is differentiable or not. The full quasi-linear system is needed.

If the transition truly is differentiable and the sampling interval is small enough, then the linear elastodynamic equations could be used. For the ice scattering problem, however, the sampling interval needed to make the trai   ions appear smooth is many orders of magnitude smaller than the insonifying wavelength. Choosing such a small sampling interval is not a

practical approach. Thus, the quasi-linear system should be used with a sampling interval that spans the material transition.

In either case, whether the transition has infinitesimal width or is smooth with finite but small width, use of the quasi-linear system yields computationally efficient solutions to the ice scattering problem. The efficiency is possible without resorting to explicitly matching boundary conditions at the interfaces between ice, air, and water.

As an aside, I present the following heuristic argument for why the quasi-linear system is needed.

- The quasi-linear system is the full system of equations derived from first principles assuming infinitesimal strain and a heterogeneous continuum in Eulerian coordinates.

- Internal boundary conditions are implicitly satisfied by the quasi-linear system regardless of the material contrast across the boundary.

- If the position of a high-contrast internal boundary $\left(\begin{array}{c} \text{is} \\ \text{is not} \end{array} \right)$ explicitly identified and tracked then the $\left(\begin{array}{c} \text{linear} \\ \text{quasi-linear} \end{array} \right)$ system $\left(\begin{array}{c} \text{may} \\ \text{must be} \end{array} \right)$ be considered.

  - In the case where the boundary is tracked, boundary conditions must be matched explicitly in one way or another.

  - In the case when the boundary is not tracked, the quasi-linear system, in effect, is the linear system with quasi-linear source terms added. These terms are negligible away from boundaries and the system is linear in these regions. Near a boundary, however, the quasi-linear source terms gain strength and act to enforce the boundary conditions automatically.

2.7 Summary

In this chapter I have developed a set of quasi-linear equations of motion (2.18), which describe wave propagation in a heterogeneous continuum where the material properties may change abruptly at internal interfaces. I have shown that the magnitude of density gradients in the model determines if the full quasi-linear system is required or if the simpler linear elastodynamic equations may be used. If local density differences are large, say $R_\Delta \simeq R/M$, then the full quasi-linear system must be used.

These results apply to my solution of the ice scattering problem in the following way. For convenience, I have decided to implement the heterogeneous formulation rather than track boundaries and explicitly match boundary conditions. Since some of the internal boundaries in the problem are high-contrast boundaries, I must use the full quasi-linear system of equations. The next chapter discusses how I solve the equations numerically.

Chapter 3

Numerical Development

3.1 Overview

Having completed the development of the extended elastodynamic equations, it is time to consider how these equations are solved. If scatter from complex ice geometries that approximate the real world is to be considered, numerical solutions are the only choice. The numerical method must admit the possibility of discontinuous solutions since I have posed the problem as elastic wave propagation through a heterogeneous continuum with abruptly changing material properties. Such solutions are called weak solutions and may be found using either the finite element method or the finite difference method. The former starts with an integral statement of the weak solution and ends up solving for the unknown solution by inverting a matrix problem of the form $Ax = b$. For 1-D hyperbolic problems this can be done efficiently with modest coding effort. For higher dimensions the inversion is computationally expensive and for hyperbolic systems, it is unnecessary [64]. Explicit finite difference methods start with the partial differential equations and may be formulated to guarantee that if the scheme converges to a solution it is the unique weak solution, i.e., it contains discontinuities that satisfy physically admissible boundary conditions at internal

material interfaces. Explicit finite difference methods are computationally more efficient than finite element methods for spatial dimensions higher than one. For this reason, the finite difference method is used here.

There are an infinite number of finite difference approximations to any given partial differential equation. The question, then, is which approximation should be used. The numerical solutions should mimic the physical solutions as closely as possible, i.e., small phase and amplitude distortions relative to the true solution. High order accuracy schemes are often suggested because they produce good results for less computational effort on coarser grids than low order schemes. The problem with coarse grids for ice scattering experiments is that the ice thickness is small with respect to the acoustic wavelength in water, say $\lambda/10$, and thus a coarse grid, say $\Delta x = \lambda/5$, would not adequately sample the ice. This leads to the consideration of low order of accuracy difference schemes, namely $O(k, h^2)$ or $O(k^2, h^2)$, where k and h are the temporal and spatial discretization interval. Although this restriction significantly reduces the selection of difference schemes the choices are still infinite in number. As shown in the next section, a conservation law difference scheme is required to match the conservation law form of the analytic partial differential equation. This choice and a further restriction that the scheme be monotone, to be defined later, guarantees that if the solution converges then the solution is the unique weak solution that satisfies physically admissible internal boundary conditions, e.g., continuity of normal velocity and stress, and so forth. Three well known schemes are considered: Lax-Friedrichs, which is $O(k, h^2)$, Lax-Wendroff, which is $O(k^2, h^2)$, and Leap-frog, which is $O(k^2, h^2)$. For reasons that will become clear, the preferred choice is Lax-Wendroff with some locally added dissipation that makes the scheme $O(k, h^2)$ in the vicinity of material discontinuities.

Once the difference scheme for the interior domain has been selected, the computational boundary treatment is considered. Ideally the boundary scheme acts like an acoustic diode,

43

allowing energy to pass out of the domain without reflecting any energy back in. As might be expected, this is not possible but close approximations to the ideal may be designed. For this study the boundary is handled with two treatments simultaneously: a one-way wave equation on the perimeter and a sponge region separating the interior domain from the computational boundary. In principle, the combination of these two methods can reduce the side reflections to arbitrarily small levels even in strongly heterogeneous media. In practice, for only modest effort the side reflections are reduced to a few tenth of a decibel at mid to high frequency. As will be seen, the low frequencies are problematic because of their long wavelength and the relative thinness of the absorbing region.

Source injection is handled using an extension of the work by Kelly et al. [26] to inject not only pressure but also velocity as required by the analytic equations. Both pressure and velocity are derived from a single displacement potential. This approach provides for analytic compatibility between the pressure and velocity even in the near-field, where the source injection takes place.

Finally, the Lax-Wendroff scheme is certified by comparing results from numerical experiments with analytic solutions for simple problems: cylindrical spreading, free surface reflections, and reflections from an elastic half space. Also, the scheme, which in homogeneous media is known to be second order accurate, is shown to have an order of accuracy slightly less than second order in a strongly heterogeneous media.

3.2   Interior domain

This section covers the selection of an appropriate finite difference scheme to be used in the interior of the computational domain. First, I discuss general conservation law difference schemes, which set a framework for selecting a specific difference formulation. Next, I develop the numerical analysis tools to be used in evaluating three difference schemes.

Finally, I make a preliminary selection of the scheme to be used for the scattering study. The selected scheme is certified in a later section, where I compare numerical results with analytic solutions and confirm order of accuracy.

3.2.1 General conservation law difference schemes

The best way to approximate and integrate analytic partial differential equations in conservation law form is to use finite difference schemes in conservation law form. This section is drawn heavily from the work of Sod [57, Ch. IV] and details of derivations and proof of theorems may be found there or in his citations. I state the results of his work as it applies to my problem and go from there to the details of my own development and analysis.

For convenience of analysis consider the scalar hyperbolic 1-D conservation law,

$$u_{,t} = -f_{,x}(u), \tag{3.1}$$

where $f(u)$ is the flux of a conserved quantity u out of a control volume (or line segment in this 1-D case). I show later how the analysis results of this simple equation applies to the full elastodynamic equations. Now, multiplying both sides by a smooth function, $\phi(x,t)$, which tends to zero as x and t tend to infinity, integrating by parts, and taking the initial condition $\phi(x,0) = 0$ yields the integral equation

$$\int\int \phi_{,t}u + \phi_{,x}f(u) \; dx \; dt = 0. \tag{3.2}$$

If solutions of the integral equation are smooth, the process can be reversed to derive the differential conservation law Equation (3.1). If, however, the solution is spatially discontinuous, say $u = v(x,t)$, then the fluxes, $f(v)$, in general are spatially discontinuous and the differential conservation law becomes invalid at the points of discontinuity. There is no such problem with the integral solution, which involves differentiation only of the smooth

45

function ϕ. Strictly speaking then, for the discontinuous solution $u = v(x,t)$, the integral equation $\int\int \phi_{,t} v + \phi_{,x} f(v) \; dx \; dt = 0$ is valid but not the differential equation $v_{,t} = -f_{,x}(v)$.

I wish to solve for discontinuous fields using discrete approximations to the conservation law differential equation (3.1). To be certain of finding the unique weak solution $u = v(x,t)$, two restrictions are placed on the difference scheme [57]. First, the scheme must satisfy a discrete version of the conservation law in Equation (3.1). The second restriction is that the scheme be a so-called monotone scheme, which is defined below. This guarantees that the solution at a discontinuity is physically admissible.

Consider these two restrictions further. A general statement for the update equation of a one-step explicit finite difference scheme may be written

$$u_m^{l+1} = Q u_m^l, \tag{3.3}$$

where Q is the update or transition matrix,

$$u_m^l = u(x_0 + mh, t_0 + lk), \tag{3.4}$$

$h = \Delta x$, and $k = \Delta t$. Furthermore, a finite difference scheme is said to be in conservation law form if it can be written as

$$\frac{u_m^{l+1} - u_m^l}{k} = -\frac{F^l(x_0 + \frac{h}{2}) - F^l(x_0 - \frac{h}{2})}{h}. \tag{3.5}$$

The function F is the numerical flux and has $2q$ arguments. Specifically,

$$\begin{aligned} F^l(x_0 + \frac{h}{2}) &= F(u_{-q+1}^l, u_{-q+2}^l, \cdots, u_q^l), \\ F^l(x_0 - \frac{h}{2}) &= F(u_{-q}^l, u_{-q+1}^l, \cdots, u_{q-1}^l). \end{aligned} \tag{3.6}$$

For the case $q = 1$, the most compact conservation law difference scheme, the numerical fluxes are

$$\begin{aligned} F^l(x_0 + \frac{h}{2}) &= F(u_0^l, u_1^l), \\ F^l(x_0 - \frac{h}{2}) &= F(u_{-1}^l, u_0^l). \end{aligned} \tag{3.7}$$

46

This is the case used in everything to follow. Consistency with the analytic conservation law, Equation (3.1), requires that $F(u,u) = f(u)$, where u is a solution to the analytic equation.

Compare the conservation law of the analytic form in Equation (3.1) with the numerical form in Equation (3.5). The notion of a conservation law difference scheme leads to

Theorem 3.1. *If a difference scheme can be stated in the conservation law form of Equation (3.5) and if the scheme converges to a solution, $u(x,t)$, then u is a weak solution of the analytic conservation law partial differential equation (3.1).*

Proof of this theorem was originally given by Lax and Wendroff [35] and is discussed by Sod [57].

Weak solutions are not necessarily unique, so Theorem 3.1 helps but is not enough. The unique solution is desired. This is the one solution which is physically admissible.

The second restriction placed on the difference scheme guarantees the unique weak solution if the solution converges. This restriction involves the notion of a monotone difference scheme. Sod [57] states that the finite difference scheme for $q = 1$

$$u_m^{l+1} = Q u_m^l = H(u_{m-1}^l, u_m^l, u_{m+1}^l) \tag{3.8}$$

is monotone if H is a monotone increasing function of its arguments. Specifically,

$$\frac{\partial H}{\partial u_{m+q}^l} \geq 0 \quad \text{for} \quad q = -1, 0, 1. \tag{3.9}$$

Furthermore, if H satisfies the consistency condition $H(u,u,u) = f(u)$ and can be written in the form

$$H(u_{m-1}^l, u_m^l, u_{m+1}^l) = u_m^l - \frac{k}{h}[F(u_0^l, u_1^l) - F(u_{-1}^l, u_0^l)], \tag{3.10}$$

then the monotone difference scheme can be written in conservation law form. This leads to

47

Theorem 3.2. *If a monotone difference scheme in conservation law form converges to a solution, $u(x,t)$, then u is the unique weak solution that satisfies physically admissible boundary conditions at all internal discontinuities.*

Proof of this theorem was introduced by Harten et al. [20] and is discussed by Sod [57].

The physically admissible internal boundary conditions for the elastodynamic equations reduce to continuity of normal velocity and stress with zero shear stress for fluid-solid interfaces and continuity of all velocity and stress fields for a welded solid-solid interface.

One more useful theorem by Sod [57] is

Theorem 3.3. *A monotone difference scheme in conservation law form is at most first order accurate in time.*

These three theorems are used to select an appropriate finite difference approximation to the elastodynamic equations for the ice scattering study. A monotone finite difference scheme in conservation law form guarantees convergence to the weak solution that satisfies all internal boundary conditions. Having had stability problems in the past, I use a monotone scheme because of this guarantee. A monotone scheme, however, is at most first order accurate in time. This is a restriction that I want to side-step in some way since a first order accurate scheme is dominated by temporal truncation errors of $O(k)$, which are much larger than the spatial truncation errors of $O(h^2)$. On the other hand, higher order schemes produce solutions with oscillations near discontinuities in the field. In severe cases, these oscillations grow and lead to nonlinear instability, a broad class of instabilities not predicted by linear numerical analysis. One way around this is to use added dissipation and make the scheme monotone in the vicinity of material interfaces. This approach is discussed in detail later.

3.2.2 Numerical analysis

There are an infinite number of finite difference schemes that are consistent with the an-
alytic partial differential equations developed in Chapter 2. I must choose one of these to
use for the scattering study. The scheme must be stable in the presence of high-contrast
discontinuities and have modest phase and amplitude distortion. Stability is guaranteed if
the scheme is monotone near discontinuities. This section focuses on phase and amplitude
distortions of the finite difference scheme, otherwise known as numerical dispersion and
dissipation. To evaluate the dispersion and dissipation characteristics of a given difference
scheme I use the Fourier analysis technique [54,65], which is presented in this section in
a general way. The next section uses the technique to investigate three specific difference
schemes.

Although the extended elastodynamic equations derived in Chapter 2 are quasi-linear,
the quasi-linear terms are only needed at the boundary between differing materials. Else-
where, the quasi-linear terms are of lower order and do not contribute significantly to the
solution. In a sense, the quasi-linear terms act to enforce internal boundary conditions
and do not affect the solution that propagates through the homogeneous media between
interfaces. With this in mind, the quasi-linear terms are dropped and the dispersion and
dissipation analysis is done on the linear system of equations for which the Fourier analysis
method is well suited.

The dispersion relation for the model equation $u_{,t} = -cu_{,x}$ with propagation speed c
is computed assuming a modal solution $u \sim e^{-i(\xi x - \omega t)}$, where ξ is horizontal wavenumber
and ω is radial frequency[†]. The dispersion relation is $\omega = c\xi$. Generally, linear partial
differential equations yield polynomial dispersion relations. In contrast, linear difference

---

[†]In this chapter, which involves considerable numerical analysis, I use the symbol ξ to mean horizontal
wavenumber. This avoids any confusion that might be created using the symbol k, which is reserved for the
temporal increment $k = \Delta t$. Later, I need the vertical wavenumber, which is given the symbol η
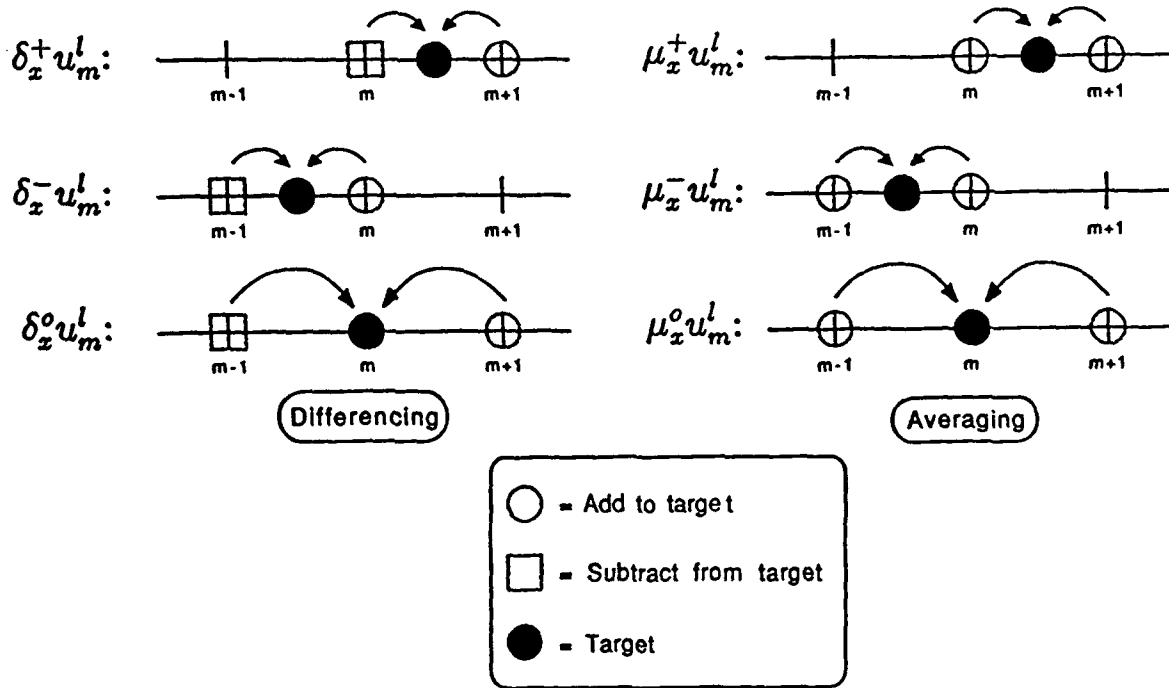
Figure 3.1: Average and difference operators in 1-D. The 2-D operator notation is defined in Table 3.1. The boxes signify subtracting the operand and the circles signify adding the operand. This graphical notation is used later in describing the finite difference schemes to be considered for the ice scattering problem.

equations yield trigonometric dispersion relations. The essence of choosing a particular difference scheme is to match the polynomial dispersion relation of the analytic equation as closely as possible using trigonometric functions. Tradeoffs between phase error, amplitude error, and computational intensity determine the final choice.

A useful compact notation for differencing and averaging is defined for 2-D operations in Table 3.1 and shown graphically for 1-D operations in Figure 3.1. Similar notation applies for differences and averages in the y direction and for time. There should be no confusion between the averaging operator, μ_x^0 and the like, and the Lamé parameter μ since context always makes the distinction clear.

Description	Operator
Forward difference	$\delta_x^+ u_{m,n}^l = \frac{1}{h}(u_{m+1,n}^l - u_{m,n}^l)$
Backward difference	$\delta_x^- u_{m,n}^l = \frac{1}{h}(u_{m,n}^l - u_{m-1,n}^l)$
Central difference	$\delta_x^0 u_{m,n}^l = \frac{1}{2h}(u_{m+1,n}^l - u_{m-1,n}^l)$
Forward average	$\mu_x^+ u_{m,n}^l = \frac{1}{2}(u_{m+1,n}^l + u_{m,n}^l)$
Backward average	$\mu_x^- u_{m,n}^l = \frac{1}{2}(u_{m,n}^l + u_{m-1,n}^l)$
Central average	$\mu_x^0 u_{m,n}^l = \frac{1}{2}(u_{m+1,n}^l + u_{m-1,n}^l)$

Table 3.1: Differencing and averaging notation for writing finite difference schemes compactly. These operations are shown graphically for 1-D in Figure 3.1.

Recall that any explicit linear one-step difference scheme may be written

$$u_m^{l+1} = Q u_m^l, \tag{3.11}$$

where Q is a linear finite difference operator. Substituting a modal solution of the form

$$u_m^l \sim e^{-i(\xi m h - \omega l k)} = z^l e^{-i\xi m h} \tag{3.12}$$

into the difference equation (3.11) yields an equation for the amplification factor

$$z = z(\xi, k, h) = e^{i\omega k}, \tag{3.13}$$

which is complex in general. For notational convenience later, I define $\bar{\xi} \equiv \xi h$, $\bar{\eta} \equiv \eta h$, and $\bar{\omega} \equiv \omega k$.

Both the dispersion and dissipation may be obtained directly from the amplification factor. Note that the the radial frequency in the discrete approximation is complex in general,

$$\omega = \omega_R + i\omega_I, \tag{3.14}$$

where $\omega_R = \Re(\omega)$, $\omega_I = \Im(\omega)$, and $\Re(\cdot)$ and $\Im(\cdot)$ are the real and imaginary part of $(\cdot)$. With this decomposition, the amplification factor may be written

$$z = e^{i\omega k} = e^{i\omega_R k} e^{-\omega_I k} = g e^{i\omega_R k}. \tag{3.15}$$

51

The magnitude of the amplification factor

$$g = g(\xi; k, h) = |z| = e^{-\omega_I k} \qquad (3.16)$$

is the dissipation of the difference scheme, or more precisely, the gain per time step for a given wavenumber, ξ. If the gain is less than unity then there is numerical dissipation in the difference scheme. Gains greater than unity indicate an unstable scheme.

The dispersion relation of the difference scheme is[†]

$$\omega_R = \omega_R(\xi; k, h) = \Re(\omega) = \frac{1}{k} \tan^{-1}\left(\frac{\Im(z)}{\Re(z)}\right), \qquad (3.17)$$

which is the phase change per unit time, or radial frequency, for a give wavenumber, ξ.

These expressions describe the behavior of the difference scheme for all wavenumbers and are useful for selecting the stable limit of the time step, k, for a given spatial increment, h. In the ice scattering experiments, however, I intentionally limit the source spectrum to excite only low wavenumbers; thus, the phase and amplitude errors of interest are also in the low wavenumber regime. Because of this, a figure of merit is needed to reveal the performance of each scheme for low wavenumbers.

I have chosen for a figure of merit the number of time steps allowed before a specified phase or amplitude distortion occurs and call this number the time step limit. The distortion limits are set at a maximum phase error of $\pi/4$ and a maximum amplitude error of 1 dB

[†]In general the phase of the amplification factor, ωk, is complex. For convenience when talking about the dispersion of a difference scheme I use the notation ω rather than the more cumbersome notation $\Re(\omega)$ or ω_R. It will be clear from context whether I am referring to the complex frequency or only its real part. Occasionally, I use $\Re(\omega)$ where a precise statement is required.

in the frequency band of the source.

Given the radial frequency, $\omega(\xi; k, h)$, which is also the phase shift per unit time, the phase error is $\omega(\xi; k, h) - \omega_{true} = \omega(\xi; k, h) - c\xi$, since $\omega = c\xi$ is the analytic dispersion relation. The phase time step limit is given by

$$N_\phi = \frac{\pi/4}{|\omega(\xi; k, h) - c\xi|k}. \tag{3.18}$$

Similarly, the amplitude time step limit is computed from the gain per time step, g, as

$$N_A = \frac{1}{|20\log_{10} g(\xi; k, h)|}. \tag{3.19}$$

For interpretation, it is convenient to normalize the analysis and express the wavenumber in terms of the grid points per wavelength. Using a characteristic length, $L_o = h$, and velocity $C_o = c$, all the dimensional quantities in N_ϕ and N_A are normalized and determined as functions of dimensionless wavelength, $\lambda^* = 2\pi/\xi^*$, where $\lambda^* = \lambda/L_o$ and $\xi^* = \xi L_o$. Dimensionless wavelength defined in this way is exactly the number of grid points per wavelength. The time step limits in terms of the dimensionless wavelength are written after dropping the *'s as

$$\begin{aligned} N_\phi &= \frac{\pi/4}{|\omega(\lambda; k, h) - \xi(\lambda; k, h)|k}, \\ N_A &= \frac{1}{|20\log_{10} g(\lambda; k, h)|}. \end{aligned} \tag{3.20}$$

These numbers are used as figures of merit for each of the difference schemes to be considered in the next section. The larger the value of N_ϕ and N_A, the better the scheme in terms of coming close to the exact solution.

As mentioned earlier, the foregoing analysis is based on the 1-D scalar wave equation $u_{,t} = -cu_{,x}$. How does this apply to the elastodynamic equations? First, for the dispersion and dissipation analysis I reduce the full set of heterogeneous quasi-linear equations to a

linear, homogeneous set. The 2-D equations expressed in velocity and stress can then be written

$$\underline{u}_{,t} = \underline{\underline{A}}\,\underline{u}_{,x} + \underline{\underline{B}}\,\underline{u}_{,y},\qquad(3.21)$$

where

$$\underline{u} = (v_1, v_2, \sigma_{11}, \sigma_{22}, \sigma_{12})^T \equiv (u, v, \sigma, \tau, \chi)^T\qquad(3.22)$$

and

$$\underline{\underline{A}} = \begin{pmatrix} \cdot & \cdot & \frac{1}{\rho} & \cdot & \cdot \\ \cdot & \cdot & \cdot & \cdot & \frac{1}{\rho} \\ \lambda + 2\mu & \cdot & \cdot & \cdot & \cdot \\ \lambda & \cdot & \cdot & \cdot & \cdot \\ \cdot & \mu & \cdot & \cdot & \cdot \end{pmatrix}, \quad \underline{\underline{B}} = \begin{pmatrix} \cdot & \cdot & \cdot & \cdot & \frac{1}{\rho} \\ \cdot & \cdot & \cdot & \frac{1}{\rho} & \cdot \\ \cdot & \lambda & \cdot & \cdot & \cdot \\ \cdot & \lambda + 2\mu & \cdot & \cdot & \cdot \\ \mu & \cdot & \cdot & \cdot & \cdot \end{pmatrix}.\qquad(3.23)$$

Now, suppose a plane wave propagates along an arbitrary axis, say x', which is at an angle θ with respect to the reference x-axis as shown in Figure 3.2. For this plane wave, rotate the coordinates of Equation (3.21) using

$$\begin{aligned} x' &= x\cos\theta + y\sin\theta \\ y' &= -x\sin\theta + y\cos\theta \end{aligned}\qquad(3.24)$$

and write the 1-D result as

$$\underline{u}'_{,t} = \underline{\underline{A}}\,\underline{u}'_{,x'}.\qquad(3.25)$$

The matrix $\underline{\underline{A}}$ is not diagonal, but since the system is hyperbolic [23], it has a complete set of eigenvectors and can be diagonalized [74, p. 116], i.e., $\underline{\underline{A}} = \underline{\underline{T}}\,\underline{\underline{\Lambda}}\,\underline{\underline{T}}^{-1} \leftrightarrow \underline{\underline{\Lambda}} = \underline{\underline{T}}^{-1}\underline{\underline{A}}\,\underline{\underline{T}}$. Using this and the fact that $\underline{\underline{A}}$ and hence $\underline{\underline{T}}$ and its inverse are temporally and spatially constant for this analysis leads to the diagonalized system

$$\underline{w}_{,t} = \underline{\underline{\Lambda}}\,\underline{w}_{,x},\qquad(3.26)$$

54
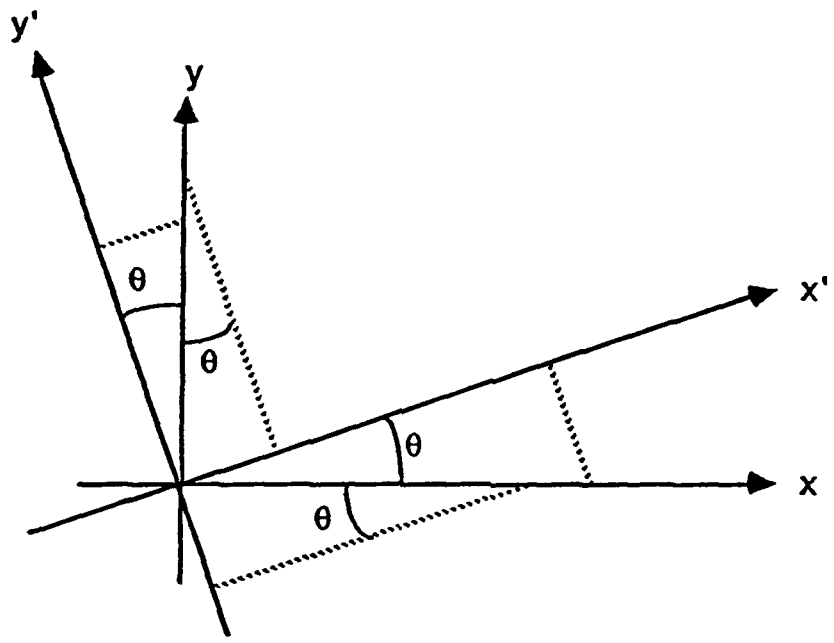
Figure 3.2: Rotated coordinate system aligned with plane wave. For a plane wave propagating in the x' direction, the coordinate rotation here is used to convert the 2-D system of Equation (3.21) to the 1-D system of Equation (3.25).

where $\underline{w} = \underline{\underline{T}}^{-1}\underline{u}'$. Each of the equations in the 1-D system is independent and the characteristic variables, w_i, propagate to the left at a velocity λ_i, which may be positive, negative, or zero. Normalizing the equation using a characteristic velocity, C_o, length, L_o, and density, ρ_o yields compressional velocities of ± 1 with the shear velocities less than unity in magnitude. Each of the independent equations of the normalized system behaves exactly like the model equation $u_{,t} = -c u_{,x}$ upon which the dispersion and dissipation analysis is based with velocities $c = \pm 1$ for the compressional mode or $c = \pm C_s/C_o$ for the shear mode. The shear mode tends to have less error than the compressional mode in most cases. A specific example of the difference between the modes is shown later.

Only angles of propagation $0° < \theta < 45°$ need to be considered due to the symmetry of the grid as shown in Figure 3.3. To span this range I use the discrete values $\theta = 0°, 15°, 30°, 45°$.

The 2-D dispersion relation, for different values of θ, is calculated by assuming a modal solution of the form

$$\underline{u}(x,y,t) = \underline{u}(mh, nh, lk) = \underline{u}^l_{m,n} \sim \underline{Z}^l_o e^{-i(\xi mh + \eta nh)} = \underline{Z}^l_o e^{-i(\bar{\xi}m + \bar{\eta}n)}. \qquad (3.27)$$

Substitution into the normalized homogeneous 2-D wave equation (3.21) yields the modal update equation

$$\underline{Z}^{l+1}_o = -i(\bar{\xi}\underline{\underline{A}} + \bar{\eta}\underline{\underline{B}})\underline{Z}^l_o$$

$$\equiv \underline{\underline{D}}\,\underline{Z}^l_o. \qquad (3.28)$$

The horizontal and vertical wavenumbers, $\bar{\xi}$ and $\bar{\eta}$, together define the magnitude of the wavevector, $\bar{\Xi} \equiv \sqrt{\bar{\xi}^2 + \bar{\eta}^2}$ and the direction of propagation, $\theta = \tan^{-1}(\bar{\eta}/\bar{\xi})$. Conversely,

$$\bar{\xi} = \bar{\Xi}\cos\theta, \bar{\eta} = \bar{\Xi}\sin\theta. \qquad (3.29)$$

The matrix $\underline{\underline{D}}$ is called the amplification matrix and is analogous to the amplification factor, z, in Equation (3.13). It is the eigenvalues of $\underline{\underline{D}}$ that determine the dispersion
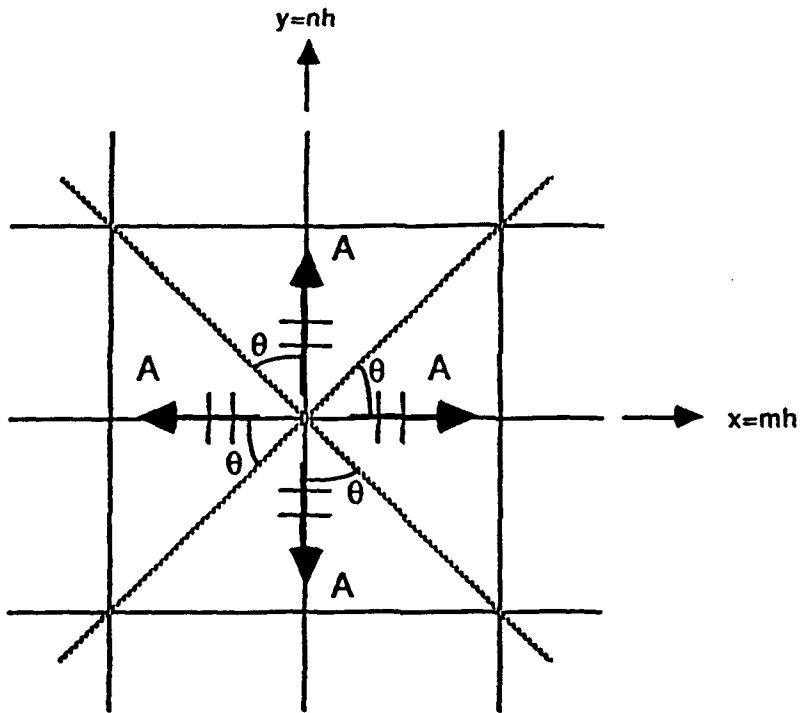
Figure 3.3: All plane waves marked "A" behave the same on the grid with $\Delta x = \Delta y = h$. All plane waves rotated counter-clockwise by θ, for $0° < \theta < 45°$, from a plane wave marked "A" behave the same way on the equally spaced grid. Finally, all plane waves rotated by $-\theta$ behave the same as those rotated by $+\theta$ because of mirror symmetry with respect to the x-axis and y-axis. From these symmetry arguments, it may be seen that only the plane wave propagation angles $0° < \theta < 45°$ need to be investigated.
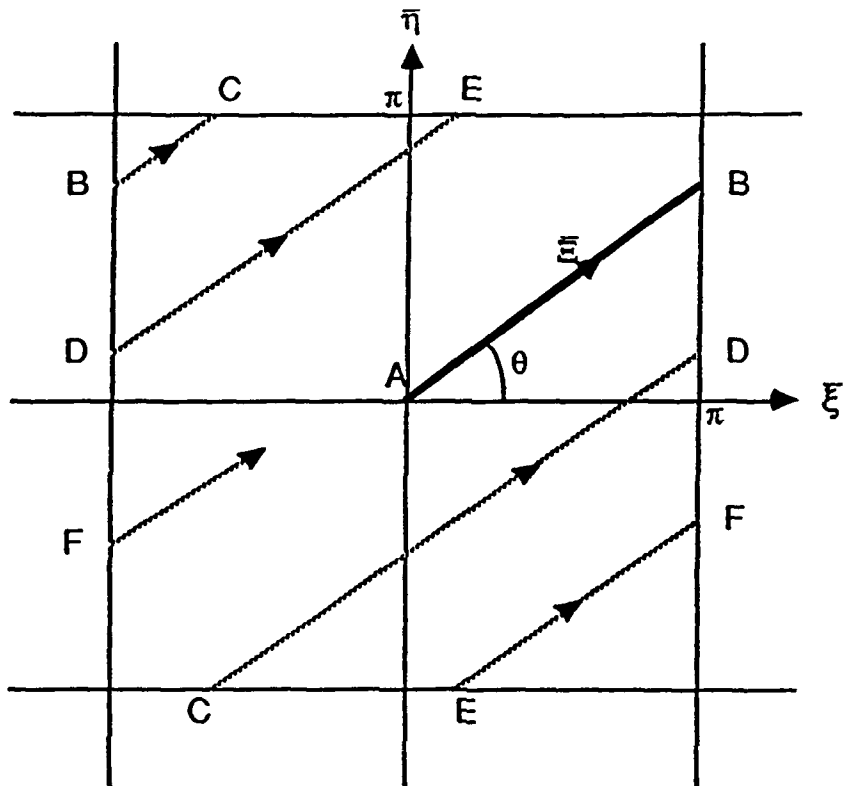
Figure 3.4: Wavenumber coordinate system in which 2-D dispersion and dissipation is evaluated. The wavenumbers $\bar{\xi}$ and $\bar{\eta}$ are both periodic in $[\pm\pi]$. The range of $\bar{\xi} \in [\pm\pi], \bar{\eta} \in [\pm\pi]$ is designated the fundamental coordinate region. The magnitude of the wavevector $\bar{\Xi}$ in the fundamental coordinate region, is restricted to $0 < |\bar{\Xi}| < \sqrt{2}\pi$ and wraps around periodically as shown.

and dissipation characteristics of the 2-D system. Slices through the 2-D dispersion and dissipation functions are computed by choosing a direction of propagation, θ, with respect to the grid and a range of wavevector magnitudes, $0 \leq \bar{\Xi} \leq \pi/\cos\theta$ as shown in Figure 3.4. I only consider the fundamental leg of the wavevector between A and B in the figure. Subsequent legs are aliases and I avoid them by operating in the range with both $\bar{\xi} \ll \pi$ and $\bar{\eta} \ll \pi$ or, equivalently, $\bar{\Xi} \ll \pi$.

3.2.3 Three difference schemes

Theorems 3.1-3.3 prove that a unique weak solution to the elastodynamic equations is guaranteed by a monotone difference scheme, which is at most first order accurate in time. For the normalized elastodynamic equations three schemes are examined of which only one is monotone, namely Lax-Friedrichs. The other two, Lax-Wendroff and Leap-frog, are second order accurate and not monotone. These schemes were chosen because of their higher accuracy in the smooth parts of the solution. Lax-Wendroff is less dissipative than Lax-Friedrichs, which makes it more attractive for an energy analysis. Leap-frog is non-dissipative, which makes it more attractive still. An attempt is made to patch these higher order schemes in the neighborhood of material discontinuities to make them locally monotone and hence guarantee the unique weak solution. The attempt is successful for Lax-Wendroff but not for Leap-frog. Each of the three schemes is analyzed for its dispersion and dissipation characteristics and evaluated for its usefulness in the ice scattering problem.

The effort to make the schemes locally monotone is necessitated by the high density contrast in the ice scattering problem. Other applications, such as geophysical seismic modeling, do not generally contain high-contrast boundaries and are less demanding on the finite difference scheme, in terms of stability.

The analysis is done for the linear homogeneous elastodynamic equations (3.21). The analytic system is approximated using the finite difference equation

$$\underline{u}_{m,n}^{l+1} = Q\underline{u}_{m,n}^{l},\tag{3.30}$$

which updates the field variables from time step l to $l+1$. The field variables are defined as

$$\underline{u}_{m,n}^{l} = (u_{m,n}^{l}, v_{m,n}^{l}, \sigma_{m,n}^{l}, \tau_{m,n}^{l}, \chi_{m,n}^{l})^{T},\tag{3.31}$$

which is a discrete analogy to the variable definition given in Equation (3.22).

The amplification matrix for each scheme is written in unnormalized form while the dispersion and dissipation curves are computed for unit velocity, which facilitates interpretation. By so doing, the dispersion curves can be compared directly with the dispersion curve of the model equation $u_{,t} = -u_{,x}$, i.e., $\omega = \xi$, to see the numerical phase distortion of the difference scheme. Finally, to keep things simple, only the response for the compressional mode is shown. In most cases the phase and amplitude errors for the shear mode are less than those for the compressional mode for any fixed wavenumber. In no case are the errors significantly worse for shear. Later I give a specific example of compressional versus shear errors for the Lax-Wendroff scheme to illustrate this point.

Lax-Friedrichs

The 2-D Lax-Friedrichs difference scheme for the elastodynamic equations (3.21) is written

$$\underline{u}_{m,n}^{l+1} = \left[\mu_x^0\mu_y^0 + k(\underline{\underline{A}}\,\delta_x^0 + \underline{\underline{B}}\,\delta_y^0)\right]\underline{u}_{m,n}^l \tag{3.32}$$

and may be visualized as the averaging and differencing operation shown in Figure 3.5.

Substituting the modal solution $\underline{u}_{m,n}^l \sim \underline{Z}_o^l e^{-i(\xi m + \eta n)}$ and simplifying yields the amplification matrix

$$\underline{\underline{D}}_{LF} = \begin{pmatrix} \cos\bar\xi\cos\bar\eta & \cdot & \frac{ik}{\rho}\sin\bar\xi & \cdot & \frac{ik}{\rho}\sin\bar\eta \\ \cdot & \cos\bar\xi\cos\bar\eta & \cdot & \frac{ik}{\rho}\sin\bar\eta & \frac{ik}{\rho}\sin\bar\xi \\ ik(\lambda+2\mu)\sin\bar\xi & ik\lambda\sin\bar\eta & \cos\bar\xi\cos\bar\eta & \cdot & \cdot \\ ik\lambda\sin\bar\xi & ik(\lambda+2\mu)\sin\bar\eta & \cdot & \cos\bar\xi\cos\bar\eta & \cdot \\ ik\mu\sin\bar\eta & ik\mu\sin\bar\xi & \cdot & \cdot & \cos\bar\xi\cos\bar\eta \end{pmatrix}. \tag{3.33}$$

The eigenvalues of $\underline{\underline{D}}_{LF}$ are computed for $\bar\xi$ and $\bar\eta$ using Equation (3.29) with $\theta = 0°, 15°, 30°, 45°$ and $0 \le \bar\Xi \le \pi/\cos\theta$. From the eigenvalues, the dispersion and dissipation for the Lax-Friedrichs scheme are computed using Equation (3.17) and (3.16). The results are shown in
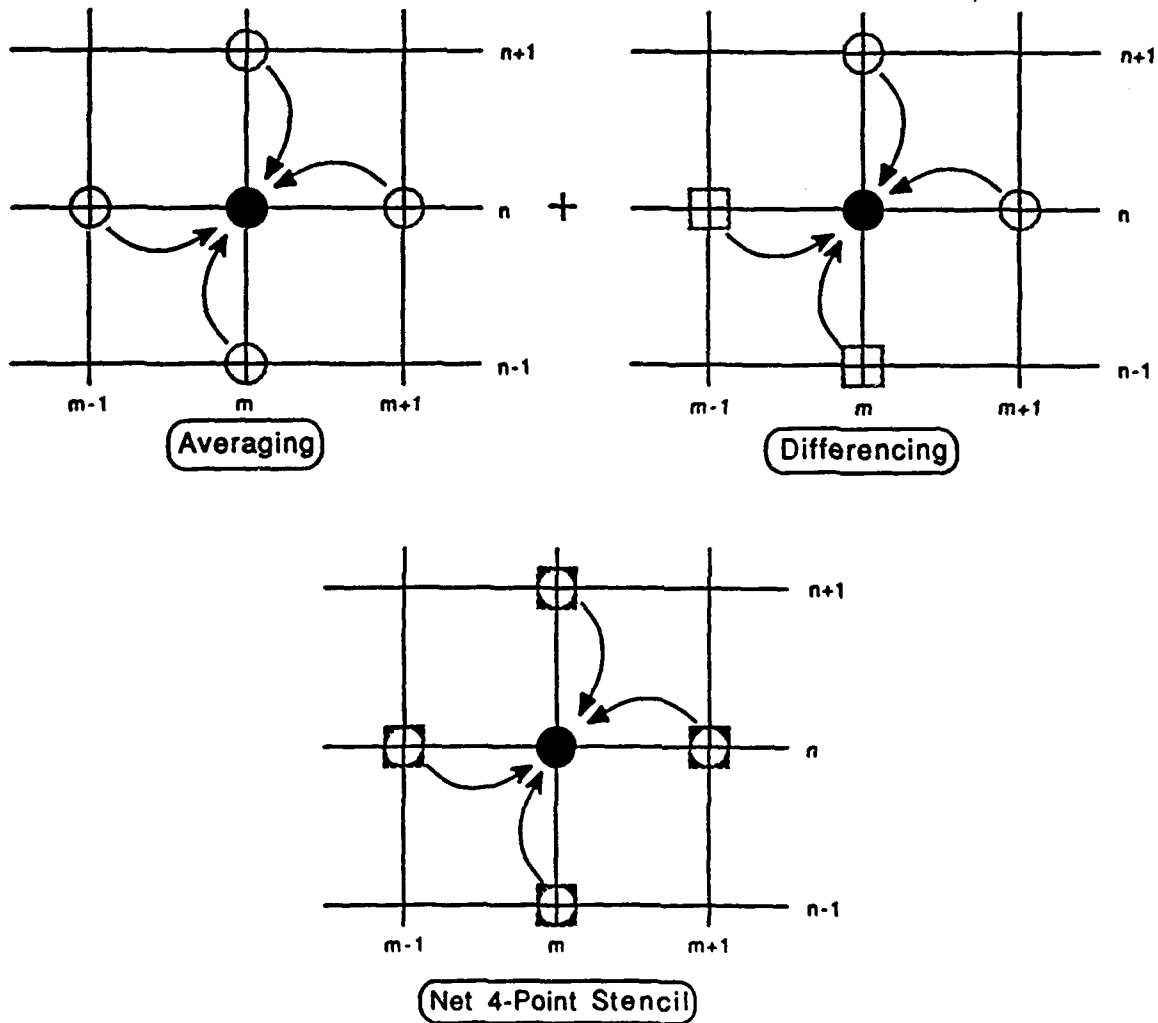
Figure 3.5: Graphical visualization of the Lax-Friedrichs scheme. The result of one complete operation is the sum of two parts, an averaging and a differencing part. The net operation involves the four point stencil shown.

Figure 3.6 for the full range of normalized wavenumbers and for values of $\frac{k}{h}$ not exceeding the stability limit, $\left(\frac{k}{h}\right)_{max} = 1/\sqrt{2}$.

The curves in Figure 3.6 show that plane waves propagating in different directions have different phase and amplitude distortions, implying anisotropy in the grid. Compare the dispersion curve for $\theta = 0°$ with that for $\theta = 45°$. In the former the group velocity, the slope of the dispersion curve, $v_g = \frac{\partial \xi}{\partial \omega}$, is always in the correct direction while in the latter the low wavenumbers have forward group velocity and the high wavenumbers have reverse group velocity. At $\theta = 45°$ the high wavenumbers are propagating backwards from the direction in which they should be moving. As an aside, note that comments about group velocity are only valid at the extremes of high and low wavenumber, where dissipation is small. For the mid-range of wavenumbers the concept of group velocity is invalidated by the large dissipation [65].

The curves of Figure 3.7 show the phase and amplitude time step limits for the compressional mode of the elastodynamic equations using Lax-Friedrichs for $\theta = 0°$. The curves for the higher values of θ are not significantly different from those for $\theta = 0°$ and are not shown. For a center frequency of $50\,Hz$ in water with $C_p = 1500\,m/s$ and a grid point spacing of $0.5\,m$ there are 60 grid points per wavelength. In this case, the upper curve in Figure 3.7 shows that $O(10^4)$ time steps may be taken before a $\pi/4$ phase error accumulates while the lower curve shows that only $O(10)$ time steps are required before a $1\,dB$ amplitude error occurs. Considering that the ice scattering experiments require $O(10^{\cdot})$ time steps to complete, the Lax-Friedrichs scheme is not an appropriate choice. The excess attenuation of the scheme would render an energy analysis useless.

In summary, the Lax-Friedrichs scheme is first order accurate in time and may be formulated as a monotone scheme. This guarantees that the numerical solution converges to the unique solution of Equation (3.21) and satisfies internal boundary conditions at the
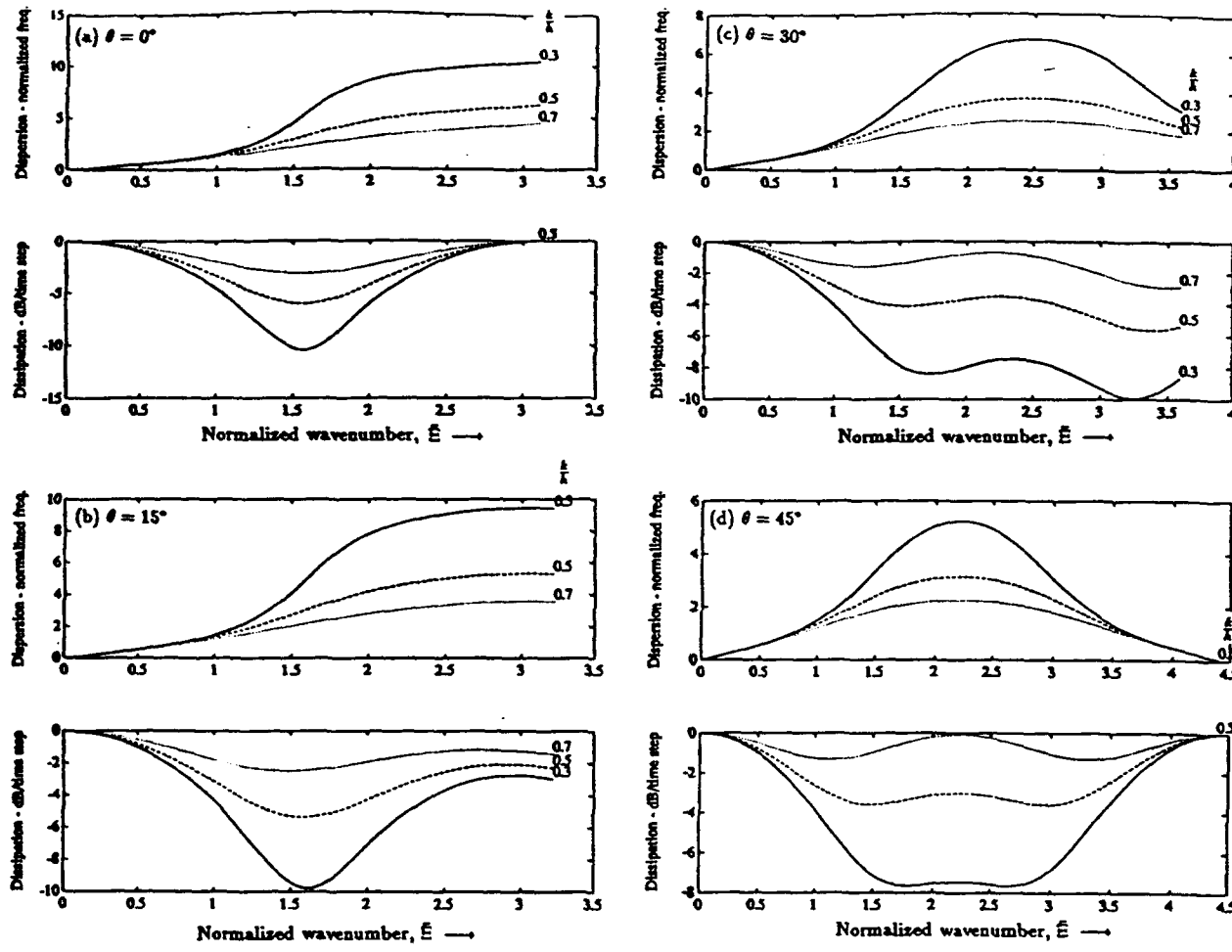
Figure 3.6: Lax-Friedrichs dispersion and dissipation characteristics for the compressional mode of the elastodynamic equations. The curves in (a)-(d) correspond to propagation angles $\theta = 0°, 15°, 30°, 45°$. For values of the wavenumber, where dissipation is small, the slope of the dispersion curve is the group velocity, $v_g = \frac{\partial \xi}{\partial \omega}$ [65]. At high wavenumbers and at high propagation angles the numerical group velocity is backwards. The dissipation curve shows negative gain, i.e., attenuation, per time step.

63
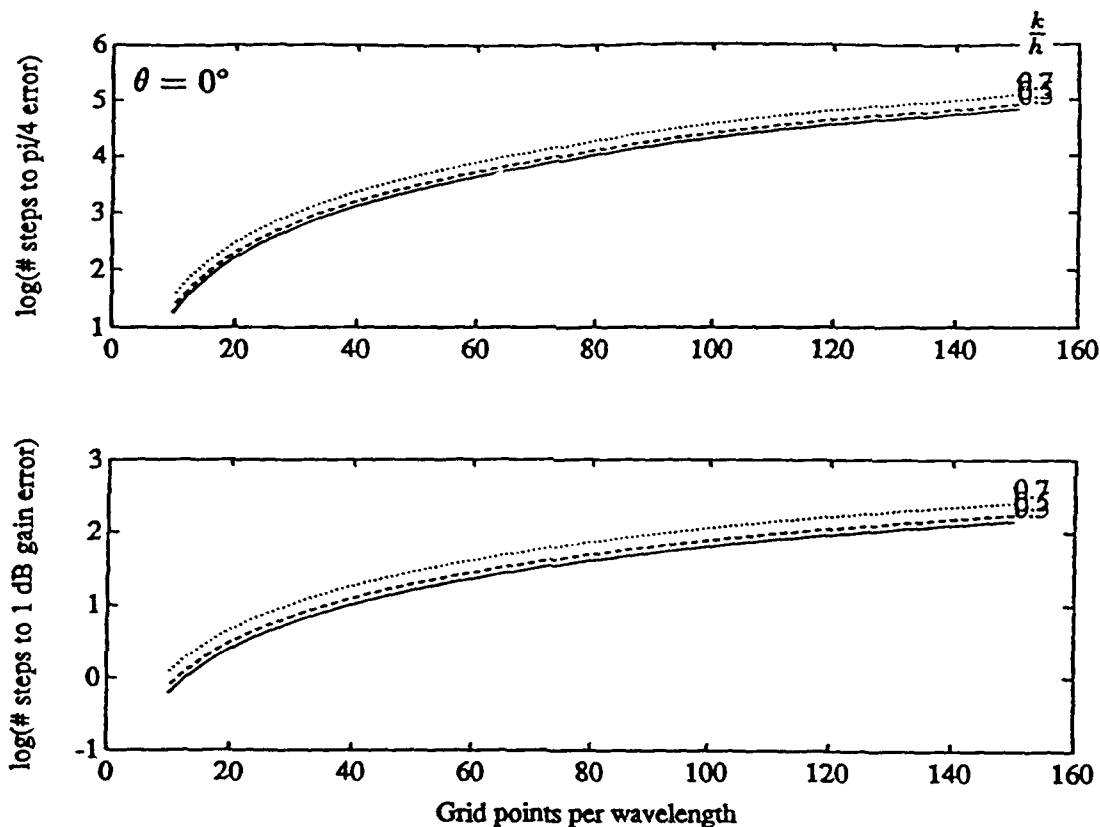
Figure 3.7: Time step limits for the compressional mode of the elastodynamic equations using Lax-Friedrichs with $\theta = 0°$. The upper curves show the number of time steps before a $\pi/4$ phase shift occurs and the lower curve shows the number of time steps before a $1\,dB$ amplitude error occurs. For a choice of $h = 0.5\,m$ and $C_p = 1500\,m/s$ there are 60 grid points per wavelength at $50\,Hz$. The upper curves show that $O(10^4)$ time steps can be taken before the phase error limit is reached. The lower curve, however, shows that only $O(10)$ time steps can be taken before a significant amplitude error occurs. This is the weakness of the Lax-Friedrichs scheme.

interface between different materials. The scheme is so dissipative, however, that the results cannot be used to compute energy partitioning. This leads to the Lax-Wendroff scheme with locally added dissipation.

Lax-Wendroff

The Lax-Wendroff difference scheme is $O(k^2, h^2)$ and so by Theorem 3.3 cannot be monotone. Furthermore, higher order schemes tend to have oscillatory solutions near discontinuities, which in extreme cases grow without bound. To correct this problem and to guarantee convergence to the unique solution, a monotone scheme is developed by adding dissipation to the scheme. For the general 1-D conservation law equation

$$u_{,t} = f_{,x} \tag{3.34}$$

the Lax-Wendroff scheme with added dissipation may be written in three steps as

$$
\begin{aligned}
u_{m+\frac{1}{2}}^{l+\frac{1}{2}} &= \mu_x^+ + \frac{k}{2}\delta_x^+ f_m^l, \\
\tilde{u}_m^{l+1} &= u_m^l + k\delta_x^- f_{m+\frac{1}{2}}^{l+\frac{1}{2}}, \\
u_m^{l+1} &= \tilde{u}_m^{l+1} + \alpha h^2 \delta_x^+ \delta_x^- u_m^l
\end{aligned}
\tag{3.35}
$$

and may be visualized as shown in Figure 3.8. The last step is where the added dissipation is introduced by setting $\alpha \neq 0$.

For the elastodynamic Equations (3.21) the three step Lax-Wendroff formulation with added dissipation may be written in a conservation law monotone form as

$$
\begin{aligned}
\underline{u}_{m+\frac{1}{2},n+\frac{1}{2}}^{l+\frac{1}{2}} &= \mu_x^+ \mu_y^+ \underline{u}_{m,n}^l + \frac{k}{2}(\underline{A}\,\mu_y^+ \delta_x^+ + \underline{B}\,\mu_x^+ \delta_y^+)\underline{u}_{m,n}^l, \\
\underline{\tilde{u}}_{m,n}^{l+1} &= \underline{u}_{m,n}^l + k(\underline{A}\,\mu_y^- \delta_x^- + \underline{B}\,\mu_x^- \delta_y^-)\underline{u}_{m+\frac{1}{2},n+\frac{1}{2}}^{l+\frac{1}{2}}, \\
\underline{u}_{m,n}^{l+1} &= \underline{\tilde{u}}_{m,n}^{l+1} + \alpha h^2 (\delta_x^+ \delta_x^- + \delta_y^+ \delta_y^-)\underline{u}_{m,n}^l
\end{aligned}
\tag{3.36}
$$

and may be visualized as shown in Figure 3.9. The last step is only executed if dissipation

65
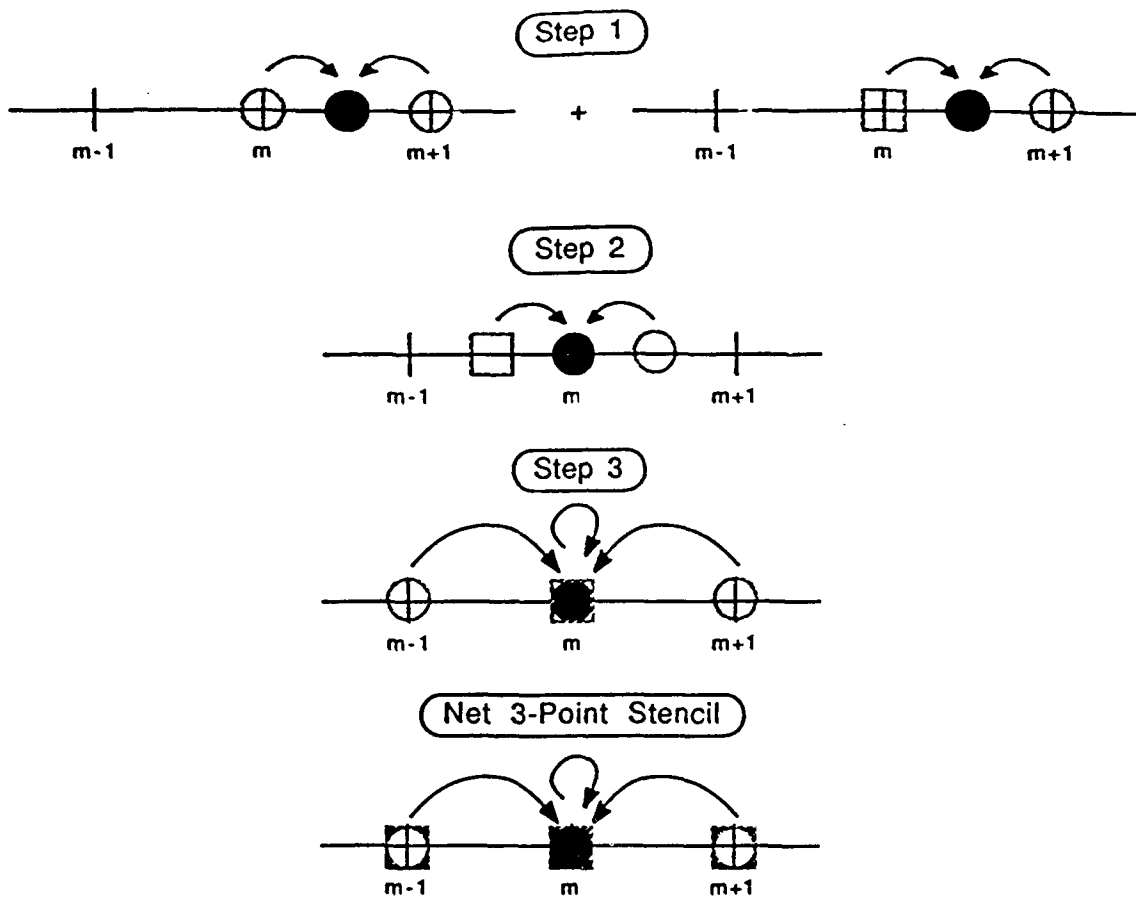
Figure 3.8: Visualization of Lax-Wendroff scheme for 1-D conservation law. The scheme is three steps. The first step updates the field to a half time increment, $l + \frac{1}{2}$. The second step updates to the whole time increment, $l + 1$. The third step is only used if added dissipation is needed.
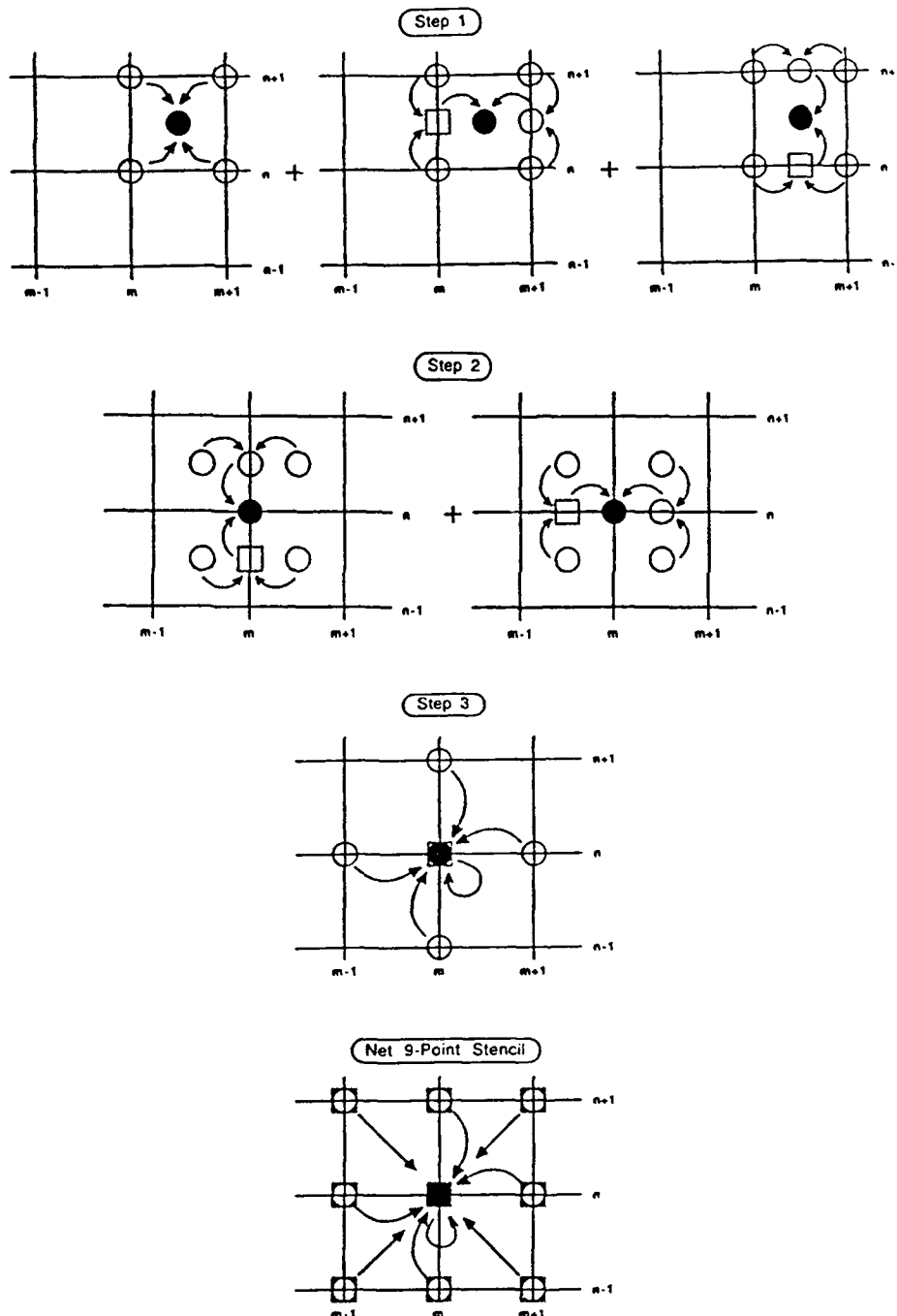
Figure 3.9: Visualization of the Lax-Wendroff scheme in 2-D. This is a 2-D version of the operation shown in Figure 3.8. The result of the first step, in this case, is the field estimate at cell centers at half time increments, $l + \frac{1}{2}$. The second step brings these estimates back to the cell corners at the whole time increment, $l + 1$. Again, the last step is needed only if added dissipation is to be added. The net operation is defined on a 9-point stencil. Contrast this with the 4-point stencil of the Lax-Friedrich scheme. The operation count for Lax-Wendroff is about three times greater than for Lax-Friedrichs.

67

is needed to stabilize the scheme near the material boundaries [57]. The need for the dissipation is determined by computing the discrete Laplacian of the field at each grid point, i.e., $(\delta_x^+ \delta_x^- + \delta_y^+ \delta_y^-)\underline{u}_{m,n}^l$, and if the curvature of the field is large then the dissipation is added. If the field is smooth then nothing is done at that grid point.

The amplification matrix for the Lax-Wendroff scheme is computed using the modal solution $\underline{u}_{m,n}^l \sim \underline{Z}_o^l e^{-i(\xi m + \eta n)}$. Substitution into Equation (3.36) and simplification yields the rather cumbersome result

$$
\underline{\underline{D}}_{LW} = \begin{pmatrix} a & b & c & 0 & e \\ b & g & 0 & e & c \\ k & l & m & n & 2b \\ p & q & r & s & 2b \\ u & v & w & w & y \end{pmatrix}, \tag{3.37}
$$

where

$$
a = 1 - 2\frac{k^2}{h^2}(C_p^2 \cos^2(\bar{\eta}/2)\sin^2(\bar{\xi}/2) + C_s^2 \cos^2(\bar{\xi}/2)\sin^2(\bar{\eta}/2))
$$
$$
-4\alpha(\sin^2(\bar{\xi}/2) + \sin^2(\bar{\eta}/2)),
$$

$$
b = -\frac{k^2}{2h^2}(C_p^2 - C_s^2)\sin\bar{\xi}\sin\bar{\eta},
$$

$$
c = -\frac{i}{\rho}\frac{k}{h}\cos^2(\bar{\eta}/2)\sin\bar{\xi},
$$

$$
e = -\frac{i}{\rho}\frac{k}{h}\cos^2(\bar{\xi}/2)\sin\bar{\eta},
$$

$$
g = 1 - 2\frac{k^2}{h^2}(C_s^2 \cos^2(\bar{\eta}/2)\sin^2(\bar{\xi}/2) + C_p^2 \cos^2(\bar{\xi}/2)\sin^2(\bar{\eta}/2))
$$
$$
-4\alpha(\sin^2(\bar{\xi}/2) + \sin^2(\bar{\eta}/2)),
$$

$$
k = -i\rho C_p^2 \frac{k}{h}\cos^2(\bar{\eta}/2)\sin\bar{\xi},
$$

$$
l = -i\rho(C_p^2 - 2C_s^2)\frac{k}{h}\cos^2(\bar{\xi}/2)\sin\bar{\eta},
$$

$$
m = 1 - 2\frac{k^2}{h^2}C_p^2 \cos^2(\bar{\eta}/2)\sin^2(\bar{\xi}/2)
$$
$$
-4\alpha(\sin^2(\bar{\xi}/2) + \sin^2(\bar{\eta}/2)),
$$

68

$$n = -2\frac{k^2}{h^2}(C_p^2 - 2C_s^2)\cos^2(\bar{\xi}/2)\sin^2(\bar{\eta}/2),$$

$$p = -i\rho(C_p^2 - 2C_s^2)\frac{k}{h}\cos^2(\bar{\eta}/2)\sin\bar{\xi},$$

$$q = -i\rho C_p^2\frac{k}{h}\cos^2(\bar{\xi}/2)\sin\bar{\eta},$$

$$r = -2\frac{k^2}{h^2}(C_p^2 - 2C_s^2)\cos^2(\bar{\eta}/2)\sin^2(\bar{\xi}/2),$$

$$s = 1 - 2\frac{k^2}{h^2}C_p^2\cos^2(\bar{\xi}/2)\sin^2(\bar{\eta}/2)$$
$$-4\alpha(\sin^2(\bar{\xi}/2) + \sin^2(\bar{\eta}/2)),$$

$$u = -i\rho C_s^2\frac{k}{h}\cos^2(\bar{\xi}/2)\sin\bar{\eta},$$

$$v = -i\rho C_s^2\frac{k}{h}\cos^2(\bar{\eta}/2)\sin\bar{\xi},$$

$$w = -\frac{k^2}{2h^2}C_s^2\sin\bar{\xi}\sin\bar{\eta},$$

$$y = 1 - 2\frac{k^2}{h^2}C_s^2(\cos^2(\bar{\eta}/2)\sin^2(\bar{\xi}/2) + \cos^2(\bar{\xi}/2)\sin^2(\bar{\eta}/2))$$
$$-4\alpha(\sin^2(\bar{\xi}/2) + \sin^2(\bar{\eta}/2)). \tag{3.38}$$

Compressional and shear speed, C_p and C_s, are related to the Lamé parameters by $C_p^2 = (\lambda + 2\mu)/\rho$ and $C_s^2 = \mu/\rho$. The eigenvalues of the amplification matrix $\underline{D}_{LW}$ are computed for the angles $\theta = 0°, 15°, 30°, 45°$, the range of normalized wavenumbers $0 \leq \bar{\Xi} \leq \pi/\cos\theta$, for zero added dissipation, $\alpha = 0$, and for selected values of $\frac{k}{h} < 1$, which is the stability limit for this scheme. From the eigenvalues, the dispersion and dissipation characteristics are computed using Equation (3.17) and (3.16). The results are plotted in Figure 3.10. The anisotropy of the difference scheme is evident. Note especially at the larger angles $\theta = 30°, 45°$ the reverse group velocity for all values of $\frac{k}{h}$.

An interesting feature of this scheme is that it is stable up to $\frac{k}{h} = 1.0$. Compare this to the work on another 2-D Lax-Wendroff scheme by Santosa [54] who found a stability limit of $\frac{k}{h} < 0.6125$, a 40 % reduction. At what cost is my scheme more stable? Two costs actually. First, I have a 9-point stencil using the averaging operators, $\mu_{x,y}^{\pm}$, in the
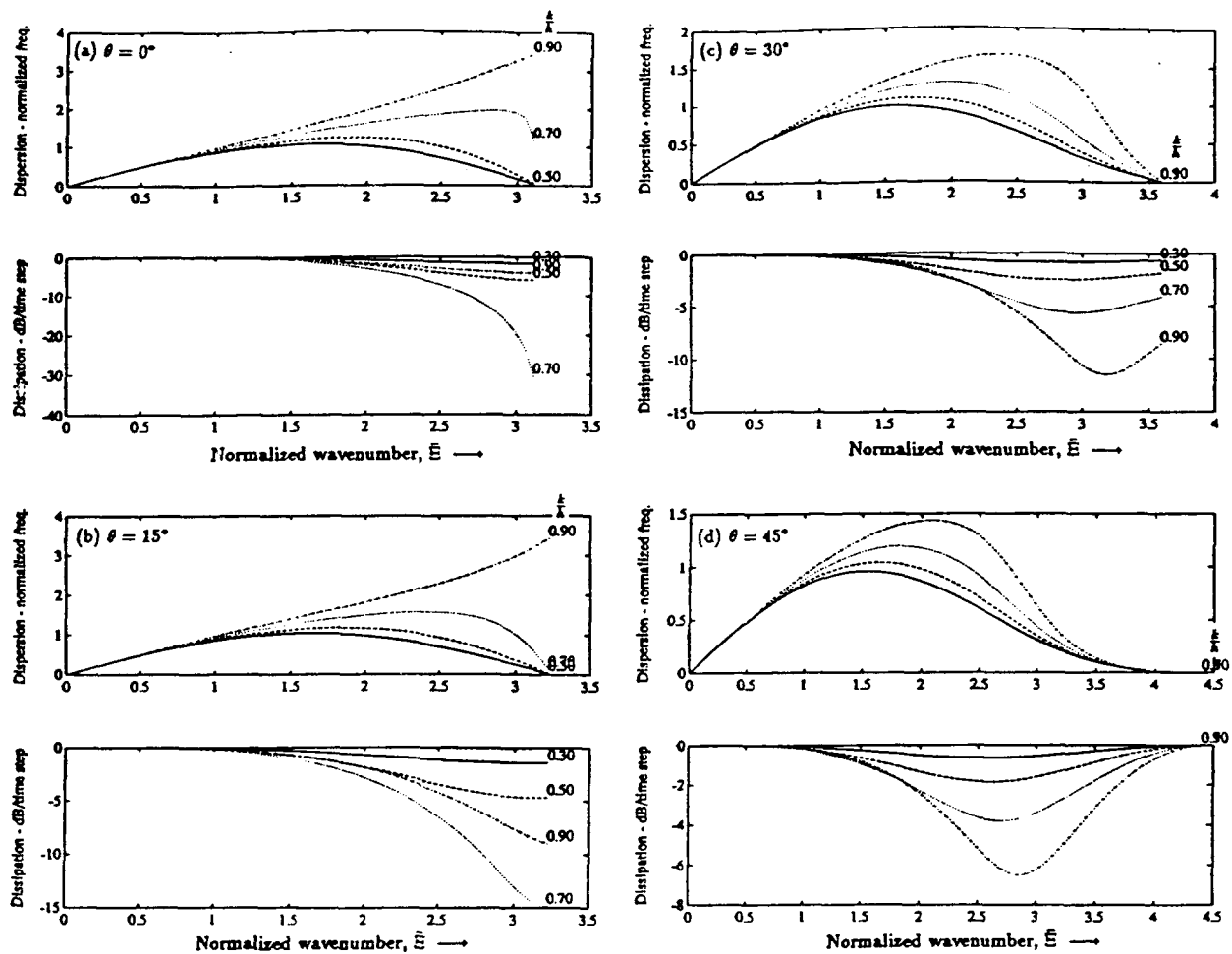
Figure 3.10: Lax-Wendroff dispersion and dissipation characteristics for the compressional mode of the elastodynamic equations. The curves in (a)-(d) correspond to propagation angles $\theta = 0°, 15°, 30°, 45°$. A comparison of the Lax-Wendroff dissipation characteristics with those of the Lax-Friedrichs scheme, shown in Figure 3.6, reveals considerably less attenuation at the low wavenumbers.

Lax-Wendroff equation (3.36) while Santosa uses a 5-point stencil with no averaging, hence my operation count is higher than his. The second cost is already noted above, in portions of the θ-$\bar{\Xi}$ space I have reverse group velocity; Santosa's scheme always has forward group velocity.

The curves in Figure 3.11 show the number of time steps allowed before a phase error of $\pi/4$ or an amplitude error of $1\,dB$ occurs. Only the results for $\theta = 0°$ are shown since they are representative of the results for the higher values of θ. In both cases, for 60 grid points per wavelength, corresponding to $f_o = 50\,Hz$, $h = 0.5\,m$, and $C_p = 1500\,m/s$, $O(10^4)$ time steps are required before the specified error limits are reached. Since most experiments only require $O(10^3)$ time steps the Lax-Wendroff scheme looks like an acceptable choice.

I stated earlier that the shear mode numerical errors are comparable to those of the compressional mode. To illustrate this consider Figure 3.12, which shows the phase and amplitude time step limits for the compressional (P) and shear (S) mode with $\frac{k}{h} = 0.9$. This example is for ice using $C_p = 3500\,m/s$ and $C_s = 1600\,m/s$, which are the values to be used in the scattering experiments. For the phase and amplitude errors the time step limits are comparable at any fixed wavenumber. At a fixed frequency, however, the limits are not comparable. This is due to the difference in wavelength for a fixed frequency. For example, at $f_o = 50\,Hz$ and $h = 0.5\,m$ there are 140 grid points per wavelength for the compressional mode and 64 grid points per wavelength for the shear mode. The phase and amplitude time step limit for the former is $O(10^6)$ and for the latter, $O(10^4)$. Both are adequate, however, for the scattering experiments.

Up to now I have ignored the issue of added dissipation, simply saying it is added when necessary. It is important to have the extra dissipation near material discontinuities to make the scheme monotone and guarantee the unique and stable solution. If, however, dissipation is added indiscriminately the performance of the Lax-Wendroff scheme quickly
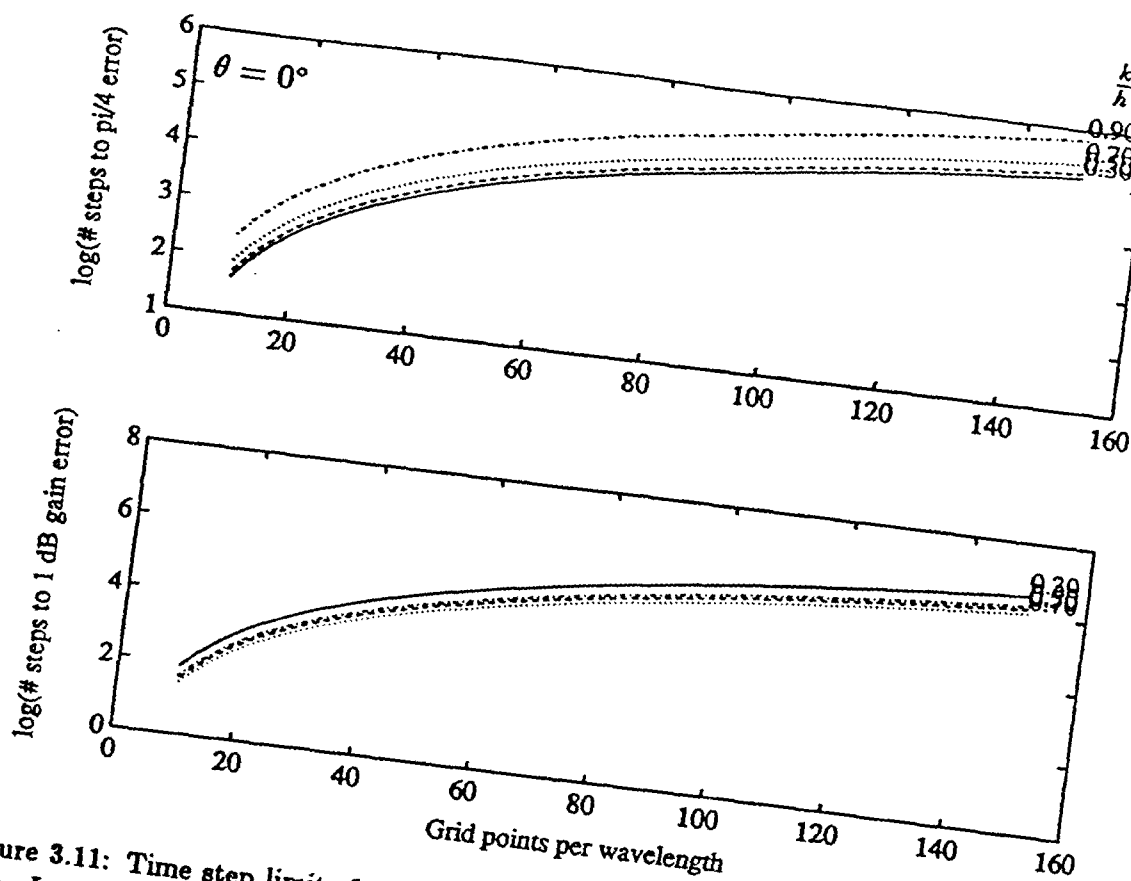
Figure 3.11: Time step limits for the compressional mode of the elastodynamic equations using Lax-Wendroff with $\theta = 0°$. The upper curves show the number of time steps before a $\pi/4$ phase error occurs and the lower curve shows the number of time steps before a $1\,dB$ amplitude error occurs. For a choice of $h = 0.5\,m$ and $C_p = 1500\,m/s$ there are 60 grid points per wavelength at $50\,Hz$. The upper and lower curves show that $O(10^4)$ time steps can be taken before the phase or amplitude error limit is reached. For the scattering models under consideration only $O(10^3)$ time steps are anticipated so there is no concern for contaminating the solution with numerical phase or amplitude distortion using this scheme.

72
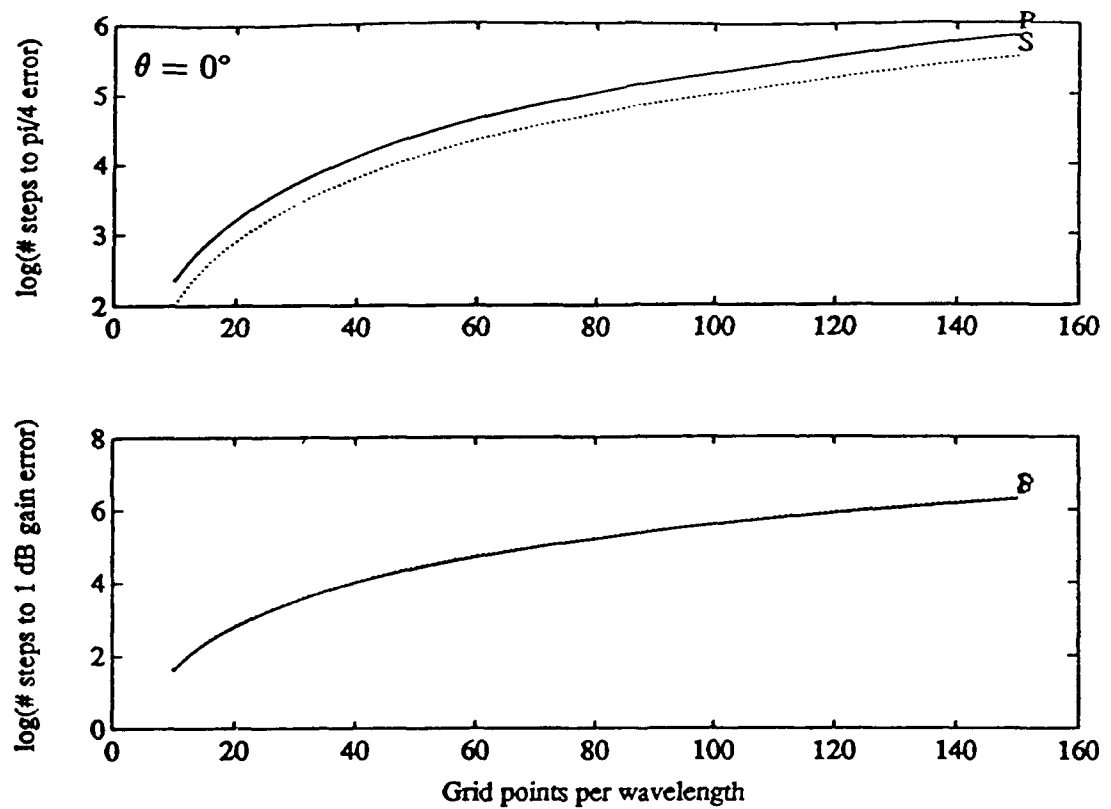
Figure 3.12: Time step limits for the compressional (P) and shear (S) modes of the elasto-dynamic equations using Lax-Wendroff with $\theta = 0°$ and $\frac{k}{h} = 0.9$. The propagation speeds are $C_p = 3500\,m/s$ and $C_s = 1600\,m/s$. At other values of θ and $\frac{k}{h}$ the shear mode time step limits are never significantly less than those for the compressional mode and are often larger.

degrades. Even for very small values of the dissipation coefficient, α, the amplitude time step limit is reduced by a factor of 10. Added dissipation must be introduced carefully. I have chosen the following way to implement the added dissipation.

Notice in Figure 3.10 that at $\theta = 45°$ both the group velocity and the dissipation of the diagonal $2x$-wave, illustrated in Figure 3.13, is zero. If this wave is ever excited, say at an air-ice-water corner, it will stay in place due to its zero group velocity and it will not be attenuated because the dissipation is zero. Furthermore, the causative agent exciting the wave in the first place probably remains active, hence the wave grows. These are parasitic modes that must be eliminated from the solution. The added dissipation scheme is designed to detect the diagonal $2x$-waves by computing the curvature of the field in the two diagonal directions at each grid point. If either curvature exceeds a preset threshold then the $2x$-wave is evidently beginning to grow. In this case, extra dissipation is added to the update scheme by setting α to a fixed non-zero value in Equation (3.36). This decision is made independently for each grid point at each time step. Figure 3.14 shows the added dissipation scheme in action. Due to source injection errors, caused by differences between the analytic source function and the discrete approximation, high wavenumber noise is generated in the field around the source location. The figure shows how added dissipation is introduced only where the field is rough and leaves the smooth portion of the field unchanged. This is the desired effect. Where the solution is ragged, a monotone $O(k, h^2)$ scheme is used while in the smooth part of the solution a higher order accurate $O(k^2, h^2)$ scheme is used. An estimate of the excess attenuation in units of $dB/timestep$ from this experiment is shown in Figure 3.15 and is compared to the analytic excess attenuation for the Lax-Wendroff scheme with and without added dissipation. The estimate tracks the analytic result for no added dissipation very closely even though dissipation was added at a few grid points near the source. The added dissipation has no effect on the propagation of the pulse through the

74
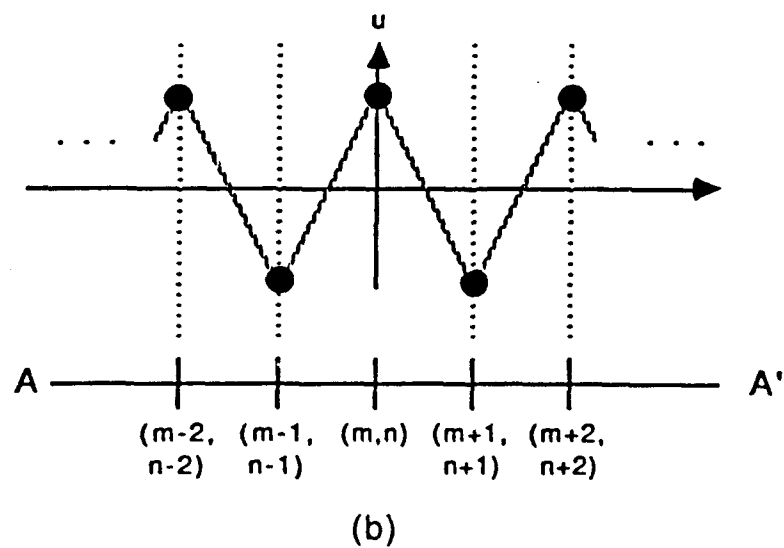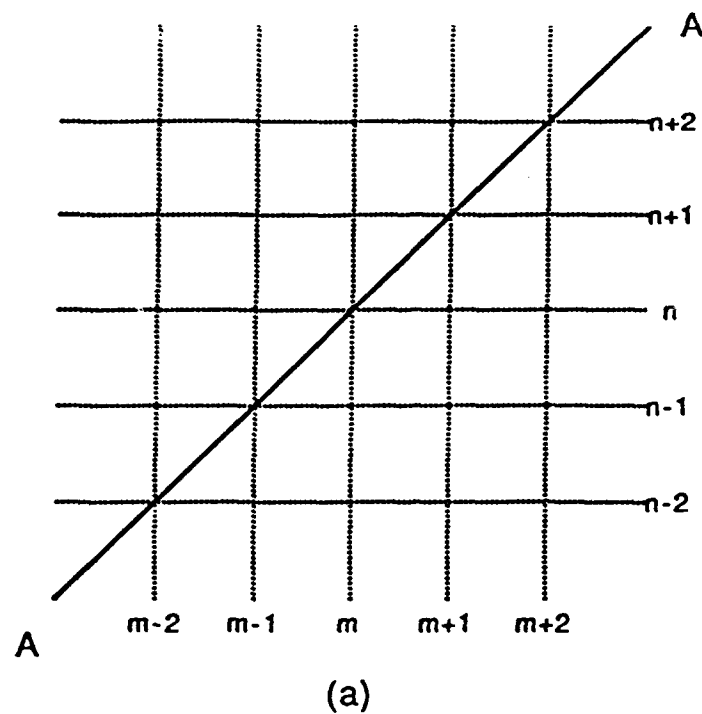
Figure 3.13: $2x$-wave. This is the highest wavenumber that can be supported by the grid. Pictured is the $2x$-wave in the diagonal direction. A similar figure applies along the x-axis and the y-axis.

75
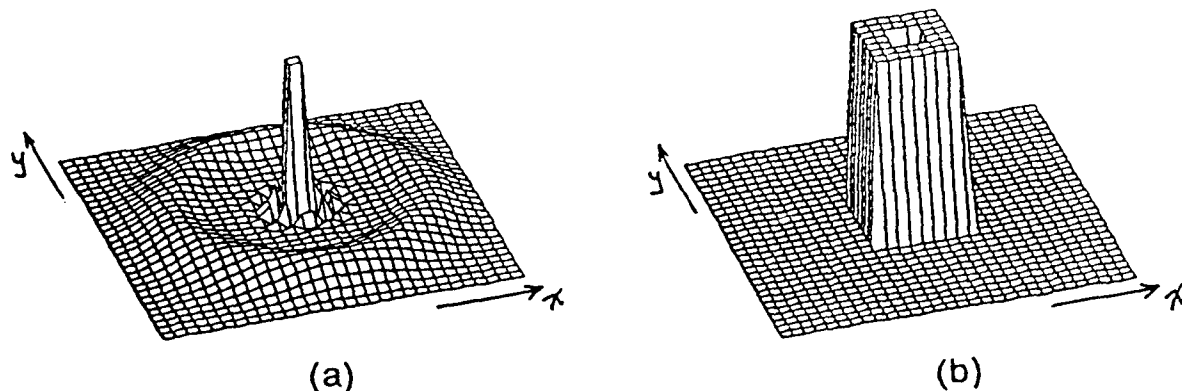
Figure 3.14: Added dissipation mask. Only in the portions of the field where the curvature is large should added dissipation be used. In (a) the updated field is shown with some regions that are smooth and others that are ragged. The mask in (b) shows where the added dissipation is used. Note that where the field is smooth, no dissipation is added. In these regions the Lax-Wendroff scheme remains second order accurate. Where dissipation is added, the scheme becomes first order.

water since the field is smooth away from the source. This experiment confirms that added dissipation is applied locally and does not change the relatively low inherent numerical dissipation of the second order Lax-Wendroff scheme.

In the ice scattering problem, where there is a relatively thin sheet of ice sandwiched between half spaces of air and water, the effect of added dissipation is more pronounced. In this case, the added dissipation is introduced at the grid points on either side of the two ice interfaces. Since the ice sheet is modeled with only six grid points in thickness, the added dissipation significantly affects plate waves, which only travel in the ice sheet. Figure 5.30 shows a map of the energy density lost to added dissipation in one of the scattering experiments. Because of the energy loss in the plate, direct quantitative estimates involving plate waves cannot be made. Since propagation in the water, however, is not affected by the added dissipation, indirect estimates may be made for the plate wave energy. These estimates are discussed in Chapter 5.
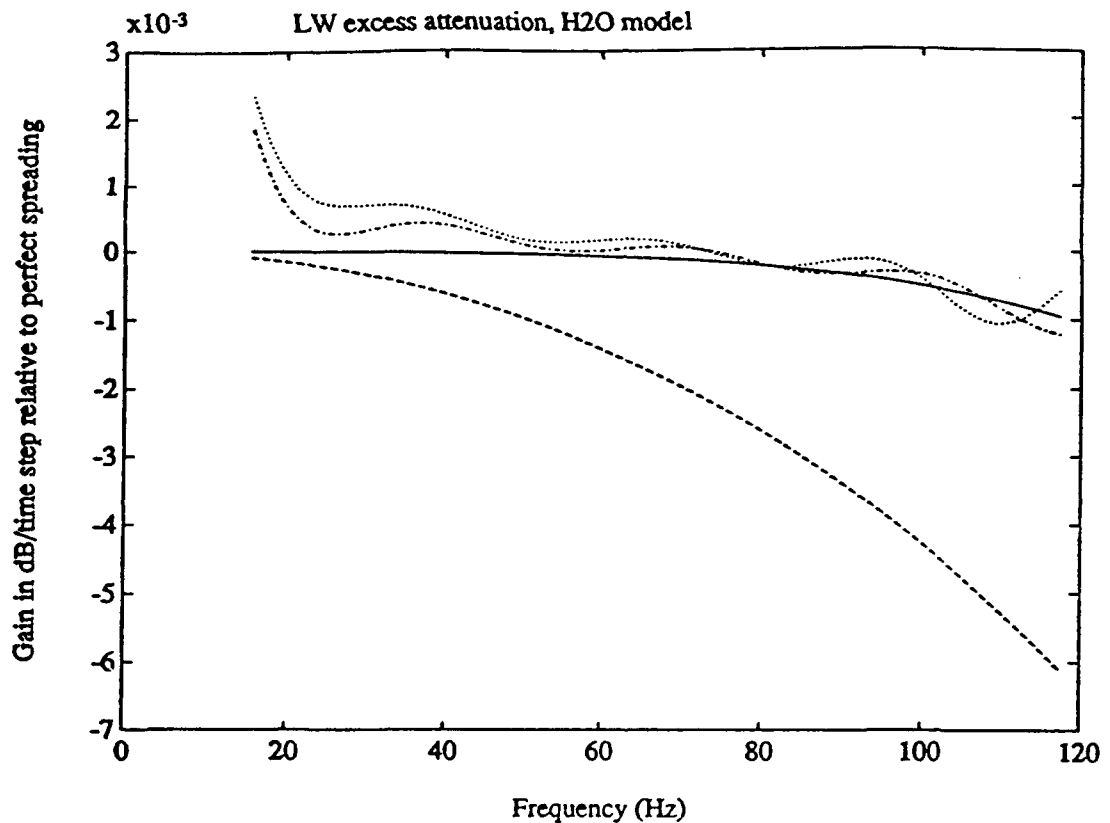
Figure 3.15: Excess attenuation for Lax-Wendroff. The upper two dashed curves are numerical estimates of the excess attenuation from an experiment in homogeneous water. The solid curve is the predicted excess attenuation with no added dissipation. The lower dashed curve is the excess attenuation predicted if the added dissipation with $\alpha = 0.01$ is used globally at every time step. Clearly, the added dissipation is being applied only locally and the global response is that of Lax-Wendroff without added dissipation.
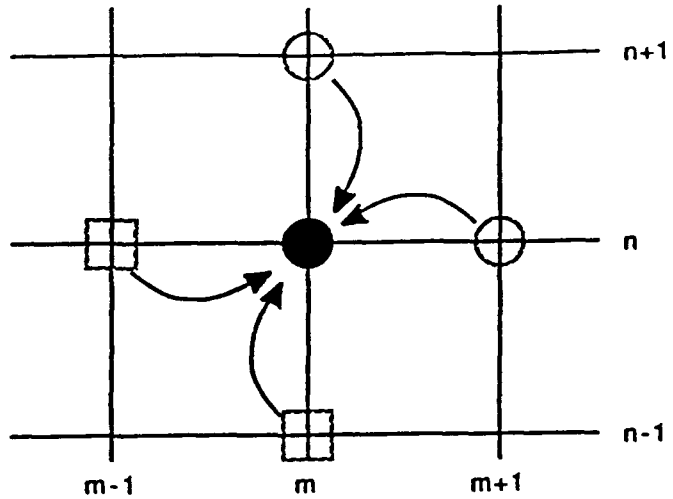
Figure 3.16: Visualization of the Leap-frog difference scheme. As with Lax-Friedrichs, this is a 4-point stencil for time step l. By contrast, however, Leap-frog adds information from time step l to the value $u_{m,n}^{l-1}$. Thus, Leap-frog is a two time step scheme, while Lax-Friedrichs uses information from the previous time step only.

Leap-frog

In contrast to the previous two schemes, which use information only from the previous time step, Leap-frog uses information from the previous two time steps. The scheme has truncation errors of $O(k^2, h^2)$. For the elastodynamic equations (3.21) the Leap-frog scheme may be written

$$\underline{u}_{m,n}^{l+1} = \underline{u}_{m,n}^{l-1} + 2k(\underline{\underline{A}}\,\delta_x^0 + \underline{\underline{B}}\,\delta_y^0)\underline{u}_{m,n}^l \tag{3.39}$$

and may be visualized as in Figure 3.16. Because Leap-frog is a two step scheme, $\underline{\underline{D}}_{FR}$ is an unwieldy 10×10 amplification matrix. The matrix is composed of 2×2 blocks, which are derived from the update equation for each field variable and are of the form

$$\begin{pmatrix} u_{m,n}^{l+1} \\ u_{m,n}^l \end{pmatrix} = \begin{pmatrix} 2k(a\delta_x^0 + b\delta_y^0) & 1 \\ 1 & 0 \end{pmatrix} \begin{pmatrix} u_{m,n}^l \\ u_{m,n}^{l-1} \end{pmatrix}. \tag{3.40}$$

Each block in $\underline{\underline{D}}_{FR}$ is either the matrix in Equation (3.40) or a 2×2 matrix of zeros. The coefficients a and b in the update matrix are either Lamé parameters or buoyancy as
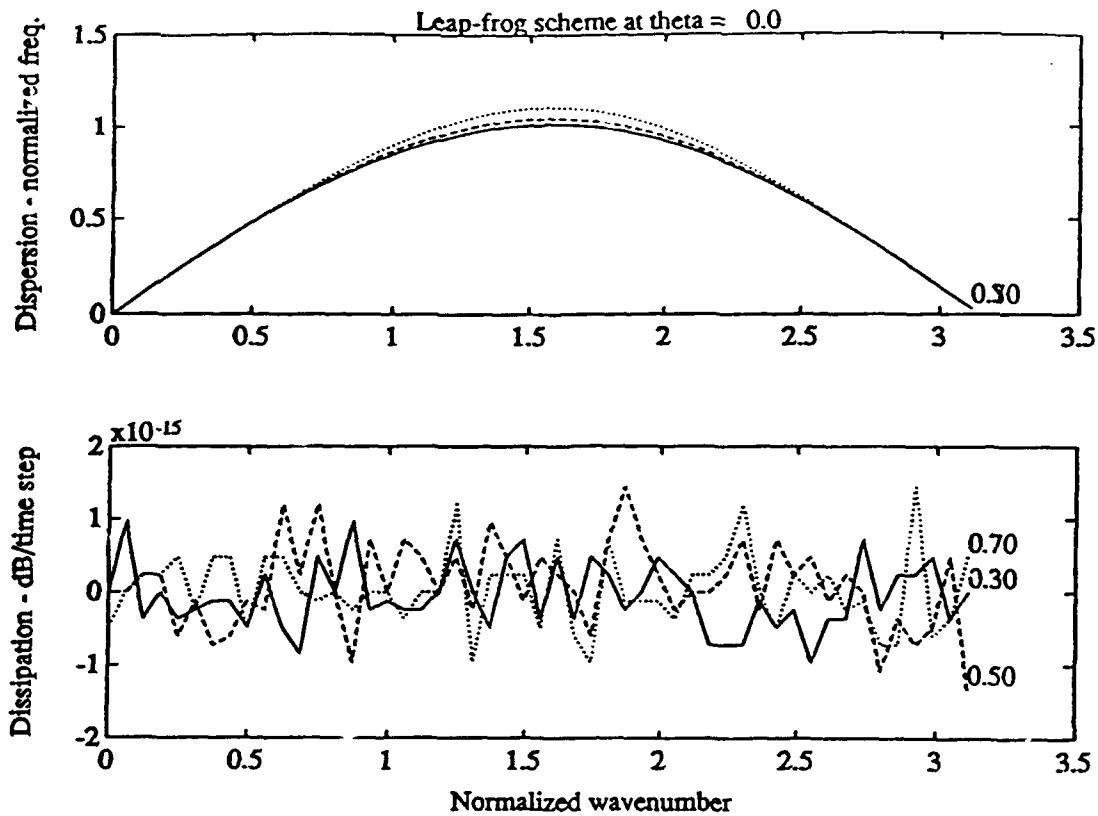
Figure 3.17: Leap-frog dispersion and dissipation for the compressional mode of the elastodynamic equations. Only the results for $\theta = 0$ are shown since this scheme is fatally flawed for global use in the ice scattering application. Two factors lead to this conclusion: the reverse group velocity for high wavenumbers and the lack of any dissipation. The high wavenumber content of discontinuous fields propagate in the wrong direction without attenuation and destroy the solution.

prescribed by the analytic equations. Assuming a modal solution as for the other schemes, the non-zero blocks of the amplification matrix for Leap-frog are of the form

$$
\begin{pmatrix}
-4ki(a\sin\bar{\xi} + b\sin\bar{\eta}) & 1 \\
1 & 0
\end{pmatrix}.
\tag{3.41}
$$

The eigenvalues of the amplification matrix determine the dispersion and dissipation characteristics. Results are shown in Figure 3.17 for $\theta = 0$. Two points are noteworthy. First, the scheme is non-dissipative, which would seem to be a positive attribute for the energy

79

balance analysis. The second point is the reverse group velocity for all components with a normalized wavenumber $\bar{\Xi} > \pi/(2\cos\theta)$. These points lead to the undoing of the Leap-frog scheme for the ice scattering problem.

As a graphic example, consider the 1-D experiment using Leap-frog to solve $u_{,t} = u_{,x}$ with initial condition $u(x,0) = \delta(x - x_o)$. The analytic initial condition contains all wavenumbers while the analogous discrete initial condition, the Kronecker delta, contains all the discrete wavenumbers supported by the grid. The analytic solution to this problem is a delta function propagating to the left at unit velocity. Figure 3.18 shows the result using Leap-frog – a far cry from the analytic solution. All the wavenumbers $\bar{\xi} > \pi/2$ have reverse group velocity and propagate to the right without attenuation. The wavenumber $\bar{\xi} = \pi/2$ has zero group velocity and does not move at all. The lower wavenumbers have forward group velocity and propagate in the correct direction but at the wrong speed. Trefethen shows a similar result in [65, Fig. 12]. Without dissipation the discontinuous initial condition is dispersed over the entire field. Compare the Leap-frog dispersion and dissipation curves to those of Lax-Wendroff in Figure 3.10(a), where the components with reverse group velocity are all strongly attenuated - usually many dB per time step. Results of the 1-D experiment using Lax-Wendroff instead of Leap-frog are shown in Figure 3.19. Despite the reverse group velocity inferred from the dispersion curves for Lax-Wendroff at $\frac{k}{h} = 0.65$, the dispersive tail is virtually non-existent because of the large amount of dissipation at the high wavenumbers. This fact also accounts for the amplitude reduction, especially at early time, as the pulse propagates. The higher wavenumber components are being filtered out of the solution leaving a broader relatively low wavenumber pulse.

The Kronecker delta initial condition is a severe test but closely resembles the spatial characteristics of the line source used to excite the 2-D grid in the scattering experiments. The spatial wavenumbers excited by the source range over the entire spectrum even though
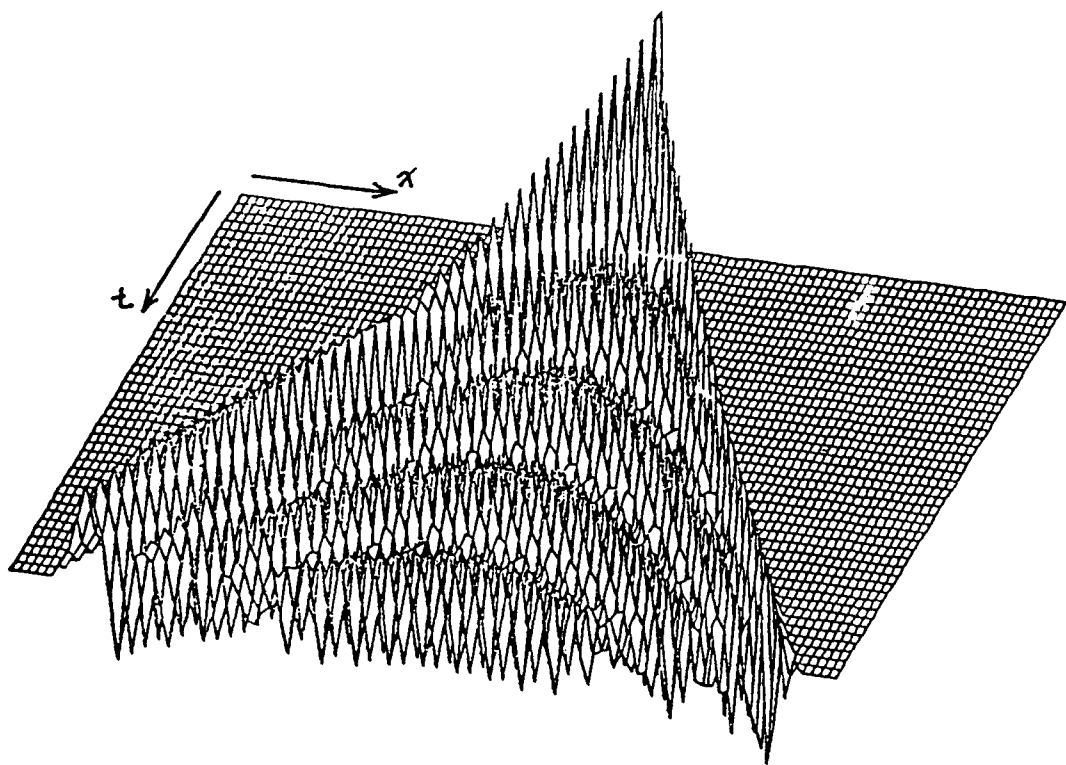
Figure 3.18: Propagation of a Kronecker delta using Leap-frog with $\frac{k}{h} = 0.95$. The reverse group velocity identified in Figure 3.17 is doing its work. The $2x$-waves are to the right, the $4x$-waves are in the middle and the low wavenumber waves are to the left. With no intrinsic dissipation mechanism, this dispersive propagation destroys the solution of a pulse traveling to the left at unit speed. Since discontinuous fields are an integral part of the ice scattering problem the Leap-frog scheme cannot be used.
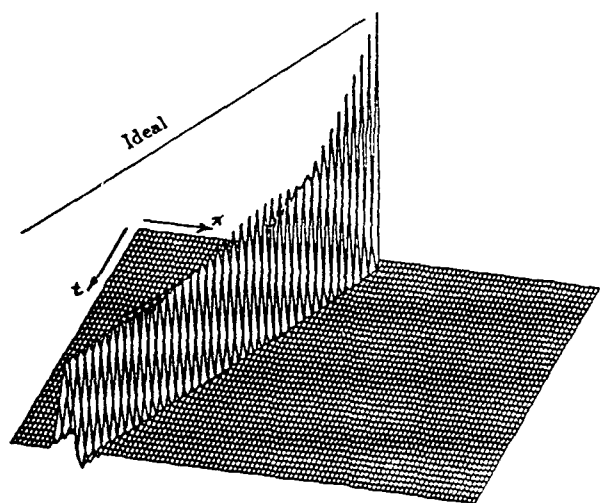
(a)
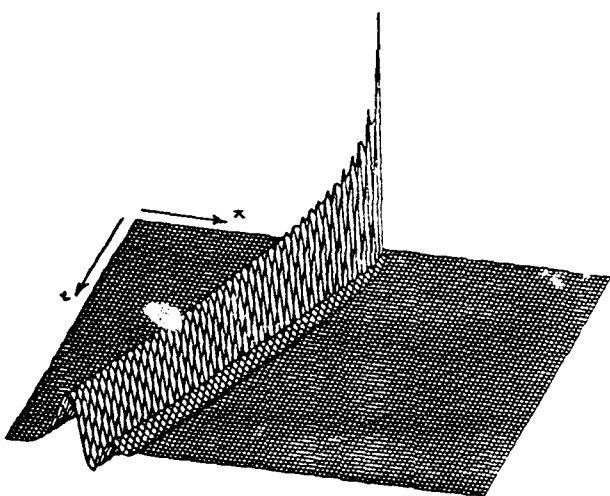
(b)

Figure 3.19: Propagation of a Kronecker delta using Lax-Wendroff with $\frac{k}{h} = 0.95$ in (a) and $\frac{k}{h} = 0.65$ in (b). In contrast to the dispersive propagation seen in Figure 3.18 for Leap-frog, propagation using the Lax-Wendroff scheme shows a reasonable approximation to the analytic solution of the delta function moving to the left at unit speed, especially for the case of $\frac{k}{h} = 0.95$. The trajectory of the delta function for the analytic solution is shown by the line marked "Ideal" in (a). In (b), with $\frac{k}{h} = 0.65$, the intrinsic attenuation of the scheme at the high wavenumbers eliminates any dispersive tail due to the reverse group velocity.

the temporal spectrum is band limited to low frequencies and hence low wavenumbers. This behavior is a result of injecting the source in the near-field, where there is a logarithmic singularity at zero range. In the source discussion later, I show there are also high wavenumber errors generated near the source due to a mismatch between the analytic source function and the finite difference approximation. This mismatch is caused by truncation errors and is accentuated by being in the near-field. Thus, the chosen difference scheme must handle both analytical and numerical near-field source effects without generating spurious waves that contaminate the solution. Hence the Kronecker delta test is an appropriate, albeit severe, test for the usefulness of any given difference scheme.

Could added dissipation be used to filter out the high wavenumber dispersive tails in Leap-frog? Unfortunately, the smallest bit of added dissipation causes Leap-frog to be unconditionally unstable. Here is a 1-D demonstration using the model equation $u_{,t} = u_{,x}$. The Leap-frog scheme with added dissipation is

$$u_m^{l+1} = u_m^{l-1} + [2k\delta_x^0 + \alpha h^2 \delta_x^+ \delta_x^-]u_m^l. \tag{3.42}$$

Using the modal solution $u_m^l = z^l e^{-i\bar{\xi}m} = e^{i\bar{\omega}l}e^{-i\bar{\xi}m}$ the dispersion relations is

$$\sin(\bar{\omega}) = -\frac{k}{h}\sin\bar{\xi} + 2i\alpha\sin^2(\bar{\xi}/2). \tag{3.43}$$

The equation may be solved for frequency, $\bar{\omega} = \omega k$, which is complex if $\alpha > 0$ and real only if $\alpha = 0$. Furthermore, there are two frequencies that satisfy the dispersion relation. Designating the solutions $\bar{\Omega}_1 = \Omega_1 k$ and $\bar{\Omega}_2 = \Omega_2 k$, the properties of the sine function reveal that $\bar{\Omega}_2 = \pi - \bar{\Omega}_1$. Thus, if the frequency is complex, $\Im(\bar{\Omega}_1) = -\Im(\bar{\Omega}_2)$ and one or the other must be negative. Finally, from the definition of the modal solution, $|z| = e^{-\Im(\bar{\omega})} = e^{-\Im(\omega)k}$. Stability requires $\Im(\omega) > 0$, but there is always a solution that has a negative imaginary part if $\alpha > 0$; thus, the scheme must be unstable. The conclusion is that Leap-frog with added dissipation is unconditionally unstable. Consequently, because of the reverse group

83

velocity of the high wavenumbers and the lack of dissipation there is no hope of handling discontinuous solutions with Leap-frog.

3.2.4 Discussion

A great deal has been learned from the dispersion and dissipation analysis of the three proposed difference schemes. If only one difference scheme is to be used throughout the computational domain then the appropriate choice of the three is Lax-Wendroff. This scheme has the flexibility of being second order accurate in smooth regions of the solution and being able to handle discontinuities with locally added dissipation. The time step limit for amplitude and phase errors is large enough to insure that numerical dispersion and dissipation will be negligible for the ice scattering experiments. The positive features of the Lax-Wendroff scheme come at the cost of a factor of three in operation count compared with either Lax-Friedrichs or Leap-frog. Despite the computational burden, Lax-Wendroff is used for the scattering studies in this thesis. At the end of this chapter, numerical solutions generated using Lax-Wendroff are compared with known results as a final certification of the method before the scattering studies are begun.

3.3   Computational boundary

Because of limited computer resources the infinite domain of the physical scattering problem must be reduced to finite size. The boundaries at the edge of the computational domain must not cause reflections, which contaminate the interior solution. I use two methods together to handle this problem. Neither is novel - they both come directly from the literature [18,27].

The first method is based on characteristic variables of the hyperbolic system of equa-
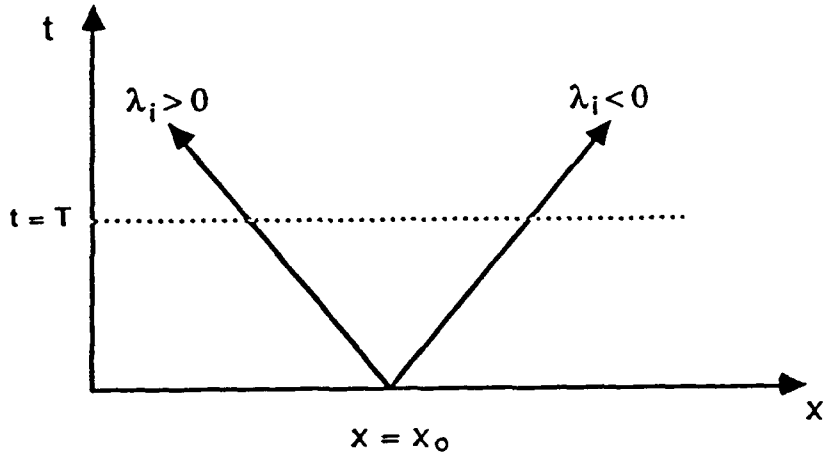
Figure 3.20: Characteristics of $\underline{w}_{,t} = \underline{\Lambda}\,\underline{w}_{,x}$. The characteristic variables w_i follow the characteristic paths shown, propagating the initial condition $w_i(0,x)$ from time $t = 0$ to a later time $t = T$. Those variables corresponding to $\lambda_i < 0$ propagate to the right while those corresponding to $\lambda_i > 0$ propagate to the left.

tions for a homogeneous 1-D medium [18]. Starting with the hyperbolic system of equations

$$\underline{u}_{,t} = \underline{\underline{A}}\,\underline{u}_{,x} \tag{3.44}$$

observe that the matrix $\underline{\underline{A}} = \underline{\underline{T}}\,\underline{\underline{\Lambda}}\,\underline{\underline{T}}^{-1}$, where $\underline{\underline{\Lambda}} = \mathrm{diag}(\lambda_1,\lambda_2,\cdots)$, can be diagonalized since it has a complete set of eigenvectors [74, p. 116]. This suggests a change of variables such that

$$\underline{w}_{,t} = \underline{\underline{\Lambda}}\,\underline{w}_{,x}, \tag{3.45}$$

where $\underline{w} = \underline{\underline{T}}^{-1}\underline{u}$ are the characteristic variables. Each of the individual equations in (3.45) describes 1-D wave propagation of the characteristic variable w_i moving to the left if the eigenvalue $\lambda_i > 0$ and to the right if $\lambda_i < 0$ as shown in Figure 3.20 [22]. Consider the right boundary. In the ideal case, those characteristic variables corresponding to eigenvalues $\lambda_i > 0$ are set to zero. By so doing, waves are allowed to propagate to the right past the right boundary, but nothing can propagate back in to the left. Following the work of Gottlieb et al. [18] this is implemented as follows.

85
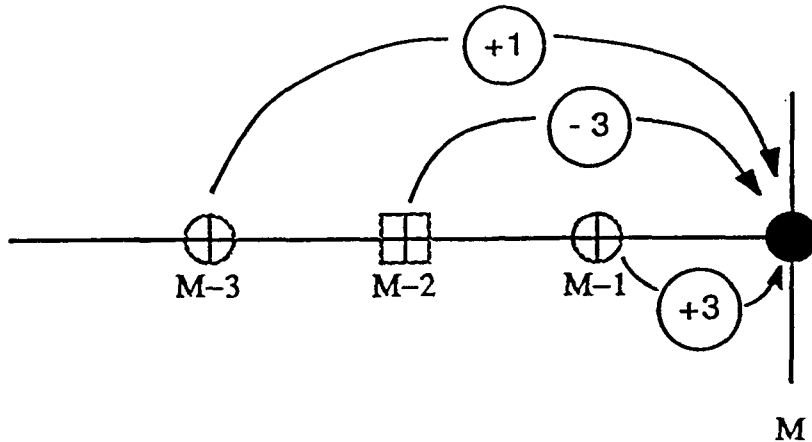
Figure 3.21: Extrapolation of interior field variables to the computational boundary. A second order Lagrange extrapolation scheme is used. The extrapolated values are combined to form the characteristic variables, w_i, which propagate as shown in Figure 3.20.

- Using a Lagrange polynomial scheme, compute extrapolations of the interior field variables at the boundary grid point, i.e., $\underline{\tilde{u}}_M^l = \underline{\tilde{u}}_M^l(u_{M-1}^l, u_{M-2}^l, \cdots)$ [52]. Specifically, at the right boundary I use the second order extrapolation

$$\underline{\tilde{u}}_M^l = 3(u_{M-1}^l - u_{M-2}^l) + u_{M-3}^l, \tag{3.46}$$

which may be visualized as shown in Figure 3.21.

- Compute the extrapolated characteristic variables from $\underline{\tilde{w}} = \underline{T}^{-1}\underline{\tilde{u}}$ with zero components corresponding to the variables propagating into the grid, left in this case, which means those variables corresponding to $\lambda_i > 0$. As an example suppose the

eigenvalues are organized such that $\lambda_1, \lambda_2 > 0$, $\lambda_3 = 0$, and $\lambda_3, \lambda_4 < 0$, then

$$\underline{\underline{T}}^{-1}\underline{\tilde{u}} = \begin{pmatrix} \underline{\tilde{w}}_1 \\ \underline{\tilde{w}}_2 \\ \underline{\tilde{w}}_3 \\ \underline{\tilde{w}}_4 \\ \underline{\tilde{w}}_5 \end{pmatrix} \tag{3.47}$$

and set

$$\underline{\tilde{w}} \equiv \begin{pmatrix} 0 \\ 0 \\ \underline{\tilde{w}}_3 \\ \underline{\tilde{w}}_4 \\ \underline{\tilde{w}}_5 \end{pmatrix} . \tag{3.48}$$

- Compute the updated values of the true field variables at the grid boundary $\underline{u}^l_M = \underline{\underline{T}}\,\underline{\tilde{w}}$.

This procedure determines field variables as the appropriate linear combinations of the characteristic variables with no wave components propagating into the grid. By a suitable coordinate rotation $x \rightarrow x'$, as shown in Figure 3.22, each of the four sides of the computational boundary is handled in a similar manner. In addition, the corners are handled by a 45^0 rotation.

While the concept of this operation is intuitively simple, the implementation is tedious at best. All the matrix inversions and multiplications must be carried out symbolically and the whole thing is rather messy. Since the details of this procedure are not enlightening they are not given here.

These absorbing boundaries work well for normal incidence in homogeneous media. In the ice scattering models there are many situations where homogeneous material does not
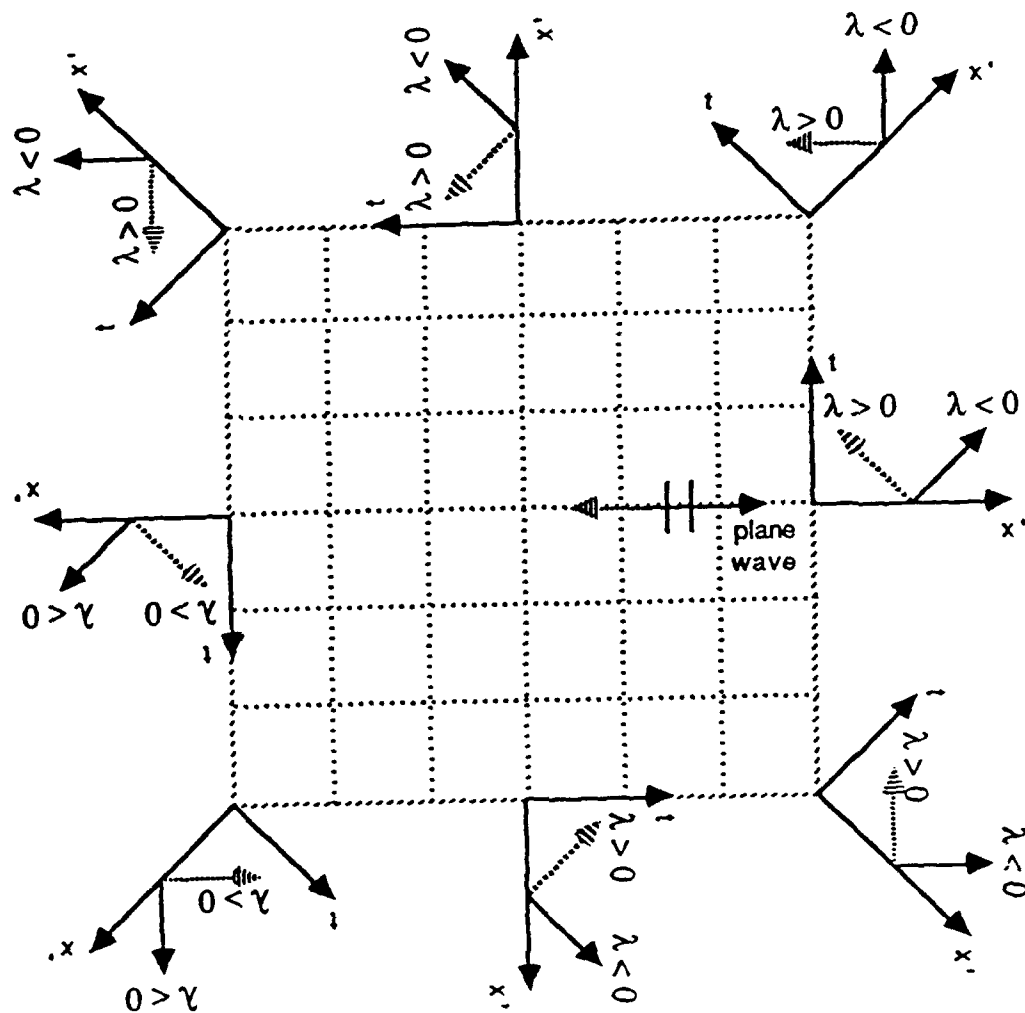
Figure 3.22: Coordinate rotations to compute absorbing one-way boundaries. The characteristic variables, w_i, in the rotated coordinate system propagate to the left for $\lambda_i > 0$ or to the right for $\lambda_i < 0$. To implement the absorbing boundaries, the variables that propagate to the left, toward the interior of the grid, are set to zero. Those that propagate to the right, out of the grid, are allowed to pass.
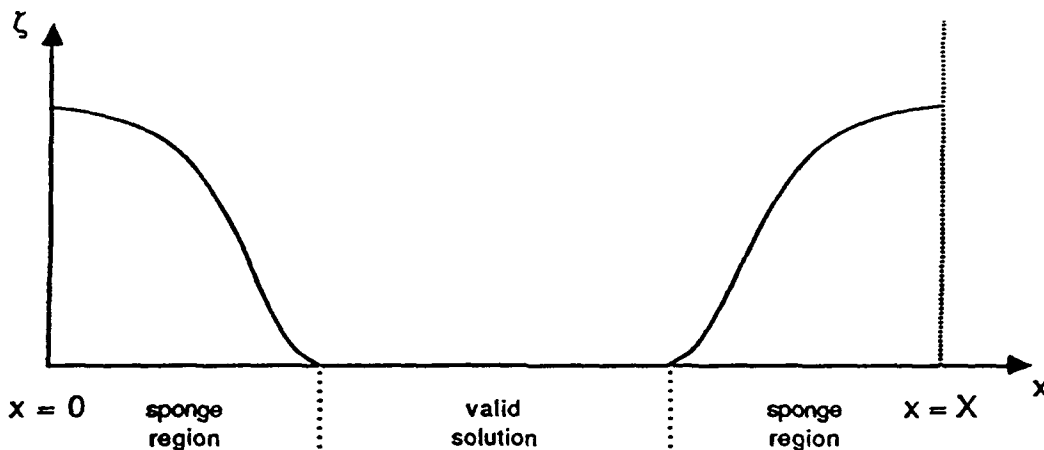
Figure 3.23: 1-D example of sponge region absorbing boundaries. The full computational domain is $0 < x < X$. Only in the interior, where the attenuation factor, ς, is zero, is the computed solution valid. In the sponge region, where $\varsigma \neq 0$, the solution is being attenuated to limit spurious reflections from the grid boundary.

lie along the boundary and where oblique incidence occurs. Thus, the characteristic variable absorbing boundary condit'on is only a first line of defense. A sponge or attenuation region is used around the entire grid to increase the effectiveness of the absorbing boundary. Kosloff and Kosloff [27] suggest and analyze a scheme for directly attenuating the field using

$$\tilde{\underline{u}}^{l+1} = Q\underline{u}^l,$$

$$\underline{u}^{l+1} = (1 - \varsigma)\tilde{\underline{u}}^{l+1}, \tag{3.49}$$

where Q is the interior finite difference operator and ς is a spatially varying factor that goes from zero in the interior to a maximum value of ς_{max} at the boundary as shown schematically in Figure 3.23. They found that spurious reflections can be minimized from the sponge layer if the slope of the attenuation factor, $(1 - \varsigma)$, is minimized at the interior and exterior boundary of the sponge layer. To achieve this they chose the function

$$\varsigma = \frac{\varsigma_{max}}{\cosh^2(\varphi)}, \tag{3.50}$$

89

where φ is the normalized range variable and increases toward the interior of the domain from zero at the boundary.

The only open question left by Kosloff and Kosloff is how to scale the dimensional range for a specific problem to the normalized range, φ, and how to pick the attenuation at the boundary, $(1 - \varsigma_{max})$. The matter of range scaling is addressed by looking at the attenuation factor ς and its slope, $\varsigma' = \frac{d\varsigma}{d\varphi}$, specifically,

$$\varsigma = \frac{\varsigma_{max}}{\cosh^2 \varphi},$$
$$\varsigma' = \frac{-2\varsigma_{max}\sinh \varphi}{\cosh^3 \varphi}. \tag{3.51}$$

Figure 3.24 shows a plot of ς and ς' for normalized range values $0 \leq \varphi \leq 4$. Clearly, most of the effect of ς occurs within this range. The slope is identically zero at $\varphi = 0$ and approaches zero again as φ increases for $\varphi > \simeq 0.6$. At a value of $\varphi = 9$, ς and ς' are $O(10^{-7})$. I have picked this normalized range to be the limit of the sponge region. Using this value, I calculate the attenuation factor

$$\varsigma(x) = \frac{\varsigma_{max}}{\cosh^2(\frac{9x}{\chi})}, \tag{3.52}$$

where χ is the width of the sponge region and x is the range from the edge of the grid, both in convenient units, say grid points.

The sponge region, then, is defined by two parameters, the width of the region, χ and the gain at the boundary $(1 - \varsigma_{max})$. Experience has shown that a value of $\chi \geq \lambda$ and $(1 - \varsigma_{max}) = 0.9$ produces adequate absorption of the waves incident at oblique angles and of the diffractions and other contaminations due to heterogeneous properties at the boundary.

Choosing the width of the sponge region is interesting because once chosen, it is fixed for all wavenumbers that propagate in the grid. The propagation distance through the sponge region, measured in wavelengths, is greater for high wavenumber modes. As a result, these

90

Attenuation factor and slope
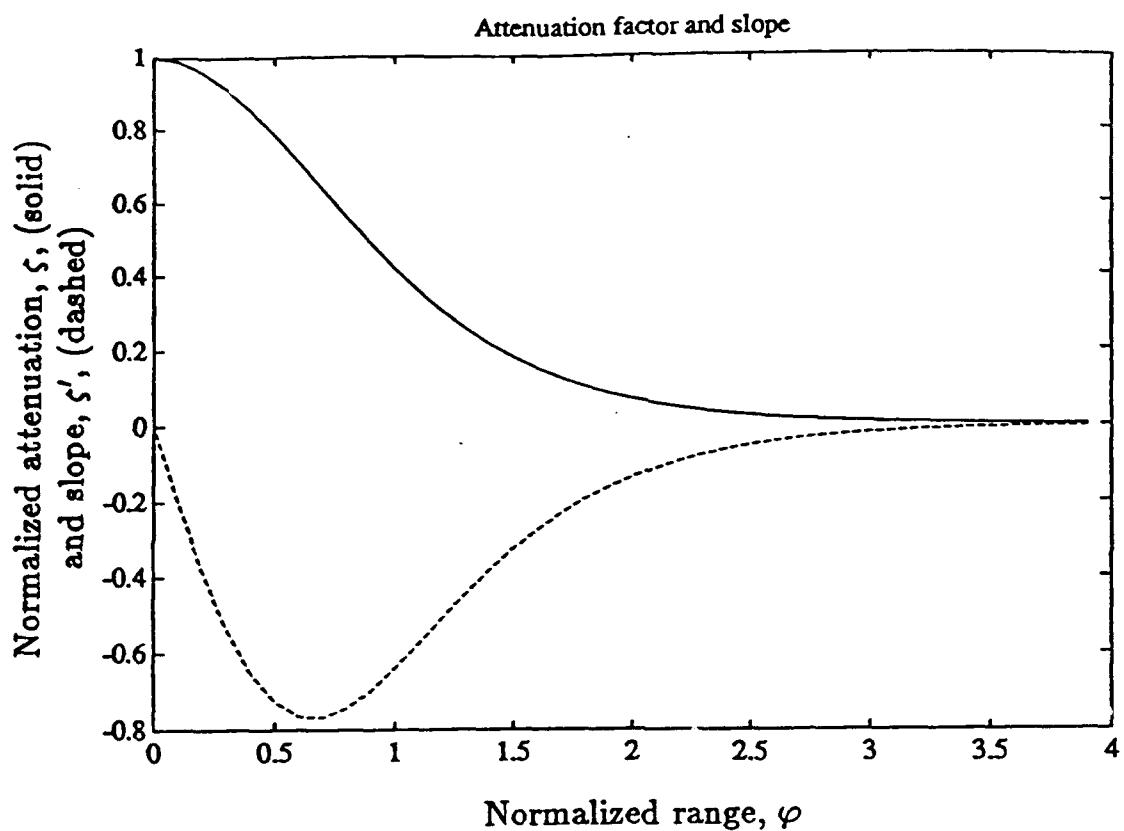
Figure 3.24: Absorbing boundary attenuation factor, ς, and its slope ς'. The solid curve shows the normalized attenuation as a function of range from the computational boundary. The dashed line shows the slope of the attenuation factor. Experience has shown that a zero slope for the attenuation factor at the edges of the absorbing region minimizes spurious reflections from the edges [27]. At a normalized range of $\varphi = 9$ (not shown) both the attenuation and slope are down to $O(10^{-7})$.

Pressure @ 54 ms
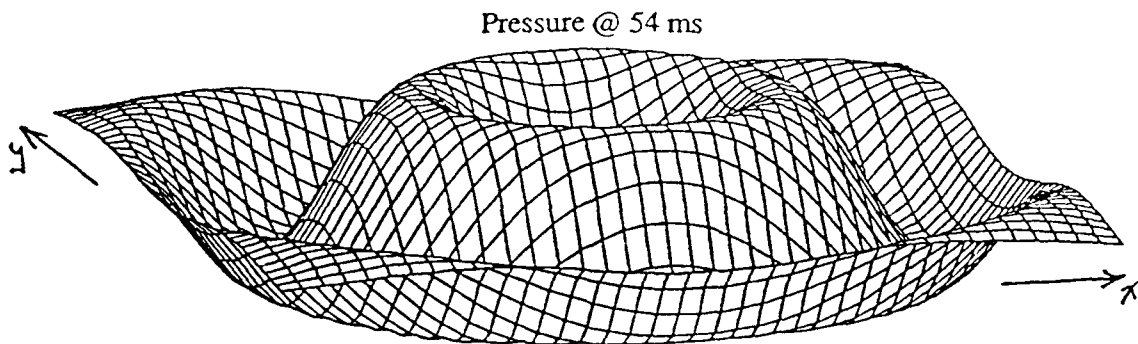
Figure 3.25: Pressure snapshot with absorbing boundaries on all sides in a homogeneous water model. The sponge region is 45 grid points wide, which corresponds to 15 mesh points in this plot. Due to the smooth transition between the interior and the absorbing region, there is no obvious reflection from the absorbing layer.

modes are attenuated more effectively than those of the low wavenumbers. Thus an increase in the sponge layer thickness affects the low wavenumber modes most strongly. Finally, it is not practical to try and attenuate the modes associated with very low wavenumbers. For these modes, the sponge region must be so thick that it begins to dominate the computation time of the entire problem. As a result, it is important to minimize the energy in these modes by an appropriate choice of the source spectrum.

As a test of the effectiveness of the hybrid absorbing boundaries I ran an experiment with homogeneous water using $\mathcal{X} = 0.75\lambda$ at $50\,Hz$. Figure 3.25 shows one pressure field measured during the experiment. There is no discontinuity apparent at the transition between the interior domain and the sponge region. Figure 3.26(b) shows a set of estimated source signatures computed from a time series recorded by a line of receivers $4.75\,m$ above the source. The signatures are time-shifted and amplitude-corrected to a reference distance of $1\,m$. The top signature is the analytic source signature and is the reference against which the experimental signatures are compared. The slight phase shift between the analytic and experimental signatures is due to the locally added dissipation near the source injection point. For the grid size chosen, side reflections are expected at a time of about $70\,ms$.

(a)
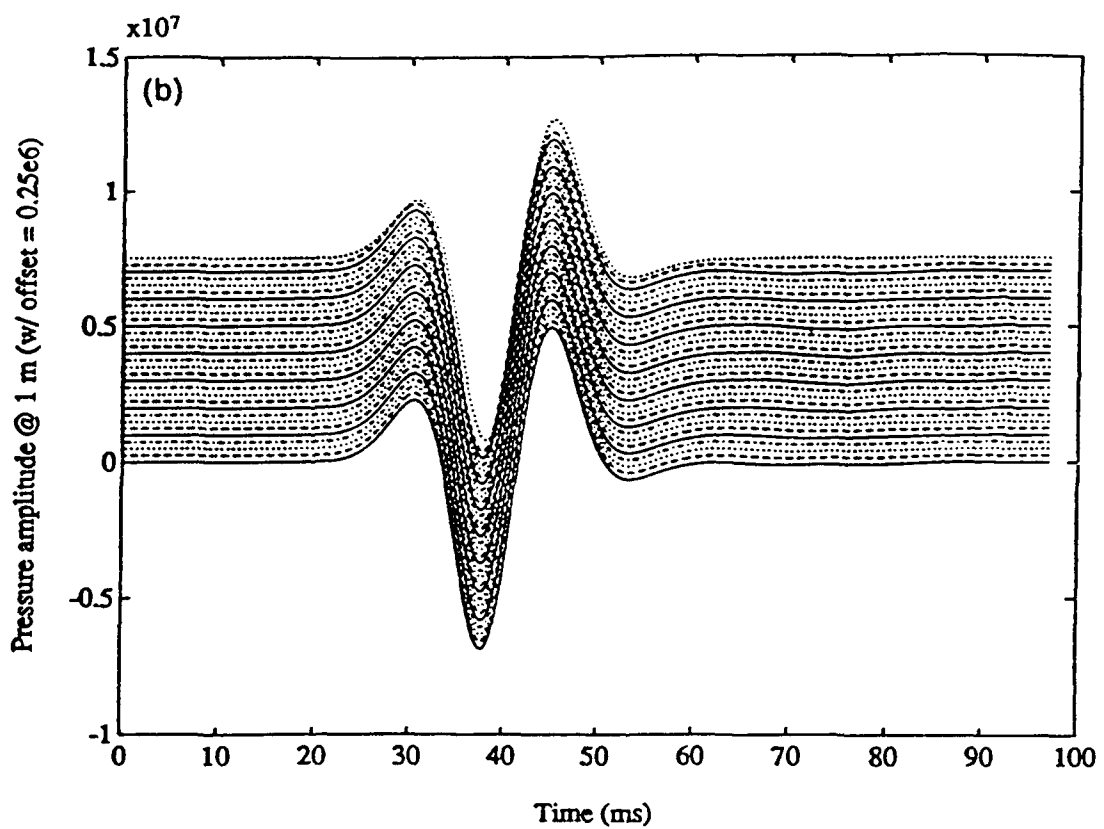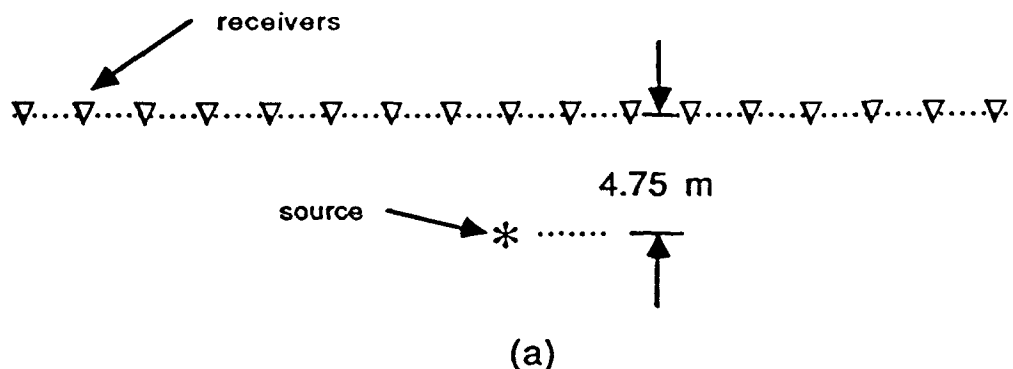
Figure 3.26: (a) Geometry of absorbing boundary test in homogeneous water. (b) Time-shifted and amplitude-corrected signatures referenced to a distance of 1 m from the source. The top trace is the analytic source function. The rest of the signatures are experimental measurements from a line of receivers 4.75 m above the source shown in (a). The slight phase shift between the analytic signature and the experimental measurements is due to the added dissipation in the vicinity of the source injection point. Reflections from the side of the computational domain occur at a time of about 70 ms. The reflection is small.
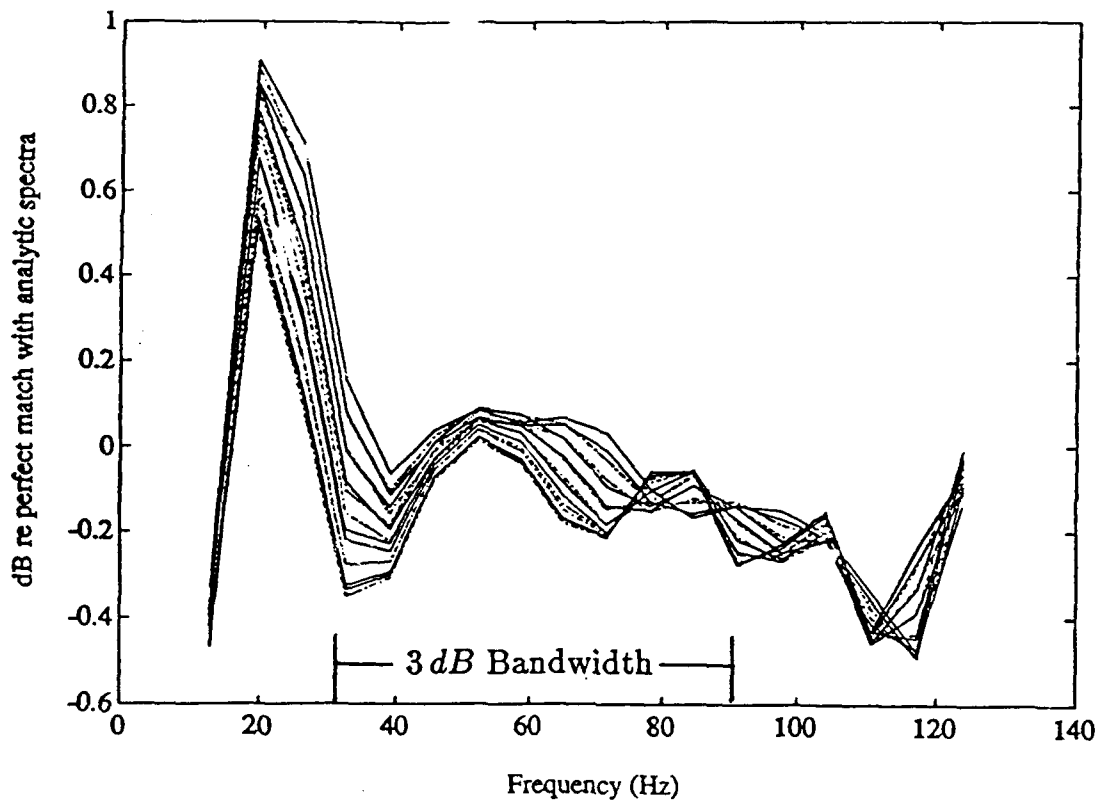
Figure 3.27: Signature measurement error. The average error over the $3\,dB$ power bandwidth is about $0.2\,dB$, which is about a 2% error. The larger error at low frequency is due to the thinness of the sponge region relative to the wavelength. At both low and high frequency the error grows because of reduced signal strength. The downward trend from $50 - 100\,Hz$ is due to the excess attenuation of the Lax-Wendroff scheme.

Perturbations in the traces at that time indicate small reflections. To gauge the size of the reflections more precisely, consider Figure 3.27, which shows the difference in dB between the analytic source spectrum and each of the experimental signature spectra. The $3\,dB$ power bandwidth for the source is nominally $30 - 90\,Hz$ with a center frequency of about $55\,Hz$. The error in this bandwidth averages about $0.1 - 0.2\,dB$, which is consistent with the small perturbations seen in Figure 3.26.

The effect of fixed sponge thickness for all wavenumbers is seen in Figure 3.27. At low frequency two effects cause larger errors. First, the wavenumber is small hence the relative

thickness of the sponge region is small which leads to less absorption. The second effect is that of low signal-to-noise ratio (SNR). At both low and high frequencies errors increase because the round-off errors of the finite difference scheme are random and reduce the SNR relative to the analytic spectrum. The downward trend from $50 - 100\,Hz$ is due to the excess attenuation of the Lax-Wendroff scheme for the number of time step taken.

This experiment confirms that a sponge width of $\chi \geq \lambda$ effectively suppresses side reflections with the help of the one-way absorbing boundary conditions along the perimeter. A schematic of the boundary treatment is shown in Figure 3.28. One advantage of the sponge region is that absorption may be increased, if desired, by increasing the region width. As the width increases, the lower frequencies are removed more effectively. Increasing absorption, however, comes at the cost of increased computer time, which may be a significant factor.

3.4   Source injection

The source injection scheme is patterned after that of Kelly et al. [26] and Alterman and Karal [3]. They break the computational domain into two parts: a homogeneous fluid source region, the interior domain, and a heterogeneous region, the exterior domain, that may have mixed fluid and elastic materials. In the interior domain, finite differences are used to compute the residual field, $\underline{U}_R$, the field due to all propagation phenomenon other than the direct source field, $\underline{U}_S$. The source field is known analytically within the source region and is computed using the technique discussed below. In the exterior domain, the total field is the sum of the source and the residual field, $\underline{U}_T = \underline{U}_S + \underline{U}_R$, and is computed using finite differences. Figure 3.29 shows the source injection operation schematically. The update procedure goes as follows.

- Suppose the total field in the exterior domain is known.
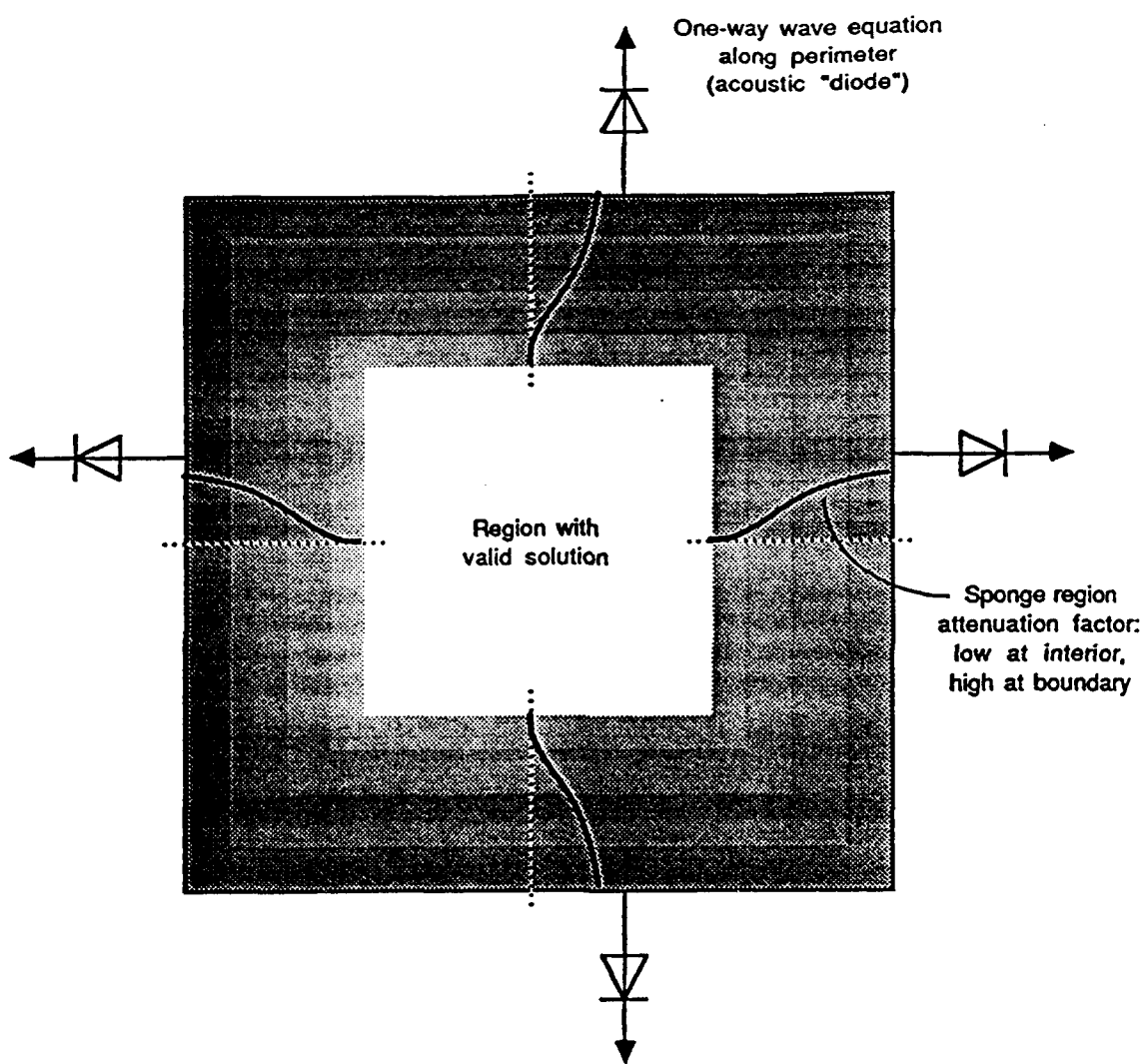
Figure 3.28: Boundary treatment to minimize spurious reflections. Two methods are used: one-way absorbing boundaries at the edge, which are, in effect, acoustic diodes, and a sponge region, where the field is gradually dissipated. The darkness of the shading in the sponge region indicates the degree of dissipation being applies, low at the interior boundary and maximum at the exterior boundary. Only the interior solution is a valid approximation to the governing partial differential equations. The solution in the sponge region should not be used.

96
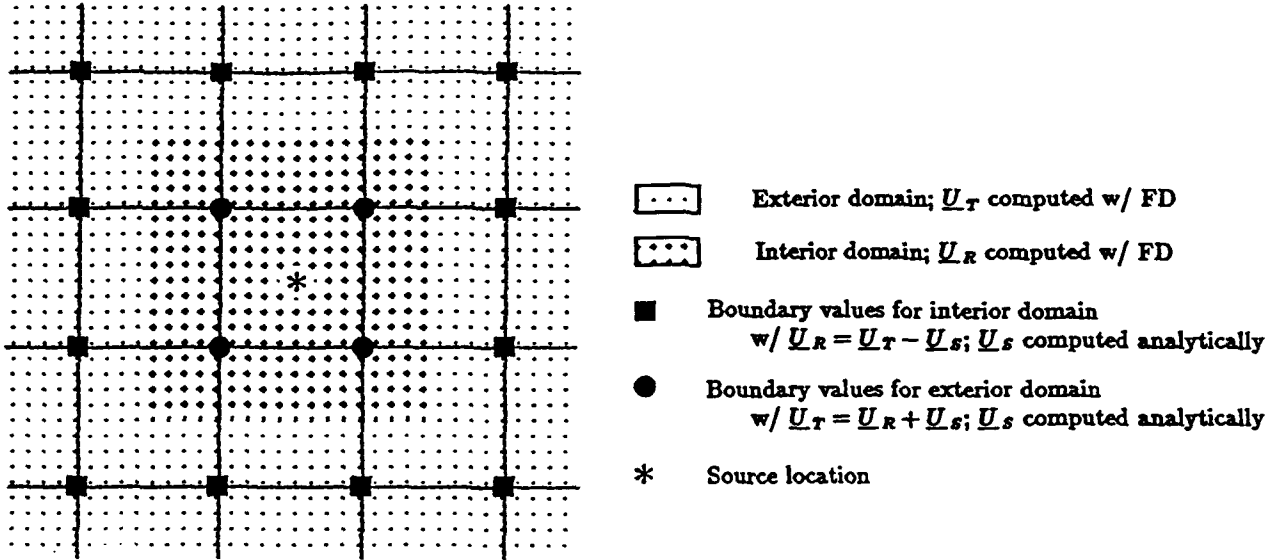
Figure 3.29: Source injection scheme with two domains. Three acoustic fields are used: the total acoustic field, $\underline{U}_T$, the source field, $\underline{U}_S$, and the residual field, $\underline{U}_R = \underline{U}_T - \underline{U}_S$. At the inner and outer boundary the source field is known analytically since the injection region is required to be in a homogeneous fluid. In the exterior domain $\underline{U}_T$ is computed with finite differences using boundary values $\underline{U}_R + \underline{U}_S$ computed from the interior domain and the source function. In the interior domain the residual field is computed with finite differences using boundary values $\underline{U}_T - \underline{U}_S$ computed from the exterior domain and the source function.

- At the perimeter of the interior domain, indicated by the symbol ■, compute the residual field by subtracting the analytic source function for the given range and time from the total field, $\underline{U}_R = \underline{U}_T - \underline{U}_S$.

- Use the residual field on the boundary to update the residual field in the interior domain using finite differences.

- Now turn the problem around. At the perimeter of the exterior domain, indicated by the symbol ●, compute the total field by adding the analytic source function for the given range and time to the residual field, $\underline{U}_T = \underline{U}_R + \underline{U}_S$. Use the total field on the boundary to update the total field in the exterior domain using finite differences.

- Now, with the total field known in the exterior domain, the process starts over.

In this way the solution ping-pongs back and forth, alternately computing the residual field in the interior domain and the total field in the exterior domain.

This scheme was originally designed for the second order elastic wave equation and only displacement is discussed in the cited references. The first order system I am solving needs stress and velocity; the original development has thus been modified. Also, there was no effort to calibrate the source level in the cited references which is done here.

In the interior domain, the inhomogeneous wave equation for a line source in 2-D geometry is

$$\nabla^2 \psi_d - \frac{1}{C_p^2}\psi_{d,tt} = -4\pi\delta(r - r_o)s(t), \tag{3.53}$$

where C_p is the compressional velocity of the medium, ψ_d is the displacement potential, and $s(t)$ is the time variation of the source at the point $r = r_o$. The time variation is chosen to be a scaled differentiated Gaussian pulse,

$$s(t) = -2A\Omega(t - t_s)e^{-\Omega(t-t_s)^2}, \tag{3.54}$$

98

where the center frequency ω_o is related to the parameters

$$\Omega = \left(\frac{\omega_o}{2}\right)^2,$$

$$t_s = \frac{4\pi}{\omega_o}. \tag{3.55}$$

The units of $s(t)$ are L^2 and the amplitude A has units of $L^2 T$. In a moment I discuss how the value of A might be chosen for calibrated source levels, but first, let me proceed with the development. From Morse and Feshbach [49, p. 891], the solution to the inhomogeneous wave equation (3.53) is

$$\psi_d = \frac{1}{2\pi} \int_{-\infty}^{\infty} i\pi S(\omega) H_0^{(2)}(\frac{\omega}{C_p}|r - r_o|) e^{i\omega t} \, d\omega, \tag{3.56}$$

where $S(\omega)$ is the Fourier transform of $s(t)$. Since the first order elastodynamic equations are based on velocity and not displacement it is convenient to compute the velocity potential from the displacement potential in Equation (3.56) as

$$\psi_v = \psi_{d,t}$$

$$= -\frac{1}{2\pi} \int_{-\infty}^{\infty} \pi \omega S(\omega) H_0^{(2)}(\frac{\omega}{C_p}|r - r_o|) e^{i\omega t} \, d\omega. \tag{3.57}$$

Now the transform of the differentiated Gaussian time variation is simply $i\omega$ times the transform of the underlying Gaussian pulse, i.e.,

$$S(\omega) = A i\omega \sqrt{\frac{\pi}{\Omega}} e^{-\frac{\omega^2}{4\Omega}} e^{-i\omega t_s}. \tag{3.58}$$

Using this in the velocity potential, Equation (3.57), yields the specialized result

$$\psi_v = -\frac{i}{2\pi} A\pi \sqrt{\frac{\pi}{\Omega}} \int_{-\infty}^{\infty} \omega^2 e^{-\frac{\omega^2}{4\Omega}} H_0^{(2)}(\frac{\omega}{C_p}|r - r_o|) e^{i\omega(t-t_s)} \, d\omega. \tag{3.59}$$

The remaining task is to compute the amplitude A. Different values of the center frequency ω_o produce different peak excursions of the time variation. By looking for the extrema of

99

$s(t)$, which occur at $t = \frac{1}{\omega_o}(4\pi \pm \sqrt{2})$ with peak-to-peak excursion $s_{pp} = \frac{A\omega_o}{\sqrt{2}e^{\frac{1}{2}}}$, then the calibrated source amplitude is

$$A = \frac{e^{\frac{1}{2}}s_{pp}\sqrt{2}}{\omega_o} \tag{3.60}$$

for a fixed s_{pp}. Setting the value of A by this method allows direct control over the amplitude of the source function which permits calibrated comparisons between experiments at different frequencies.

The last step is to determine velocity and pressure from the velocity potential function, Equation (3.59). Velocity is simple to compute using the definition of the velocity potential,

$$\begin{aligned}
v_s &= \frac{\partial \psi_v}{\partial r}, \\
&= \frac{i}{2\pi C_p} A\pi\sqrt{\frac{\pi}{\Omega}} \int_{-\infty}^{\infty} \omega^3 e^{-\frac{\omega^2}{4\Omega}} H_1^{(2)}\left(\frac{\omega}{C_p}|r - r_o|\right) e^{i\omega(t-t_s)}\, d\omega, \tag{3.61}
\end{aligned}$$

where I have used the derivative of a Hankel function defined as

$$\frac{d}{dx} H_0^{(2)}(\alpha x) = -\alpha H_1^{(2)}(\alpha x). \tag{3.62}$$

The source velocity as defined is actually a vector in the radial direction but since this is understood I only write the magnitude of the vector and dispense with the unit radial vector and other vector notation.

For the derivation of the source pressure, I go back to the conservation of momentum Equation (2.7). A linearized statement written in terms of the velocity potential is

$$\frac{\partial}{\partial r}(\rho\psi_{v,t} + P) = 0, \tag{3.63}$$

where pressure is defined as $P = -\frac{1}{3}\sigma_{ii}$. Integrate with respect to r and set the constant of integration to zero, which sets the arbitrary datum for the velocity potential to zero. Solving for source pressure yields

$$\begin{aligned}
p_s &= \rho\psi_{v,t}, \\
&= \frac{i\rho}{2\pi} A\pi\sqrt{\frac{\pi}{\Omega}} \int_{-\infty}^{\infty} \omega^3 e^{-\frac{\omega^2}{4\Omega}} H_0^{(2)}\left(\frac{\omega}{C_p}|r - r_o|\right) e^{i\omega(t-t_s)}\, d\omega. \tag{3.64}
\end{aligned}$$

100

Pulling this all together, the analytic source function is computed using the equations

$$
\Omega = \left(\frac{\omega_o}{2}\right)^2,
$$

$$
t_s = \frac{4\pi}{\omega_o},
$$

$$
\mathcal{A} = \frac{e^{\frac{1}{2}} s_{pp} \sqrt{2}}{\omega_o},
$$

$$
v_s = \frac{i}{2\pi C_p} \mathcal{A}\pi\sqrt{\frac{\pi}{\Omega}} \int_{-\infty}^{\infty} \omega^3 e^{-\frac{\omega^2}{4\Omega}} H_1^{(2)}(\frac{\omega}{C_p}|r - r_o|) e^{i\omega(t-t_s)}\, d\omega,
$$

$$
p_s = \frac{i\rho}{2\pi} \mathcal{A}\pi\sqrt{\frac{\pi}{\Omega}} \int_{-\infty}^{\infty} \omega^3 e^{-\frac{\omega^2}{4\Omega}} H_0^{(2)}(\frac{\omega}{C_p}|r - r_o|) e^{i\omega(t-t_s)}\, d\omega \qquad (3.65)
$$

with $s_{pp} = 1$ and ω_o and r chosen as source parameters.

When computing the source velocity and pressure I perform the inverse Fourier transform in Equation (3.65)[4,5] numerically using the mixed radix FFT by Singleton [55]. The Hankel functions are evaluated by an algorithm based on the polynomial approximations presented in Abramowitz and Stegun [1, p. 369]. Figure 3.30 shows the pressure and radial velocity for a source with frequency of 0.1 dimensionless Hz at unit range, which is $\lambda/10$ units from the source point and is in the near-field. In this region the pressure and velocity are not in phase as seen in the figure. These signatures are similar to those used to excite the grid for the scattering experiments.

3.5 Certification of numerical design

In section 3.2.3 I discussed the Lax-Wendroff scheme and later determined that it is the most suitable scheme of three considered for the ice scattering experiments. In this section I compare the performance of Lax-Wendroff with the source and absorbing boundaries discussed above against known solutions and confirm order of accuracy for a heterogeneous
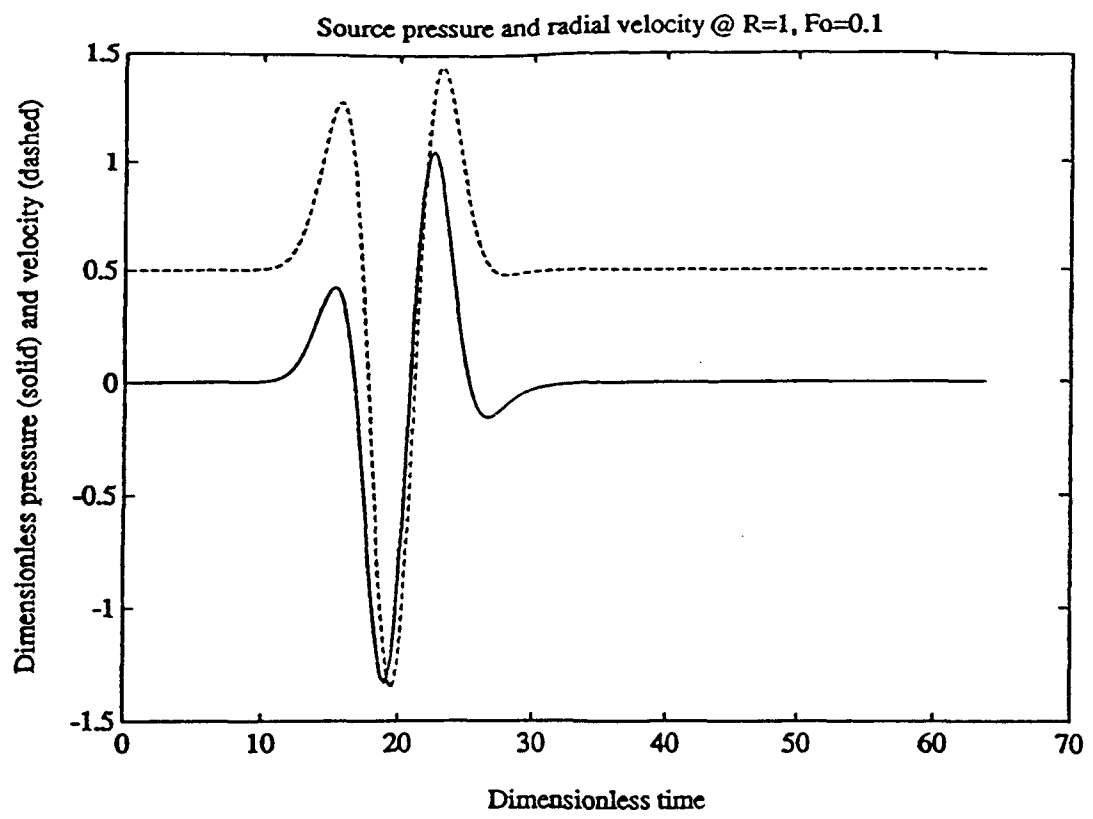
Figure 3.30: Source pressure and radial velocity (with offset = 0.5). These signatures are generated for a source with dimensionless center frequency of $0.1\,Hz$ in a material with unit sound speed at unit range. This range corresponds to $\lambda/10$ and is in the near-field, where source injection takes place. These signatures show a phase shift of approximately $\pi/4$ between pressure and velocity, which is consistent with a near-field measurement. The peak-to-peak amplitude of the time variation of the source function, s_{pp}, in Equation $(3.65)^3$ is set to unity.

air-ice-water model. The known solutions considered, in order of increasing complexity, are cylindrical spreading, reflection from a free surface, and reflection from an elastic half space.

3.5.1 Cylindrical spreading

The cylindrical spreading test has already been discussed in another context, that of the added dissipation scheme. There, Figure 3.15 showed that the experimental estimate of the Lax-Wendroff excess attenuation matched the analytical prediction. This result was generated from an experiment in homogeneous water, where a line of receivers $0.25\,m$ below the source captured the outgoing signature as a function of angle at variable range. Figure 3.31(a) shows the geometry of this experiment. Figure 3.31(b) shows three traces from the time series recorded for this experiment before correction for cylindrical spreading and Figure 3.31(c) shows the same traces after correction. Each of the three traces was Fourier transformed and the spectral ratio between the first trace, which serves as a reference, and each of the other two spectra was computed. The result expressed in $dB/timestep$ is displayed in Figure 3.15. The number of time steps between the traces was computed as the difference in range divided by the grid velocity $\frac{h}{k}$. Figure 3.15 shows that the cylindrical spreading correction, $\sqrt{R}$, accounts for everything except the excess attenuation of the difference scheme. It has already been shown that as long as the experiments are limited to $O(10^3)$ time steps the excess attenuation can be ignored.

3.5.2 Free surface interface

The next certification test is the computation of a reflection coefficient for an air-water interface, virtually a free surface. Two models were needed for this test: a homogeneous water model and a half-space of air overlaying a half-space of water. In the half-space model, shown in Figure 3.32(a), a compressional line source was placed $10.5\,m$ below the
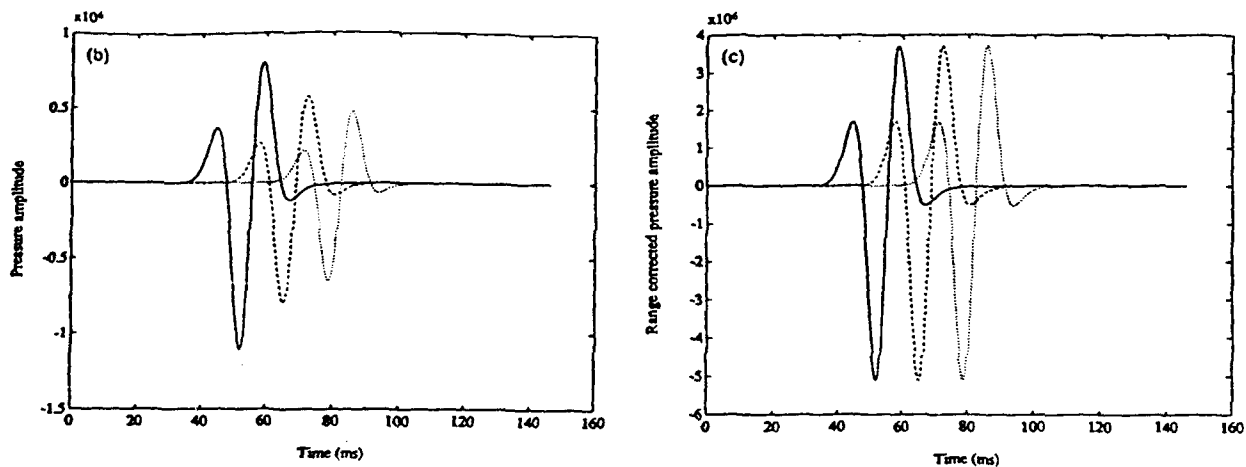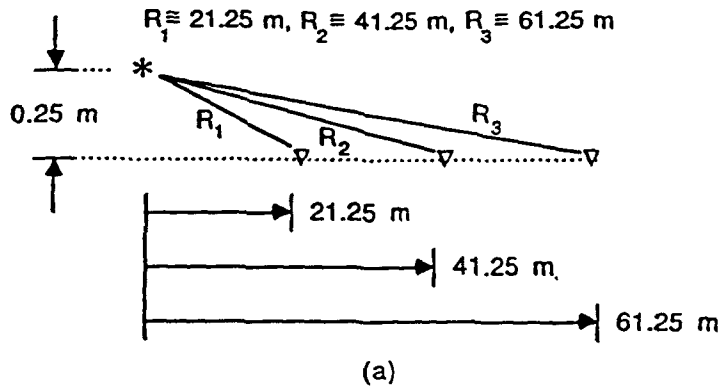
Figure 3.31: Amplitude correction for cylindrical spreading. Figure (a) shows the geometry of the homogeneous water experiment. In (b) three raw pressure traces are shown from the line of receivers 0.25 m below the source. The slant ranges for the traces are: 21.25 m (solid); 41.25 m (dashed); and 61.25 m (dotted). Figure (c) shows the amplitude-corrected pressures using $\sqrt{R}$ as the cylindrical spreading correction.

104

water surface and a line of receivers 0.75 m below the interface recorded the time series. For the homogeneous experiment I replaced the air half-space with a half-space of water and ran the test again. The time series from the homogeneous water experiment was subtracted from that of the half-space experiment to produce a set of reflection only traces. An example of this operation on one of the traces is shown in Figure 3.32(b). The reflection coefficient is nearly -1 as expected. The set of reflection only traces shown in Figure 3.33 was time-shifted and amplitude-corrected to a reference distance 1 m from the source. The top signature in this set is the analytic source signature used to excite the grid. I have assumed the negative polarity of the reflection is known and plotted all the signatures with positive polarity for convenience. The free surface reflection coefficient versus angle and frequency is computed as the ratio of the spectrum of each trace with the spectrum of the analytic source function. Averaging with respect to frequency at each grazing angle yields the reflection coefficient versus angle. This result is plotted in Figure 3.34. Over a broad range of grazing angles the air-water interface is being properly modeled as a pressure release boundary. Finally, an average over angle gives a free surface reflection coefficient of 1.01.

3.5.3   Fluid/solid interface

To estimate the plane wave reflection coefficient from an elastic half space another pair of experiments were run. A 55 Hz center frequency line source was used for both experiments. The first experiment is a two half-space problem, shown in Figure 3.35(a), with the source placed 12.5 m below an ice half-space. A line of receivers 10.25 m below the ice and 2.25 m above the source recorded the time series. Again, a homogeneous water experiment was run to determine the source only field. The reflection only field was computed by subtracting the latter time series from the former. The resulting reflections were time-shifted and amplitude-corrected to a reference distance 1 m from the source with the results shown
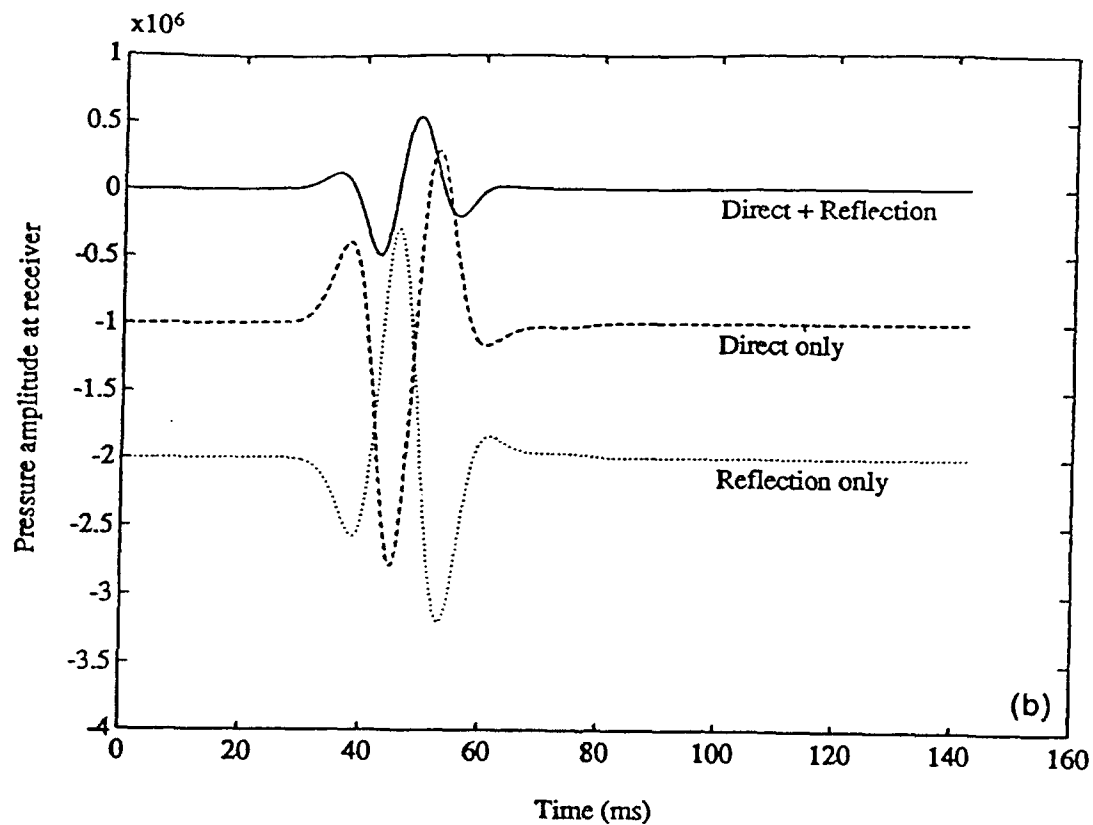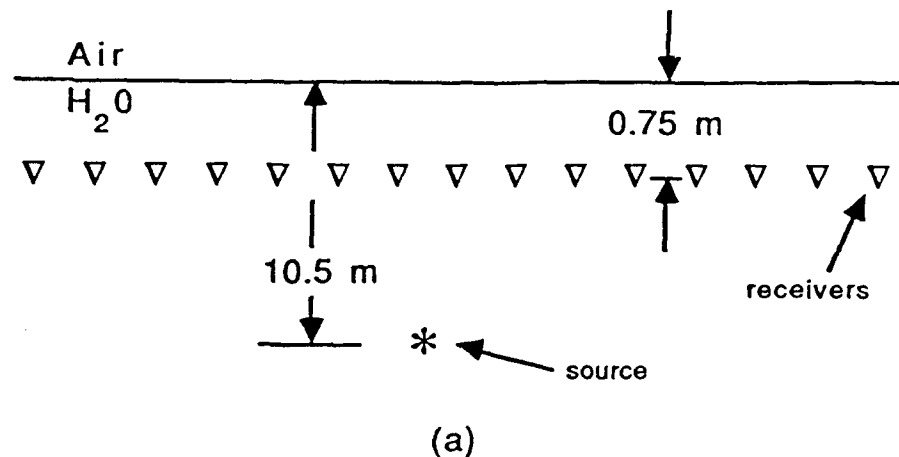
Figure 3.32: Computation of a reflection only trace. Figure (a) shows the geometry of the half-space experiment with air above water. In (b) the top trace is a time series recorded from the half-space model with air and water. (Note: the direct only trace is displaced by -1 and the reflection only trace is displace by -2.) The middle trace is a time series recorded from the homogeneous water experiment. The bottom trace is the difference of the first two. Note the reflection has negative polarity with respect to the direct wavelet.
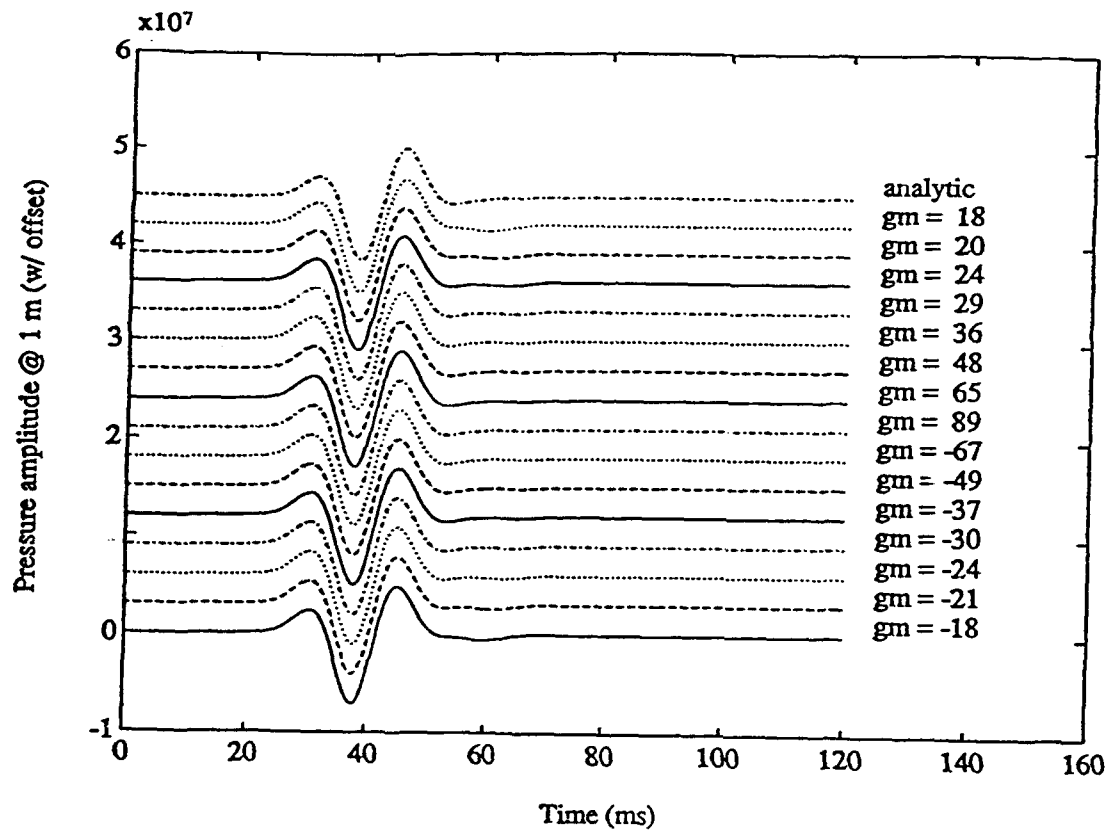
Figure 3.33: Time-shifted and amplitude-corrected reflections versus grazing angle. Each trace is corrected to a reference distance $1\,m$ from the source and flipped in polarity to facilitate comparison with the analytic signature, which is shown at the top. The grazing angle for each reflection is shown at the right.
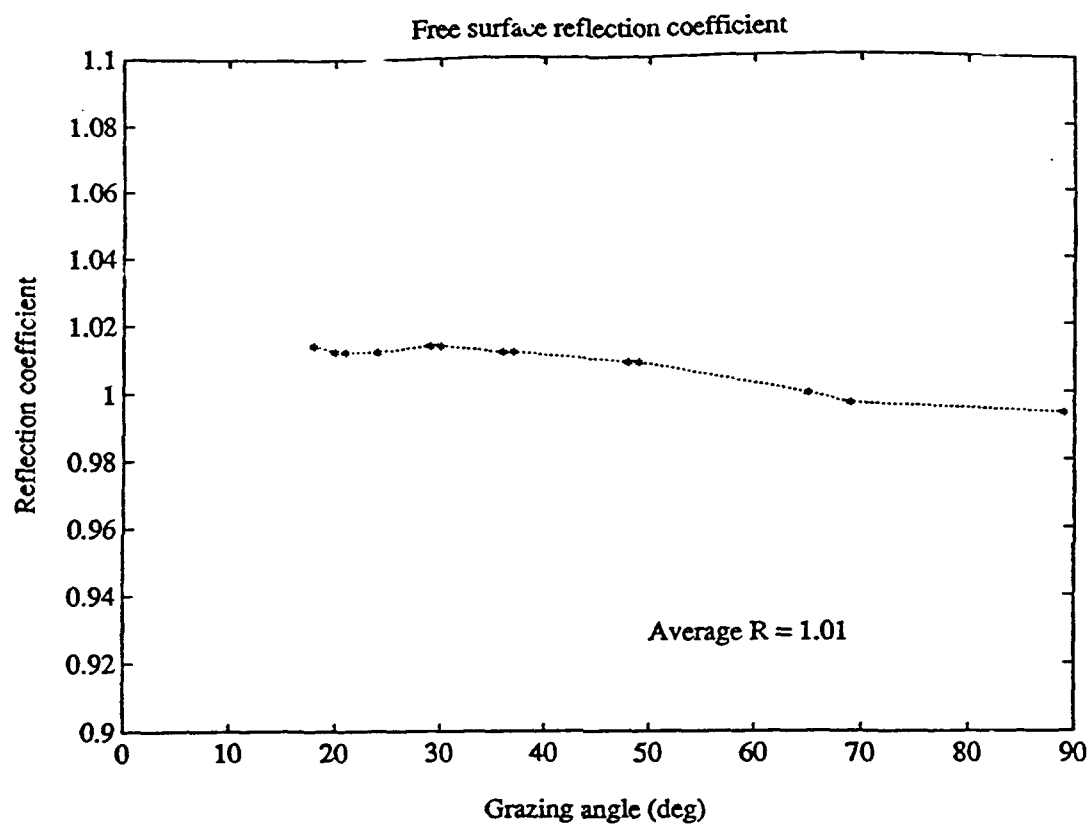
Figure 3.34: Reflection coefficient vs. grazing angle. The plotted values are reflection coefficients averaged over frequency. As indicated, the average over angle yields a value of 1.01 for the experimental estimate of the reflection coefficient from an air-water interface.

in Figure 3.35(b). The elastic half-space has created several effects that were not seen in the free surface experiment. There is a head wave arriving earlier than the water path reflection and there is a Scholte wave [48, p. 169] that arrives later. In addition, the phase and amplitude of the water path reflection change with angle.

My intent is to compare the reflection coefficients estimated from this experiment with the plane wave reflection coefficients predicted by the Zoeppritz equation [5, p. 41]. Figure 3.36 shows the geometry of the plane wave reflection experiment. The plane wave grazing angle is γ, which can be related to all the other angles in the problem. The reflection coefficient is compactly written

$$R(\gamma) = \frac{z_l \cos^2 2\theta_s + z_t \sin^2 2\theta_s - z}{z_l \cos^2 2\theta_s + z_t \sin^2 2\theta_s + z}. \tag{3.66}$$

Each of the terms may be written exclusively in terms of the grazing angle γ, as for example the longitudinal wave impedance

$$z_l = \frac{\rho_e C_p}{\cos \theta_p} = \frac{\rho_e C_p}{\left(1 - \left(\frac{C_p}{c}\right)^2 \sin^2 \theta\right)^{\frac{1}{2}}} = \frac{\rho_e C_p}{\left(1 - \left(\frac{C_p}{c}\right)^2 \cos^2 \gamma\right)^{\frac{1}{2}}}. \tag{3.67}$$

Similarly,

$$
\begin{aligned}
z_t &= \frac{\rho_e C_s}{\left(1 - \left(\frac{C_s}{c}\right)^2 \cos^2 \gamma\right)^{\frac{1}{2}}}, \\
z &= \frac{\rho c}{\sin \gamma}, \\
\cos^2 2\theta_s &= \left(1 - 2\left(\frac{C_s}{c}\right)^2 \cos^2 \gamma\right)^2, \\
\sin^2 2\theta_s &= 4\left(\frac{C_s}{c} \cos \gamma\right)^2 \left(1 - \left(\frac{C_s}{c}\right)^2 \cos^2 \gamma\right)^2.
\end{aligned}
\tag{3.68}
$$

The reflection coefficient is complex in general. For a given set of material properties and angles, the magnitude, $|R|$, and phase, $\angle R$ are computed. The reflection coefficient becomes complex when $\gamma < \cos^{-1}\left(\frac{c}{C_p}\right)$. This is the critical angle for the compressional head wave. For $\gamma > \cos^{-1}\left(\frac{c}{C_p}\right)$ the reflection coefficient is real.

109
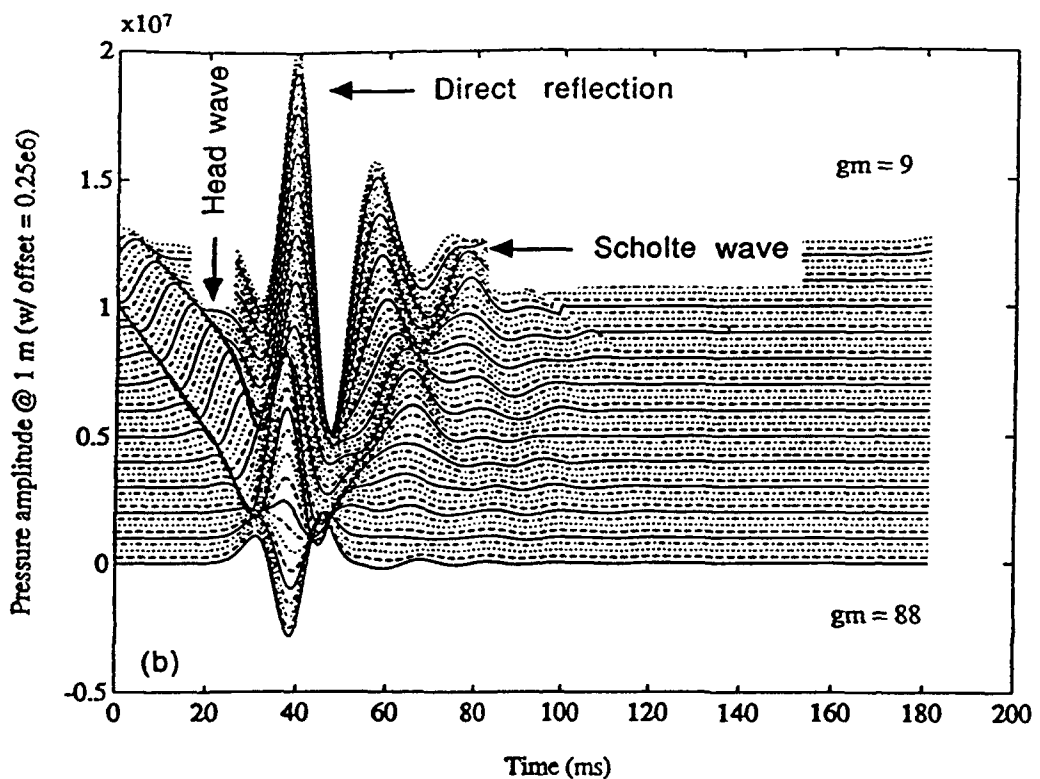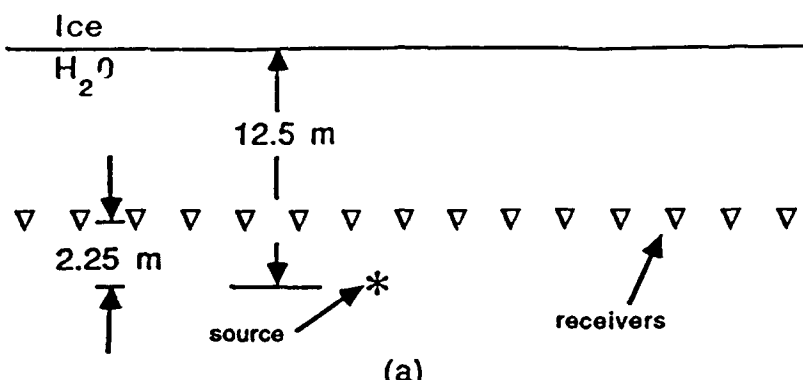
Figure 3.35: Fluid/solid interface experiment. Figure (a) shows the geometry of the experiment with a half-space of ice above a half-space of water. Figure (b) shows the time-shifted and amplitude-corrected reflections from the ice-water interface referenced to 1 m from the source. Due to the impulsive line source, the pure reflections occur in concert with a compressional head wave arriving early and a Scholte wave arriving late. The central water path reflection is isolated using a window for estimation of the plane wave reflection coefficient. The top reflection corresponds to a grazing angle of 9° and the bottom reflection is for near normal incidence with a grazing angle of 88°.

110
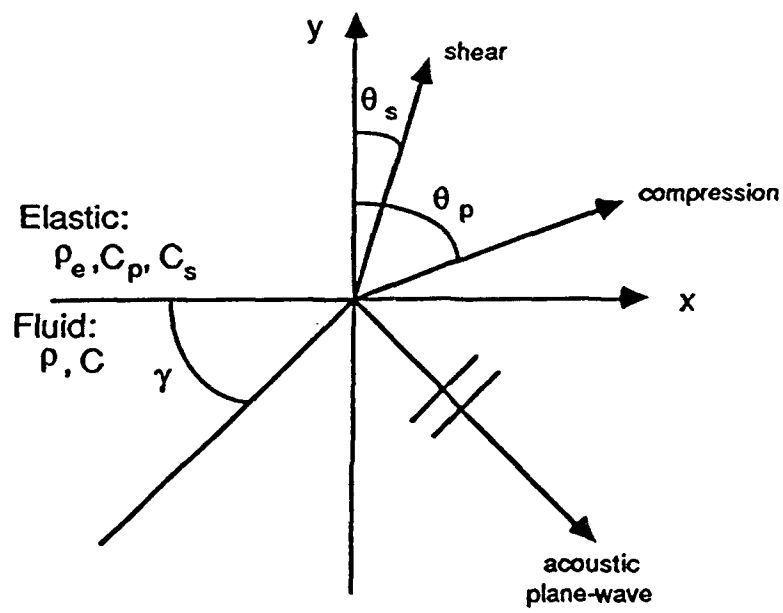
Figure 3.36: Geometry of plane wave interaction with a fluid/solid interface. The incident plane wave impinges at a grazing angle, γ, and generates a compressional plane wave in the solid propagating at θ_p with respect to the normal and a shear plane wave at θ_s. The reflected plane wave in the fluid has an amplitude and phase determined by Zoeppritz equation (3.66). The fluid properties are density, ρ, and compressional velocity, c. The elastic properties are density, ρ_e, compressional velocity, C_p, and shear velocity, C_s.

Figure 3.35(b) shows the reflection only time series from an impulsive line source with a center frequency of 55 Hz. Using ray geometry, the range of grazing angles is $9° \leq \gamma \leq 88°$. The head and Scholte wave mentioned above are due to the impulsive line source and are not directly predicted by the Zoeppritz equation. These non-plane wave components are partially eliminated from the analysis using a boxcar window with cosine tapers centered at 40 ms. The windowed reflections are Fourier transformed and divided (complex) by the source spectrum to yield the complex reflection coefficient as a function of frequency and angle. The final reflection coefficient estimate is computed as the average over frequency. Specifically,

$$\hat{R}(\gamma) = \frac{1}{N} \sum_{i=1}^{N} \frac{\tilde{r}(f_i, \gamma)}{\tilde{p}(f_i)}, \tag{3.69}$$

where

$$
\begin{aligned}
\hat{R}(\gamma) &= \text{numerical estimate of } R(\gamma), \\
N &= \text{\# frequency samples used in the average,} \\
f_i &= i^{th} \text{ frequency,} \\
\gamma &= \text{grazing angle,} \\
\tilde{r}(f_i, \gamma) &= \int r(t, \gamma) e^{-i2\pi f_i t} \, dt, \text{ Fourier transform of reflection,} \\
r(t, \gamma) &= \text{reflection time series at angle } \gamma, \\
\tilde{p}(f_i) &= \int p(t) e^{-i2\pi f_i t} \, dt, \text{ source spectrum,} \\
p(t) &= \text{analytic pressure signature.}
\end{aligned}
\tag{3.70}
$$

A plot of the magnitude and phase of the reflection coefficient estimate is shown in Figure 3.37. These are compared with the predictions of the Zoeppritz equation at the same grazing angles. The agreement is qualitatively satisfying. The numerical estimate tracks the analytic curves closely except at the following special angles.

- Compressional and shear wave critical angles: The numerical reflection magnitude curve does not show these critical angle resonances at $\gamma \simeq 64°$ for the compressional

112
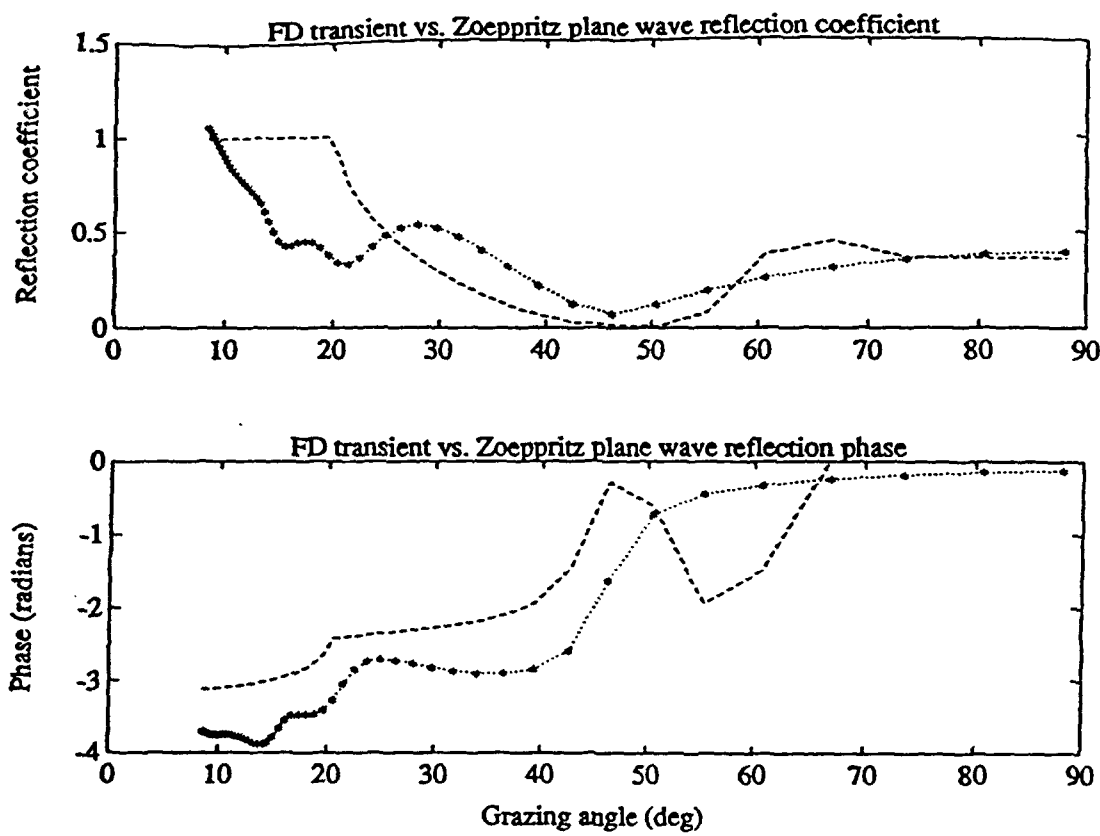
Figure 3.37: Magnitude (a) and phase (b) of experimental versus analytic plane wave reflection coefficient for an ice-water interface. The stars are the experimental plane wave reflection coefficient estimates. The dashed line is the analytic prediction using the Zoeppritz equation (3.66) evaluated at the same angles as the experimental estimate. The agreement is qualitatively correct for both magnitude and phase. The resonance features of the analytic equations, such as the phase matching of the compressional head wave, are not seen in the estimates due to the transient nature of the source.

wave and $\gamma \simeq 19°$ for the shear wave. The resonant phenomenon are not contained in the reflection only wavelets used in this analysis. The head and Scholte waves contain this information, but they have been removed.

- Brewster angle: The phase of the numerical reflection estimate does not track the analytic phase near the Brewster angle, where $R \rightarrow 0$. Once again, the Brewster angle phenomenon is a resonance behavior, which is not modeled in the experiment so agreement with the analytic prediction is not expected.

Except for the angles where resonance plays a part, the numerical reflection coefficient estimate is approximately correct. Considering the difficulties of the estimation and the relatively crude removal of the head and Scholte waves, the overall agreement is satisfying.

3.5.4 Order of accuracy

The truncation error of the Lax-Wendroff scheme is $O(k^2, h^2)$ for homogeneous material properties, which is another way of saying the order of accuracy is 2 [57]. Ideally the Lax-Wendroff scheme remains second order accurate, or nearly so, for a heterogeneous model. As a proxy for the various ice scattering models to be run, I use the ice edge model shown in Figure 3.38 to numerically evaluate order of accuracy for the Lax-Wendroff scheme.

My estimation of order of accuracy is based on the Taylor series expansion of the solution at some fixed time T_f. Suppose, the time step is $\Delta t = k$ then the fixed time $T_f = t_N = Nk$. If the Taylor expansion of the exact solution at time $t_n = nk$,

$$u(t_n) = u(t_{n-1}) + ku_{,t}(t_{n-1}) + \frac{k^2}{2!}u_{,tt}(t_{n-1})\cdots, \tag{3.71}$$

is matched by the Taylor expansion of the difference solution, $v(t_n)$, up to but not including the term containing k^m then the scheme has truncation errors of k^m. Define a new time step, $\tilde{k} = \beta k$, such that the fixed time $T_f = Nk = N\frac{\tilde{k}}{\beta} \equiv \tilde{N}\tilde{k}$. Then, for the same scheme

114
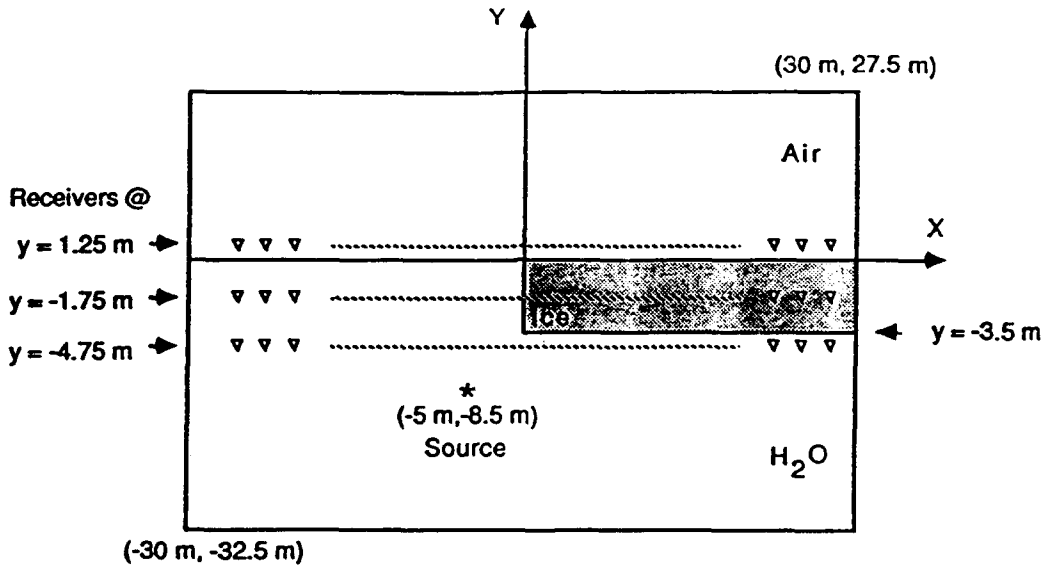
Figure 3.38: Ice edge model. The location of the source and the receiver rows is shown. The material properties are as follows: for air, $C_p = 340\,m/s$ and $\rho = 1.2\,Kg/m^3$; for ice, $C_p = 3500\,m/s$, $C_s = 1600\,m/s$, and $\rho = 910\,Kg/m^3$; and for water, $C_p = 1500\,m/s$ and $\rho = 1000\,Kg/m^3$. The ice is nominally $3.5\,m$ thick and the center frequency of the source is $50\,Hz$. The model is run with three spatial increments: $h = 0.25\,m$, $0.5\,m$, and $1.0\,m$.

as before, the truncation error is $O(\tilde{k}^m) = O((\beta k)^m)$. One measure of the error of the numerical solution due to a time step change from k to $\tilde{k} = \beta k$ is defined as

$$E_\beta = \left[\frac{\langle \int |u(t_{\tilde{n}}) - v(t_{\tilde{n}})|^2 \, dt_{\tilde{n}} \rangle}{\langle \int |u(t_n) - v(t_n)|^2 \, dt_n \rangle} \right]^{\frac{1}{2}}. \tag{3.72}$$

For a particular difference scheme the truncation error is

$$|u(t_n) - v(t_n)| = C_m k^m \frac{\partial^m}{\partial t^m} u(t_n) + O(k^{m+1}). \tag{3.73}$$

With this truncation error the scheme is said to be m^{th} order accurate. Since u and v are discrete time functions as written, i.e., $u(t_{\tilde{n}}) = u(\tilde{n}\tilde{k}) = u(\tilde{n}\beta k)$, etc., the integrals can be written as summations and Equation (3.72) becomes

$$E_\beta = \left[\frac{\langle \sum_{\tilde{n}=1}^{\tilde{N}} [\tilde{C}_m \frac{\partial^m}{\partial t^m} u(t_{\tilde{n}})]^2 \rangle \cdot \tilde{k}^{2m+1}}{\langle \sum_{n=1}^{N} [C_m \frac{\partial^m}{\partial t^m} u(t_n)]^2 \rangle \cdot k^{2m+1}} \right]^{\frac{1}{2}}. \tag{3.74}$$

115

The truncation errors, $C_m \frac{\partial^m}{\partial t^m} u(t_n)$, are random. If they are assumed to be independent identically distributed Gaussian random variables with zero mean and variance σ^2 then the operand of each expectation in Equation (3.74) has a Chi-squared distribution with mean $\tilde{N}\sigma^2$ for the numerator and $N\sigma^2$ for the denominator [51, p. 187]. Using this in the error ratio leads to the simple conclusion that

$$E_\beta = \beta^m. \qquad (3.75)$$

Finally, the order of accuracy is computed as

$$O_{oa} = \ln_\beta E_\beta = m \ln_\beta \beta = m. \qquad (3.76)$$

This is a lot of work to compute an order of accuracy, which is known ahead of time. The procedure is instructive, however, as a paradigm for the estimate of order of accuracy from experimental data. Suppose three experiments are run with $h = \hat{h}, 2\hat{h}, 4\hat{h}$ and corresponding time steps of $k = \hat{k}, 2\hat{k}, 4\hat{k}$. Using the finest grid, i.e., $h = \hat{h}$, as a reference, errors between the reference and the other solutions can be computed. If $u^l_{m,n}(\hat{k}, \hat{h})$ is the reference solution then the error energy of the $k = 2\hat{k}$ experiment is computed as

$$\sum_{m,n,l} |u^l_{m,n}(\hat{k}, \hat{h}) - u^l_{m,n}(2\hat{k}, 2\hat{h})|^2 \cdot (2\hat{h})^2 \cdot 2\hat{k}, \qquad (3.77)$$

where the indices m, n, and l must be aligned to the coarse grid by decimating the reference solution in both space and time. A similar error energy estimate may be computed for the $4\hat{k}$ experiment. Note, if the field $u^l_{m,n}$ is a snapshot measured at some fixed time $t = t_o$ for all m and n, then the error energy sum is computed only over m and n. Similarly, for a time series measured at a fixed depth $y = y_o$ for all m and l, then the energy sum is computed only over m and l.

In an analogy to the error ratio of Equation (3.74), I form the approximate error ratio

$$E_2 = \left[\frac{\text{error energy for } \hat{k} \text{ vs. } 4\hat{k} \text{ experiment}}{\text{error energy for } \hat{k} \text{ vs. } 2\hat{k} \text{ experiment}} \right]^{\frac{1}{2}}. \qquad (3.78)$$

116

This statement defines a time multiplication factor of $\beta = 2$. Thus, once a numerical estimate for E_2 is computed, the order of accuracy is determined as $O_{oa} = \ln_2 E_2$. Ideally, the value of O_{oa} for Lax-Wendroff is 2. This ideal is almost achieved except in regions near the source and material boundaries, where $O_{oa} \simeq 1$ as intended using added dissipation.

Now for a few of the details. Three scattering experiments are run for the ice edge model. Only the space and time step varied, maintaining a constant ratio $\frac{k}{h}$. In all the experiments, the wavelength in water, λ, at the center frequency of $55\,Hz$ is used as a measure of the physical dimensions of the problem. The physical modeling domain is fixed at $\simeq 2\lambda \times 2\lambda$, while the dimensions of the grid change depending on the spatial increment, h. The reference model is run with $h = 0.25\,m \simeq \lambda/100$ and then two test runs are conducted with $h = 0.5\,m \simeq \lambda/50$ and $1.0\,m \simeq \lambda/25$. An error ratio and the corresponding order of accuracy are computed for seven datasets: three time series – below, through, and above the ice; and four pressure snapshots ranging from the beginning of the source pulse to late in the record. To compute the error energy for the various paired experiments a proper space and time alignment is determined. Small differences between the experimental geometries produce some misalignments.

- The time alignment for the different time series datasets is exact. The misalignment in time for the various snapshots is never greater than $0.6\,ms$, which at $50\,Hz$, corresponds to a phase error of $\simeq \frac{\pi}{17} \simeq 11°$. With a phase error tolerance of $\pi/4$ this misalignment is negligible.

- Spatial misalignment is caused by the fact that the source is always located at a cell center, which is never the same place if the spatial increment changes. It is possible, however, to fix the range from the source to the lower left corner of the ice edge for all the experiments. The spatial misalignment between the experiments is never greater than $1.25\,m$, which at $50\,Hz$ and $C_p = 1500\,m/s$, corresponds to a time error

117
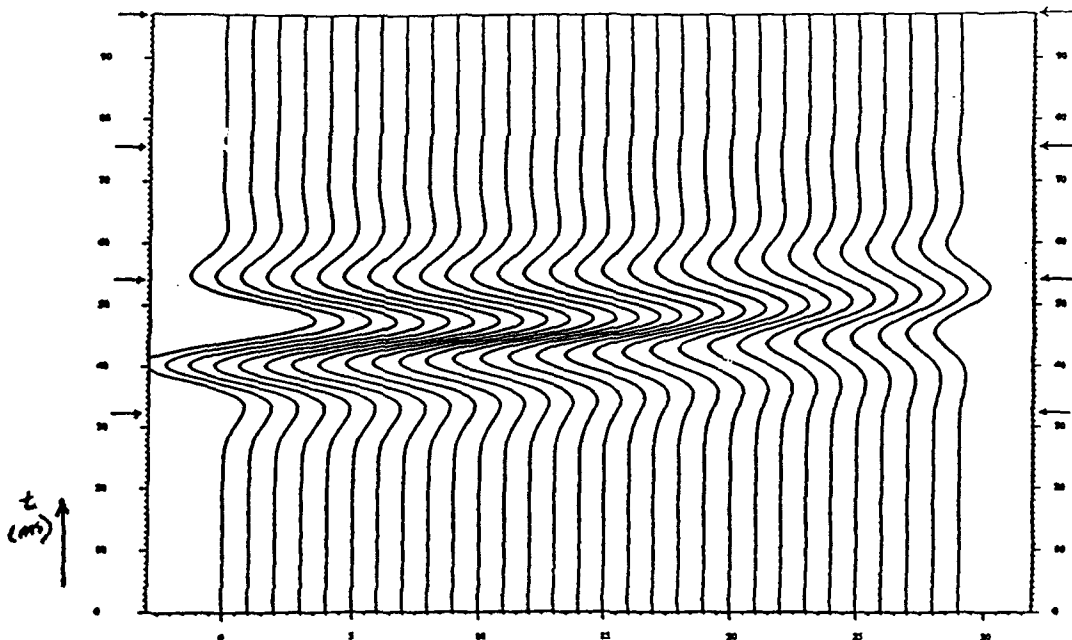
Figure 3.39: Typical pressure time series recorded below the ice for order of accuracy experiments. In this case the receivers were 1.25 m below the ice and 3.75 m above the source. The horizontal index is trace number at a spacing of 0.5 m per trace. The source is located between trace 4 and 5. Snapshots are taken at the times indicated: 32.4 ms, 54.1 ms, 75.7 ms, and 97.4 ms. The air-water interface is to the left and the ice sheet is to the right. The edge of the ice is located between trace 14 and 15.

of 0.8333 ms or a phase error of $\simeq \frac{\pi}{12} = 15°$. Again, this misalignment is negligible.

- The ice thickness in the $h = 0.25 m$ and $h = 0.5 m$ experiments is 3.5 m while that in the $h = 1.0 m$ is only 3.0 m due to the coarseness of the grid. This is the largest geometric difference between the three experiments but is representative of the problems with increasing the spatial increment to reduce computer run time.

Figure 3.39 shows a typical pressure time series from the experiments. This one was recorded 1.25 m below the ice with a spatial increment of 0.5 m. Figure 3.40 shows a typical pressure snapshot; this one is also from the $h = 0.5 m$ experiment. Results of the order of accuracy estimates for the seven datasets are shown in Table 3.2. The range of order of
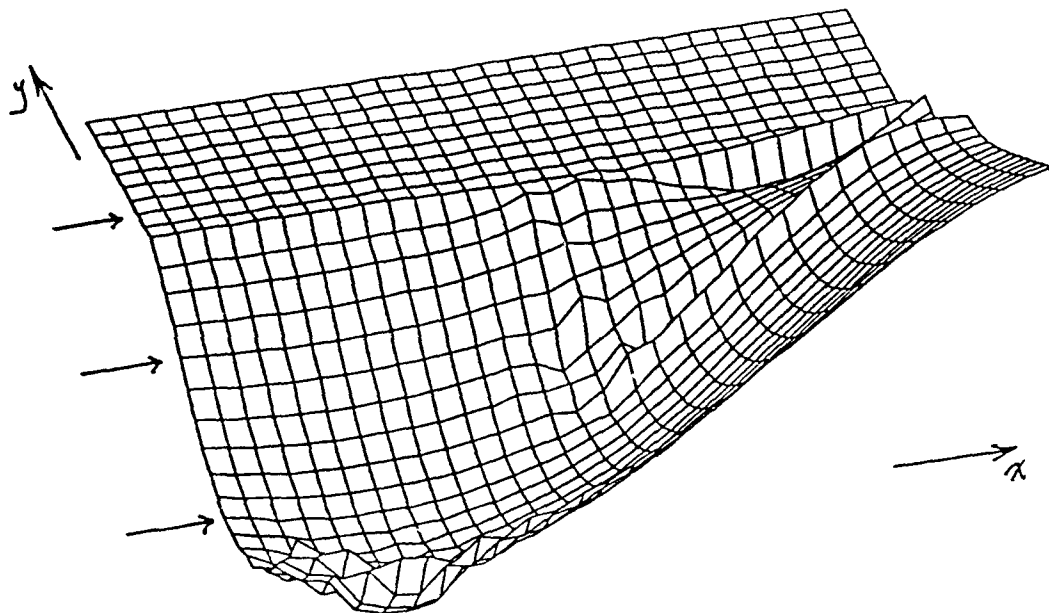
Figure 3.40: *Typical pressure snapshot for order of* accuracy experiments. This snapshot was taken at the time 54.1 *ms*. The air-water and air-ice interface can be seen by an abrupt drop in pressure. Also, the ice plate is seen to the right, where it is undergoing compressional and flexural deformation. The receiver rows are marked on the left.

Description	Code	Order of accuracy
Time Series below ice	T_{-1}	1.47
Time Series through ice	T_0	0.89
Time Series above ice	T_{+1}	0.61
Snapshot at 32.4 ms	S_{32}	0.07
Snapshot at 54.1 ms	S_{54}	1.81
Snapshot at 75.6 ms	S_{75}	1.74
Snapshot at 97.4 ms	S_{97}	2.02

Table 3.2: Estimates of order of accuracy for three pressure time series and four pressure snapshots. The snapshot S_{32} is considered irrelevant in estimating order of accuracy because it is dominated by source errors. Time Series T_o and T_{+1} are low order accurate because they are recorded near the air interface, where added dissipation is used. The remaining estimates show that the order of accuracy is superlinear, i.e, *o.o.a.* > 1, and compare well with the prediction for Lax-Wendroff of 2.0
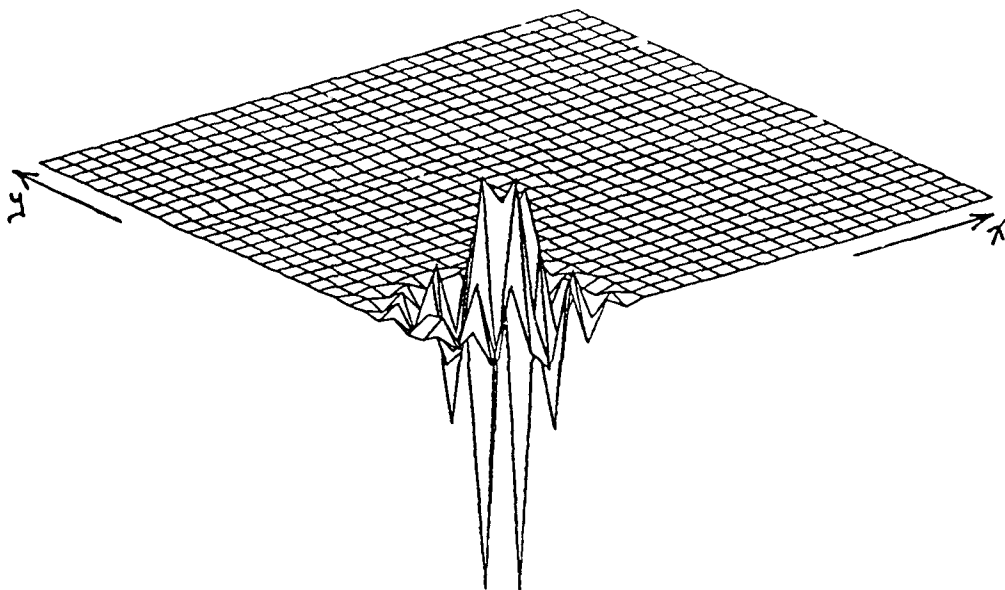
Figure 3.41: Error between pressure snapshots for the $h = 0.25\,m$ and $0.5\,m$ experiment at $32.4\,ms$. Almost all of the error energy is located in a small region around the source injection point. A rapidly changing field in the proximity of the logarithmic singularity and the coarse spatial sampling lead to large errors. Since the discrepancy is dominated by sampling effects and not by the difference scheme, the estimate of order of accuracy from this dataset is irrelevant.

accuracy estimates is large but consistent with the design of the finite difference scheme. The very low estimate for the S_{32} dataset is dominated by source errors. Figure 3.41 shows the error between the $h = 0.25\,m$ and the $h = 0.5\,m$ experiment at the time $32.4\,ms$. The error is dominated by effects near the source. Two things are going on here: 1) source errors cause added dissipation to be used which makes the scheme first order accurate at best and 2) since the injection takes place in the near-field of the source, near the logarithmic singularity, large differences in the injected source function occur for different h independent of the finite difference scheme used. Since the latter effect has nothing to do with the difference scheme, the order of accuracy estimated from this snapshot is irrelevant.

The low order of accuracy estimate for T_0 and T_{+1} is consistent with the fact that

added dissipation is used close to the time series receivers during the entire experiment. This reduces the second order Lax-Wendroff scheme to first order. To a lesser extent, the time series dataset below the ice, T_{-1}, has added dissipation during parts of the experiment, hence the lower estimate of order of accuracy. The three remaining snapshot data sets, S_{54}, S_{75}, and S_{97}, have high estimates for the order of accuracy. For these snapshots the source is less active, as may be seen in Figure 3.40, and only small portions of the grid near the material interfaces have the added dissipation active. These snapshots give the best picture of the global order of accuracy for the Lax-Wendroff scheme in a heterogeneous medium.

If the three low order estimates for T_0, T_{+1}, and S_{32} are excluded, it is evident that the order of accuracy for the global scheme is superlinear, i.e., *o.o.a.* > 1, and compares well with the second order accuracy predicted for the Lax-Wendroff scheme. Considering the complexity of the model, the limited computational domain, and the misalignment of the time and space samples, this estimate is satisfying. The analysis of order of accuracy is consistent with the design of the numerical scheme with low order accurate, but stable, schemes operating in heterogeneous regions and high order accurate schemes operating in homogeneous regions. The heterogeneous and homogeneous regions are detected automatically and the scheme is adjusted accordingly.

3.6   Summary

This has been a long chapter. To help the reader develop a succinct view of what has been done I itemize the highlights here.

- The unique solution for discontinuous models is guaranteed by a monotone difference formulation, which is at most first order accurate.

- The first order accurate Lax-Friedrichs scheme, while stable and offering the unique solution, is too dissipative for computing an accurate energy balance.

- Lax-Wendroff is second order accurate and hence is not monotone but can be made so by explicitly adding dissipation. A modified scheme is described that adds dissipation only near discontinuities and allows the overall formulation both to be second order accurate and to provide stable unique discontinuous solutions. The numerical phase and amplitude distortion of the Lax-Wendroff scheme is sufficiently mild to allow long time experiments to be run without fear of introducing numerical artifacts.

- While the non-dissipative Leap-frog scheme appears to be desirable for computing energy balances, it is not suitable for computing discontinuous solutions. The lack of dissipation is a two-edged sword. It provides for accurate energy estimates of smooth solutions, but it forces high wavenumber components of discontinuous solutions to disperse in the wrong direction without attenuation. The latter undesirable trait cannot be tamed with added dissipation as was done with Lax-Wendroff.

- Absorbing boundary conditions are designed by using a one-way wave equation on the perimeter of the computational domain augmented by a sponge layer surrounding the interior computational region. The one-way wave equation handles normal incidence energy in homogeneous media. The sponge layer attenuates the more complicated fields due to non-normal incidence and heterogeneous media.

- The source is injected using a modified version of a standard scheme to patch an analytic source function into a discrete numerical grid solution.

- Lax-Wendroff is chosen as the difference scheme to use in the ice scattering experiments. The overall design including the source and absorbing boundaries, is certified

by comparing numerical and analytic solutions for several simple propagation experiments. Furthermore, order of accuracy for the scheme is estimated from experimental scatterjing data for a truncated ice plate model. The estimated order of accuracy is superlinear and compares well with the predicted value of 2 for Lax-Wendroff in an infinite homogeneous medium.

Chapter 4

Data analysis methods

4.1 Overview

The numerical modeling algorithm developed in the last two chapters is used to simulate scatter from elemental roughness features. The simulations are carried out in a fashion similar to physical experiments. An acoustic source excites the propagation medium and waves travel out and encounter the rough ice, which in turn, causes scatter. Receivers capture various field quantities as a function of time and space. The data from these receivers must be reduced to enable interpretation. The data reduction process is the subject of this chapter.

To facilitate understanding of the algorithms, I first introduce an illustrative example, which is carried through the chapter. The model used is a triangular keel under $3\,m$ of ice and is representative of the scattering experiments discussed in the next chapter.

During the course of the experiments various field quantities are computed using the finite difference method. These are the quantities available for recording and storage during the experiment and are introduced in the signals section, Section 4.3, as the *recorded signals*. Post processing allows for the computation of a variety of *derived signals*, which are also

discussed in Section 4.3. These derived signals include the scattered field and the flexural and longitudinal field in the ice plate.

With the host of recorded and derived signals available, a corresponding host of quadratic quantities, such as power and energy, may be computed. Section 4.4 presents definitions and discusses the calculations needed to compute these quantities.

The angular dependence of the scattered field is an important characteristic that must be computed from the data. I study the angular dependence by computing a plane wave decomposition using an extension of Radon transforms. The development of the extension and the analysis of its characteristics is done in Section 4.5.

4.2 Illustrative example

I present here a scattering model, which is used to transform the analysis methods developed later in this chapter from the abstract to the concrete by way of example. The model is shown in Figure 4.1. It comprises a relatively small keel, about $\frac{\lambda}{3}$ wide by $\frac{\lambda}{6}$ deep, under an otherwise uniform sheet of $3\,m$ ice. A differentiated Gaussian pulse with a center frequency of $55\,Hz$ is used for the source indicated with a "∗" in the figure. The range from the source to the keel's center of mass, marked with a "·", is about 3λ, where $\lambda = 27\,m$ is the wavelength in water at $55\,Hz$. The grazing angle, Γ, between the under surface of the ice and a line from the source to the keel's center of mass is $-7°$, where the naming convention used for angles is shown in Figure 4.2. The sponge region used for the illustrative example is only $15\,m$ thick, which corresponds to $\simeq \lambda/2$ in water at the center frequency of the source, $55\,Hz$. This relatively thin sponge region reduces the computation time for the result but allows reflections from the computational boundary to contaminate the solution. In the scattering experiments of Chapter 5 the sponge region is $60\,m$ or $\simeq 2\lambda$, which reduces contamination from spurious boundary reflections to an acceptable level.
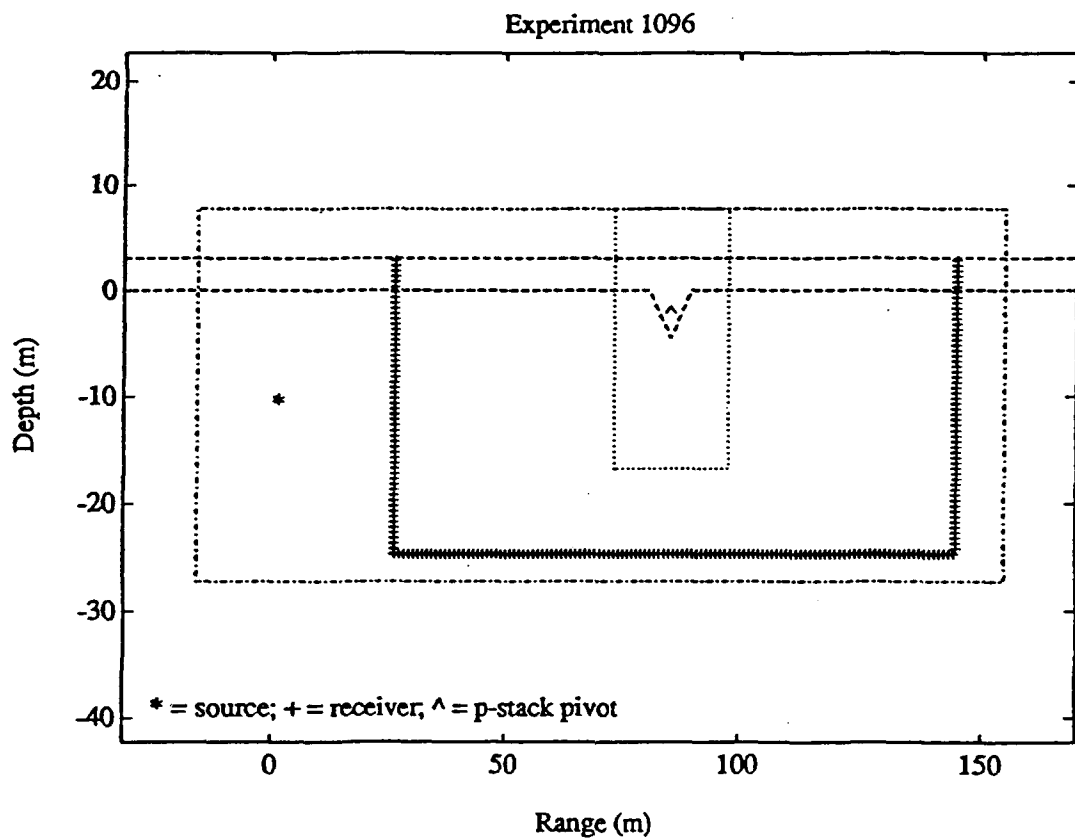
Figure 4.1: Scattering model from which data is used to illustrate the analysis procedures developed in this chapter. The model is of a 9 m wide by 4.5 m deep triangular keel positioned under an otherwise uniform sheet of 3 m ice. The grazing angle between the source, shown with a "*", and the keel's center of mass, shown with a "^", is $\Gamma = -7°$. The nomenclature for the angles is defined in Figure 4.2. A box receiver array is placed around the keel as indicated by the "+" marks. The keel's center of mass is also the pivot point for the array processing as described in Section 4.5.
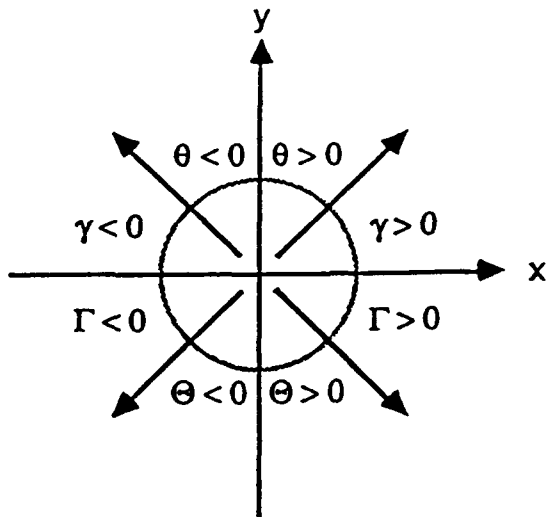
Figure 4.2: Nomenclature for grazing and incidence angles above and below the x-axis.

Two types of data sets are generated during the execution of the scattering experiment: snapshots and time series. Snapshots of the field variables are recorded at a few fixed times for the entire field inside the dashed box around the scatterer. Time series of the field variables are recorded for all times at each receiver location marked by a "+" in the box array around the keel. Five field variables – horizontal and vertical velocity, horizontal and vertical normal stress, and shear stress – are recorded in both the snapshots and time series. These data sets are used as examples to illustrate the characteristics of the analysis methods developed in the sequel.

4.3 Signals

During an experiment, various physical field quantities are sampled and recorded as signals in the form of snapshots and time series. The signals may be decomposed in several ways. I decompose the total field into three parts: the source, the coherent component, and the scattered component. This decomposition provides for detailed studies of the scattering

phenomenon isolated from the sometimes overwhelming influence of the source and coherent field. An example of this technique applied in physical experiments may be seen in Levin and Robinson [36].

4.3.1 Recorded signals

Five field variables are available for recording as snapshots or time series. The recorded signals are samples of the total full-wave field excited in the experiment and include all the field components: source, reflections, scatter, plate waves, radiated head waves, evanescent waves, etc. The recorded field variables are

$$
\underline{u}_T = \begin{pmatrix} v_1 \\ v_2 \\ \sigma_{11} \\ \sigma_{22} \\ \sigma_{12} \end{pmatrix}_T = \begin{pmatrix} \text{horizontal velocity} \\ \text{vertical velocity} \\ \text{horizontal normal stress} \\ \text{vertical normal stress} \\ \text{shear stress} \end{pmatrix},
\qquad (4.1)
$$

where the subscript T denotes the total field. In a fluid the horizontal and vertical normal stress are equal and are simply denoted as the normal stress. Also, the shear stress is zero in a fluid. Figure 4.4a shows the total normal stress recorded by the box array around the keel in Figure 4.1.

4.3.2 Derived signals

Given the total field measurements discussed above, many field decompositions are possible. How the decomposition proceeds depends on where the field measurements are made, namely, in water, which only supports acoustic fields, or in ice, which supports elastic fields. Data measurements in the water are decomposed into source and scattered components. For data measurements in the ice, only the scattered elastic component is available, but it, in

128

turn, may be decomposed into two plate modes: flexural and longitudinal. Decomposition of the acoustic and elastic fields are now discussed in detail.

Acoustic fields

In the water below the ice it is possible to compute the source excitation field alone. This is done by running a model with source and receiver geometry fixed as for the scattering experiment but with homogeneous water for the model. The measured field is the direct arrival from the source without contamination from reflections and scatter due to inhomogeneities. In the true scattering experiment the measured field includes this direct arrival as part of the total field. I define the residual field, $\underline{u}_R$, as the difference between the total field, $\underline{u}_T$, and the source excitation, $\underline{u}_E$. Specifically,

$$\underline{u}_R \equiv \underline{u}_T - \underline{u}_E. \tag{4.2}$$

The residual field data contains information about everything that is not homogeneous water, in other words, only the inhomogeneities of the model. An example of the residual field for flat ice is seen in Figure 4.3b.

The residual field is physically meaningful only in the water below the ice. In the ice a residual field computed using Equation (4.2) cannot be interpreted physically since the source field used in the calculation is measured in water and would be applied in a different material. Because of the lack of physical interpretation I do not compute a residual field in ice or air. In the water, however, the residual field is the reflected and scattered signal from the interface-scatterer complex. While I do not use the residual field directly, it provides a useful intermediate step for interpreting the acoustic field in terms of constituent parts.

A special residual field is that derived from an experiment with a flat interface, either ice or free, and no scatterer. I define this field as being entirely coherent since it is essentially a specular reflection of the incident field. It is designated $\underline{u}_C$. Note that all the scattering

129
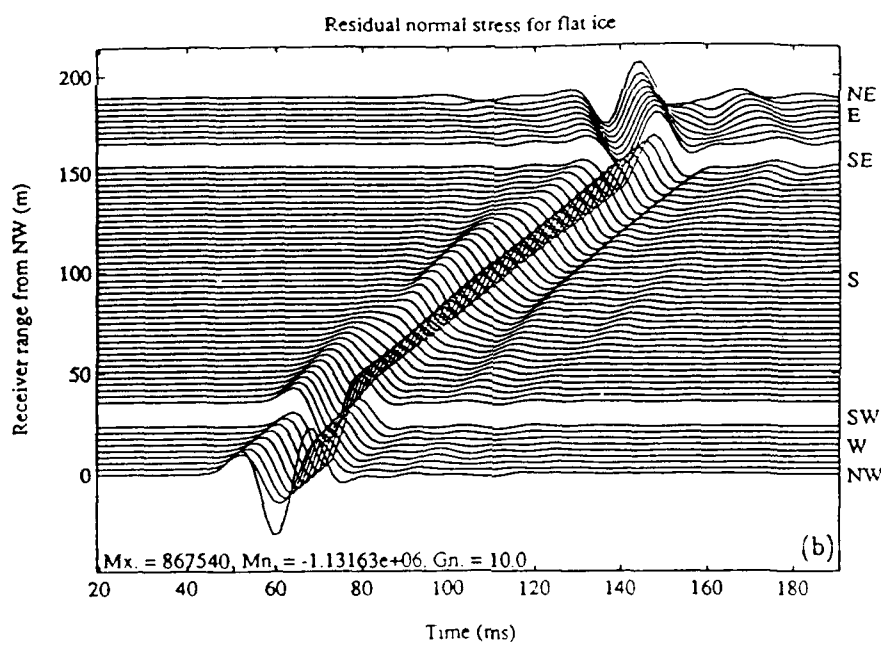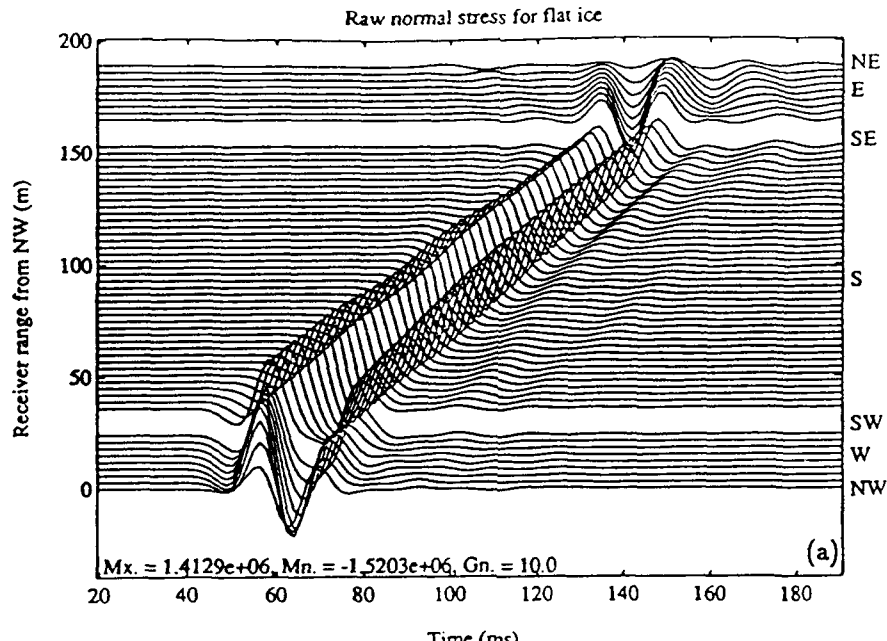
Figure 4.3: (a) Total and (b) residual field for $3\,m$ flat ice. The geometry is exactly as in Figure 4.1 except that there is no keel. In the total field (a), both the direct arrival from the source and the reflected arrival from the ice are present though they overlap in time. In the residual field (b), only the reflection from the ice is present. The direct arrival from the source has been removed. Thus, only information about the inhomogeneities of the model are present in the residual field.

and flat interface experiments in this thesis are really deterministic experiments, and the concept of a statistically coherent signal is not meaningful for any single experimental result. Instead, I am using the term *coherent* to suggest a flat interface reference against which the scattered field due to a particular roughness element can be compared.

Using the coherent field and the residual field for a scattering experiment the scattered field is defined as

$$\underline{u}_S \equiv \underline{u}_R - \underline{u}_C. \tag{4.3}$$

Note that the scattered field may also be derived directly from the raw total fields involved. Specifically,

$$\underline{u}_S = \underline{u}_T \mid_{\text{scatter}} - \underline{u}_T \mid_{\text{coherent}},$$
$$= \underline{u}_{T_s} - \underline{u}_{T_c}. \tag{4.4}$$

The nomenclature suggested by Equation (4.4) is that a flat interface experiment is a *coherent* experiment and an experiment with a roughness element is a *scattering* experiment. Equation (4.4) is an easier way to compute the scattered field with no need for the intermediate step of the residual and coherent field. Furthermore, this is the only physically meaningful way to compute the scattered field in the ice plate.

In the water, the scattered field comprises only two velocity components and the normal stress, or

$$\underline{u}_S = \begin{pmatrix} v_1 \\ v_2 \\ \sigma_{11} \end{pmatrix}_S = \begin{pmatrix} v_1 \\ v_2 \\ \sigma_{22} \end{pmatrix}_S \equiv \begin{pmatrix} v_1 \\ v_2 \\ \sigma \end{pmatrix}_S. \tag{4.5}$$

As an example, consider Figure 4.4, which shows the total field and the scattered field for the illustrative example presented in Section 4.2. The coherent field used in this case is the one shown in Figure 4.3(a), which corresponds to the reflected field from a flat ice plate. In

131

Raw normal stress around keel

Mx. = 1.4129e+06, Mn. = -1.5203e+06, Gn. = 10.0

(a)

Scattered normal stress around keel

Mx. = 80230, Mn. = -71150, Gn. = 10.0

(b)
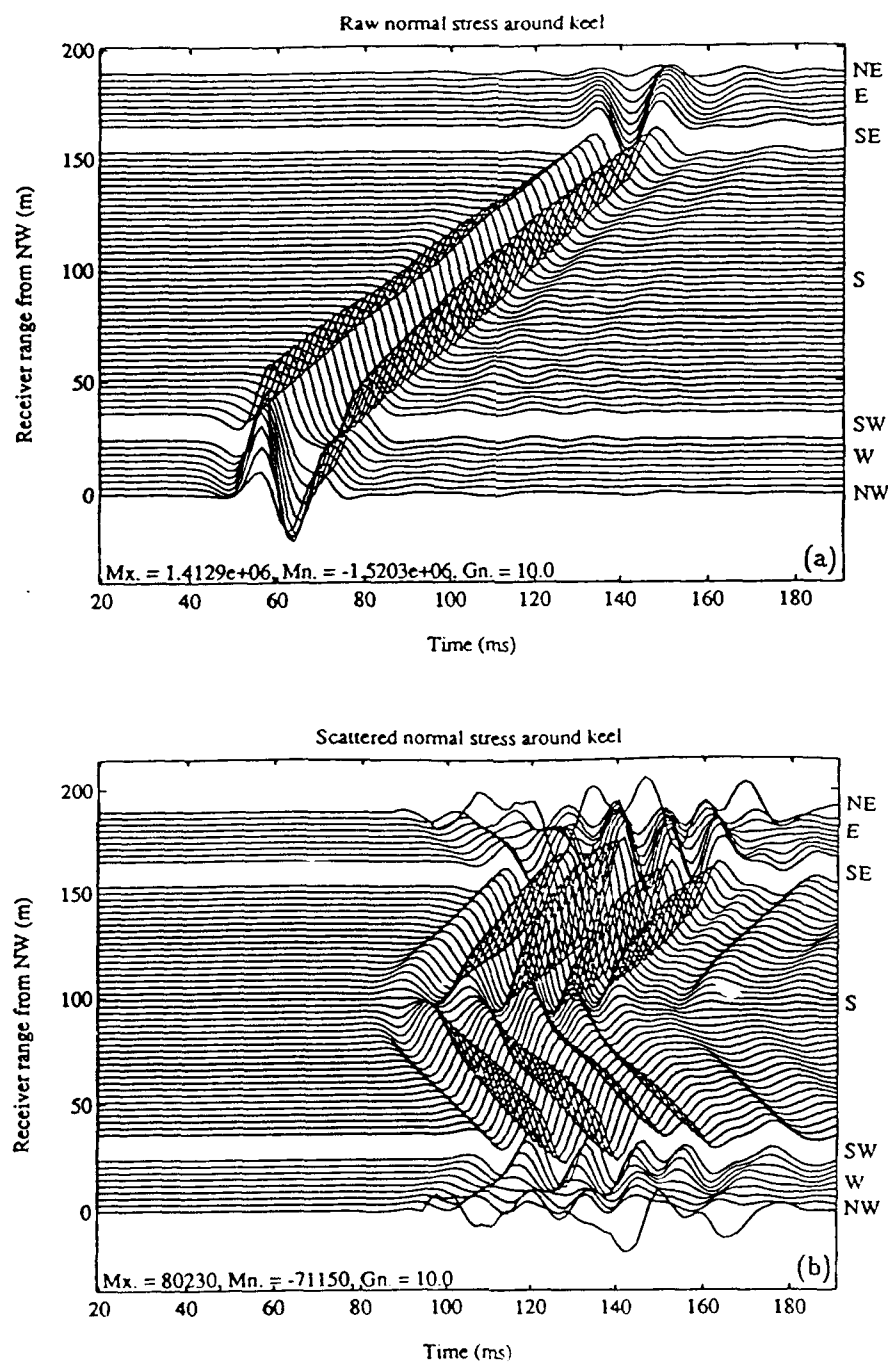
Figure 4.4: Total field (a) and the scattered field (b) from the single keel model shown in Figure 4.1. The large signal seen in (a) is the combination of the direct arrival and the reflected event from the flat ice on either side of the keel. The diffraction from the keel is seen but its amplitude is much smaller than that of the earlier signal. The scattered field seen in (b) is computed from the total field by subtracting the coherent field shown in Figure 4.3a.

132

Figure 4.4(b) all of the source and flat ice arrivals have been removed leaving the scattered field in isolation. This process breaths vitality into the scattering element. The scatterer, in effect, acts spontaneously, radiating energy from an enigmatic array of notional sources[†]. If some of the sources happen to be anti-sources, or sinks, they draw energy out of the coherent field and deliver it elsewhere. By inference, the observed scattered field is the radiated interference pattern of the notional source-sink assemblage. It is not the intent of this study to discover the scattering source array details; rather, I estimate the farfield energy flux radiation pattern and from that deduce a model of the energy paths which must exist through the scatterer.

Elastic fields

In an elastic material, all five field quantities are non-zero in general. That is

$$\underline{u}_T = \begin{pmatrix} v_1, & v_2, & \sigma_{11}, & \sigma_{22}, & \sigma_{12} \end{pmatrix}^T. \tag{4.6}$$

As mentioned above it is impossible to compute a physically meaningful residual field in the ice. It is possible, however, to compute the scattered field. This is the field due only to the scatterer in the absence of the source and the coherent component. Like the residual field, this field cannot be measured directly. Nevertheless, it corresponds to the field generated by the apparent spontaneous action of the scatterer, just as in the acoustic case.

If an elemental scatterer has flat ice on either or both sides, as opposed to a free surface, then the scattered wave in the ice may be further decomposed into longitudinal and flexural components. Only these two modes are present in thin ice at low frequency. Specifically, the Rayleigh-Lamb spectrum evaluated for $3\,m$ flat ice with free surfaces reveals that only

---

[†]This concept is similar to that of exploding reflector models frequently used in exploration seismology [37].
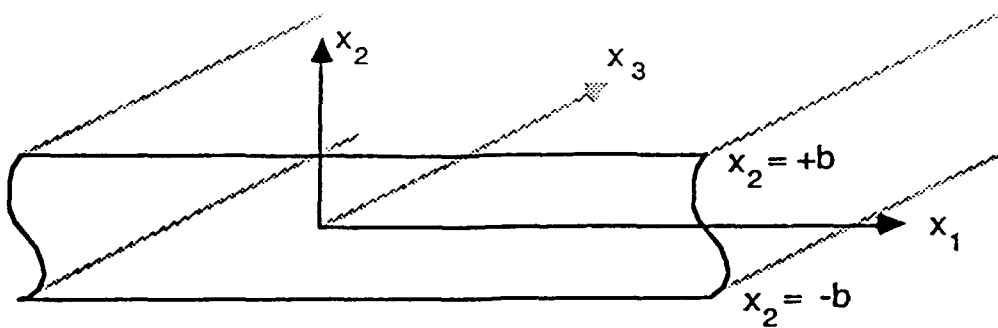
Figure 4.5: Ice plate and coordinate system used to derive expressions for the symmetric and anti-symmetric Lamb modes.

the lowest order symmetric (longitudinal) and anti-symmetric (flexural) modes are present at $55\,Hz$ [48, p. 202]. The next higher mode, which is anti-symmetric, is absent until a frequency of $\simeq 270\,Hz$ is reached. These results for unloaded ice are similar to the semi-loaded case of an ice plate floating on water [50].

An extension of work by Achenbach [2, p. 220ff.] leads to expressions for the mode shapes of each of the five elastic field components for the flexural and longitudinal mode. Consider an ice plate as shown in Figure 4.5. With the coordinate system as shown, an elastic wave equation may be written in two unknowns: a scalar potential for compressional waves, φ, and a vector potential for shear waves, $\underline{\psi}$. The pair of equations is

$$\varphi_{,ii} = \frac{1}{C_p^2}\varphi_{,tt},$$

$$\underline{\psi}_{,ii} = \frac{1}{C_s^2}\underline{\psi}_{,tt}, \tag{4.7}$$

where C_p is the compressional wave speed and C_s is the shear wave speed. Displacement is defined as

$$\underline{v} = \underline{\nabla}\varphi + \underline{\nabla} \times \underline{\psi}. \tag{4.8}$$

The plane strain assumption used herein yields a non-zero result in the curl operation of Equation (4.8) only for the x_3 component of $\underline{\psi}$. Thus, for convenience I define $\psi \equiv \psi_3$ and

134

Equation (4.7) reduces to two scalar equations.

In a thin ice sheet the propagating modes of interest are standing waves in the x_2 direction and propagate only in the x_1 direction. This leads to the the wave potential ansatz

$$\varphi(x_i, t) \sim \Phi(x_2) e^{-i(\xi x_1 - \omega t)},$$

$$\psi(x_i, t) \sim \Psi(x_2) e^{-i(\xi x_1 - \omega t)}. \tag{4.9}$$

Substitution into the wave equation (4.7) yields the standing wave modes

$$\Phi(x_2) = A_1 \sin(p x_2) + A_2 \cos(p x_2)$$

$$\Psi(x_2) = B_1 \sin(q x_2) + B_2 \cos(q x_2), \tag{4.10}$$

where $p^2 = (\frac{\omega^2}{C_p^2} - \xi^2)$ and $q^2 = (\frac{\omega^2}{C_s^2} - \xi^2)$. The scaling coefficients A_i and B_i are determined by the boundary conditions on the surfaces of the plate. They have no influence, however, on the symmetry of the standing waves and, as will be seen shortly, there is no need to determine them explicitly.

Finally, substituting the modal solution, Equation (4.10) and Equation (4.9), into the equation for particle displacement, Equation (4.8), leads to a separation of the wave motion into symmetric and anti-symmetric components. Dropping the common propagating factor $e^{-i(\xi x_1 - \omega t)}$, the displacements are written

$$v_1 = \underbrace{-i\xi A_2 \cos(p x_2) + q B_1 \cos(q x_2)}_{\substack{\text{mirror symmetric} \\ \text{(longitudinal)}}} \underbrace{- i\xi A_1 \sin(p x_2) - q B_2 \sin(q x_2)}_{\substack{\text{mirror anti-symmetric} \\ \text{(flexural)}}},$$

$$v_2 = \underbrace{-p A_2 \sin(p x_2) + i\xi B_1 \sin(q x_2)}_{\substack{\text{mirror symmetric} \\ \text{(longitudinal)}}} \underbrace{- p A_1 \cos(p x_2) + i\xi B_2 \cos(q x_2)}_{\substack{\text{mirror anti-symmetric} \\ \text{(flexural)}}}, \tag{4.11}$$

135

where the axis of symmetry is the midline of the plate at $x_2 = 0$. From this analysis, it is evident that the horizontal and vertical displacements in a thin plate may be decomposed into two additive components: a symmetric component, called the longitudinal mode, and an anti-symmetric component, called the flexural mode.

The constitutive equations relating stress to displacement are

$$\sigma_{ij} = \lambda \upsilon_{k,k} \delta_{ij} + \mu(\upsilon_{i,j} + \upsilon_{j,i}). \tag{4.12}$$

Since the constitutive equations are linear it follows that the stress may also be decomposed into symmetric and anti-symmetric modes. Substitution of the longitudinal displacement mode into the constitutive equation yields

$$
\begin{aligned}
\sigma_{11} &= -(\lambda p^2 + (\lambda + 2\mu)\xi^2)A_2 \cos(px_2) - i2\mu\xi q B_1 \cos(qx_2), \\[2mm]
\sigma_{22} &= -(\lambda \xi^2 + (\lambda + 2\mu)p^2)A_2 \cos(px_2) - i2\mu\xi q B_1 \cos(qx_2), \\[2mm]
\sigma_{12} &= \mu[2i\xi p A_2 \sin(px_2) + (\xi^2 - q^2)B_1 \sin(qx_2)].
\end{aligned}
\tag{4.13}
$$

Similarly, the flexural modes are found to be

$$
\begin{aligned}
\sigma_{11} &= -(\lambda p^2 + (\lambda + 2\mu)\xi^2)A_1 \sin(px_2) + i2\mu\xi q B_2 \sin(qx_2), \\[2mm]
\sigma_{22} &= -(\lambda \xi^2 + (\lambda + 2\mu)p^2)A_1 \sin(px_2) - i2\mu\xi q B_2 \sin(qx_2), \\[2mm]
\sigma_{12} &= \mu[-2i\xi p A_1 \cos(px_2) + (\xi^2 - q^2)B_2 \cos(qx_2)].
\end{aligned}
\tag{4.14}
$$

Diagrams of the mode shapes are shown in Figure 4.6. For the longitudinal mode, all

136
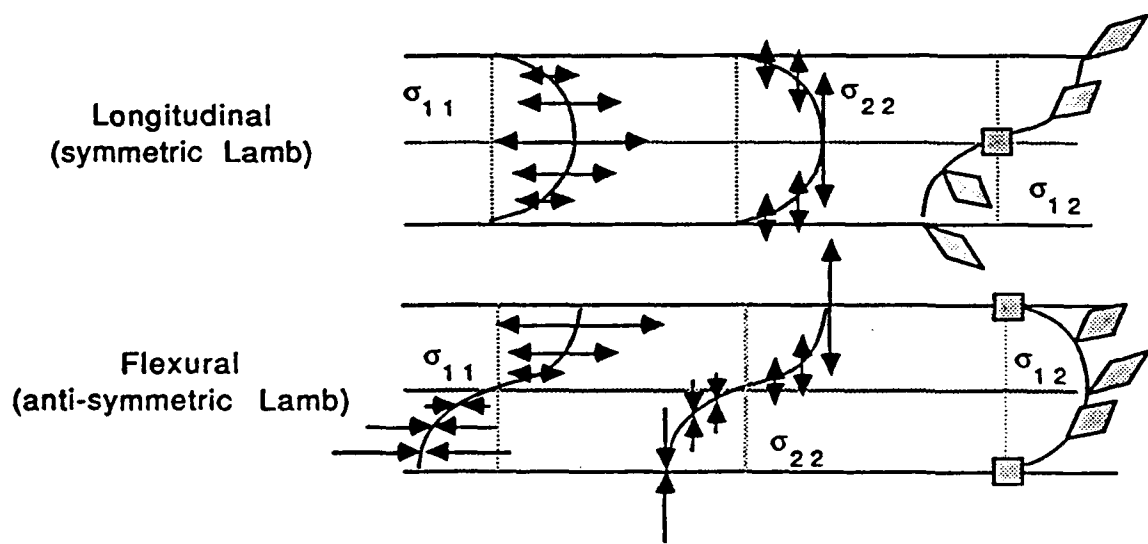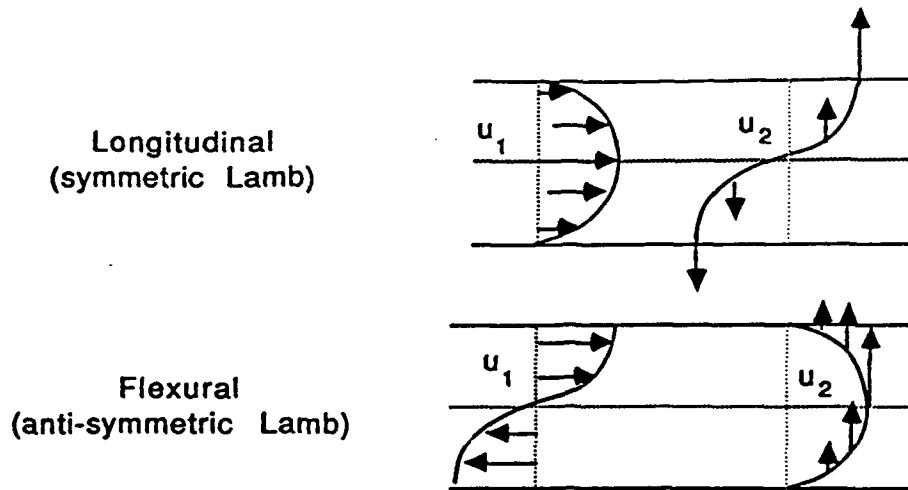
Figure 4.6: Mode shapes of the five elastic components for the two plate modes: longitudinal and flexural. The longitudinal mode is mirror symmetric for all the elastic components and the flexural mode is mirror anti-symmetric.

137

Comp.	Long.	Flex.
v_1	S^+	S^-
v_2	S^-	S^+
σ_{11}	S^+	S^-
σ_{22}	S^+	S^-
σ_{12}	S^-	S^+

Table 4.1: Symmetry of the longitudinal and flexural wave components in a plate. v_1 and v_2 are the particle displacements in the horizontal and vertical direction. σ_{11} and σ_{22} are the horizontal and vertical normal stress while σ_{12} is the shear stress. The symbol S^+ indicates an even function of x_2 and S^- indicates an odd function. The evenness or oddness is not to be confused with the mirror symmetry of the two modes. The longitudinal mode is mirror symmetric for all components and the flexural mode is mirror anti-symmetric for all components.

the field variables are mirror symmetric about the midline of the plate. Conversely, for the flexural modes, all the field variables are mirror anti-symmetric. Given the scattered field in the ice, I exploit this symmetry property to compute the two components of the plate waves. An examination of the diagrams and the modal equations leads to the results shown in Table 4.1, which identifies those components that are even functions of x_2, S^+, and those that are odd, S^-.

The decomposition algorithm is simple. Any scattered field component, say v_1, may be decomposed into its even and odd part such that

$$v_1(x_2) = v_1(x_2)_e + v_1(x_2)_o, \tag{4.15}$$

where the even and odd part are determined by

$$v_1(x_2)_e = [v_1(x_2) + v_1(-x_2)]/2,$$

$$v_1(x_2)_o = [v_1(x_2) - v_1(-x_2)]/2. \tag{4.16}$$

The scattered field in the ice may thus be decomposed into flexural and longitudinal components such that

$$\underline{u}_S = \underline{u}_F + \underline{u}_L. \tag{4.17}$$

138

4.4 Power and energy

Having decomposed the raw measurements of a scattering experiments into constituent parts, it is of interest to determine quantitatively the partitioning of energy into each part. In contrast to the linear quantities discussed in the last section, velocity and stress, quadratic quantities are discussed here. These quantities open the way to understanding the transduction mechanism between acoustic energy in the water and elastic energy in the ice. In this section I define several quadratic quantities of interest and present examples using data from the test model discussed in Section 4.2.

4.4.1 Preliminaries

I start with the conservation of mechanical energy and use the consequences to develop definitions for power flux and energy flux.

For an adiabatic process, conservation of energy is concerned only with the mechanical state of a deformed body. In particular, a body can only change the total energy content of its interior through the action of applied tractions on its surface. Specifically, for a body as shown in Figure 2.1, conservation of energy may be written

$$\frac{dE}{dt} = \int_{\partial D} T_i v_i \, dS, \tag{4.18}$$

where E is the total energy inflow into the body, T_i is the applied traction to the surface of the body, and v_i is the particle velocity at the surface. The quantity $T_i v_i$ is the rate of work per unit surface area. Using the traction stress relation, $T_i = \sigma_{ij} n_j$, on the right side of Equation (4.18) leads to

$$\int_{\partial D} T_i v_i \, dS = \int_{\partial D} \sigma_{ij} v_i n_j \, dS \equiv - \int_{\partial D} \phi_i n_i \, dS, \tag{4.19}$$

where n_i is the outward normal on the surface. The power flux,

$$\phi_i = -\sigma_{ij} v_j, \qquad (4.20)$$

is computed from the five elastic field variables that are measured during the execution of a scattering experiment. The direction of the power flux vector points in the direction of power flow. Using Equations (4.18), (4.19) and (4.20) together leads to

$$\frac{dE}{dt} = -\int_{\partial D} \phi_i n_i \, dS, \qquad (4.21)$$

which says the rate at which a body gains energy, on the left, is the negative of the power flux through the surface of the body, on the right. If the power flux is out of the body, then the rate of energy gain is negative. The integral of Equation (4.21) over time yields the net energy inflow

$$E = -\int_t \int_{\partial D} \phi_i n_i \, dS \, dt \equiv -\int_{\partial D} \mathcal{E}_i n_i \, dS, \qquad (4.22)$$

where the energy flux, $\mathcal{E}_i$, is defined as

$$\mathcal{E}_i = \int_t \phi_i \, dt. \qquad (4.23)$$

Figure 4.7(a) shows the power flux for the field around the keel in the illustrative example at a time of 105.8 ms. The arrows point in the direction of power flow. This snapshot of the power flux around the keel shows in what direction power is flowing; whence it is coming and where it is going. By looking at these paths, the transduction mechanism of acoustic energy to elastic energy in the ice may be characterized.

4.4.2 Extensions

Source energy

Consider the simplest of experiments, that of an isotropic source in a homogeneous fluid. If the source is inside a closed box of receivers, the total energy inflow, E_T, computed using

140
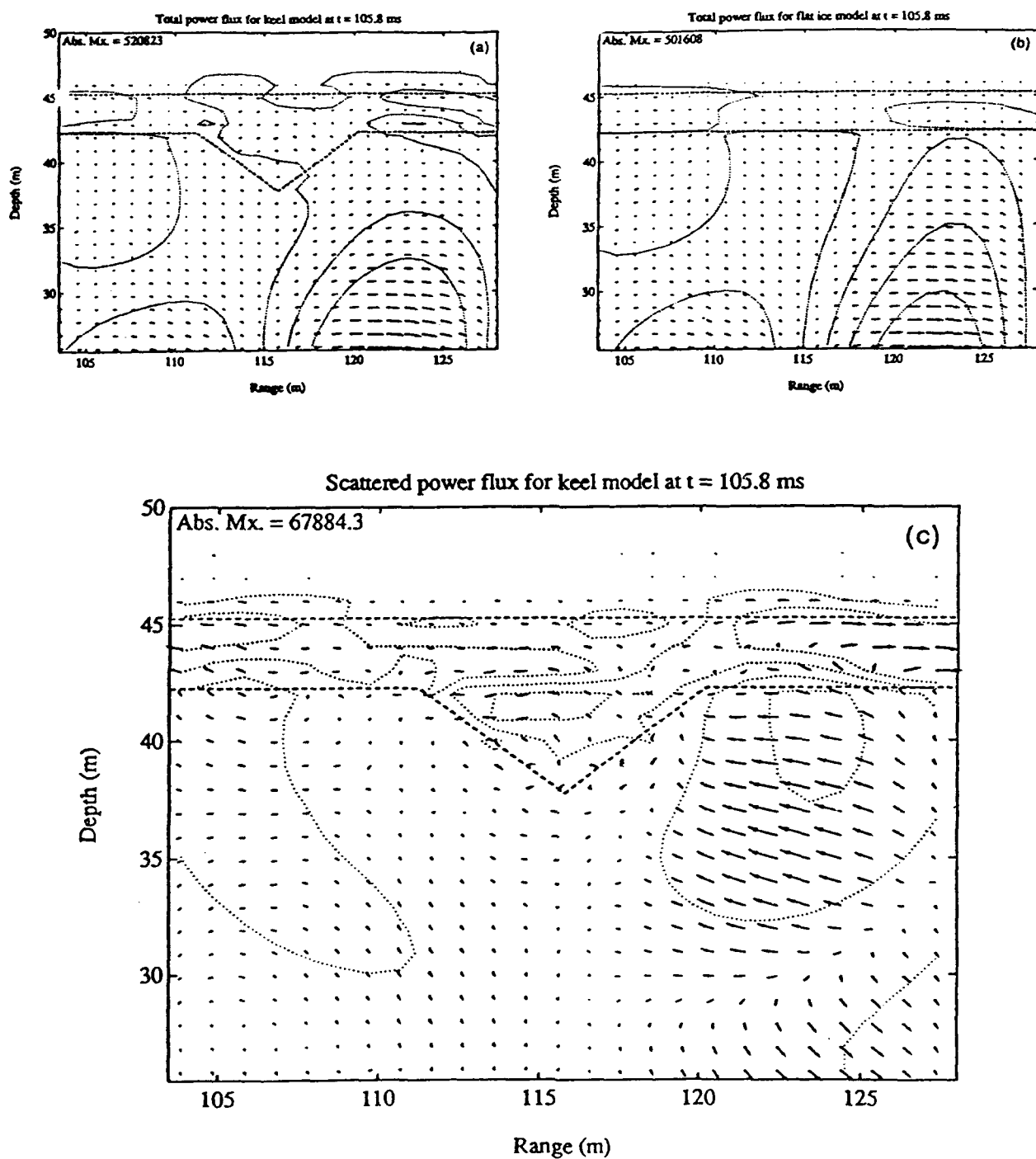
Figure 4.7: Power flux around keel at $105.8\,ms$. The keel is outlined with a dashed line and the dotted contours are lines of constant horizontal normal stress. The arrows point in the direction of power flow. Pictured are (a) the total power flux for the scattered experiment, $\underline{\Phi}_{T_s}$, (b) the total power flux for the coherent experiment, $\underline{\Phi}_{T_c}$, and (c) the scattered power flux $\underline{\Phi}_S = \underline{\Phi}_{T_s} - \underline{\Phi}_{T_c}$.

Equation (4.22) with the time series recorded around the box is negative and is an estimate of the source energy, i.e., $E_E \equiv -E_T$, where the subscript E denotes the excitation function.

The source energy contained in the arc angle subtended by the scatterer is derived by first writing the total energy delivered by an isotropic line source to the farfield as

$$E_E = \int_\theta \frac{\mathcal{E}_E(\theta)}{r} \cdot r \, d\theta = \mathcal{E}_E \int_\theta d\theta = 2\pi \mathcal{E}_E, \tag{4.24}$$

where $\mathcal{E}_E(\theta)$ is the radial energy flux measured at unit distance from the source and is constant with respect to θ, since the source is isotropic.

From an experiment with a box array around a source, σ_{ij} and v_j are measured along the perimeter of the box and are used to compute $\phi_i = -\sigma_{ij} v_j$ and

$$E_E = -E_T = \int_t \int_{\partial D} \phi_i n_i \, dS \, dt. \tag{4.25}$$

Now, from Equation (4.24) the isotropic radial energy flux of the source is

$$\mathcal{E}_E = \frac{E_E}{2\pi}. \tag{4.26}$$

Using this and the experimental geometry in Figure 4.8, the energy delivered by an isotropic source to a scatterer subtending an arc of θ_S is simply

$$E(\theta_S) = \theta_S \mathcal{E}_E = \frac{\theta_S E_E}{2\pi}. \tag{4.27}$$

Scattered power flux

It might appear that the scattered power flux, $\underline{\phi}_S$, is computed as

$$(\phi_i)_S = -(\sigma_{ij})_S (v_j)_S \tag{4.28}$$

using the scattered field, Equation (4.3) or (4.4), and the definition of power flux, Equation (4.20). However, this is only part of the scattered power flux.

142
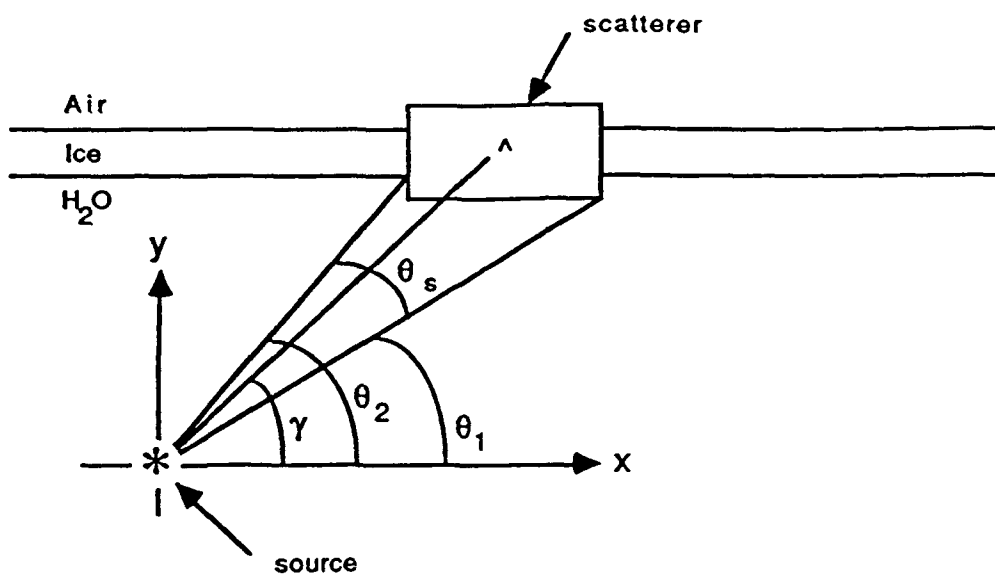
Figure 4.8: Plane wave approximation using an isotropic line source. With the scatterer in the farfield of the source, the phase and amplitude variations across the small arc angle subtended by the scatterer are negligible. The grazing angle is defined as $\gamma = \theta_1 + \theta_S/2$, where θ_S is the arc angle subtended by the scatterer. Energy also travels out at other angles around the source, but it intersects flat ice or a flat free surface and is reflected rather than scattered back into the water. The reflected field is subtracted for analysis of the scattered field.

Starting with the definition of the scattered field in Equation (4.4), the total field from the scattering experiment is written

$$\underline{u}_{T_s} = \underline{u}_S + \underline{u}_{Tc}. \qquad (4.29)$$

The power flux for the total field is then

$$
\begin{aligned}
\underline{\phi}_{T_s} &= -\underline{\sigma}_{T_s} \underline{v}_{T_s}, \\
&= -[\underline{\sigma}_S + \underline{\sigma}_{Tc}][\underline{v}_S + \underline{v}_{Tc}], \\
&= -\underbrace{[\underline{\sigma}_S \underline{v}_S + \underline{\sigma}_{Tc} \underline{v}_S + \underline{\sigma}_S \underline{v}_{Tc}]}_{\equiv -\underline{\phi}_S} - \underbrace{\underline{\sigma}_{Tc} \underline{v}_{Tc}}_{\equiv -\underline{\phi}_{Tc}}, \\
&= \underline{\phi}_S + \underline{\phi}_{Tc}. \qquad (4.30)
\end{aligned}
$$

Alternatively, the scattered power flux may be computed as

$$\underline{\phi}_S = \underline{\phi}_{T_s} - \underline{\phi}_{Tc}. \qquad (4.31)$$

An example of the scattered power flux is shown in Figure 4.7(c). The cross terms in the scattered power flux are non-zero only in portions of the domain where the scattered field overlaps in space and time with the coherent field. These terms are needed for an exact energy balance such that

$$E_{T_s} = E_S + E_{Tc}. \qquad (4.32)$$

Similarly, the power flux of the two plate waves in the ice contains cross terms between the flexural and longitudinal components. Using the plate wave decomposition of Equation (4.17) in the scattered power flux definition in Equation (4.30)[3] leads to

$$\underline{\phi}_S = -[\underline{\sigma}_F + \underline{\sigma}_L][\underline{v}_F + \underline{v}_L] - \underline{\sigma}_{Tc}[\underline{v}_F + \underline{v}_L] - [\underline{\sigma}_F + \underline{\sigma}_L]\underline{v}_{Tc},$$

144

$$= -\underbrace{\left[\underline{\underline{\sigma}}_F \underline{v}_F + \underline{\underline{\sigma}}_{Tc} \underline{v}_F + \underline{\underline{\sigma}}_F \underline{v}_{Tc}\right]}_{\equiv -\underline{\phi}_F}$$

$$-\underbrace{\left[\underline{\underline{\sigma}}_L \underline{v}_L + \underline{\underline{\sigma}}_{Tc} \underline{v}_L + \underline{\underline{\sigma}}_L \underline{v}_{Tc}\right]}_{\equiv -\underline{\phi}_L}$$

$$-\underline{\underline{\sigma}}_L \underline{v}_F - \underline{\underline{\sigma}}_F \underline{v}_L. \tag{4.33}$$

The last two cross terms in this equation integrate to zero for contours that cut the ice vertically. Two factors lead to this conclusion: 1) for vertical contours, only the horizontal power flux contributes to the net energy inflow and 2) from Table 4.1 the horizontal power flux in the cross terms is an odd function of x_2 and thus integrates to zero[†]. Because of this and the fact that vertical arrays through the ice are used for all scattering experiments, the last two cross terms in Equation (4.33) are henceforth ignored in energy calculations.

To summarize, the important power and energy flux quantities are computed as follows. For both the acoustic and elastic fields, the scattered power flux is

$$\underline{\phi}_S = -\left[\underline{\underline{\sigma}}_S \underline{v}_S + \underline{\underline{\sigma}}_{Tc} \underline{v}_S + \underline{\underline{\sigma}}_S \underline{v}_{Tc}\right],$$

$$= \underline{\phi}_{Ts} - \underline{\phi}_{Tc}. \tag{4.34}$$

Scattered power flux may be computed using either snapshot or time series data.

For the plate waves in the ice, the flexural and longitudinal power flux are

---

[†] Take the first cross term for example and refer to Figure 4.6:

$$\underline{\underline{\sigma}}_L \underline{v}_F = (\sigma_{11})_L (v_1)_F + (\sigma_{12})_L (v_2)_F \sim S^+ S^- + S^- S^+ \sim S^-.$$

By similar reasoning, the second cross term is also S^-.

$$\underline{\phi}_F = -[\underline{\sigma}_F \underline{v}_F + \underline{\sigma}_{Tc} \underline{v}_F + \underline{\sigma}_F \underline{v}_{Tc}],$$

$$\underline{\phi}_L = -[\underline{\sigma}_L \underline{v}_L + \underline{\sigma}_{Tc} \underline{v}_L + \underline{\sigma}_L \underline{v}_{Tc}]. \tag{4.35}$$

In principle, both snapshots and time series may be used to compute the plate wave power flux, but I only compute this quantity for the time series data.

The energy flux corresponding to each power flux variable is

$$\mathcal{E}_S = \int_t \underline{\phi}_S \, dt, \quad \mathcal{E}_F = \int_t \underline{\phi}_F \, dt, \quad \mathcal{E}_L = \int_t \underline{\phi}_L \, dt. \tag{4.36}$$

Since energy flux requires a time integral, this quantity is only computed using time series data.

Energy inflow for each of these modes is defined as

$$E_S = -\int_{\partial D} \underline{\mathcal{E}}_S \cdot \hat{n} \, dS, \quad E_F = -\int_{\partial D} \underline{\mathcal{E}}_F \cdot \hat{n} \, dS, \quad E_L = -\int_{\partial D} \underline{\mathcal{E}}_L \cdot \hat{n} \, dS, \tag{4.37}$$

where $\hat{n}$ is the outward pointing normal of the enclosing receiver array.

For the total field of the coherent experiment

$$\mathcal{E}_{Tc} = \int_t \underline{\phi}_{Tc} \, dt, \quad E_{Tc} = -\int_{\partial D} \underline{\mathcal{E}}_{Tc} \cdot \hat{n} \, dS. \tag{4.38}$$

146

Similarly, for the scattering experiment the total field energy flux and inflow is

$$\mathcal{L}_{T_s} = \int_t \underline{\phi}_{T_s} \, dt, \quad E_{T_s} = -\int_{\partial D} \mathcal{L}_{T_s} \cdot \hat{n} \, dS. \tag{4.39}$$

Global energy balance

A global energy balance is achieved if

$$E_{T_s} = E_{T_c} + E_S,$$

$$= E_{T_c} + E_S|_{\text{water}} + E_S|_{\text{ice}},$$

$$\underbrace{E_{T_s}}_{\substack{\text{total field} \\ \text{scattered energy}}} = \underbrace{E_{T_c}}_{\substack{\text{total field} \\ \text{coherent energy}}}$$

$$+ \overbrace{\underbrace{E_S|_{\text{water}}}_{\substack{\text{scattered} \\ \text{in water}}} + \underbrace{E_F}_{\substack{\text{flexural} \\ \text{plate wave}}} + \underbrace{E_L}_{\substack{\text{longitudinal} \\ \text{plate wave}}}}^{\Sigma = 0}. \tag{4.40}$$

In the physical world the global energy balance in Equation (4.40) is exact. The numerical modeling method used to generate the scattered data, however, is not exact. I discussed in Chapter 3 the excess attenuation of the Lax-Wendroff scheme in a homogeneous medium and concluded that the loss is negligible for the contemplated experiments. When ice and air are added to the model, however, added dissipation at the interface between materials comes into play. The dissipation stabilizes the scheme at the expense of some energy loss. The loss is roughly 10% of the total energy entering the volume, and for a global energy balance, it must be included. The situation is shown schematically in Figure 4.9. For convenience, loss due to the added dissipation is lumped into a single notional sink indicated by the

147
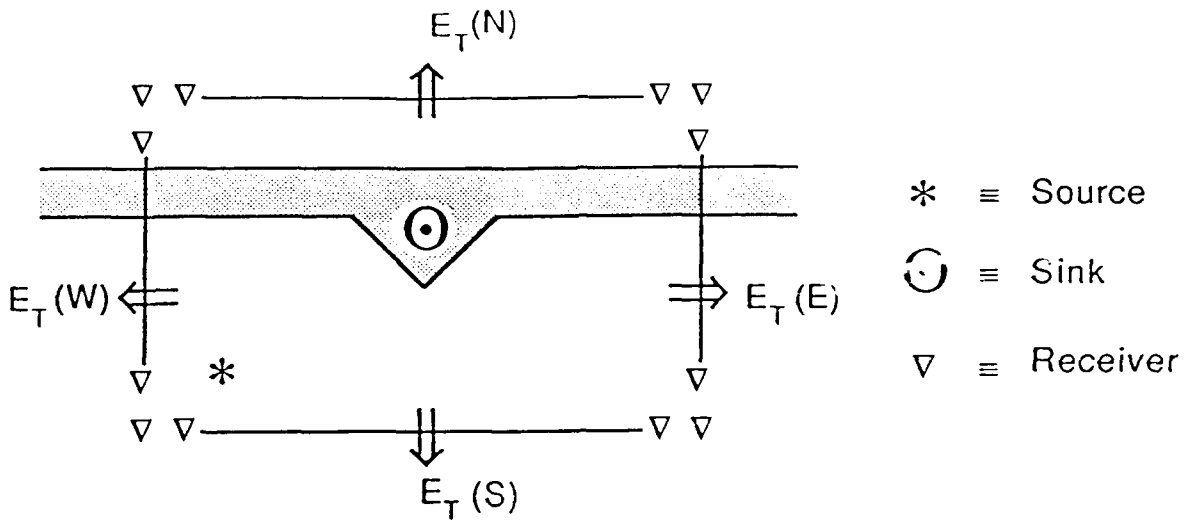
Figure 4.9: Schematic of global energy balance. Energy flows into and out of the control volume, being forced by an interior source. In the absence of attenuation the net energy captured in the control volume is zero. However, added dissipation used to stabilize the modeling scheme acts as an energy sink and the net energy gain of the control volume is positive. The distributed loss due to added dissipation is lumped into a single notional sink.

symbol $\odot$. A plot of the actual energy density lost to added dissipation for a semi-circular keel is shown in Figure 4.10. The energy is only attenuated at the edges of the ice and no extra loss is introduced in the field propagating in the water away from the ice. Thus, to be precise about the global energy balance, an extra term for the energy lost to added dissipation must be added to Equation (4.40) which becomes

$$
\underbrace{E_{T_s}}_{\substack{\text{total} \\ \text{field} \\ \text{scattered} \\ \text{energy}}} = \underbrace{E_{T_c}}_{\substack{\text{total} \\ \text{field} \\ \text{coherent} \\ \text{energy}}} + \underbrace{E_S|_{\text{water}}}_{\substack{\text{scattered} \\ \text{in water}}} + \underbrace{E_F}_{\substack{\text{flexural} \\ \text{plate wave}}} + \underbrace{E_L}_{\substack{\text{longitudinal} \\ \text{plate wave}}} + \underbrace{E_A}_{\substack{\text{added} \\ \text{dissipation}}} .
$$

$$(4.41)$$

Consider the two geometrically identical experiments pictured in Figure 4.11. In the first experiment, a flat ice layer is modeled, and in the second, a scatterer is introduced. For the moment ignore the notional sink associated with the added dissipation. Conservation
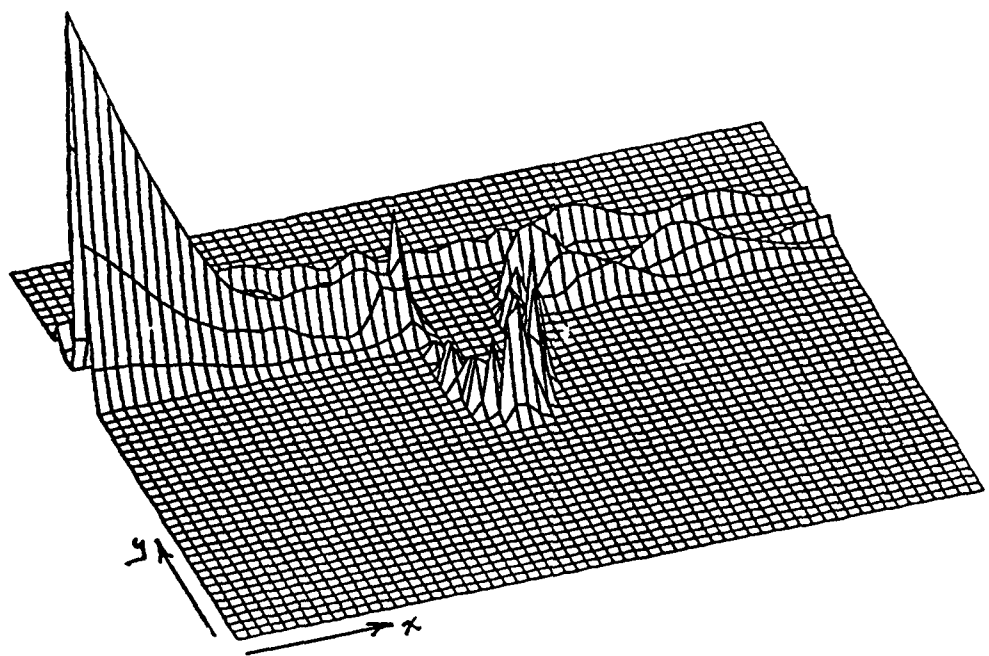
Figure 4.10: Energy density lost to added dissipation in Experiment 38 dir cussed in Chapter 5. Energy is only dissipated at the edges of the ice. Propagation in the water away from the ice is not affected. (This figure is the same as Figure 5.30.)
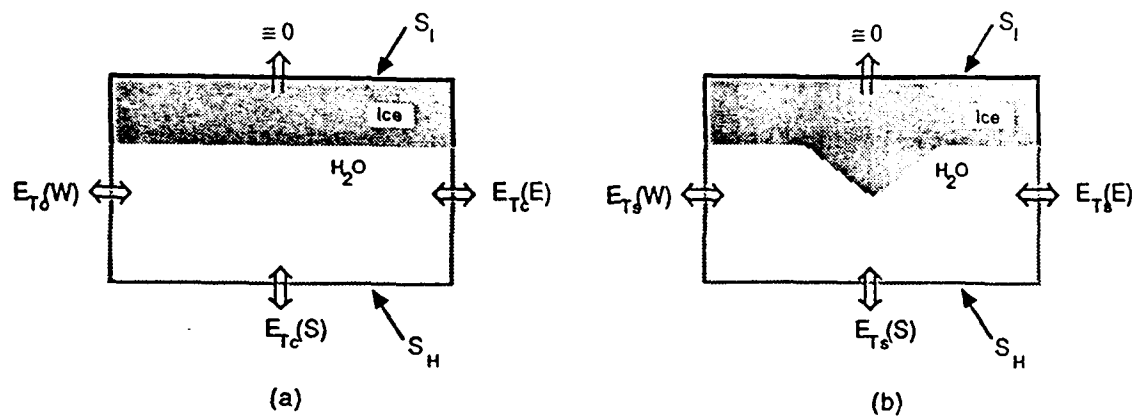
Figure 4.11: Energy balance in experiment with air interface. (a) Experiment with air above flat ice layer. Energy radiation to the air is nearly zero. This is the coherent experiment and is the baseline against which a rough surface experiment is compared. (b) Experiment with air above rough ice. Energy radiation to the air is again essentially zero. The energy available for scatter must be drawn out of the coherent field with a consequent energy deficit therein. In general, the scatterer transfers energy from the coherent field to the environment – both to the water and to the ice plate.

of energy dictates that the energy inflow into the control volume is the same in both cases since no sources or sinks have been added. The four sides of the control volume are denoted as north, east, south and west in an obvious manner. The energy inflow of the total field through each side is indicated, as for example $E_{Tc}(w)$, which is the coherent energy inflow through the west side. Experiments show that energy inflow through the north side is typically three orders of magnitude smaller than that of the other three sides. For convenience then, I assume there is no energy inflow through the north side. Since the total energy inflow is identical for the two experiments, the energy balance must be

$$E_{Tc}(W) + E_{Tc}(S) + E_{Tc}(E) = E_{Ts}(W) + E_{Ts}(S) + F_{Ts}(E)$$

$$E_{Ts}(S_H) - E_{Tc}(S_H) + E_{Ts}(S_I) - E_{Tc}(S_I) = 0$$

$$\underbrace{E_S(S_H)}_{\substack{\text{scattered energy} \\ \text{inflow in water}}} + \underbrace{E_S(S_I)}_{\substack{\text{scattered energy} \\ \text{inflow in ice}}} = 0, \tag{4.42}$$

150

where the second step is possible by redefining the enclosing contour from the north, east, south, and west sides to a water contour, $S_{H_2O} \equiv S_H$, and an ice contour, $S_{Ice} \equiv S_I$. As shown in Figure 4.11 the water contour, S_H, includes the south side and the lower portion of the east and west side. The ice contour, S_I, includes the north side, through which there is no energy inflow, and the upper portion of the east and west side. Thus, Equation (4.42) shows that the scattered energy inflow in the water is exactly balanced by the inflow in the ice. One is positive and the other is negative. The scatterer, then, acts like a balanced differential source-sink pair. The scatterer is, in effect, a transducer, providing a window for energy flow from the domain of locally and momentarily high energy density to the domain of lower energy density. In the absence of the scatterer there is little energy transfer between the water and the ice[†]. Experiments with many scatterers show that during the course of an experiment, energy flows both ways: from the ice into the water and vice versa. The scatterer tends to be a net sink on the water side with positive inflow and a net source on the ice side with negative inflow. Absolute quantification of this tendency cannot be made because of the added dissipation, which is discussed below. The scatterer scavenges energy from the forward propagating coherent field and injects this energy as plate waves into the ice. Figure 4.7(c) is a snapshot showing the scattered power flux paths from the coherent field in the water to the ice plate through a keel. The time integral of this action results in a net energy transfer from the coherent forward propagating field into plate waves in the ice.

Now suppose the effects of the added dissipation are included. The energy balance of Equation (4.42) is disturbed, and the new balance is

$$E_S(S_H) + E_S(S_I) = E_A, \tag{4.43}$$

[†]A small head wave component is injected into the ice at short range. The head wave energy radiates back into the water as it propagates down range.

where the energy inflow of the added dissipation is positive. Energy is trapped in the ice by the added dissipation as shown in Figure 4.10. This is an artifact of the finite difference stabilization procedure, which for the moment, must be dealt with to facilitate interpretation of the scattering experiments. The added dissipation makes it impossible to measure directly the energy inflow in the ice. The energy inflow in the water, however, is not affected by the added dissipation, and because of the energy balance in Equation (4.43), any energy deficit measured in the water must be balanced by an energy surplus in the ice.

4.5   Serpentine array processing

The array processing tool I use to compute specular energy loss is the Radon transform or slant stack. It has the advantage of being a linear transformation, and hence, the angular distribution of energy flux can be calibrated, in principle. In practice, however, the Radon transform has the disadvantage of relatively low angular resolution for a given array aperture, which leads to a bias in the energy flux estimate. The next several sections introduce the conventional Radon transform for linear arrays, extend the technique to non-linear line arrays, or *serpentine arrays*, discuss array calibration, and discuss bias issues.

4.5.1   Definitions

The Radon transform for a linear array of receivers is defined by Chapman [8] as

$$\underline{\tilde{u}}\,(p,\tau) \equiv \int_{-\infty}^{\infty} \underline{u}\,(x,\tau + px)\,dx \qquad (4.44)$$

and transforms a space-time process, $\underline{u}\,(x,t)$, into a slowness-intercept time process, $\underline{\tilde{u}}\,(p,\tau)$. For 2-D plane geometry, the result of the transformation, $\underline{\tilde{u}}\,(p,\tau)$, is exactly the plane wave

decomposition of the data, $\underline{u}(x,t)$, where p is the horizontal slowness of the plane wave and r is the independent time variable. This is a perfect match to the 2-D modeling algorithm developed in Chapter 2 and 3. I use the Radon transform to quantify the scattered energy flux in the specular direction.

The Radon transform is equivalent to steering or phasing a linear array about a designated pivot point and integrating along the length of the steered array. The result is an estimate of the plane wave component propagating in the steered direction. A linear array of given length, L, steered away from broadside has an effective length, L', which decreases as the angle away from broadside increases [56, p. 11-11]. The effective length is equal to the projection of the linear array onto a line perpendicular to the steered direction. In what follows, I refer to these foreshortened arrays as either *projected arrays*, in a geometric context, or *virtual arrays*, in a more general context. Analysis of the projected array length and the projected element distribution is deferred to the next section.

Figure 4.12 shows how the phase shift is computed for a linear array assuming it lies along the x-axis of the coordinate system. Specifically, signals recorded on the linear array are advanced by the amount $\frac{x\sin\theta}{c} = px$, where p is the horizontal slowness. The result of the phase shifting is to bring into phase alignment any plane wave component of the wave field that is propagating at the angle θ. Integration along the projected array provides an estimate of the plane wave component. There is, however, hemispheric ambiguity due to the projection of a 2-D wave field onto a linear array. This is caused by a lack of phase detection in the direction perpendicular to the linear array and gives rise to hemispheric ambiguity in the up-down direction. In contrast, phase detection along the length of a linear array is quite good, depending on the length of the array, and left-right ambiguity is less of a problem.

If the field variables have been recorded on a serpentine array, that is any line array
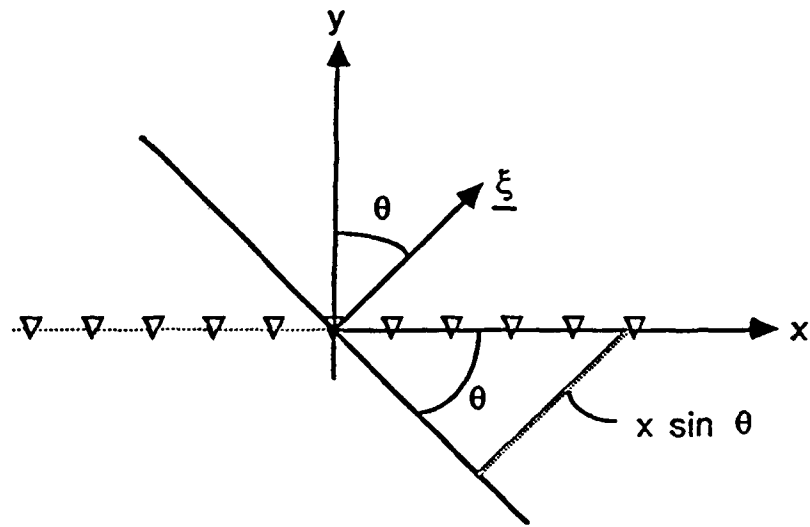
Figure 4.12: Beamforming interpretation of the Radon transform for linear arrays. For each value of slowness, $p(\theta) = \frac{\sin\theta}{c}$, the signals recorded on the linear array are advanced by the amount $\frac{x\sin\theta}{c} = px$. This procedure brings plane wave components of the wave field propagating at the angle θ into phase alignment. Integrating along the length of the projected array yields an estimate of the plane wave component propagating at the angle θ. There is a hemispheric ambiguity due to the projection of a 2-D wave field onto a linear array.
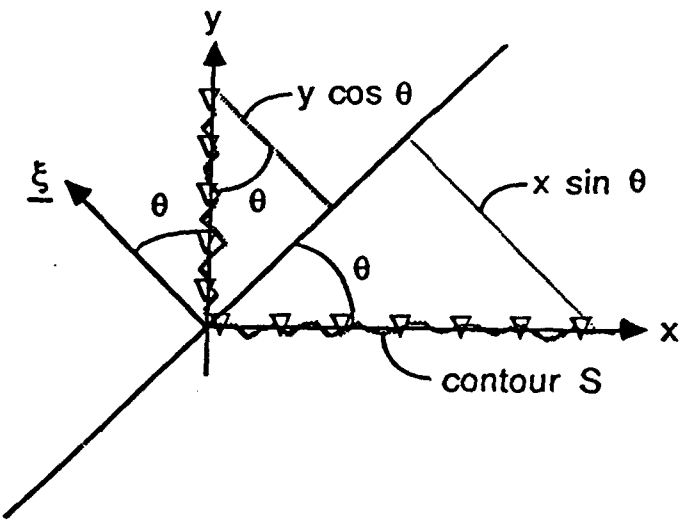
Figure 4.13: Geometry to compute phase delays for serpentine arrays. For a serpentine array, signals recorded along the x-axis are advanced by the amount $\frac{x\sin\theta}{c} = px$ and those recorded along the y-axis are advanced by the amount $\frac{y\cos\theta}{c} = (\frac{1}{c^2} - p^2)^{\frac{1}{2}}y$. Integrating along the length of the projected array yields an estimate for the plane wave component of the wave field propagating at the angle θ. The hemispheric ambiguity problem is abated by the use of serpentine arrays.

which is not linear, then phase shifts in both the x and y directions are needed[†]. Figure 4.13 shows the geometry needed to compute the appropriate time delays. In this case, assuming only propagating modes, signals recorded along the x-axis are advanced by the amount px and those recorded along the y-axis are advanced by the amount $\frac{y\cos\theta}{c} = (\frac{1}{c^2} - p^2)^{\frac{1}{2}}y$. Again, this is equivalent to projecting the serpentine array elements onto a virtual linear array for the estimation of a plane wave component propagating in the direction θ. The major advantage of serpentine arrays is their ability to abate the up-down hemispheric ambiguity problem by enabling phase discrimination of waves propagating in any direction.

[†]Any planar array of receiving elements, whether regularly or randomly place, is also a serpentine array since it is possible to connect the elements of a planar array with one continuous line segment. Hence, all the subsequent work for serpentine arrays also applies to planar arrays.

The slowness vector is defined for propagating modes as

$$\underline{p} = \begin{pmatrix} p \\ \pm(\frac{1}{c^2} - p^2)^{\frac{1}{2}} \end{pmatrix} = \frac{1}{c} \begin{pmatrix} \sin\theta \\ \cos\theta \end{pmatrix},$$

(4.45)

where c is the sound speed and $|\underline{p}| = \frac{1}{c}$. Note, the wave vector, $\underline{\xi} = \omega\underline{p}$. Using the slowness vector defined in Equation (4.45) to beamform data recorded on a serpentine array, the Radon transform of Equation (4.44) becomes

$$\underline{\tilde{u}}(p,\tau) = \int_{\underline{x}_{\bullet}} A(\underline{x},p)\underline{u}(\underline{x},\tau + \underline{p} \cdot \underline{x}) \, dS,$$

(4.46)

where $\underline{x}_{\bullet}$ is the position along the serpentine line S. $A(\underline{x},p)$ compensates for the *projection gain* of the transformation, which is discussed later in Section 4.5.3. For the moment, consider $A(\underline{x},p)$ to be an equalization factor. The slowness argument on the left is a scalar since the vector slowness, $\underline{p}$, is known from Equation (4.45).

Both the linear Radon transform of Equation (4.44) and the serpentine Radon transform of Equation (4.46) are unnormalized. That is, the array gain in the steered direction is a function of the array size. This can be corrected by normalizing the output of the transforms (beamformers) by the virtual array length as a function of slowness, $L'(p)$, or steering angle, $L'(\theta)$. This normalization is equivalent to requiring unity gain for the beamformer in the steered direction. The normalization is explicitly invoked later when computing the plane wave energy flux in Equation (4.69).

4.5.2 Projected arrays

As discussed above, the serpentine Radon transform of Equation (4.46) is effectively a plane wave beamformer and decomposes a given field into its plane wave components. Data from the spatially distributed receiving elements of a serpentine array are projected onto a virtual

156

array with a conveniently located pivot point such as the center of mass of the scatterer under investigation. It is instructive to look at the element distribution along the projected arrays. In practice, a uniform distribution of projected array elements is preferred; such a distribution provides a better estimation of the plane wave than does a highly skewed distribution.

For instructional purposes, consider the geometry of a simple "L" shaped array as shown in Figure 4.13. I use the coordinate rotation relations

$$
\begin{aligned}
x' &= x\cos\theta - y\sin\theta, \\
y' &= x\sin\theta + y\cos\theta,
\end{aligned}
\quad\text{and}\quad
\begin{aligned}
x &= x'\cos\theta + y'\sin\theta, \\
y &= -x'\sin\theta + y'\cos\theta.
\end{aligned}
\tag{4.47}
$$

The projected array lies along the line defined by the coordinates $(x', 0)$. Using Equations (4.47), any point on the projected array, $(x', 0)$, is defined in unprimed coordinates as

$$
\begin{aligned}
x_p &= x'\cos\theta, \\
y_p &= -x'\sin\theta,
\end{aligned}
\tag{4.48}
$$

where the subscript p stands for the *projected* array point. Thus, for a receiver located at the point (x, y), the projected receiver point on a virtual array steered to θ in unprimed coordinates is

$$
\begin{pmatrix} x_p \\ y_p \end{pmatrix} = \begin{pmatrix} x\cos^2\theta - y\cos\theta\sin\theta \\ -x\cos\theta\sin\theta + y\sin^2\theta \end{pmatrix}.
\tag{4.49}
$$

Range from the pivot point along the projected array is given by

$$
x' = x\cos\theta - y\sin\theta.
\tag{4.50}
$$

Figure 4.14 shows the result of projecting the elements of a box array onto a set of virtual linear arrays steered over the range $0° < \theta < 90°$. Each dot on a projected array is one element from the box array. The density of dots indicates the distribution of elements along the length of each projected array. If the projected elements happen to overlap exactly then

157
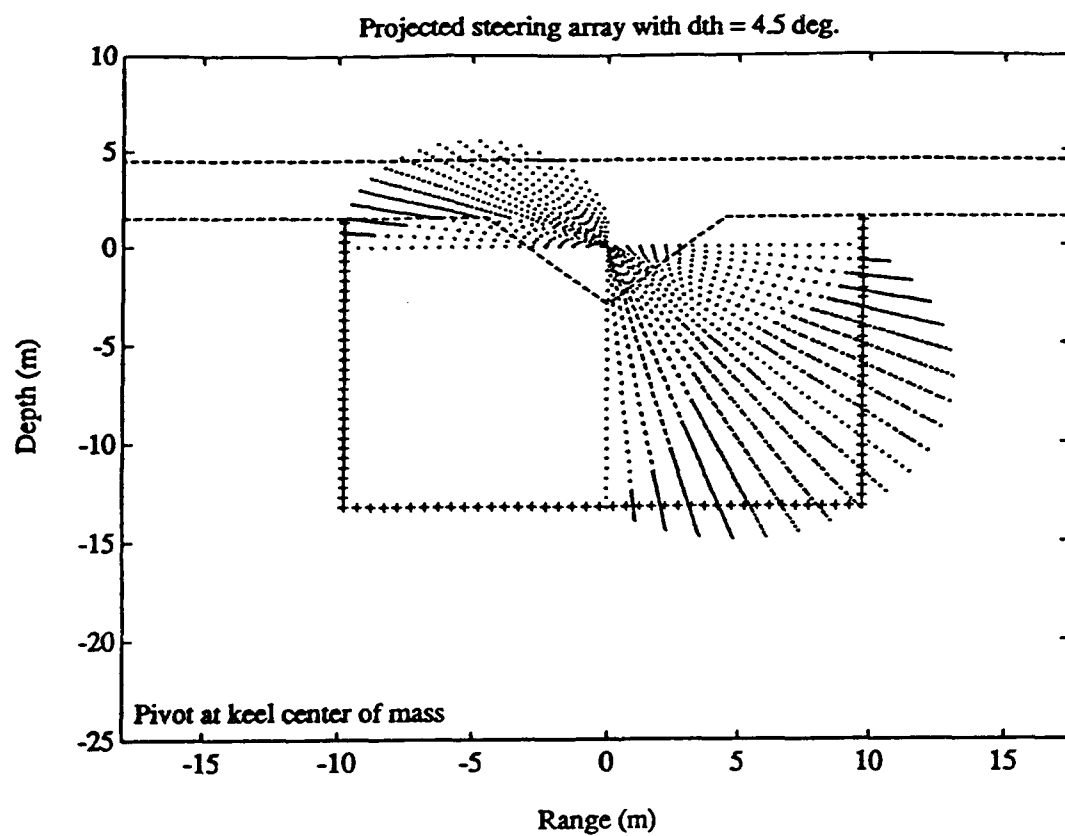
Figure 4.14: Projected arrays at equal increments of 4.5° for 15x20 m box of receivers. The horizontal projected array has a direction cosine of (0,1). The range of steering angles is $0° < \theta < 90°$. Each dot on a projected array corresponds to a receiving element around the perimeter of the box. The distribution of dots indicates the density of receiving elements on a projected array. Each steering angle has a different distribution.
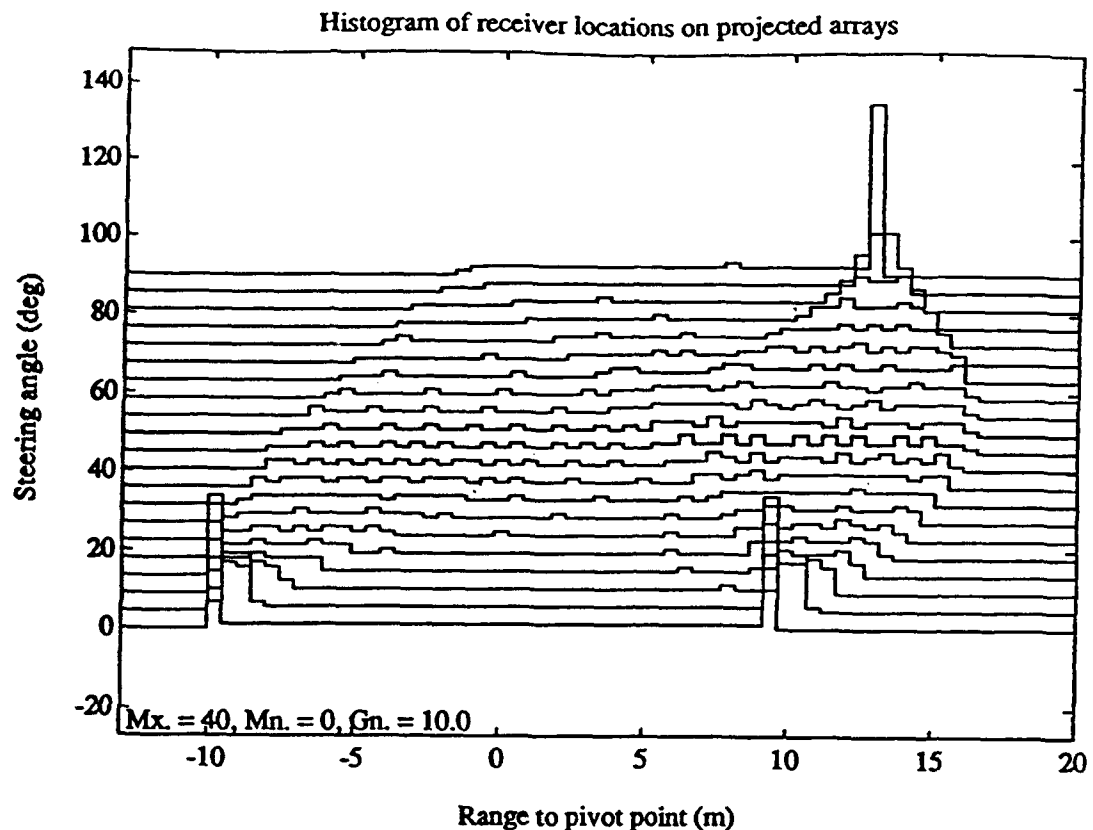
Figure 4.15: Histogram of receiver locations on the projected arrays. The bin size is $0.5\,m$, which is also the element spacing around the perimeter of the box array in Figure 4.14. Only at the steering angles of $\theta = 0°, 90°$ is there a grossly skewed element distribution.

the apparent distribution is less dense than the actual distribution. A more direct measure of the element distribution is shown in the histogram of Figure 4.15. In this example the histogram bins are $0.5\,m$ wide, which is also the receiver element spacing around the perimeter of the box array. Small bins give a detailed view of the element distribution and show, in this case, that only at the steering angles of $\theta = 0°, 90°$ is there an obviously skewed distribution. Elsewhere, the distribution is relatively uniform.

For infinite arrays the distribution of elements is immaterial to the accuracy of the plane wave decomposition. In practice, however, since the aperture is small, a highly skewed distribution further distorts the plane wave estimate by a systematic but unknown

amount. The box array I use only has this problem in a narrow range of angles around $\theta = 0°, \pm 90°, \pm 180°$, and the resulting distortions are accepted as part of the estimation error in the plane wave decomposition.

4.5.3 Characteristics

The character of the Radon transform for linear arrays in Equation (4.44) has been changed in going to the serpentine array and the transform in Equation (4.46). I distinguish these two as a line versus a serpentine Radon transform. In the line Radon transform the array is linear and assumed to be infinite in extent. A finite array is handled by setting the field $\underline{u}(x,t) = 0$ for x outside the array aperture. The serpentine Radon transform of Equation (4.46) has two complicating features: 1) the serpentine array may have different spatial extents for different angles of propagation and 2) there is the possibility that several portions of the serpentine array are projected onto a single region of the virtual linear array. These complications are now considered individually.

Figure 4.16 shows the effect of different spatial extents at different angles of propagation using a circular and an elliptical array of elements as examples. For a plane wave propagating at $\Theta = 90°$ both arrays have the same spatial extent in the y direction and hence have the same angular resolution. By contrast, at $\Theta = 0°$ the circular array has a smaller spatial extent than the elliptical array and hence has a lower intrinsic angular resolution in that direction. Thus, the ability to discriminate simultaneously propagating plane waves with serpentine arrays depends on the angle of propagation and the spatial extent of the serpentine array in those directions. Obviously, a circular array has equal angular resolution in all directions and is the preferred array geometry. In some cases a circular array of sufficient size is impractical and a compromise must be made. The extent to which the array deviates from circularity determines the extent of up-down and left-right ambiguity

160
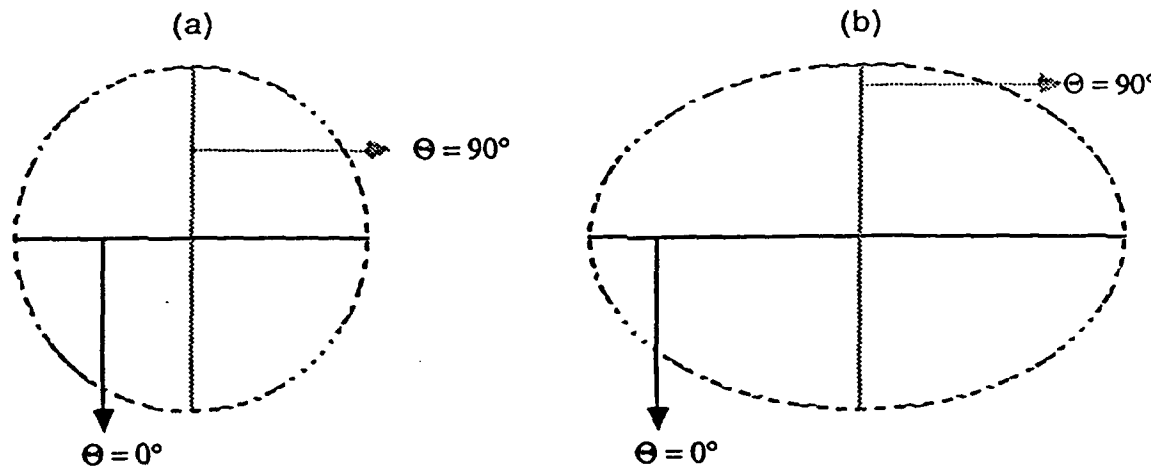
Figure 4.16: Examples of two serpentine arrays and the effect of spatial extent on angular resolution. The circular array (a) has equal angular resolution at all angles of plane wave detection. The elliptical array (b) has higher angular resolution for plane wave propagating in the vertical direction than for those propagating in the horizontal direction.

in the estimation process.

For the ice scattering experiments I have chosen the box array shown in Figure 4.1. This array is about 4λ wide and $\frac{3}{4}\lambda$ deep, where λ is the wavelength in water at $55\,Hz$. Using the $3\,dB$ beamwidth equation for linear arrays, $\theta_{BW} = \frac{0.88\lambda}{L}$, the box array has an angular resolution of about $12°$ in the direction $\Theta = 0°$ and a resolution of about $67°$ in the direction $\Theta = \pm90°$ [58, p. 41].

The second complication with serpentine arrays is that several portions of the array may be projected onto a single region of the virtual array. Refer to Figure 4.16. For all steering angles the two sides of either closed array of receivers, the circle or the ellipse, are projected onto the virtual linear array and contribute to what I call *projection gain*. Similarly, the L-shaped array shown in Figure 4.13 has a different projection gain for the angle $\theta = -45°$ than for $\theta = +45°$. Furthermore, the projection gain correction must be applied element-wise for there may be some portions of the virtual array which have only one part of the physical array projecting on it and others with several parts. Figure 4.17
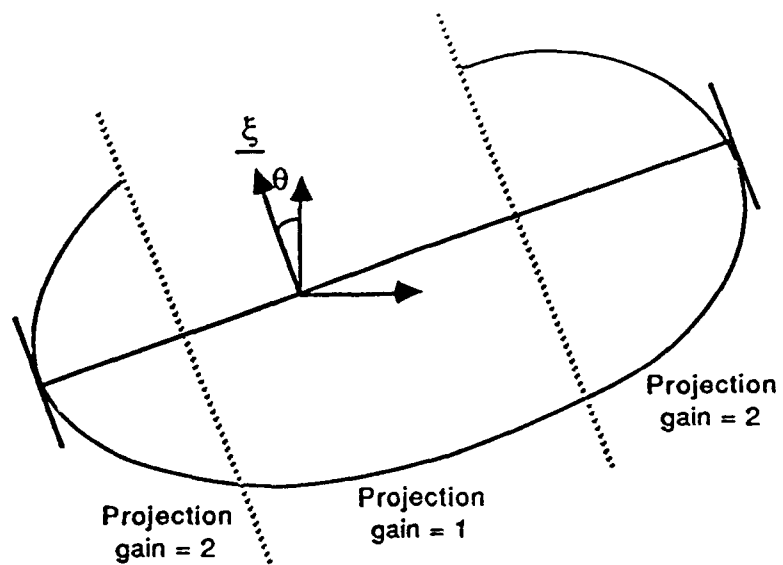
Figure 4.17: Serpentine array showing regions of different projection gain. For the steered angle shown, the projection gain at the ends of the virtual array is 2 while the projection gain in the middle of the virtual array is 1. The projection gain is a function of steering angle and array element position.

shows an example of this effect. Since the serpentine Radon transform I implement only applies to discrete arrays, I have developed a discrete method to correct for the projection gain[†]. The discrete problem is handled by

1. computing the projected location of each serpentine array element onto the virtual array,

2. sorting the projected array elements in monotonically increasing order based on the range variable $x'(\theta)$,

3. computing the inter-element spacing of the sorted array, and

4. using the inter-element spacing in a trapezoidal integration scheme to estimate the plane wave component at the selected propagation angle.

[†]Continuous apertures can be handled in a slightly different way based on the density of sensing elements on the projected array.

162

Transform	Correspondence
Fourier – temporal	$u(x,t) \rightleftharpoons \hat{u}(x,\omega)$
Fourier – spatial	$u(x,t) \rightleftharpoons \check{u}(k,t)$
Radon	$u(x,t) \rightleftharpoons \tilde{u}(p,\tau)$

Table 4.2: Table of notation for Fourier and Radon transforms

This procedure corrects for the projection gain that occurs if each element in the summation is given an equal weight of dS. Thus, the projection gain correction $A(\underline{x},p)$ in Equation (4.46) adjusts the length of dS for each element of the discrete array. Further, $A(\underline{x},p)$ does not, in general, have a closed form and the implementation of the serpentine Radon transform in Equation (4.46) must be stated algorithmicly as above.

Regardless of the receiving array geometry, linear or serpentine, the Radon transform may be thought of as a plane wave beamformer. The data from the receiving elements are projected by phase shifting onto a virtual linear array steered in the direction $\theta = \sin^{-1} pc$. The phase shifted data are then integrated along the projected array to yield an estimate of the plane wave component in the steered direction. The pivot point about which the projected arrays are rotated determine the reference point at which the estimated plane waves are measured. For the analysis of the scattered field, the pivot point is typically the scatterer's center of mass. This choice facilitates the interpretation of the scatterer as a plane wave source launching angle dependent energy into the water.

The next several pages make use of Fourier transforms, both temporal and spatial, and the Radon transform. To facilitate writing the equations I make use of the transform notation shown in Table 4.2.

It is convenient to compute the plane wave decomposition of Equation (4.46) in the frequency domain. Specifically, using the Fourier transform pair

$$\underline{u}\left(x, t + t_o\right) \overset{\text{F.T.}}{\rightleftharpoons} \hat{\underline{u}}\left(x, \omega\right) e^{+i\omega t_o}, \tag{4.51}$$

Equation (4.46) is written

$$\tilde{\underline{u}}(p,\tau) = \frac{1}{2\pi} \int_\omega \int_{\underline{x}_o} A(\underline{x},p) \overbrace{\hat{\underline{u}}(\underline{x},\omega)}^{\text{FFT}} \overbrace{e^{i\omega\underline{p}\cdot\underline{x}}}^{\text{phase shift}} \underbrace{dS\, e^{i\omega\tau}\, d\omega,}_{\text{trapezoidal quadrature}} \qquad (4.52)$$

$$\underbrace{\phantom{\frac{1}{2\pi} \int_\omega \int_{\underline{x}_o} A(\underline{x},p) \hat{\underline{u}}(\underline{x},\omega) e^{i\omega\underline{p}\cdot\underline{x}} dS\, e^{i\omega\tau}\, d\omega}}_{\text{IFFT}}$$

where the over and under braces indicate how the transform is actually computed.

In anticipation of discussing energy integrals in the next section, I present several useful relations based on the Radon transform definitions and the temporal and spatial Fourier transform. The serpentine Radon transform, Equation (4.46), for an infinite continuous planar array may be written

$$\tilde{\underline{u}}(p,\tau) = \int_{\underline{x}} \underline{u}(\underline{x},\tau + \underline{p}\cdot\underline{x})\, d\underline{x}. \qquad (4.53)$$

The projection gain correction, $A(\underline{x},p)$, is dropped since it is a constant scale factor for all p and $\underline{x}$ due to the infinite continuous nature of the aperture and the implied normalization of the transform. The temporal Fourier transform of Equation (4.53) is

$$\hat{\tilde{\underline{u}}}(p,\omega) = \int_{\underline{x}} \hat{\underline{u}}(\underline{x},\omega) e^{i\omega\underline{p}\cdot\underline{x}}\, d\underline{x}, \qquad (4.54)$$

where the arguments of $\hat{\tilde{\underline{u}}}$ depend on how the transformed space is viewed. For a 1-D process Figure 4.18 shows the relationship between ω, ξ, and p diagrammatically. A similar picture applies for 2-D processes but is much harder to draw and visualize. Because of the relationship between ω, ξ, and p, Equation (4.54) leads to the following equivalence

$$\begin{aligned}
\hat{\tilde{\underline{u}}}(p,\omega) &= \int_{\underline{x}} \hat{\underline{u}}(\underline{x},\omega) e^{i\omega\underline{p}\cdot\underline{x}}\, d\underline{x} \\
&= \int_{\underline{x}} \hat{\underline{u}}(\underline{x},\omega) e^{i\underline{\xi}(\underline{p})\cdot\underline{x}}\, d\underline{x} \\
\hat{\tilde{\underline{u}}}(p(\xi),\omega) &= \check{\underline{u}}(\xi(p),\omega), \qquad (4.55)
\end{aligned}$$
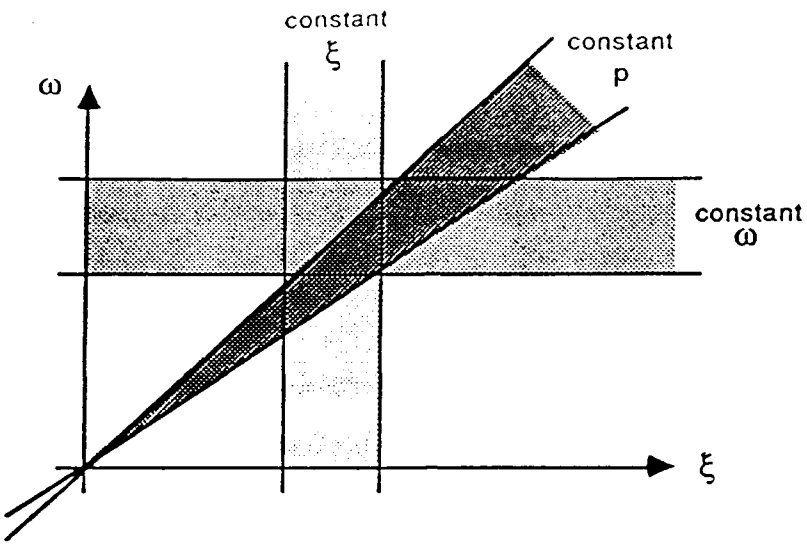
Figure 4.18: Relationship between ω, ξ, and p. This is the dual to $(x\text{-}t)$ space and may be thought of as the wavenumber-frequency space, $(\xi\text{-}\omega)$, or the slowness-frequency space, $(p\text{-}\omega)$. Lines of constant ω, ξ and p are shown. Given any two of the variables, the third is known since $\xi = \omega p$.

where I have used the spatial Fourier transform definition

$$\breve{\underline{u}}(\xi, t) \equiv \int_{\underline{x}} \underline{u}(\underline{x}, t) e^{i\underline{\xi} \cdot \underline{x}} \, d\underline{x} \tag{4.56}$$

and the relation between wavenumber and slowness $\underline{\xi} = \omega \underline{p}$. For propagating modes, the scalar arguments p and ξ in Equation $(4.55)^3$ are the horizontal component of the corresponding real vector quantity computed using Equation (4.45) for slowness and a similar expression for wavenumber.

4.5.4 Energy theorems

In this section I present two energy theorems. The first is a corollary to Parseval's theorem for Radon transformed variables, and the second has to do with plane wave energy flux. These theorems are needed to calibrate estimates of the angular energy flux distribution of the scattered field.

Corollary to Parseval's theorem

I start with Parseval's theorem for a propagating scalar space-time signal in two dimensions and its double Fourier transform,

$$\int_t \int_{\underline{x}} |u(\underline{x},t)|^2 \, d\underline{x} \, dt = \frac{1}{(2\pi)^3} \int_\omega \int_{\underline{\xi}} |\overset{\vee}{u}(\underline{\xi},\omega)|^2 \, d\underline{\xi} \, d\omega. \qquad (4.57)$$

The integral over $\underline{\xi}$ on the right is correct, strictly speaking, but since wave propagation is governed by a finite propagation speed, the integrand $|\overset{\vee}{u}(\underline{\xi},\omega)|^2$ is non-zero only for the vector values of

$$\underline{\xi} = \begin{pmatrix} \xi \\ \pm[(\frac{\omega}{c})^2 - \xi^2]^{\frac{1}{2}} \end{pmatrix} \equiv \begin{pmatrix} \xi \\ \eta_o \end{pmatrix}. \qquad (4.58)$$

Thus, the integrand may be written

$$|\overset{\vee}{u}(\underline{\xi},\omega)|^2 = 2\pi |\overset{\vee}{u}(\xi,\omega)|^2 \delta(\eta - \eta_o), \qquad (4.59)$$

where the horizontal wavenumber, ξ, ranges over $\pm(\frac{\omega}{c})$ for propagating modes and the vertical wavenumber $\eta_o \in \pm[(\frac{\omega}{c})^2 - \xi^2]^{\frac{1}{2}}$. The factor of 2π on the right is to convert the inverse length units of the delta function to radial measure. Using Equation (4.59) in Equation (4.57) leads to the modified form

$$\int_t \int_{\underline{x}} |u(\underline{x},t)|^2 \, d\underline{x} \, dt = \frac{1}{(2\pi)^2} \int_\omega \int_\xi |\overset{\vee}{u}(\xi,\omega)|^2 \, d\xi \, d\omega. \qquad (4.60)$$

For real ω, the change of variables $\xi = \omega p$ leads to

$$\int_t \int_{\underline{x}} |u(\underline{x},t)|^2 \, d\underline{x} \, dt = \frac{1}{(2\pi)^2} \int_\omega \int_p |\omega| |\overset{\hat{\vee}}{u}(p,\omega)|^2 \, dp \, d\omega, \qquad (4.61)$$

where Equation (4.55)[3] has been used on the right. The absolute value of ω is required so that the limits of integration for p are always $\pm\infty$, as opposed to $\mp\infty$, regardless of the sign of ω. Equation (4.61) is the desired corollary to Parseval's theorem.

Plane wave energy flux

Parseval's theorem is commonly used to show that so-called energy in $\underline{x}$-t space is equivalent to energy in ξ-ω space. The units of Equation (4.61), however, are not energy. I am concerned with a true energy equivalence between $\underline{x}$-t space and p-ω space. To develop the equivalence I start with the simple case of a linear array. The total energy inflow across a linear array is given by

$$E = \int_t \int_x \sigma_{ij} v_j n_i \, dx \, dt = n_i \int_t \int_x \sigma_{ij} v_j \, dx \, dt, \qquad (4.62)$$

where the direction cosine, n_i, is moved outside the integral since it is constant along the entire array. Now, I represent the stress and velocity terms using their double Fourier transforms, as for the stress,

$$\sigma_{ij}(x,t) = \frac{1}{(2\pi)^2} \int_\omega \int_\xi \breve{\sigma}_{ij}(\xi,\omega) e^{i\omega t} e^{-i\xi x} \, d\xi \, d\omega. \qquad (4.63)$$

Using this equation and the comparable one for velocity in Equation (4.62) gives

$$
\begin{aligned}
E &= \frac{n_i}{(2\pi)^4} \int_\omega \int_\xi \int_{\omega'} \int_{\xi'} \breve{\sigma}_{ij}(\xi,\omega) \breve{v}_j(\xi',\omega') \underbrace{\int_t e^{i(\omega+\omega')t} \, dt}_{2\pi\delta(\omega+\omega')} \underbrace{\int_x e^{-i(\xi+\xi')x} \, dx}_{2\pi\delta(\xi+\xi')} \, d\xi' \, d\omega' \, d\xi \, d\omega, \\
&= \frac{n_i}{(2\pi)^2} \int_\omega \int_\xi \breve{\sigma}_{ij}(\xi,\omega) \underbrace{\breve{v}_j(-\xi,-\omega)}_{\breve{v}_j^{\,*}(\xi,\omega)} \, d\xi \, d\omega, \qquad (4.64)
\end{aligned}
$$

where $(\cdot)^*$ is the complex comjugate of $(\cdot)$. The equivalence $\breve{v}_j(-\xi,-\omega) = \breve{v}_j^{\,*}(\xi,\omega)$ is due to the fact that $v_j(x,t)$ is real. Using the substitution $\xi = \omega p$ and Equation (4.55)[3] leads to the true energy inflow theorem for 1-D arrays

$$E = \int_t \int_x \sigma_{ij} v_j n_i \, dx \, dt = \frac{n_i}{(2\pi)^2} \int_\omega \int_p |\omega| \hat{\sigma}_{ij}(p,\omega) \hat{v}_j^{\,*}(p,\omega) \, dp \, d\omega. \qquad (4.65)$$

167

The sign of the energy inflow for a linear array is determined by which side of the array the outward pointing normal is chosen. When the direction of propagation and the chosen normal are in the same direction, the energy inflow is negative, a net energy outflow, for waves with group velocity and phase velocity of the same sign. Note the similarity of the true energy inflow theorem, Equation (4.65), to the corollary to Parseval's theorem, Equation (4.61).

The left most integral in Equation (4.65) is insensitive to energy propagation direction. The integral over slowness on the right, however, implicitly carries this information in the relationship between p and θ, namely $p(\theta) = \frac{\sin\theta}{c}$. The slowness-frequency functions $\hat{\sigma}_{ij}$ and $\hat{v}_j$ are commonly computed from measurements taken along the linear array under consideration. This, however, is not a requirement. The functions exist independently of any measurement array. Suppose for the moment the slowness-frequency functions for stress and velocity are known a priori. The direction cosine, n_i, on the right, then, specifies the angle of repose of the physical array used to compute the energy inflow on the left. Moreover, since $\hat{\sigma}_{ij}$ and $\hat{v}_j$ are assumed to be known, a change of n_i to n_i' on the right gives the energy inflow across a different, though not necessarily physical, linear array, this one steered in the direction n_i'. Thus, a knowledge of the slowness-frequency functions $\hat{\sigma}_{ij}$ and $\hat{v}_j$ is all that is required to determine the energy inflow across any physical or virtual linear array with a specified pivot point.

Finally, if only the energy propagating in the n_i' direction is of interest, that is energy flowing normal to the chosen physical or virtual array, then only the slowness corresponding to $p = \frac{1}{c}n_i'$ or $p = \frac{1}{c}n_1'$ need be considered. Energy flowing at normal incidence to the array steered to n_i' is then

$$E(n'_i) = dp \frac{n'_i}{(2\pi)^2} \int_\omega |\omega| \hat{\vec{\sigma}}_{ij}(n'_1, \omega) \hat{\vec{v}}_j^*(n'_1, \omega) \, d\omega. \tag{4.66}$$

This is an estimate of the energy inflow in the direction n'_i. Since I am not integrating over n'_i, information contained in Equation (4.65) has been thrown away in going to Equation (4.66), which is simply a tabulation of the energy inflow estimates for a given direction n'_i.

In practice, I compute the values of $p(\theta)$ at equal increments of θ. Using

$$dp \mid_{\text{broadside}} = d(\frac{\sin\theta}{c}) \mid_{\text{broadside}} = (\frac{\cos\theta}{c} \, d\theta) \mid_{\text{broadside}} = \frac{\Delta\theta}{c}, \tag{4.67}$$

the semi-discrete equivalent to Equation (4.66) becomes

$$E(n'_i) = \frac{\Delta\theta \, n'_i}{c(2\pi)^2} \int_\omega |\omega| \hat{\vec{\sigma}}_{ij}(n'_1, \omega) \hat{\vec{v}}_j^*(n'_1, \omega) \, d\omega. \tag{4.68}$$

Recall, Equation (4.66) was developed assuming a priori knowledge of the slowness-frequency spectra $\hat{\vec{\sigma}}_{ij}(p, \omega)$ and $\hat{\vec{v}}_j(p, \omega)$. These spectra are, of course, not known and must be estimated from the measured data. Using data collected with the box array shown in Figure 4.1 the required slowness-frequency spectra are computed using Equations (4.52) and (4.54), which is equivalent to not taking the inverse Fourier transform in Equation (4.52). The errors associated with estimating the slowness-frequency spectra in this way are considered in the next section.

The last step in estimating the average energy flux, $\bar{\mathcal{E}}(n'_i)$, around the scatterer is to divide the energy inflow in each direction by the projected array length in that direction. Here I am explicitly invoking the beamformer normalization factor that was discussed earlier. Specifically,

$$\mathcal{E}\left(n'_i\right) = \frac{E(n'_i)}{\int dx'},$$ (4.69)

where the numerator is simply the projected array length. The quantity $\mathcal{E}\left(n'_i\right)$ is an estimate of the plane wave energy flux of the scattered field in the direction n'_i.

A negative energy flux in the direction n'_i indicates that the scatterer is injecting scattered incoherent energy in that direction. A positive energy flux in the direction n'_i indicates that the scatterer is drawing energy out of the coherent field in that direction. Note that positive energy flux implies negative group velocity. In other words, the wave propagates in the direction n'_i but delivers energy in the direction $-n'_i$. The appearance of negative group velocity is due to the cross terms between the scattered field and the coherent field. Energy extracted from the forward propagating coherent field travels backward to the scatterer even while the scattered pressure field is traveling forward.

Fields with negative group velocity cannot be measured in a physical experiment, but rather, are derived fields. They describe the effect of the scatterer on the coherent, forward propagating field. In the physical experiments the total fields always have positive group velocity. An example of this effect is shown in Figure 4.19.

4.5.5 Array calibration

The receiver array shown in Figure 4.1 is the standard array I use in all the scattering experiments in the next chapter. The array is about 4λ wide and $\frac{3}{4}\lambda$ deep, where λ is the water wavelength at $55\,Hz$. It should be clear that resolution will be better near $\Theta = 0°$ than near $\Theta = \pm90°$. Figure 4.20 shows the projected array length for all projection angles $\Theta \in [\pm180°]$. The maximum array length and hence maximum resolution occurs at $\Theta \simeq \pm9°$. To estimate the resolution performance of this array I present two calibration

170
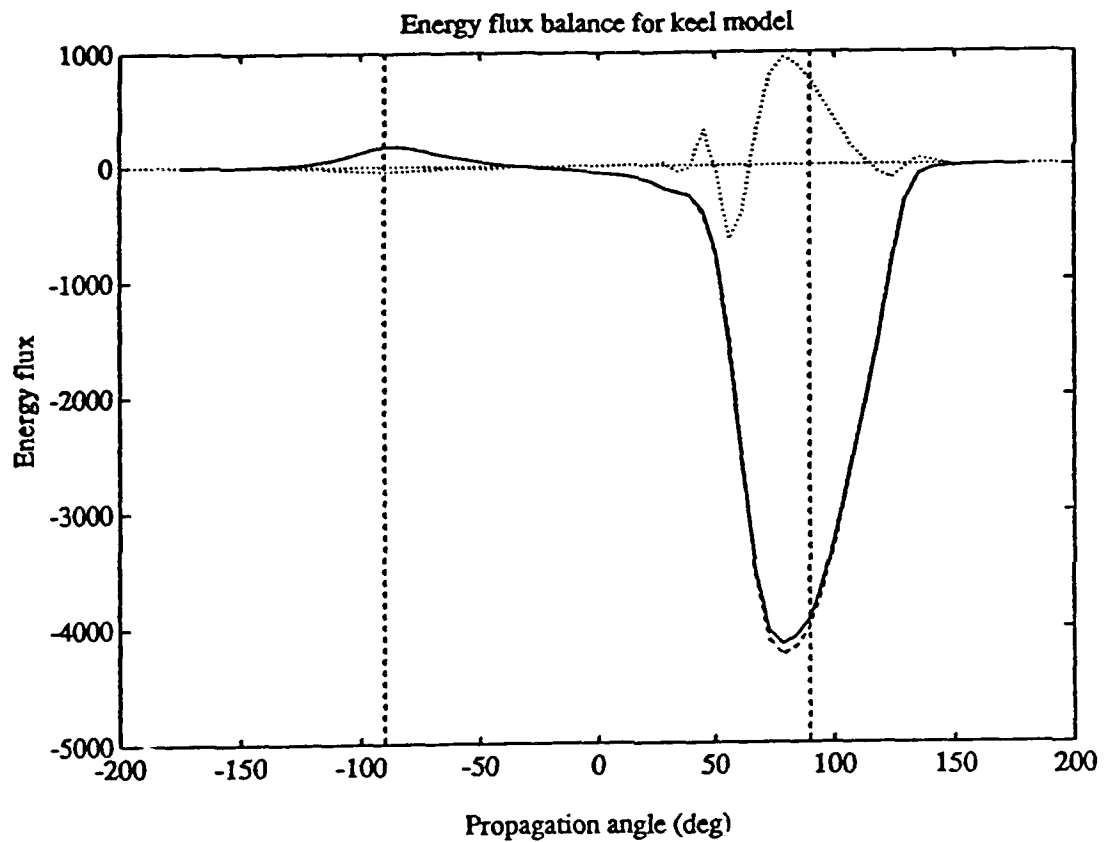
Figure 4.19: Energy flux estimate versus propagation angle. The dashed curve is the energy flux of the total field from the coherent experiment. The solid curve is from the scatter experiment. Both always have negative energy flux, except near the side lobe at $\Theta = -90°$, and hence have forward group velocity. The dotted curve, however, is the energy flux of the scattered field and is positive for some angles. In these directions energy is extracted from the coherent field to supply the scattered field. (Note that the dotted curve has been multiplied by ten for display purposes.)
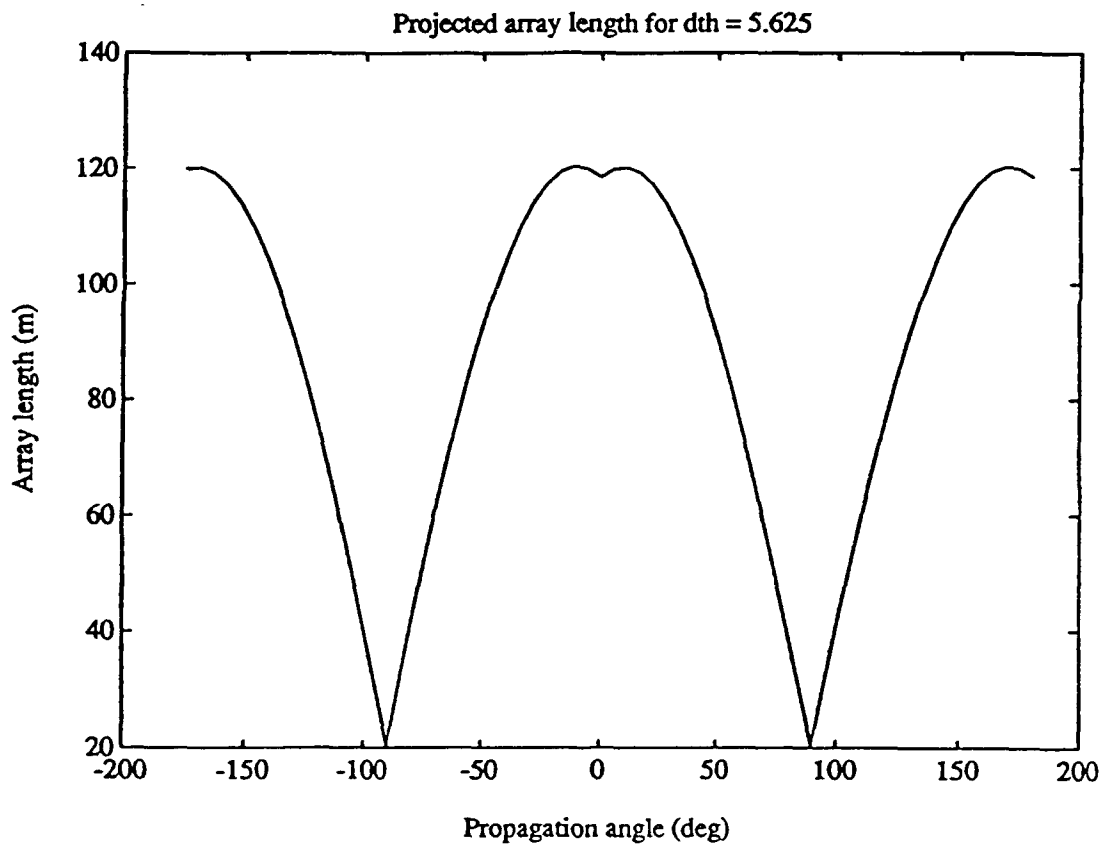
Figure 4.20: Length of projected array vs. steering angles based on the box array geometry used in the scattering experiments. The array has maximum length, and hence, maximum resolution for the vertical propagating waves. Resolution in the horizontal direction is about $\frac{1}{6}$ that in the vertical direction.

experiments. Both involve plane waves propagating across the array, which is assumed to be in homogeneous water. A differentiated Gaussian pulse shape with a center frequency of 55 Hz is used for the plane wave time series. The two cases are for plane waves propagating at 1) the intermediate angle of $\Theta = 54°$ and 2) the near grazing angle of $\Theta = 83°$. The projected array length at these angles is 85 m and 34 m, respectively. Figure 4.21 shows the normal stress time series measured at a decimated set of receiver locations around the box array. The slowness-frequency spectra of the stress and velocity are computed using Equation (4.52) without the inverse Fourier transform, then the average energy flux is computed using Equations (4.68) and (4.69). The results are shown in Figure 4.22. The variable angular resolution of the array is clear. To quantify the width of the main lobe for each angle of propagation, I use the projected array length L' in the 3 dB beamwidth equation for linear arrays, $\theta_{BW} = 0.88\lambda/L$, with $\lambda = 27\,m$ corresponding to 55 Hz [58, p. 41]. Specifically, for the plane wave at 54°, the projected array length is 85 m and the beamwidth is estimated to be $\theta_{BW} = 16°$. Similarly, for the plane wave at 83°, the projected array length is only 34 m and the beamwidth should be $\theta_{BW} = 40°$. Measurements from the computed array responses in Figure 4.22 give beamwidths of 20° and 42°, close to the predicted values. The best angular resolution is predicted to occur at $\Theta \simeq \pm 9°$ with a projected array length of about 120 m and a predicted beamwidth of 11° at 55 Hz. Thus, the box array has an angular resolution that varies from about 11° near vertical propagation to more than 40° near grazing.

The estimate of average energy flux also varies over the range of angles. The true energy flux of the plane wave is $-13.12 \times 10^{-5}\,J/m^2$. At a propagation angle of 54° the average energy flux is estimated to be -7.0×10^{-5}, a loss of 2.7 dB. Due to the relatively small depth extent of the array, there is moderate up-down ambiguity indicated by the peak at about 120°. This spurious peak draws energy out of the true peak at 54° which accounts
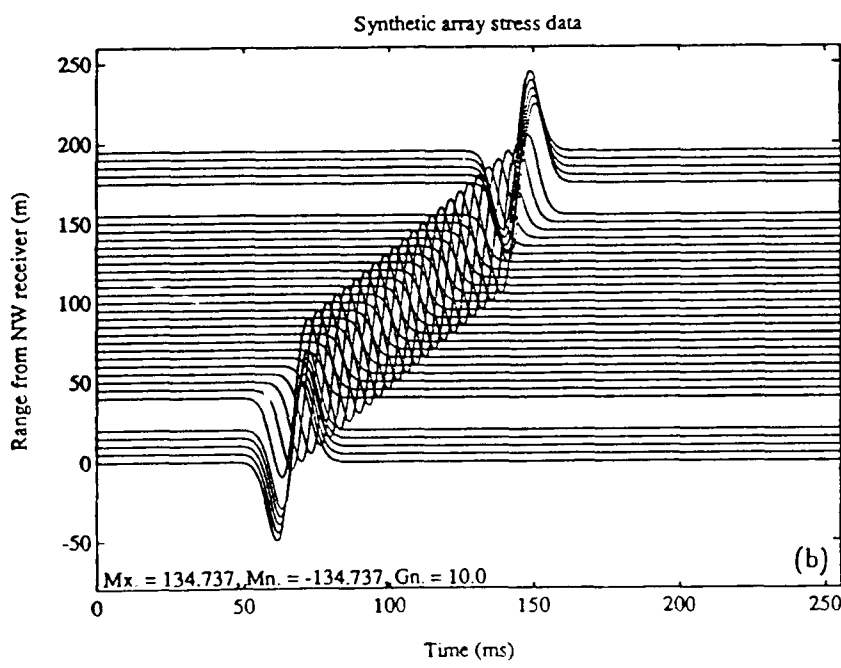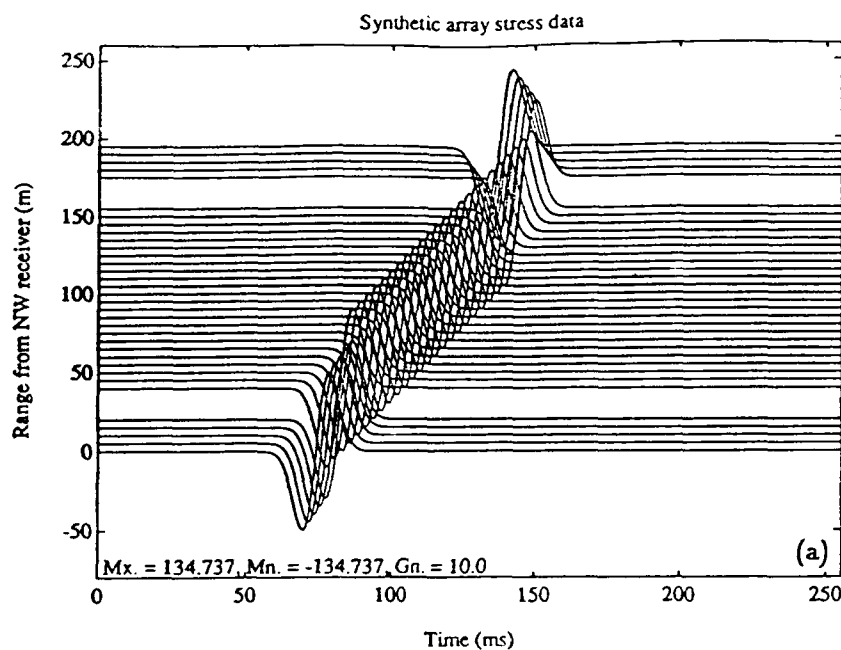
Figure 4.21: Plane wave time series measured by box array at (a) $\Theta = 54°$ and (b) $\Theta = 83°$. A differentiated Gaussian pulse shape is used with a center frequency of 55 Hz.

174
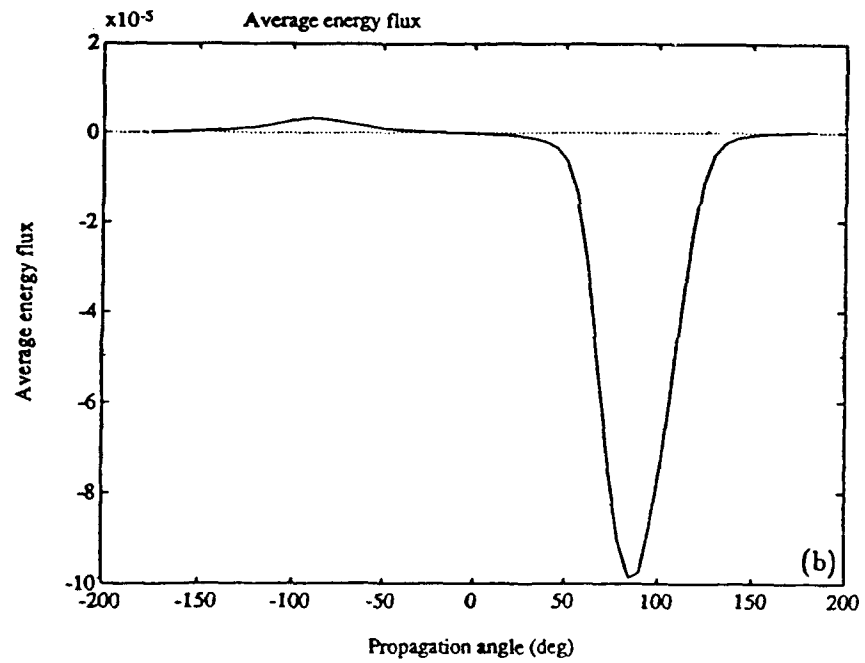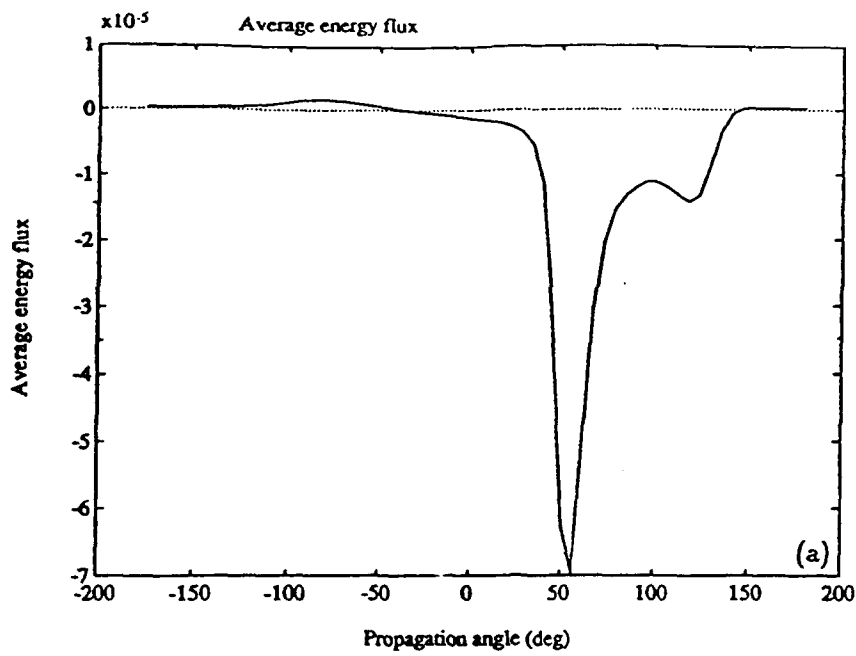
Figure 4.22: The array response of the box array to a plane wave propagating at (a) $\Theta = 54°$ and (b) $\Theta = 83°$. The variable angular resolution of the array is clearly evident. The $54°$ wave is detected with a resolution of about $20°$ while the nearly grazing wave at $83°$ is detected with a resolution of about $42°$. The up-down ambiguity of the box array is seen in (a), where a spurious detection peak occurs at about $120°$. This peak removes energy from the true peak at $54°$ and causes a bias in the energy estimate.

Prop. Angle, Θ	0	54°	83°
Resolution, θ_{BW}	$\sim 11°$	16°	40°
Energy flux error (dB)	~ -3	-2.7	-1.2

Table 4.3: Summary of the $4\lambda \times \frac{3}{4}\lambda$ box array characteristics derived from the two calibration experiments. This information is used to make quasi-quantitative calibration corrections to the angular energy flux estimates of the scattered field. More rigorous corrections would require deconvolving the energy estimates to remove the effects of the array response.

for some of the reduction in amplitude. There is only slight left-right ambiguity as evidence by the small peak near $-80°$. The 4λ width of the array is sufficiently long to effectively suppress this ambiguity.

For the 83° case, the average energy flux estimate is -9.9×10^{-5} or a loss of about 1.2 dB. There is less apparent up-down ambiguity due to the near grazing propagation angle and the loss in amplitude is due primarily to the loss of angular resolution. Again, the small left-right ambiguity near $\Theta = -80°$ is present.

It is evident that the array response may introduce errors of up to 3 dB in the estimate of the average energy flux for plane waves propagating at vertical angles. Calibrated angular estimates of energy flux would require deconvolving the raw estimates with the array response for all angles of propagation. This is a non-trivial undertaking and I am leaving this for future research, being content here with the raw estimate. However, the two calibration experiments presented in this section provide guidelines on how to interpret the raw estimates and improve the results in a quasi-quantitative way. Table 4.3 summarizes the essential characteristics of the $4\lambda \times \frac{3}{4}\lambda$ box array. As an example on how the information in Table 4.3 might be used, consider the scattered energy flux response for the illustrative example shown in Figure 4.23. There are two features worthy of analysis; the large negative peak near 50°, denoted Peak 1, and the large positive peak near 80°, denoted Peak 2. In terms of their resolution, these features are similar to the peaks in the calibration experi-

Scattered energy flux for keel model
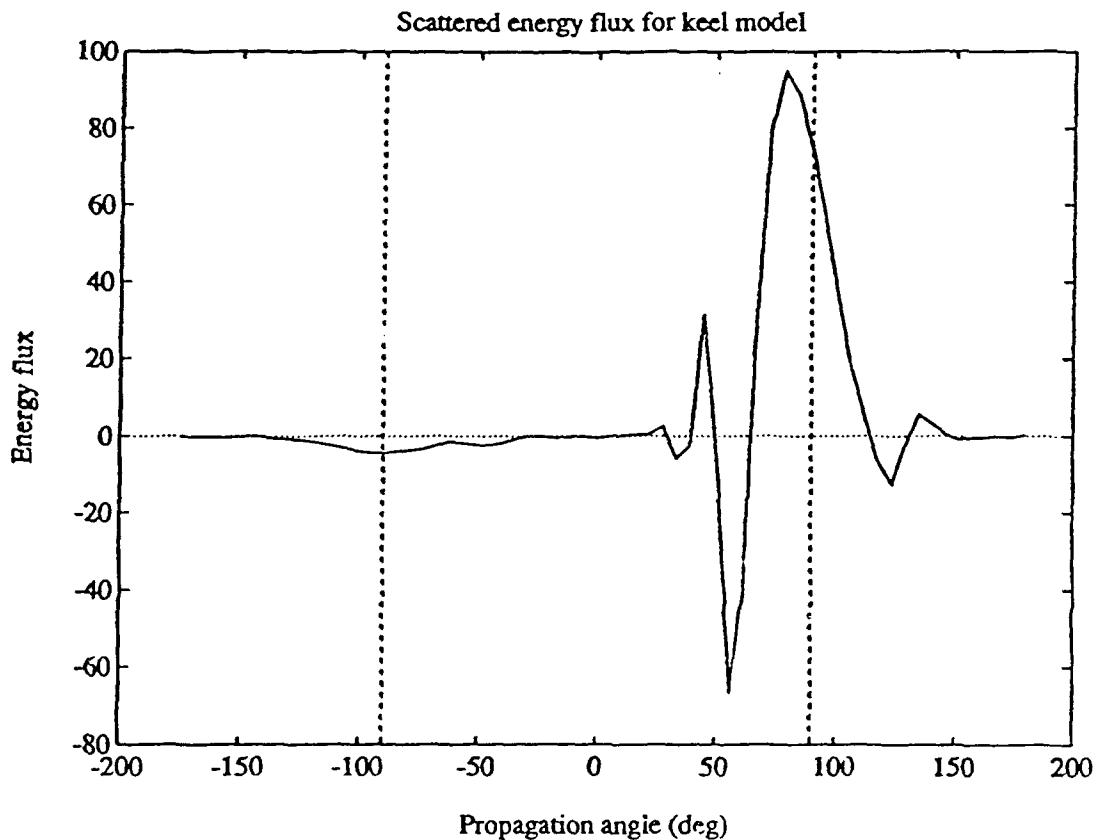
Figure 4.23: Scattered energy flux vs. angle for the keel model shown in Figure 4.1. Two prominent events are present: the negative peak near 50°, denoted Peak 1, and the positive peak near 80°, denoted Peak 2. Using the calibration information in Table 4.3 the amplitude of the two peaks is corrected to yield the result that Peak 1 and 2 have approximately the same absolute amplitude, about 120-125 J/m^2. Also, the angular resolution of the two peaks indicates that the scattered response is do .inated by two nearly plane wave components, Peak 1 is a scattered incoherent field injected into the propagating field and Peak 2 is an energy deficit in the coherent field. Peak 1 leads to a increase in background noise and Peak 2 attenuates the coherent forward propagating signal.

ments. The keel is apparently generating a scattered plane wave near 50° and a plane wave deficit in the coherent field near 80°. Adjusting the amplitudes of these two peaks using the information in Table 4.3 indicates that both peaks have an absolute average energy flux of about 120-125 J/m^2.

4.6 Summary

The following points summarize the important developments of this chapter.

- The recorded signals are horizontal and vertical velocity, v_1 and v_2, and the three stress components, horizontal and vertical normal stress, σ_{11} and σ_{22}, and shear stress, σ_{12}. The signals are measurements of the total field excited by the source and contain the direct, reflected, and scattered components. The signals may be recorded as time series or snapshots depending on the need.

- Derived signals are computed from the recorded signals. The derived signals include the scattered fields, both velocity and stress, and the plate wave components, flexural and longitudinal, excited in the ice sheet.

- Power flux, ϕ_i, for total field quantities is computed as

$$\phi_i = -\sigma_{ij} v_j \tag{4.70}$$

and energy flux is computed as

$$\mathcal{E}_i = \int_t \phi_i \, dt. \tag{4.71}$$

- Power and energy flux for the scattered field involve cross term. They are, however, conveniently computed as

$$\underline{\phi} s = \underline{\phi} T_s - \underline{\phi} T_c, \tag{4.72}$$

where $\underline{\phi}_S$ is the scattered power flux, $\underline{\phi}_{T_s}$ is the total power flux for the scatter experiment, and $\underline{\phi}_{T_c}$ is the total power flux for the coherent experiment. A similar expression applies for energy flux.

- The power and energy flux for the flexural and longitudinal plate waves cannot be computed so conveniently; the cross terms must be explicitly included. Equation (4.35) gives the exact expression.

- A global energy balance is stated in Equation (4.40). It is shown that in the absence of added dissipation, the scattered energy inflow in the water is exactly balanced by the scattered energy inflow in the ice; one is positive, the other is negative, and the two sum to zero. Added dissipation complicates this interpretation by introducing a distributed energy sink at the ice-water and ice-air interfaces.

- The angular dependence of the scattered field is computed using an extension to the Radon transform applicable to serpentine arrays. This transform computes the plane wave decomposition of a field measured on serpentine arrays and is equivalent to a linear beamformer.

Chapter 5

Scattering experiments

5.1 Overview

This chapter marks the beginning of the rough ice scattering study. The ultimate goal in doing scattering experiments is to gain insight into the physical mechanism of the scattering process. This goal is achieved by recording velocity and stress components of the acoustic and elastic fields during the numerical experiment, then manipulating and transforming them into forms which are more easily interpreted. It is important to design the models and experiments carefully. If well designed, the experimental data can be used to increase our understanding of the scattering process. Furthermore, the selected models must reflect the diversity of roughness features actually found in the Arctic.

In Section 5.2, a discussion of the types of roughness features and corresponding idealized models is given. Once the model is defined, the primary objective of the experimental design is to ensure that the scatterer is excited by a plane wave and to create a dataset that only requires farfield processing. The experimental design philosophy is discussed in Section 5.3. Once the experiment is designed and executed, the results are used to identify the scattering mechanism and characterize the specular scattering loss in terms

of magnitude and frequency dependence. Section 5.5 discusses the scattering mechanisms associated with each of the idealized models developed in Section 5.2. We will see that the specular energy loss, L_e, is dependent on frequency with the relationship $L_e \propto f^{\alpha}$. The exponent α is determined by the type of scattering object. Both the exponent α and the magnitude of the loss are discussed in Section 5.5 for a variety of scattering objects. As reviewed in Chapter 1 the observed value of α in field data is about $\frac{3}{2}$ while the computed value of α using the method of small perturbations is about 3. One result of this chapter is to suggest a scattering mechanism which agrees with the field data, i.e., $\alpha \simeq \frac{3}{2}$.

5.2 Arctic ice formations

Since any given ray in a long-range propagation path encounters the rough ice surface many times, a fundamental understanding of the scattering process must begin with an adequate description of the roughness elements themselves. Kovacs and Mellor [28] provide a revealing description, with photographs, of typical ice formations in three Arctic zones: the shore fast ice zone, the seasonal transition zone, and the central polar pack ice zone. In long-range propagation the acoustic paths are concentrated in the central polar pack ice zone, where two broad classes of formations play a role in acoustic scattering: pressure ridges and leads. These formations are reviewed here and representative idealized models are introduced for use in the numerical scattering experiments discussed in Section 5.4.

5.2.1 Pressure ridges

When differential compressive forces arise from wind and ocean currents, masses of pack ice are forced together. The motion is approximately normal to the line of contact for
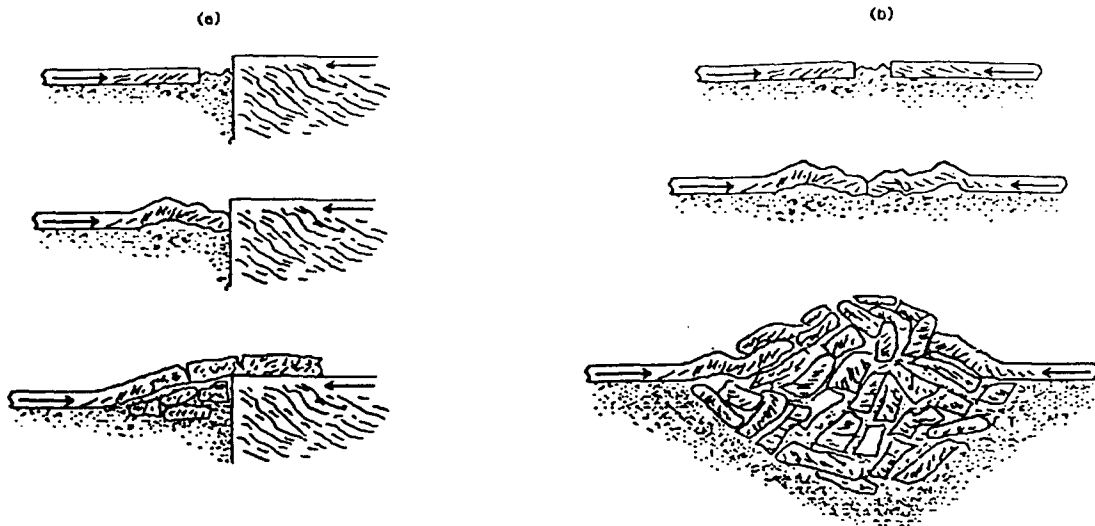
Figure 5.1: Rafted and ridged ice formation. (a) Rafted ice formations occur when two ice sheets of different thickness are forced together. There is little subsurface expression and only modest surface expression. Acoustic scatter from such a formation is dominated by the impedance contrast due to the truncation of the thicker ice sheet and the added mass of the rafted section. (This figure is similar to Figure 22 in Kovacs and Mellor [28].) (b) Pressure ridges occur when two ice sheets of comparable thickness are forced together. There is significant surface and subsurface expression to such formations with the ratio of keel to sail height being around 1:5 [72]. As is shown later, pressure ridges are the dominant scattering object in the Arctic.

compressional ridges[†]. In this situation one of two ice formations may develop: rafted ice and pressure ridges. Figure 5.1 shows the development of these formations schematically. Rafting occurs if thin ice is forced against thick ice. The thin ice fails in flexure and the edge is subsequently thrust up onto the thicker ice. This formation has small surface relief and almost no underwater relief. Acoustic scattering from such a formation is dominated by the effects of the thick, truncated ice sheet and hence is similar to the ice edge model discussed below. The added mass of the rafted section also results in scatter, but because of the relative thinness of the rafted plate, this is probably a small effect.

[†]Shear ridges are formed with motion that is approximately tangential to the line of contact. The ridges can be quite large and have lower porosity than compressional ridges [28].

Pressure ridges occur when two ice sheets of comparable thickness are forced together. In this case the leading edge of both sheets fail and a mass of broken, disoriented ice blocks aggregate along the line of failure. The blocks on the top surface of the pressure ridge, the *sail*, are held in place by gravitational forces, while the blocks on the bottom surface of the ridge, the *keel*, are held in place by buoyancy forces.

When newly formed, pressure ridges have porosity ranging from 10-40% due to their disoriented block structure. The blocks are in contact only at corners and at points along rough edges and are poorly frozen together [73]. Voids between the blocks are free flooding with water below sea level and with air and eventually snow above sea level [72]. This unconsolidated aggregation of ice blocks cannot be strained significantly in shear and hence must have an acoustic response like that of a fluid or a very "soft" solid[†].

During its first year a pressure ridge undergoes a number of changes. Erosional processes above and below the ice approximately halve the height and draft [53]. Furthermore, the interstitial space between the blocks freezes solid below sea level and fills with frozen melt-water above sea level. As a result of these changes, a multi-year pressure ridge has a high shear modulus and behaves acoustically like a solid, reasonably homogeneous, elastic material.

The idealized model for a pressure ridge, then, should consider the effects of age and, by implication, the effects of the internal composition of the pressure ridge as well as its geometry. Figure 5.2 shows two typical pressure ridge models used in the numerical scattering experiments: one for a young or fluid ridge and one for an old or elastic ridge. The material properties of the young or fluid ridge are taken to be $C_p = 3500\,m/s$, $C_s = 0\,m/s$, and $\rho = 910\,Kg/m^3$, while those of elastic ice are the same but with the shear speed set to

---

[†]The notion that composite material properties of ice-water aggregations affect acoustic properties has been demonstrated experimentally by Jezek et al. for high frequency (120, 188 KHz) reflection coefficients [25].
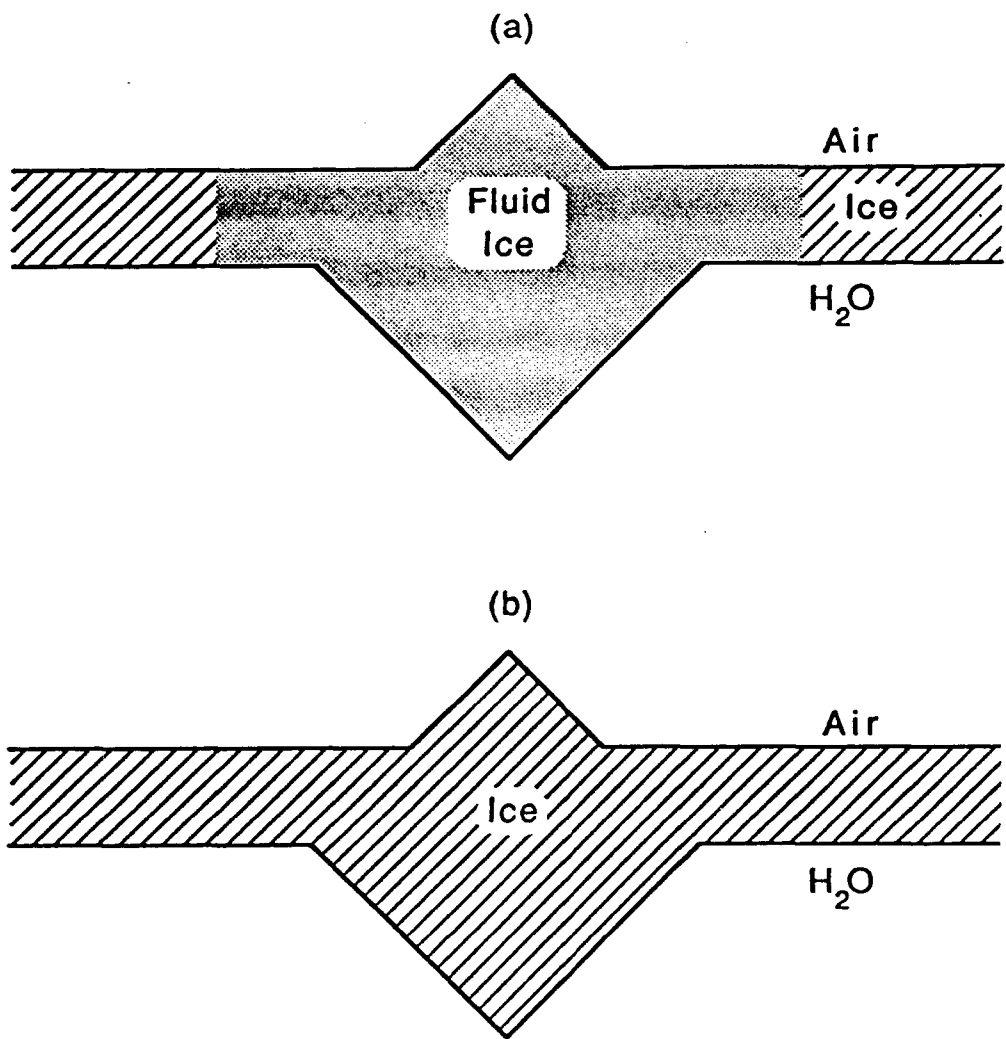
Figure 5.2: Typical pressure ridge models. (a) Young or fluid ridge connected to solid elastic ice sheets. (b) Old or elastic ridge. The ridge sizes are arbitrary as are their shapes, both of which are varied in the numerical experiments discussed in Section 5.4.

184
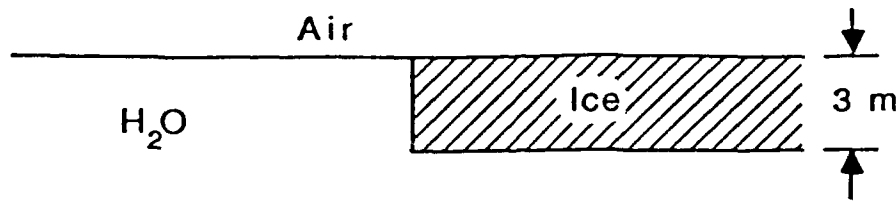
Figure 5.3: Ice edge model. With a free surface to the left and an ice sheet to the right this is the simplest scattering object I consider.

$C_s = 1600\,m/s$.

5.2.2 Leads and polynyas

In contrast to the differential compressive forces which produce pressure ridges, differential tensile forces produce leads and polynyas. These open water formations cover 1-5% of the Arctic Ocean in the winter with coverage as high as 15% in the summer [72]. Open water gaps range in size from virtually zero to tens of kilometers [28]. The fundamental component of a lead or polynya is an ice edge or a truncated ice plate. Figure 5.3 shows the idealized model I use in the numerical scattering experiments. With a semi-infinite free surface adjoining a semi-infinite ice sheet, this is the simplest scattering object I consider.

5.3 Experimental design

As discussed in the previous chapter, 2-D geometry is used in this study. A line source at a depth of $15\,m$ below the air-ice or air-water interface is used to excite an isotropic acoustic field in the water approximately $85\,m$ from the scatterer. Sound generated by the source propagates through the medium and interacts with the surface and the scatterer. The location of the source determines, in part, the complexity of the scattered wave field. For long-range propagation experiments most of the acoustic interactions with the ice are

185

approximately plane wave interactions. This section discusses how the omni-directional line source I use may be located to approximate a plane wave source.

5.3.1 Farfield approximation

For the moment, consider a spatially compact scatterer in an otherwise homogeneous medium. The effects of a surrounding horizontal interface are considered in the next section. As a source moves away from the compact scatterer, the insonifying field becomes more and more like a plane wave. At some point the difference between a true plane wave and the slightly curved wave front of an isotropic source may be ignored. To quantify the range at which this transition takes place requires a statement of permissible error tolerances both in amplitude and phase. A true plane wave has no amplitude or phase variations along a line perpendicular to the direction of propagation. For an isotropic source, the phase and amplitude variations along a line tangent to the wavefront are the quantities of concern. As these variations diminish, the wave front approximates a plane more and more closely. For the scattering experiments, the source is to be placed such that the wave front is approximately planar at the point of interaction with the scatterer. Consider the geometry in Figure 5.4. The length of the scatterer is $D = 2Z$ and the source is placed at a range R. The slant range to the edge of the scatterer is ℓ. In the farfield the pressure, σ, from a line source is of the form

$$\sigma \mid_{\frac{\omega R}{c} \gg 1} \sim \sqrt{\frac{2c}{\pi R \omega}} e^{-i\omega(\frac{R}{c}-t)} e^{i\pi/4}, \tag{5.1}$$

where c is the speed of propagation [15, p. 59]. The farfield, as defined by $R \geq R_f \simeq \frac{10c}{\omega}$, is that zone in which the cylindrically spreading wave behaves like a progressive wave packet without undergoing dispersive effects. Whether or not the field can be considered planar in this zone depends on the length tangent to the wave front over which the field is sampled. The scatterer is, in effect, sampling the curved field. The question is how far from the
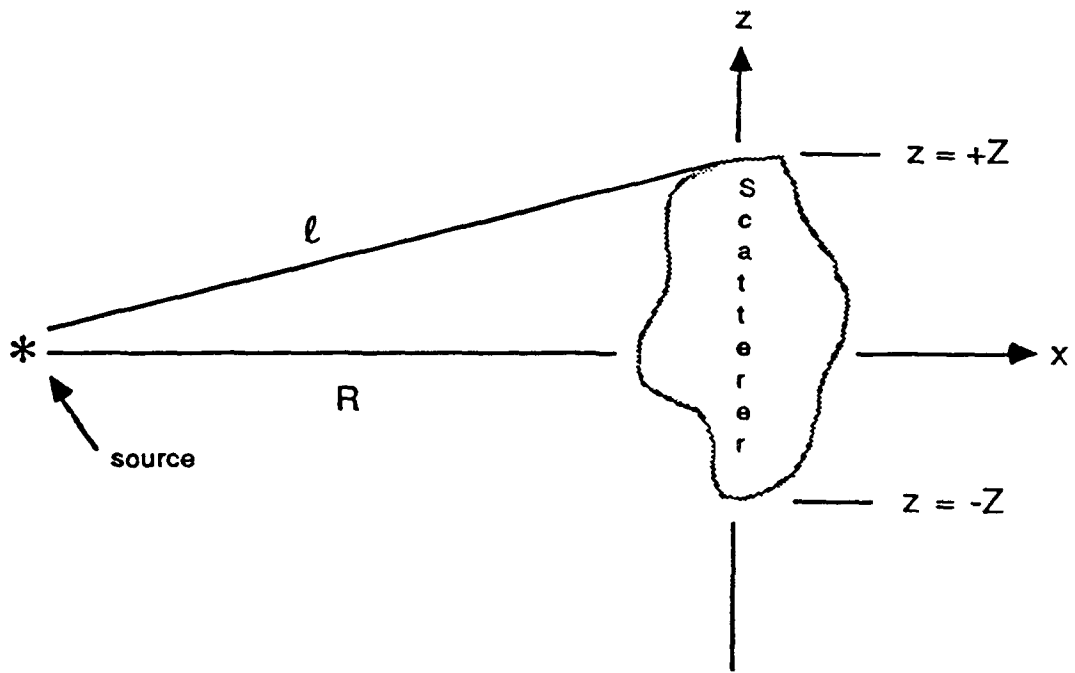
Figure 5.4: Source scatter geometry showing the difference in path length between the closest and farthest point on the scatterer. As the source is moved away from the scatterer the difference in path length becomes negligibly small. At this point the pressure field insonifying the scatterer may be considered planar.

source must the scatterer be to consider the field planar. Quantitative phase and amplitude differences between the shortest path and the longest path from the source to the scatterer are derived using Equation (5.1). The phase difference is

$$\delta\phi = \left(\frac{\omega_{max}\ell}{c} - \frac{\omega_{max}R}{c}\right) \le \epsilon_\phi, \tag{5.2}$$

where ω_{max} is the maximum frequency of the source pulse. The normalized amplitude error is

$$\delta a = \frac{\sqrt{\ell} - \sqrt{R}}{\sqrt{R}} \le \epsilon_a. \tag{5.3}$$

When the phase and amplitude errors are small, then the wave front is approximately planar at the scatterer.

Using $\ell = \sqrt{R^2 + Z^2}$ in Equation (5.2) and (5.3) and solving for R leads to the range limit criterion of

$$R \ge \left[Z^2 - \left(\frac{c\epsilon_\phi}{\omega_{max}}\right)^2\right]\frac{\omega_{max}}{2c\epsilon_\phi} \equiv R_\phi \tag{5.4}$$

for phase[†] and to

$$R \ge \frac{Z}{[(1 + \epsilon_a)^4 - 1]^{\frac{1}{2}}} \equiv R_a \tag{5.5}$$

for amplitude. The minimum range allowed for a given scatterer size is determined from

$$R_{min} \ge \max(R_\phi, R_a, R_f), \tag{5.6}$$

where R_f is the minimum range to the farfield of the line source at the lowest frequency of interest. Table 5.1 makes this concrete using a phase tolerance of $\epsilon_\phi = \pi/4$, an amplitude tolerance of $\epsilon_a = 0.1$, a maximum frequency of $\omega_{max} = 2\pi \cdot 90 \, rad/s$, a minimum frequency of $\omega_{min} = 2\pi \cdot 30 \, rad/s$, a sound speed of $c = 1500 \, m/s$, and $R_f = \frac{10c}{\omega_{min}}$.

[†]Equation (5.4) is essentially the Fresnel criterion of $R \ge D^2/\lambda$ for the farfield found by setting $\epsilon_\phi = \pi/4$ [58, p. 126].

D	Z	R_ϕ	R_a	R_f	R_{min}
2	1.0	-0.8	1.5	79.5	79.5
5	2.5	0.5	3.7	79.5	79.5
10	5.0	5.0	7.3	79.5	79.5
15	7.5	12.5	11.0	79.5	79.5
20	10.0	23.0	14.7	79.5	79.5
30	15.0	53.0	22.0	79.5	79.5
40	20.0	95.0	29.4	79.5	95.0
50	25.0	149.0	36.7	79.5	149.0

Table 5.1: Minimum separation in meters between source and scatterer for plane wave approximation. This data was generated using $\epsilon_\phi = \pi/4$, $\epsilon_a = 0.1$, $\omega_{max} = 2\pi \cdot 90 \, rad/s$, $\omega_{min} = 2\pi \cdot 30 \, rad/s$, and $c = 1500 \, m/s$. The total length of the scatterer is D meters with a half length of Z meters. R_ϕ is the minimum range to satisfy the phase error criterion, R_a is the minimum range to satisfy the amplitude error criterion, and R_f is the minimum range to the farfield of the line source at the lowest frequency of interest. R_{min} is the largest of the three values and is the minimum range that satisfies all the criteria for a give scatterer size.

5.3.2 Plane wave excitation

In the last section I showed under what conditions the isotropic line source can be considered to insonify a given scatterer with a plane wave. I use this condition to design experiments such that the scattered response is approximately that from an incident plane wave at a prescribed grazing angle. Figure 5.5 shows the geometry to be used in the experiments. The insonifying arc angle is $\theta_s = \theta_2 - \theta_1$ with a grazing angle of $\gamma = \theta_1 + \theta_s/2$. Energy directed away from the source in angles outside of θ_s intersects the flat ice or free surface and is reflected rather than scattered back into the water. This part of the field is the same as the reference field and is subtracted from the total field to isolate the effects of the scatterer. As a result of the subtraction operation, the energy traveling outside of the arc angle θ_s is removed from the scattering analysis except for the plate wave energy generated in flat ice by the isotropic source and subsequently scattered by the roughness element. The plate wave is a compressional head wave excited at the Mach angle at which the trace speed of
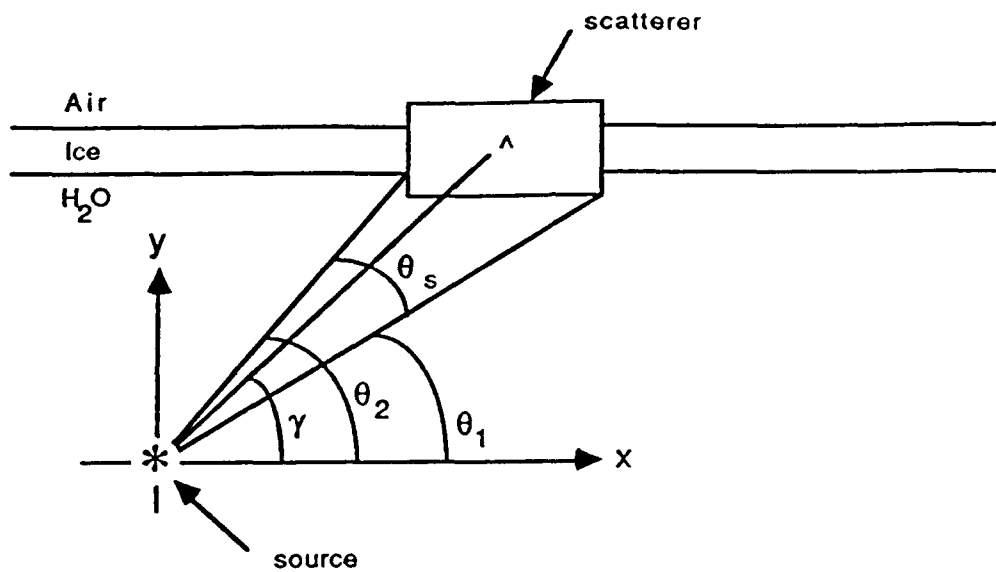
Figure 5.5: Geometry for plane wave approximations at the scatterer. As the source is drawn away from the scatterer, the direct insonifying field at the scatterer becomes progressively more like a plane wave. I define the grazing angle for this geometry as $\gamma = \theta_1 + \theta_s/2$, where θ_s is the arc angle subtended by the scatterer.

the compressional wave matches the speed of sound in the water [34]. For identification in later sections, I designate this as the *source head wave*. Although the amount of energy in this head wave is small, there is enough to interact with a scattering element and scatter energy into the water. The head wave scatter occurs prior to the direct water wave, or acoustic, scatter and the two events are somewhat separable in time.

For scattering studies near the source this head wave is an expected phenomenon and is part of the true physical field. It is modeled accurately by experiments conducted with the geometry shown in Figure 5.5. For studies in which long-range propagation paths play a part, however, the source head wave should not be present. This complicates the interpretation of the experimental data, as will be seen in subsequent sections. Future versions of the modeling algorithm should be designed to inject either an omni-directional or a narrow beam source excitation depending on the application.

5.4   Experiments

Single or elemental scatterers are the foundation upon which a hierarchy of scattering processes are built. I define an elemental scatterer to be one which has a single scattering feature surrounded by an absolutely flat interface, either a flat free surface or flat ice. The idealized models introduced in Section 5.2 are examples of elemental scatters. I use the term *inclusion* to describe any kind of roughness element except an ice edge, which is in a class by itself. Thus, floes and ridges are inclusions. Due to the difference in material properties of young versus old ridges, I consider fluid and elastic inclusions as separate types of models even if the geometric shape of the object is the same.

Floes are of interest because they are the simplest scattering objects that resemble ridge keels, albeit with the surrounding ice sheet removed. Furthermore, there are analytic solutions for scatter from circular cylinders that provide insight into acoustic scattering from
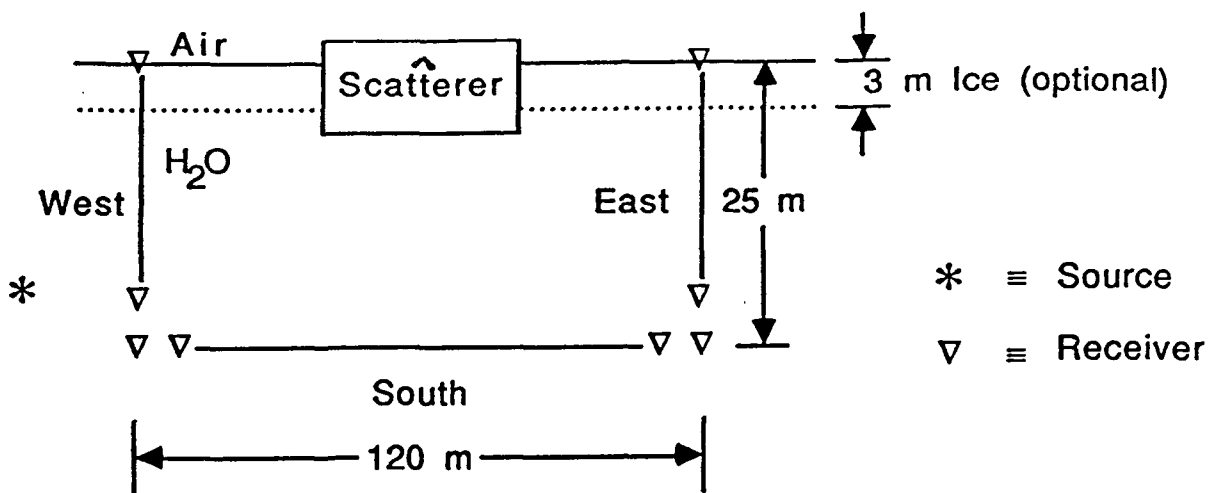
Figure 5.6: An elemental scatterer is surrounded by either a flat free surface or flat ice. The source is located according to the recommendations of Section 5.3 such that the incident field at the scatterer is nearly planar. Receivers are distributed in a box around the scatterer to capture the scattered field at all departure angles. Plate wave excitations are measured in the cases when an ice sheet is present. The reference origin for the scatterer is indicated with a "^".

floes with semi-circular cross sections. When a floe, whether fluid or elastic, is connected to a surrounding ice sheet it models a ridge keel.

This section documents eight scattering experiments. The results of the experiments are discussed in Section 5.5. Each experiment was executed in the same way. Figure 5.6 shows the geometry common to all. The scatterer is located in the midst of a flat interface between water and air. The interface may be either a flat free surface or a flat ice sheet. Roughly speaking, the response of a completely flat interface in either case is to reflect the incident field specularly. In the case of a flat ice sheet the omni-directional source excites the symmetric Lamb mode which in turn radiates a small head wave into the water. The response of the flat interface is denoted the *coherent* response against which the response of the scatterer is compared.

The scattered field is emitted in a wide range of angles and dictates that a box of

receivers be placed around the scatterer to provide adequate measurement of the field. In this way, low angle scatter is measured without the need for extraordinarily long linear arrays. The array processing for a box of receivers is a bit more complicated than that of a linear array. But a dividend is received in the form of a compact experimental geometry, which in turn, reduces the modeling computation time. As indicated in Figure 5.6, the receiver box comprises three linear arrays designated west, south, and east as shown. The reference origin for the scatterer is located in line with the top of the flat interface. It is also used as the pivot point for the plane wave decomposition. The grazing angle is the angle between the horizontal and a line drawn through the source and the pivot point. All experiments discussed in this thesis have a grazing angle of 10°. The receiver box is as shown, 120 m long by 25 m high, which corresponds to about $4\lambda \times \frac{3}{4}\lambda$, where λ is the water wavelength at 55 Hz.

Results from the eight experiments, shown schematically in Figure 5.7, are analyzed in the next section. Beside each schematic drawing in the figure is an experiment number, which is used as an identification symbol on plots in the next section. Figure 5.7 serves as a ready reference to help the reader in identifying the models being compared.

5.4.1 Fluid inclusions

A fluid inclusion, whether a floe or a keel, has zero shear modulus and approximates the condition of highly fractured, disoriented ice blocks found in newly formed pressure ridges. Two of the eight experiments shown in Figure 5.7 fall into this category.

Floes

The fluid floe model for Experiment 37 has a semi-circular cross section with a radius of 6 m. Figure 5.8 shows the scattered pressure field around the floe. This field is the difference
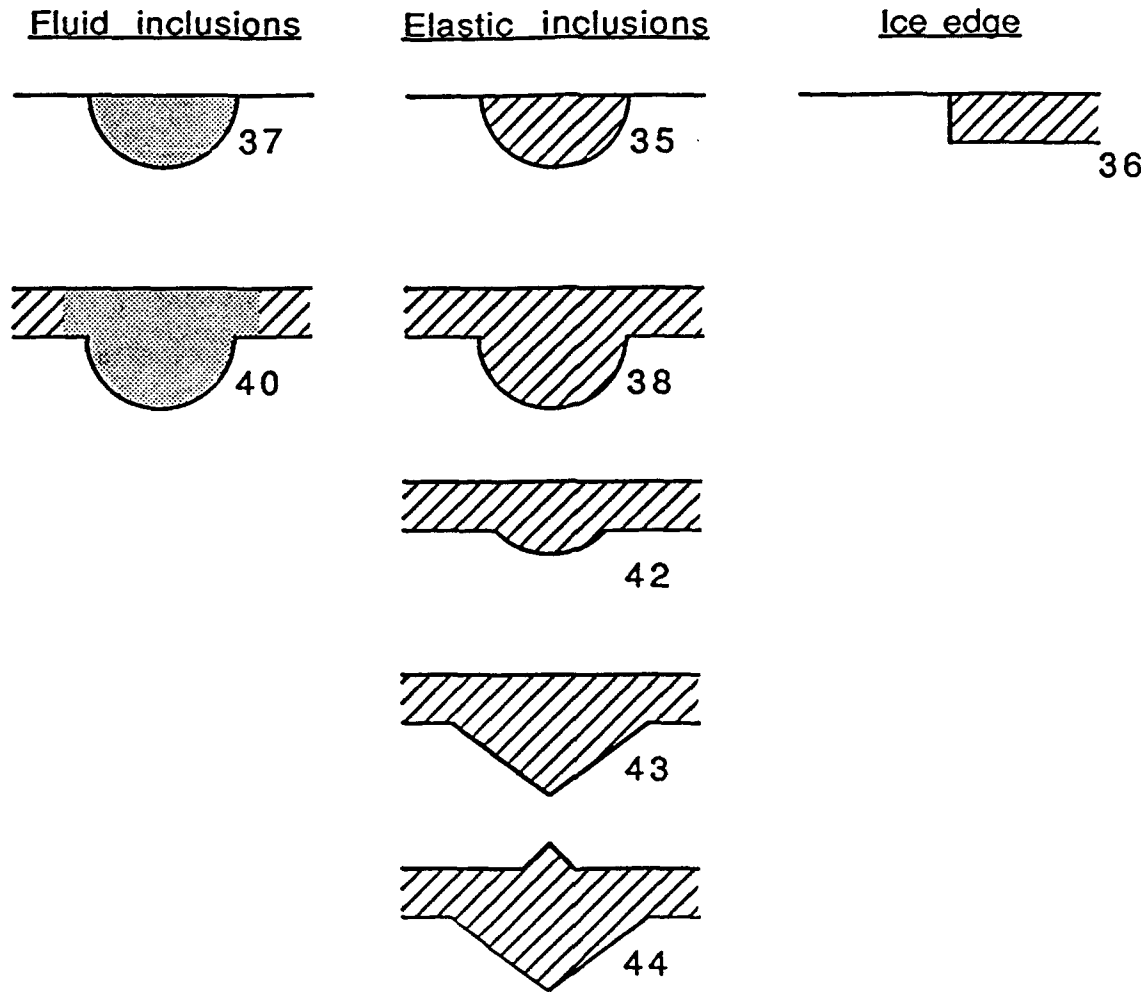
Figure 5.7: Eight scattering models. Each model has an experiment number written next to it. This number is used as an identification symbol on plots in Section 5.5. Use this figure for a ready reference to identify the models being compared. For all models the material property of ice is $C_p = 3500\,m/s$, $C_s = 1600\,m/s$, and $\rho = 910\,Kg/m^3$. For "fluid" ice the shear speed is set to zero. The material properties for water and air are respectively $C_w = 1500\,m/s$, $\rho_w = 1000\,Kg/m^3$, $C_a = 340\,m/s$, and $\rho_a = 1.2\,Kg/m^3$. In all cases, if an ice sheet is present, it is $3\,m$ thick.
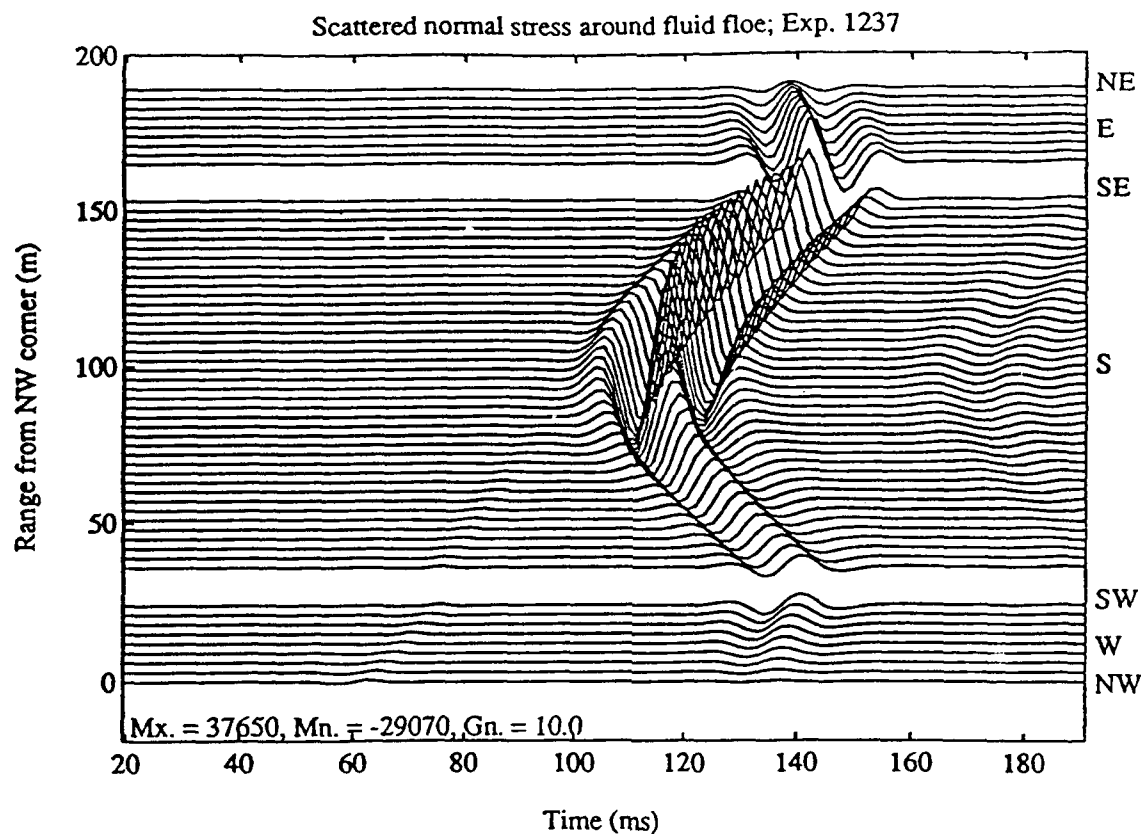
Figure 5.8: Scattered pressure field due to 6 m radius semi-circular fluid floe. The traces are broken into three groups corresponding to the three legs of the measurement array: west, south, and east. Note the phase continuity of the scattered field with respect to the mid-line of the floe. Also, note the higher amplitude of the field in the forward direction. The event that appears at about 170 ms in the middle of the south array is an artifact caused by imperfect absorbing boundaries.

between the pressure field measured with and without the floe in place. Notice the phase continuity[†] with respect to the mid-line of the floe and the higher scattering amplitude in the forward direction. These points are discussed in detail and explained in terms of an analytic solution to this problem in Section 5.5.1.

[†]By *phase continuity* I mean that a trough in the back scattered direction corresp. nds to a trough in the forward scattered direction. The term *phase discontinuity* indicates that a trough in the back scattered direction corresponds to a crest in the forward scattered direction.

Keels

Adding a 3 m ice sheet on top of the fluid floe turns it into a fluid keel. A diagram of the exact keel geometry used in Experiment 40 is shown in Figure 5.9(a). Figure 5.9(b) shows the scattered pressure field generated by the fluid keel. The field is slightly more complicated than that of the fluid floe. As discussed in Section 5.3.2, a head wave component is injected into the ice by the isotropic line source. The head wave travels down the plate and scatters at the keel causing the early arrivals beginning at about 85 ms in the middle of the south array. There are actually two discontinuities from which the head wave scatters in this model. The first is the elastic-fluid boundary encountered in the plate where the elastic ice sheet comes in contact with the wings of the fluid ice keel. At this point there is a discontinuity of shear speed, and thus μ; both go to zero in the fluid. The discontinuity causes the shear modes to either reflect back down the elastic sheet or to be converted and scattered into compressional waves. The other discontinuity is the increase in mass and change of geometry associated with the keel itself. These changes permit the head wave energy to be scattered into the water around the keel.

Subsequent to the head wave scatter, the direct acoustic scatter of the fluid keel is seen at a time of about 110 ms. The form of this part of the field is very similar to that of the fluid floe; there is phase continuity across the mid-line of the keel with larger scattered amplitude in the forward direction. The absolute amplitude of the scattered field for the fluid keel is about 2.5 times larger than that of the fluid floe. The extra scattering amplitude is due primarily to the larger mass of the keel relative to that of the floe.

5.4.2 Elastic inclusions

Elastic inclusions are representative of structures composed of solid ice with a high shear modulus. As discussed in Section 5.2, pressure ridges that have survived a year or more,

(a)
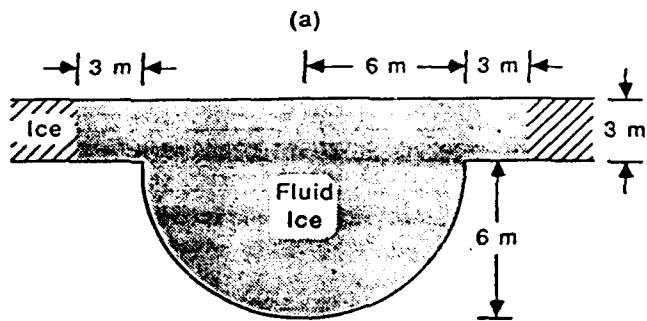
Scattered normal stress around low shear keel; Exp. 1240

(b)

Mx. = 87920, Mn. = -73960, Gn. = 10.0

Time (ms)
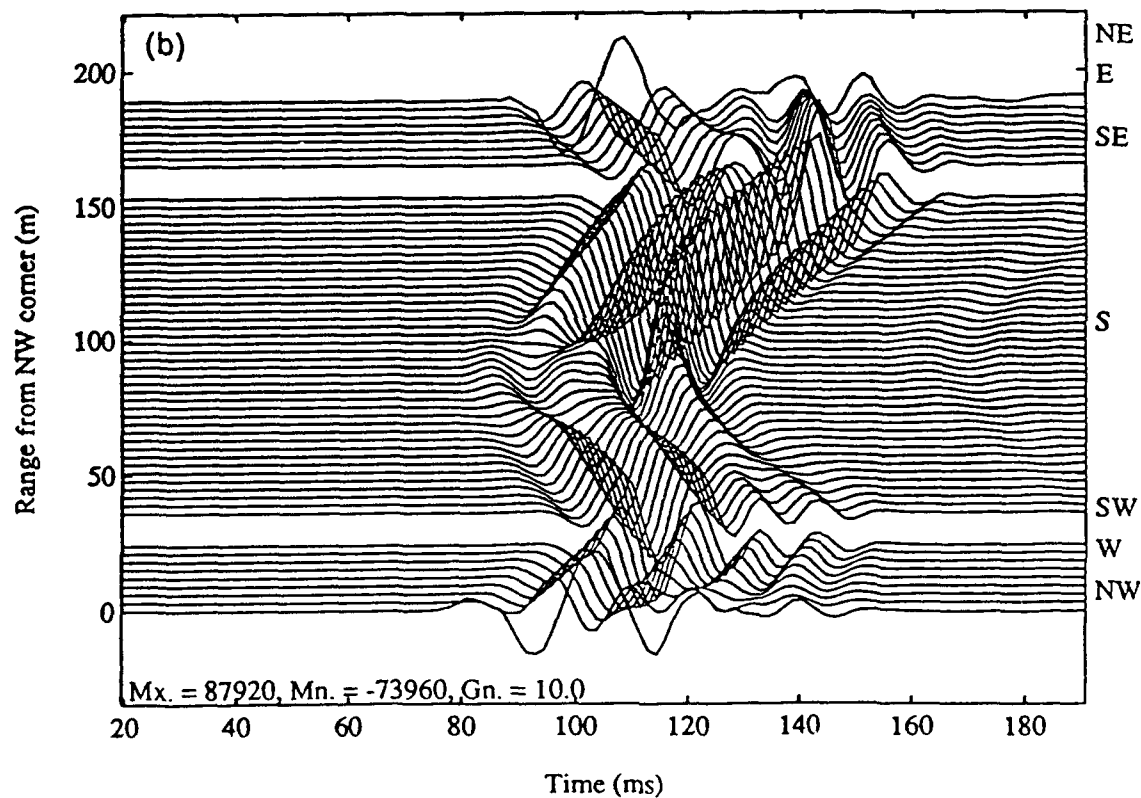
Figure 5.9: A fluid keel, Experiment 40. (a) The keel itself has a semi-circular cross section with a radius of 6 m. The ice sheet above and for 3 m on either side of the keel is modeled as fluid ice with $C_s = 0\,m/s$. The ice sheet is 3 m thick, and away from the keel, it has a shear speed of $C_s = 1600\,m/s$. (b) The scattered response of the fluid keel is similar to that of the fluid floe at times later than about 110 ms. This is the acoustic field directly scattered from the keel. At earlier times, the source head wave in the ice is converted to acoustic waves and scattered by the keel. Also, the amplitude of the scattered response of the keel is about 2.5 times that of the floe. The extra scattering amplitude is due primarily to the extra mass of the ice above the keel.

197

the multi-year ridges, are likely to be frozen solid with little or no interstitial water and hence are best modeled using an elastic inclusion. Five of the eight experimental models shown in Figure 5.7 fall into this category. One is an elastic floe and the rest are elastic pressure ridges of various shapes and sizes.

Floes

The elastic floe model for Experiment 35 is identical to that of the fluid floe in Experiment 37 except the shear speed is $C_s = 1600\,m/s$. The floe has a semi-circular cross section with a radius of 6 m. The scattered pressure field due to the elastic floe is shown in Figure 5.10. There is a striking difference in this scattered field compared to that of the fluid floe shown in Figure 5.8. In contrast to the phase continuity seen in the fluid case, the elastic floe produces a scattered field that has a phase discontinuity near the mid-line of the floe. Similar to the fluid floe, however, the scattered pressure amplitude is higher in the forward direction. These points are analyzed in detail in Section 5.5.1, where the numerical results are compared with the analytic solution for acoustic scattering from elastic cylinders.

Keels

Four of the elastic inclusion experiments use keel models. Figure 5.11 shows the exact geometry of each of the models. There is little qualitative difference in the scattered field of these models. The dominant quantitative effect is that of mass; larger mass produces larger scattered pressures. Just as the dual to the fluid floe in Experiment 35 is the elastic floe in Experiment 37, the dual to the fluid keel in Experiment 40 is the elastic keel in Experiment 38. The model is that of a 6 m radius semi-circular elastic floe beneath a 3 m ice sheet. The scattered response produced by this model is shown in Figure 5.12. Here again, the source head wave from the isotropic line source scatters at an early time, around

Scattered normal stress around elastic floe; Exp. 1235
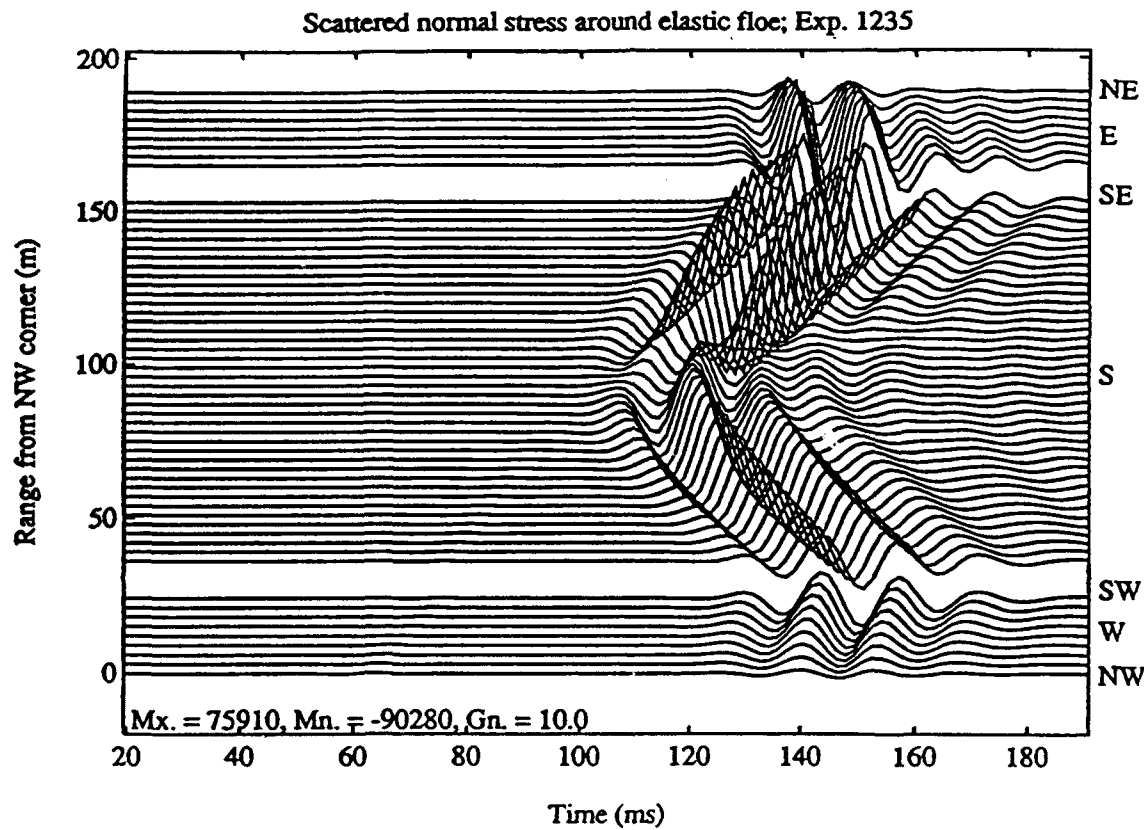
Figure 5.10: An elastic floe, Experiment 35. The geometry of the scatterer is identical to that of the fluid floe, which produced the scattered field shown in Figure 5.8. In particular, the floe has a semi-circular cross section with a radius of $6\,m$. The only difference is that the shear speed has been changed from $C_s = 0\,m/s$, in the fluid case, to $C_s = 1600\,m/s$, in the elastic case. This change in shear speed and, hence shear modulus, has changed the character of the scattered field significantly. The most obvious change is the phase discontinuity near the mid-line of the floe compared to the phase continuity in the field produced by the fluid floe.

199
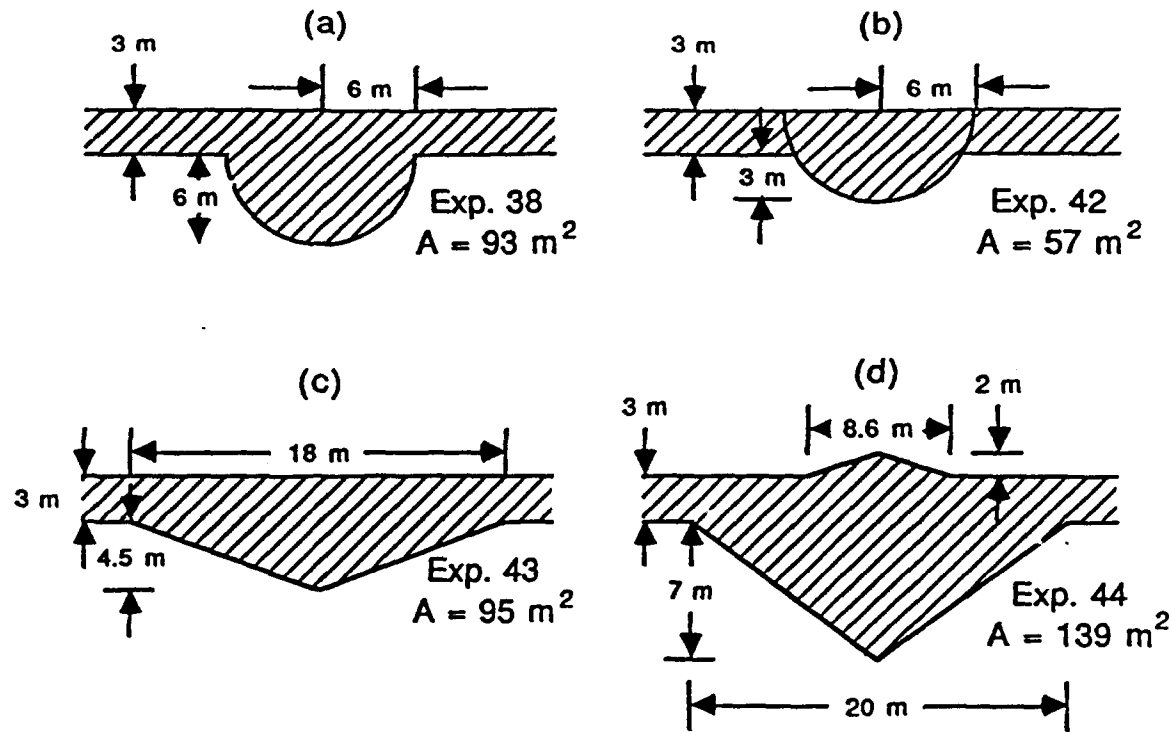
Figure 5.11: Geometry for the four elastic keel models. (a) Experiment 38, a semi-circular keel with radius of 6 m below a 3 m ice sheet. (b) Experiment 42, a semi-circular keel with radius of 6 m connected on each side to a 3 m ice sheet. (c) Experiment 43, an 18x4.5 m triangular keel below a 3 m ice sheet. (d) Experiment 44, a 20x7 m triangular keel below 3 m ice with an 8.6x2 m triangular sail above. This pressure ridge is based on a description given by Weeks [72] with a sail angle of 25° and a keel angle of 35°.

85 ms in the middle of the south array, followed by the direct acoustic scatter from the elastic keel. The latter portion of the scattered field here, in Experiment 38, is very similar to the field seen in Figure 5.10 for the elastic floe. In both cases there is a phase discontinuity near the mid-line of the keel with larger scattering amplitude in the forward direction.

The scattered field produced by the elastic inclusions in Experiments 42-44 are similar to that of Experiment 38. Because of this, I do not show the scattered field for these experiments here but use the results from these experiments in Section 5.5.

5.4.3 Ice edge

An ice edge or truncated ice plate is the fundamental building block needed to understand scatter from leads, polynyas, drifting ice, and the broken ice fields in the marginal ice zone. Hence, the last model I develop is that of the ice edge used in Experiment 36. This model is composed of a semi-infinite free surface adjoining a semi-infinite 3 m elastic ice plate as shown schematically in Figure 5.7. This, probably, is also a good model for a thick ice plate adjoining a freshly frozen lead, where the ice thickness is small, say a few tens of centimeters. In this case, the difference between a free surface and the thin ice is negligible at low frequency.

The scattered pressure field due to the ice edge is shown in Figure 5.13, where the coherent field is taken to be the response of a flat free surface.[†] Again, as for the fluid and elastic inclusions, the forward scattered pressure is larger than that in the backward direction. Also, there is a phase discontinuity in the field near the free-surface-to-ice-sheet transition.

[†]The choice for the coherent field could just as well have been flat ice. Any interpretation must implicitly acknowledge the chosen coherent model. Physically, the free surface choice might correspond to an experiment conducted with source and receiver fixed in open water then, after an ice sheet moves in for some reason, the experiment is repeated. The difference in these two experiments will yield the scattered field shown in Figure 5.13.
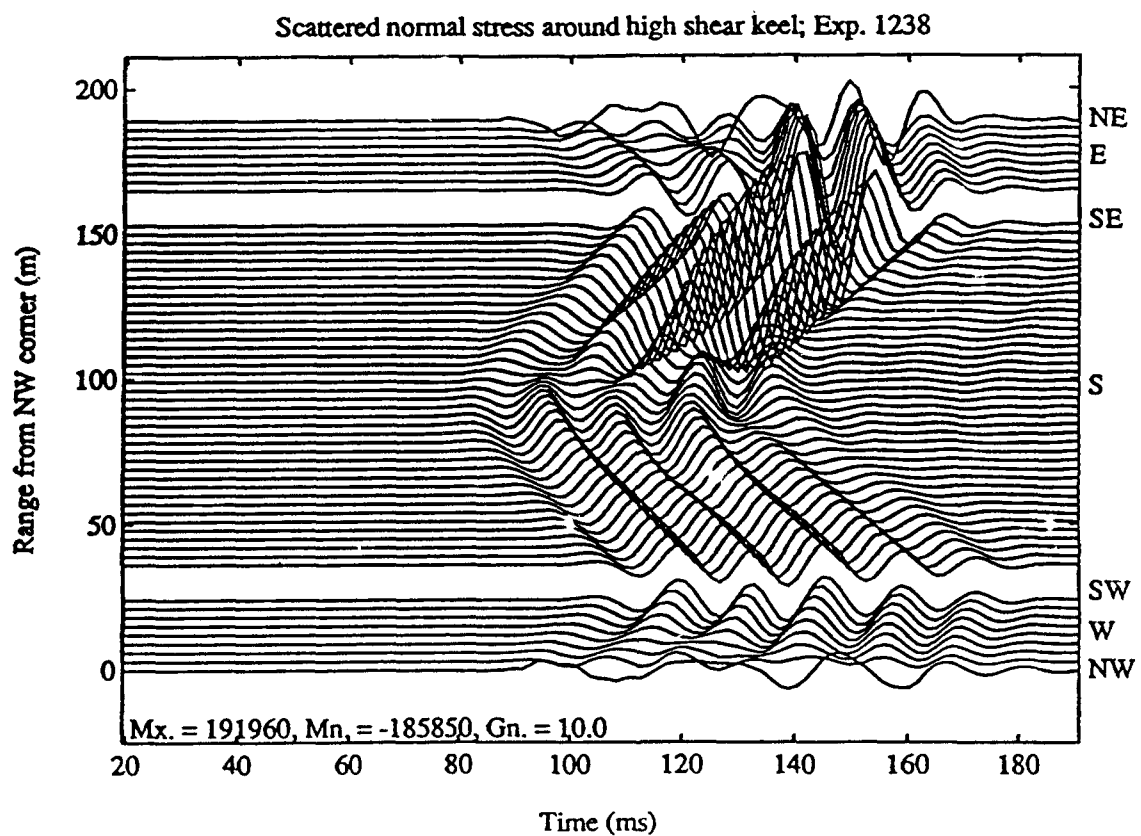
Figure 5.12: Scattered pressure from an elastic keel, Experiment 38. The early arrival spanning approximately 85 ms to 110 ms at the middle of the south array is due to the scattered field from the source head wave in the ice discussed in Section 5.3.2. The later arrival is the direct scattered field from the keel. There is a phase discontinuity near the mid-line of the keel with larger scattered amplitude in the forward direction. The scattered amplitude is about 2.3 times that of the elastic floe, which is similar to the situation for the fluid floe and keel.
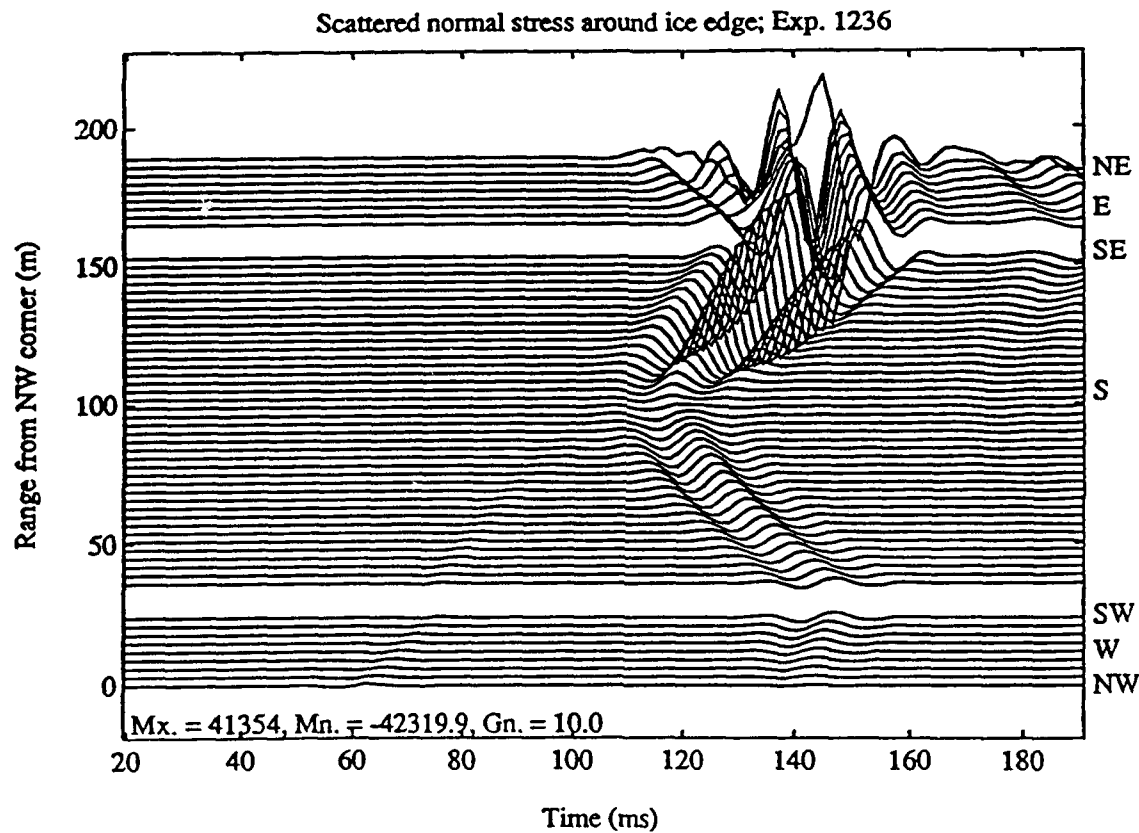
Figure 5.13: Scattered field from an ice edge, Experiment 36. This field is computed as the difference between the total response with the ice edge present and the total response for a flat free surface. The forward scattered amplitude is large and there is a phase discontinuity near the transition from the free surface to the ice sheet.
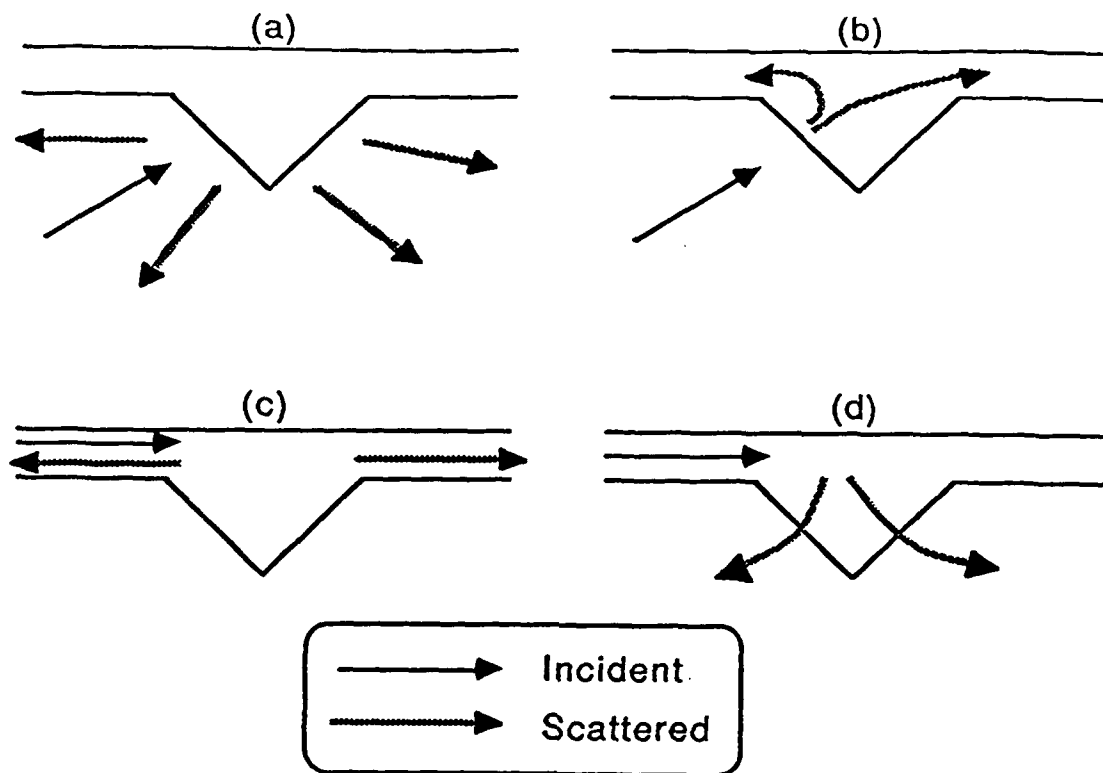
Figure 5.14: Interactions between acoustic and elastic waves. Direct wave scattering mechanisms are shown in (a) and (b). Plate wave scattering mechanisms are shown in (c) and (d). (a) Wide angle acoustic scattering from a roughness element. (b) Excitation of plate waves by an incident acoustic wave. (c) Scatter of plate waves into plate waves. (d) Scatter of plate waves into acoustic waves.

5.5 Interaction mechanisms

Interactions between a propagating wave, either in the water or in the ice plate, and a roughness element may be broadly grouped into four categories as shown schematically in Figure 5.14. The interactions involving an incident acoustic wave, shown in Figure 5.14(a) and (b), are called *direct wave* scatter and are discussed in the next section. The interactions involving an incident plate wave, shown in Figure 5.14(c) and (d), are called *plate wave* scatter and are discussed in Section 5.5.2.

For long-range propagation the principle quantity of interest is the frequency dependent

specular energy loss of the coherent field for each encounter with the ice: in other words, the specular loss per bounce. Two fields are needed for this calculation: the total field for the coherent experiment, i.e., the flat ice or flat free surface experiment, and the total field for the experiment with the roughness element. The plane wave decomposition of each is computed using the serpentine Radon transform discussed in Chapter 4, Section 4.5. The estimated normal stress and radial velocity plane waves in the specular direction are Fourier transformed to yield $\hat{\tilde{\sigma}}_{Tc}(\gamma_s, \omega)$ and $\hat{\tilde{v}}_{Tc}(\gamma_s, \omega)$ for the coherent experiment and $\hat{\tilde{\sigma}}_{Ts}(\gamma_s, \omega)$ and $\hat{\tilde{v}}_{Ts}(\gamma_s, \omega)$ for the scattering experiment, where $(\tilde{\cdot})$ is the Radon transform of $(\cdot)$, $(\hat{\cdot})$ is the temporal Fourier transform of $(\cdot)$, and γ_s is the specular grazing angle. Using the transformed stresses and velocities, the specular energy flux spectra for the coherent and scattering experiment are computed as

$$\mathcal{E}_{Tc}(\omega) = \hat{\tilde{\sigma}}_{Tc}(\gamma_s, \omega) \hat{\tilde{v}}^*_{Tc}(\gamma_s, \omega) \tag{5.7}$$

and

$$\mathcal{E}_{Ts}(\omega) = \hat{\tilde{\sigma}}_{Ts}(\gamma_s, \omega) \hat{\tilde{v}}^*_{Ts}(\gamma_s, \omega). \tag{5.8}$$

For Experiment 38, the results of this operation are shown in Figure 5.15(a) plotted with cyclic frequency, f, rather than radial frequency, ω, as the independent variable. Energy flux is a vector quantity, and in the case of the plane wave decomposition, the vector is radial. A negative energy flux in this figure indicates energy flowing away from the scatterer.

The energy reflection coefficient, R_e, is computed as the ratio

$$R_e(\omega) = \frac{\mathcal{E}_{Ts}(\omega)}{\mathcal{E}_{Tc}(\omega)}. \tag{5.9}$$

The specular energy loss, L_e, is computed as

$$L_e(\omega) = -10 \log_{10} R_e(\omega) \tag{5.10}$$

with the result, again for Experiment 38, shown in Figure 5.15(b). The modulation of the loss curve, especially noticeable at low frequency, is an artifact of imperfect absorbing

boundary conditions. I smooth these curves by hand to develop monotonic functions of loss versus frequency.

5.5.1 Direct wave scatter

In this section I discuss the direct wave scattering mechanisms associated with the acoustic water wave insonifying a roughness element. A discussion of the plate wave scattering mechanisms associated with the source head wave is deferred to the next section.

When an acoustic wave, whether planar or not, interacts with a roughness element, sound is scattered over a wide range of angles, and if an ice plate is present, sound is directed into plate waves, too. These are the direct wave scattering mechanisms pictured in Figure 5.14(a) and (b). In effect, the coherent specular field, that is the field reflected from the flat ice, supplies energy to both direct wave scattering mechanisms. In the absence of a scatterer, the coherent field, by definition, suffers no energy loss. In particular, radiation from the source head wave is considered to be part of the coherent field in this study. When a scatterer is present, however, there is a loss in the coherent field due to the direct wave scatter. This loss is the coherent field energy deficit which arises from rough surface scattering. The deficit, measured in decibels per bounce, is the principle quantity of interest in long-range propagation. Energy lost to scatter is purely a redirection of mechanical energy in the field. Globally, mechanical energy is conserved; the propagation media are assumed to be lossless.

This section describes three loss mechanisms: loss due to mass loading, loss due to wide angle scatter, and loss due to the excitation of plate waves.
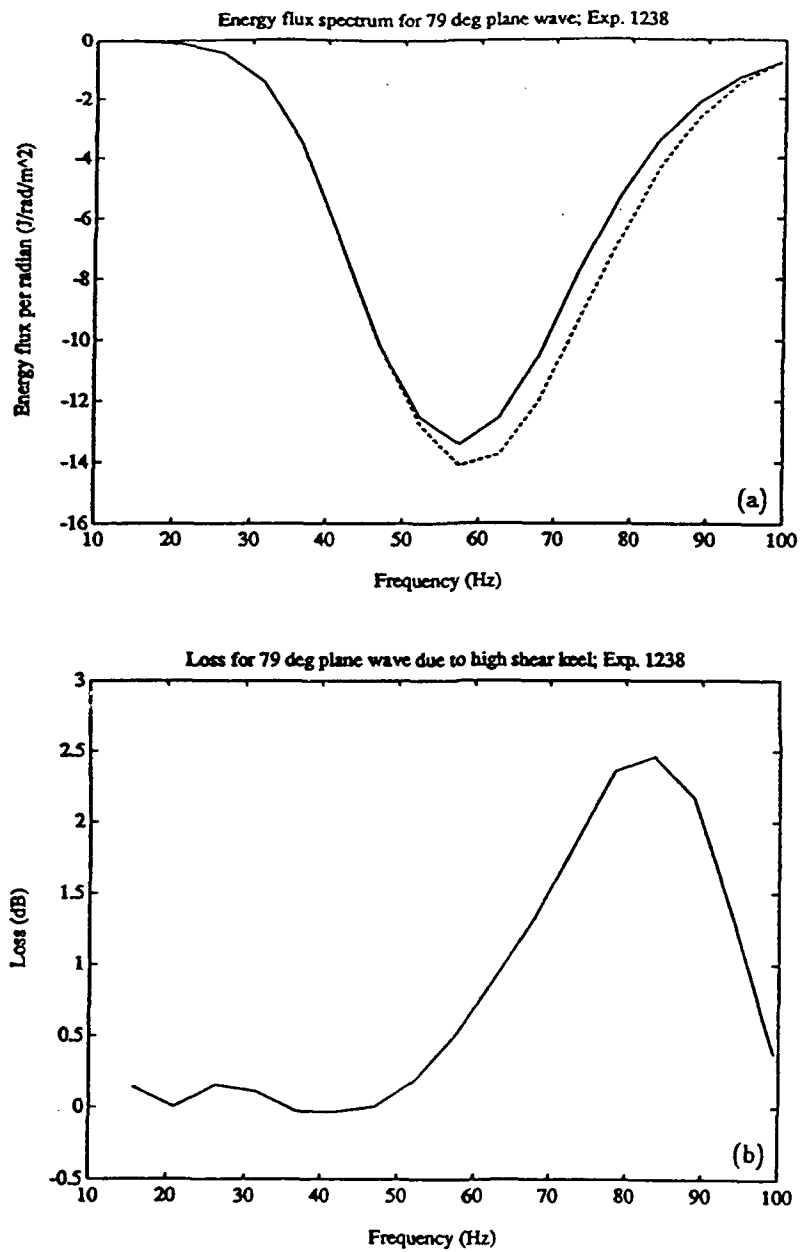
Figure 5.15: Computation of specular loss per bounce. (a) Energy flux spectrum for the coherent experiment, $\mathcal{E}_{Tc}(f)$, plotted with ($\cdots$) and the scatter experiment, $\mathcal{E}_{Ts}(f)$, plotted with (—). Energy flux is a radial vector quantity with negative values indicating energy flow away from the scatterer. Recall the source spectrum is Gaussian with a center frequency near $55\,Hz$. (b) Specular loss in decibels per bounce versus frequency. The modulation of the curve, noticeable at low frequency, is an artifact of imperfect absorbing boundary conditions. These modulations are smoothed by hand to develop a monotonic function of loss versus frequency.

207

Mass loading

In this section I show that loss is proportional to cross sectional area of the scattering object, which for fixed density, implies that loss is proportional to mass per unit length. Hence the term *mass loading* is used.

For small ka, where k is the water wavenumber, $k = 2\pi\omega/c_{H_2O} = 2\pi/\lambda_{H_2O}$, and a is a characteristic dimension of the scattering object, specular energy loss measured in decibels is proportional to the cross sectional area of the object[†]. First, I show an analytic result for semi-circular fluid floes assuming ka small. Next, for elastic keels and ka not necessarily small, I show that the relation still holds.

Consider Figure 5.16, which shows the equivalence of two experiments: scatter from a semi-circular fluid floe and scatter from a circular fluid cylinder with a source and its negative image. For this method to be exact the internal field must be a symmetric function of the cylindrical coordinate φ. Stanton [61] shows that the pressure field inside the fluid cylinder is dependent on $\cos(n\varphi)$; hence, the method of images produces an exact solution to scatter from a semi-circular fluid floe against a free surface.

Using the assumption of a plane wave harmonic source, the incident field is $P_{inc} = P_o e^{ikz_{inc}}$, which propagates in the direction x_{inc}. Trigonometric and algebraic manipulations lead to an expression for the incident and image field in terms of cylindrical coordinates, r and φ,

$$P_{inc} = P_o e^{ikr\cos(\varphi-\gamma)}, \quad P_{image} = -P_o e^{ikr\cos(\varphi+\gamma)}, \tag{5.11}$$

where γ is the grazing angle. Stanton also gives the scattered pressure for small ka and large kr of a fluid circular cylinder excited by a plane wave [61]. The sum of the scattered

---

[†]In this chapter I use k to be the wavenumber, $k = \omega/c = 2\pi/\lambda$. There is no confusion here with the temporal increment, $k = \Delta t$, as was the case in earlier chapters.

(a)

free surface

P_{inc}
(positive source)

$P_{ref} = P_{coh} + P_{scat}$

P_{inc} = incident
P_{ref} = reflected
P_{coh} = coherent
P_{scat} = scattered
P_{imag} = image

P_{imag}
(negative source)

$\Theta > 0$

P_{inc}
(positive source)

(b)

$P_{ref} = P_{imag} + P_{scat}$

$= P_{coh} + P_{scat}$
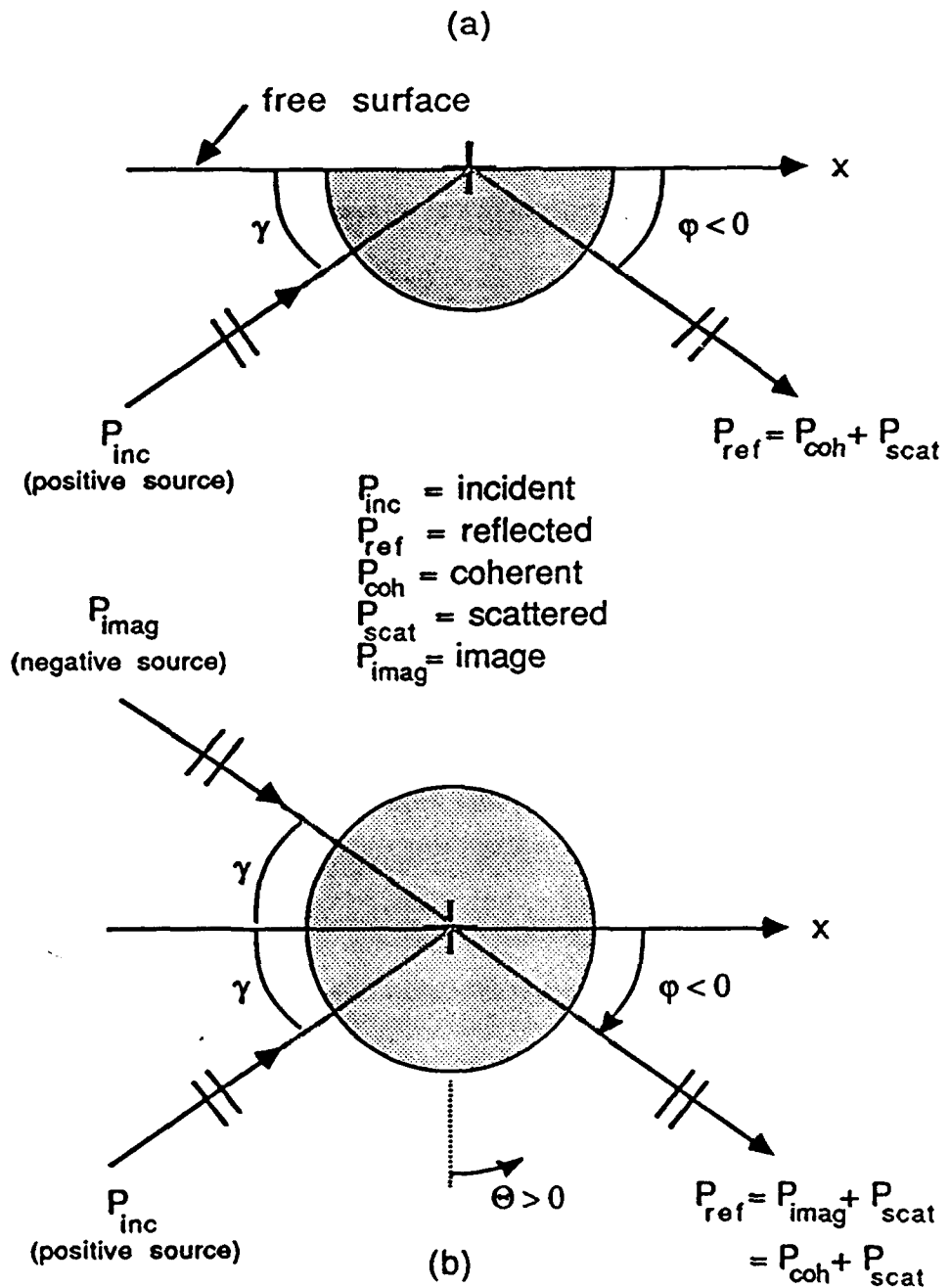
Figure 5.16: Geometry for scatter from a fluid floe. (a) This is the physical picture of a plane wave incident on a semi-circular fluid floe. The incident field arrives at a grazing angle of γ and the scattered field is measured from the positive x-axis with angle φ. (b) This is the equivalent problem but using a circular fluid cylinder and a negative image source. (Note: This geometry is also used with an elastic cylinder in the development of the elastic pseudo-floe problem.)

209

field due to the incident field and the scattered field due to the image field yields

$$P_{scat} \xrightarrow[\substack{ka \ll 1, \\ kr \gg 1}]{} -i\pi P_o (ka)^2 \sqrt{\frac{2}{\pi kr}} e^{i(kr-\pi/4)} \frac{(1-g)}{(1+g)} \sin\varphi \sin\gamma, \qquad (5.12)$$

where the density ratio is $g = \frac{\rho_{cyl}}{\rho_{H_2O}}$ and the radius of the cylinder is a. Using the reflected pressure from the scattering experiment, P_{ref}, and that from the coherent (no scatterer) experiment, P_{coh}, the specular energy reflection coefficient, R_e, may be written

$$R_e = \frac{|P_{ref}|^2}{|P_{coh}|^2} = \frac{|P_{coh} + P_{scat}|^2}{|P_{coh}|^2} = \frac{|P_{coh}|^2 + 2\Re(P_{coh}P_{scat}^*) + |P_{scat}|^2}{|P_{coh}|^2}, \qquad (5.13)$$

where $\Re(\cdot)$ means the real part and $(\cdot)^*$ means the complex conjugate. The specular energy loss is defined as

$$L_e = -10 \log_{10} R_e. \qquad (5.14)$$

To leading order, the specular energy loss may be found as follows. For fixed k the quadratic pressure terms are

$$|P_{inc}|^2 = |P_{coh}|^2 = P_o^2, \quad |P_{scat}|^2 \sim O([ka]^4) \qquad (5.15)$$

and

$$\Re(P_{coh}P_{scat}^*) \quad \sim \quad O\left(P_o^2 (ka)^2 \sqrt{\frac{2}{\pi kr}}\right),$$

$$\sim \quad O([ka]^2). \qquad (5.16)$$

Using these relations in Equation (5.13) and dropping the negligible quadratic P_{scat} term (recalling $ka \ll 1$) leads to an energy reflection coefficient of

$$R_e \sim 1 + O([ka]^2). \qquad (5.17)$$

The series approximation $\log_{10}(1 + \alpha) \simeq \alpha$ for small α leads to the specular energy loss, measured in decibels,

$$L_e \sim -10 \log_{10} R_e \sim O([ka]^2). \qquad (5.18)$$

210

The quantity a^2 is proportional to cross sectional area and thus, for fixed density, to mass per unit length. Hence, the specular energy loss, L_e, is proportional to cross sectional area of the fluid floe for fixed k or, equivalently, fixed frequency, f;

$$L_e \propto a^2. \tag{5.19}$$

Now, I show experimentally that the proportionality between loss and area applies to elastic keels as well. There are four elastic keels, corresponding to Experiment 38 and 42-44, shown in Figure 5.7. Specular loss versus frequency was computed using Equations (5.9) and (5.10) for each of these models. The cross sectional area of each keel is shown in Figure 5.11. Figure 5.17 shows the logarithm of loss, at $50\,Hz$, plotted against the logarithm of area for each of the keel experiments. A linear regression fit through the points has a slope of 1.15, which closely matches the analytic slope of unity computed for the fluid floe. This is true despite the fact that the largest keel has an area of $A = 139\,m^2$, which leads to $ka \sim 2.5$ using $a = \sqrt{A}$. Thus, even for ka not small, the loss versus area relation is a good working rule for ice scatter. Over the band of insonified frequencies, the slopes range from about 0.9 at $30\,Hz$ to 1.4 at $80\,Hz$.

Using a combination of analytic and numerical methods, I have shown in this section an empirical correspondence between cross sectional area and specular energy loss for $ka \simeq O(1)$. This correspondence is used later to justify the scaling of my experimental results to keels of various cross sectional area.

Wide angle scatter

When underwater sound interacts with a roughness element, it is scattered over a wide range of angles in a characteristic pattern. The synonymous terms *propagation angle* and *scattering angle* are defined as the angle measured from the negative y-axis. Angles with positive sign are measured counter-clockwise and those with negative sign are measured
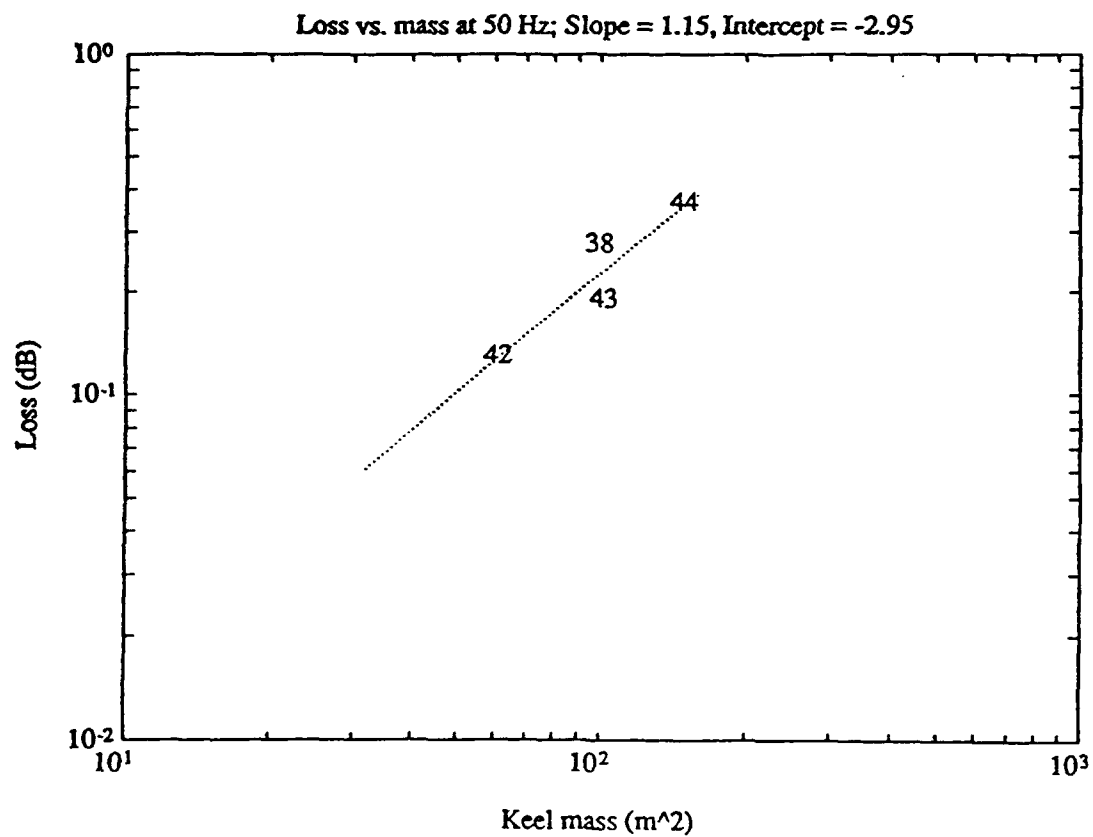
Figure 5.17: Specular energy loss versus mass for elastic keels at 50 Hz. The slope relating $\log(L_e)$ to $\log(A)$ is estimated as 1.15, which compares favorably with the slope of unity computed analytically for fluid floes.

clockwise. With the source to the left of the scatterer, positive angles indicate forward scatter and negative angles indicate backward scatter. The propagation or scattering angle is designated $\Theta = \varphi + \pi/2$, where φ and Θ are shown in Figure 5.16. The scattered pressure fields shown for the fluid and elastic inclusions in Figures 5.8, 5.9(b), 5.10, and 5.12 indicate that the scattered field for an elastic inclusion is very different from that of a fluid inclusion. Scattered intensity as a function of frequency is computed from scattered pressure as follows.

- The amplitude of the pressure measurement, $\hat{p}_i(t)$, at the ith receiver in the box array around the scatterer is corrected to pressure referenced to unit distance from the scatterer, $p_i(t)$;

$$p_i(t) = \hat{p}_i(t)\sqrt{D_i}. \tag{5.20}$$

D_i is the distance of the ith receiver from the scatterer origin, which is at the left-right midpoint of the scatterer at a height corresponding to the surrounding air interface as shown in Figure 5.6.

- The Fourier transform of each pressure measurement is computed as

$$\hat{p}_i(\omega) = \int p_i(t)e^{i\omega t}\,dt. \tag{5.21}$$

- Using the farfield relation between radial velocity and pressure, $\hat{v}(\omega) = \hat{p}(\omega)/\rho c$, and the intensity of the source excitation spectrum (subscript E) referenced to unit distance from the scatterer, $\Phi_E(\omega)$, the normalized scattered intensity, $\Phi_i(\omega)$, is computed. Specifically,

$$\Phi_i(\omega) = \frac{|\hat{p}_i(\omega)|^2/\rho c}{\Phi_E(\omega)}. \tag{5.22}$$

- Finally, the scattered intensity is represented as a two argument function $\Phi_s(\omega, \Theta_i)$, where Θ_i is the propagation angle from the scatterer origin to the ith receiver.

The scattered intensity provides quantitative insight into the wide angle scattering characteristics of the various roughness elements shown in Figure 5.7.

Fluid inclusions. The scattered intensity for the fluid floe of Experiment 37 is shown in Figure 5.18 with the analytic solution shown for comparison. The analytic solution is derived using the fluid cylinder and method of images, as was done for Equation (5.12), but more terms are retained in the series [61]. The solution uses the density inside and outside the cylinder, ρ^* and ρ, the velocity inside and outside the cylinder, c^* and c, and the acoustic wavenumber inside and outside the cylinder, $k^* = \omega/c^*$ and $k = \omega/c$. The densities and velocities are combined into the ratios $g \equiv \rho^*/\rho$ and $h \equiv c^*/c$. Using these quantities, the solution is written

$$P_{scat} \xrightarrow{kr \gg 1} 2P_o \sqrt{\frac{2}{\pi kr}} e^{i(kr - \pi/4)} \sum_{m=1}^{\infty} (-i)^m B_m \sin(m\varphi) \sin(m\gamma), \qquad (5.23)$$

where

$$B_m = -2i^m/(1 + iC_m),$$

$$C_m = \frac{\frac{J'_m(k^*a)N_m(ka)}{J_m(k^*a)J'_m(ka)} - gh\frac{N'_m(ka)}{J'_m(ka)}}{\frac{J'_m(k^*a)J_m(ka)}{J_m(k^*a)J'_m(ka)} - gh}. \qquad (5.24)$$

J_m is an mth order Bessel function of the first kind, N_m is an mth order Bessel function of the second kind, the primed functions are derivatives with respect to their arguments, and a is the radius of the cylinder. In computing the analytic solution I only used the first four terms of the series, $m = 1, 2, 3, 4$.

The agreement between the numerical estimate and the analytic solution shown in Figure 5.18 is quite good. Now we can make a quantitative evaluation of the observation, made earlier, that the forward scattered field is larger. In particular, the peak at a scattering angle of $60°$ is about $15\,dB$ higher than at the reciprocal angle of $-60°$. The intensity pattern is seen to be that of a deformed dipole.
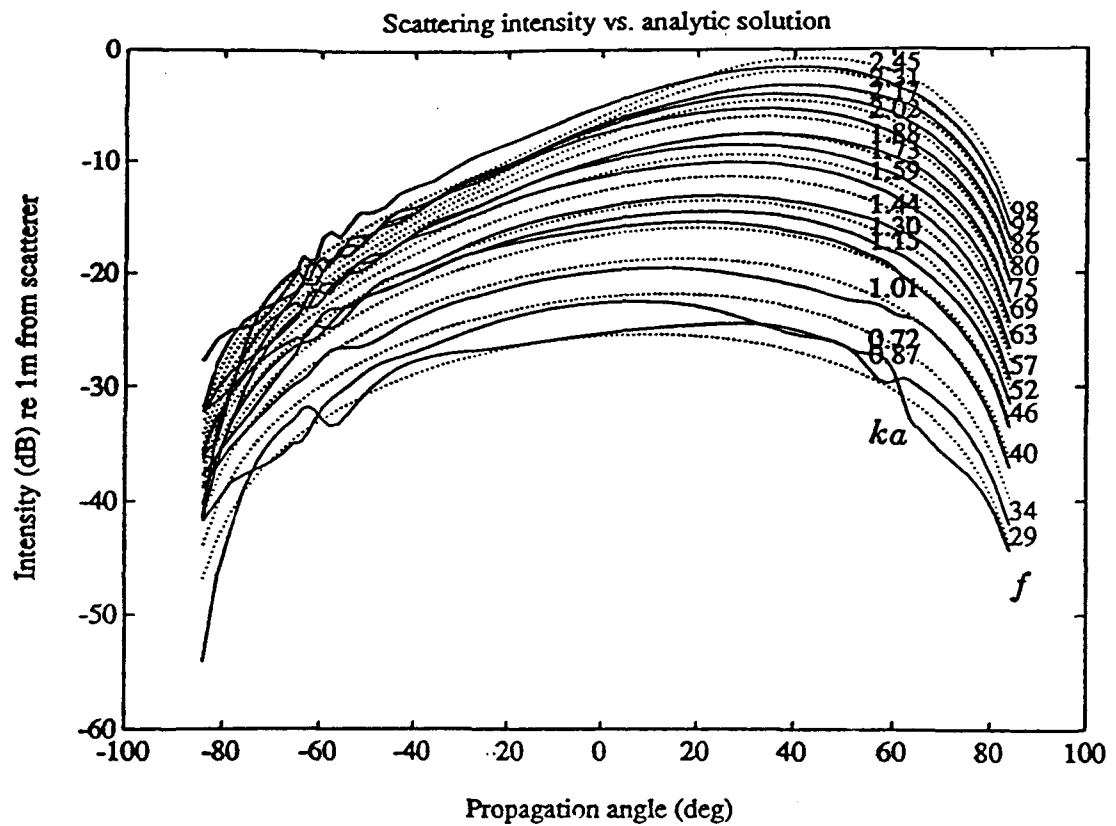
Figure 5.18: Scattered intensity for the fluid floe, Experiment 37. The solid curves are the intensity computed from the scattered pressure shown in Figure 5.8. The dotted curves are the analytic solution computed using Equation (5.23). The propagation angle is Θ as defined in Figure 5.16. Positive angles correspond to forward scatter and negative angles correspond to back scatter. The intensity is computed using Equation (5.20) thru (5.22). Agreement between the analytical and numerical solutions is quite good. The scattered intensity is a slightly deformed dipole with higher intensity in the forward direction.
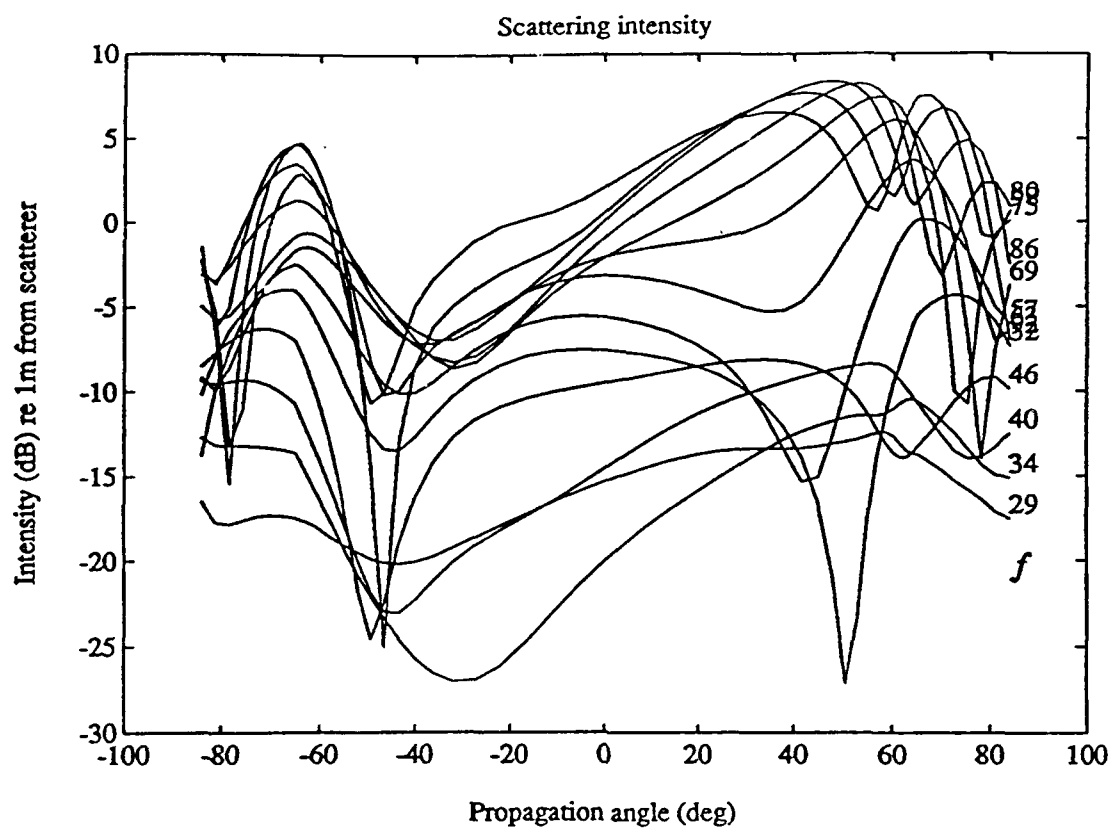
Figure 5.19: Scattered intensity for fluid keel, Experiment 40. The intensity is computed from the scattered presure field shown in Figure 5.9. The complicated behavior at the angles near grazing is due to scatter from the source head wave. At the middle angles, near $\Theta = 0$, there is less influence from the head wave and the field appears to be a deformed dipole.

The scattered intensity of the fluid keel in Experiment 40, shown in Figure 5.19, is much more complicated than that of the fluid floe shown in Figure 5.18. At the mid-range of propagation angle, near $\Theta = 0$, the intensity pattern is essentially dipolar. At the higher scattering angles, near grazing, the influence of the scattered plate waves causes severe distortions to the dipolar pattern. The plate wave scatter is caused by the source head wave discussed earlier in Section 5.3.2.

216

<u>Elastic inclusions.</u> The scattered intensity for the elastic floe of Experiment 35 is shown in Figure 5.20. Here we see a dramatic difference between the scattered intensity of the fluid floe and that of the elastic floe. The former is essentially a dipole while the latter is a quadrupole. Evidently there is a shear mode which interacts with the compressional mode to produce a null in the scattered intensity pattern. As we saw in the scattered pressure field in Figure 5.10, there is a 180° phase shift in the signal that occurs at the null; positive pressure in the forward direction corresponds to negative pressure in the backward direction and vice versa.

There is not an exact analytic solution to the elastic floe problem with which to compare the numerical result. There is, however, an exact solution to the "near by" problem of scatter from an elastic cylinder insonified by a primary source and a negative image source. For convenience, I call this the *pseudo-floe* problem. The geometry of this problem is shown in Figure 5.16. The problem is not identical to the elastic floe because the shear stress in the elastic cylinder is anti-symmetric with respect to the cylindrical coordinate φ [16]. Because of this anti-symmetry, the shear stress along the x-axis does not sum to zero and does not match the free surface boundary condition required for the elastic floe problem. As we will see, however, the analytic solution to the pseudo-floe problem provides insight into the effects of high shear modulus in the ice. Using the analytic solution for scatter from elastic cylinders [16,62], the scattered pressure for the pseudo-floe problem may be written

$$P_{scat} \xrightarrow{kr \gg 1} -i4P_o\sqrt{\frac{2}{\pi kr}}e^{i(kr-\pi/4)} \sum_{m=1}^{\infty} \sin(\eta_m)e^{-i\eta_m}\sin(m\varphi)\sin(m\gamma), \qquad (5.25)$$

where the scattering phase angle η_m is a complicated function of Bessel functions, compressional and shear wavenumbers, and density. The interested reader may find the exact expression for η_m in Stanton [62].

Evaluating the sum in Equation (5.25) for $m = 1,2,3,4$, the frequency range $20 \leq f \leq 100$, a cylinder radius of $a = 6\,m$, and using elastic ice material properties produces

217
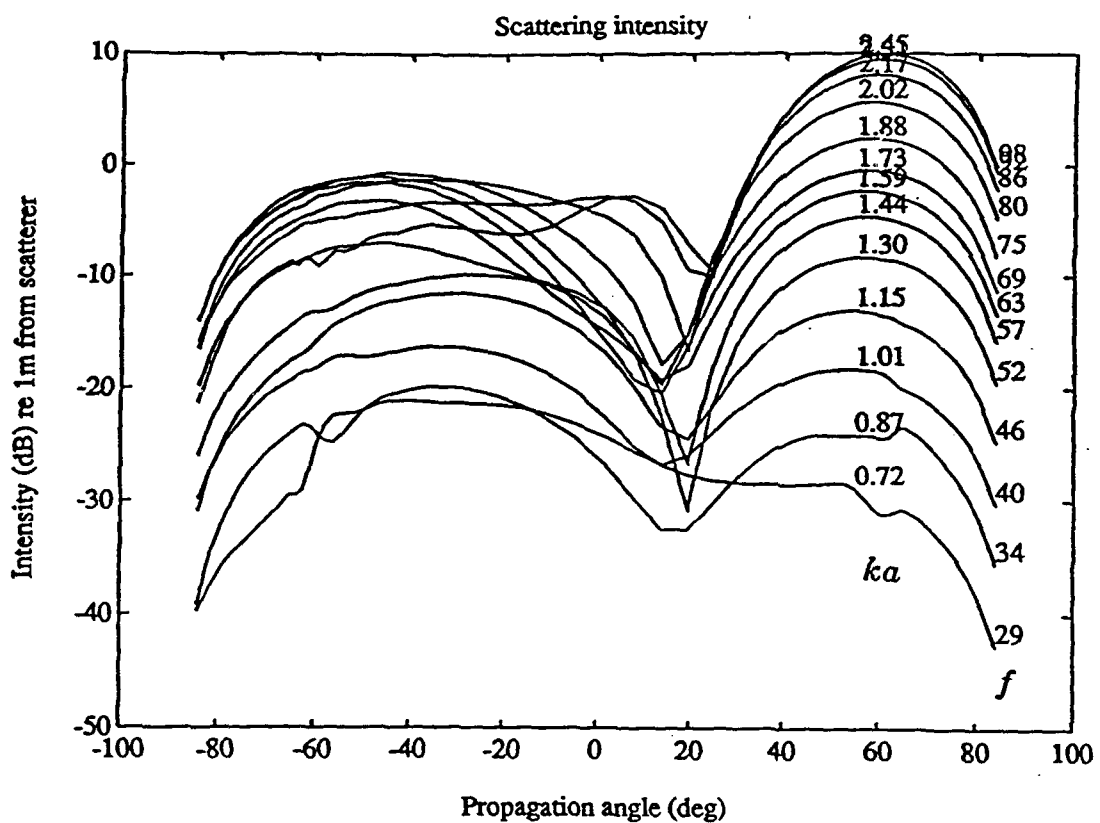
Figure 5.20: Scattered intensity for the elastic floe, Experiment 35. The intensity is computed from the scattered pressure field shown in Figure 5.10. There is not an exact analytic solution with which to compare the numerical estimate but the analytic solution to a "near by" problem, called the pseudo-floe problem, is shown in Figure 5.21. The notable feature in both figures is the presence of the deep null at the angles near normal incidence. The elastic floe scatters in a quadrupole pattern in contrast to the dipole pattern seen for the fluid floe.

Analytic elastic scattering intensity
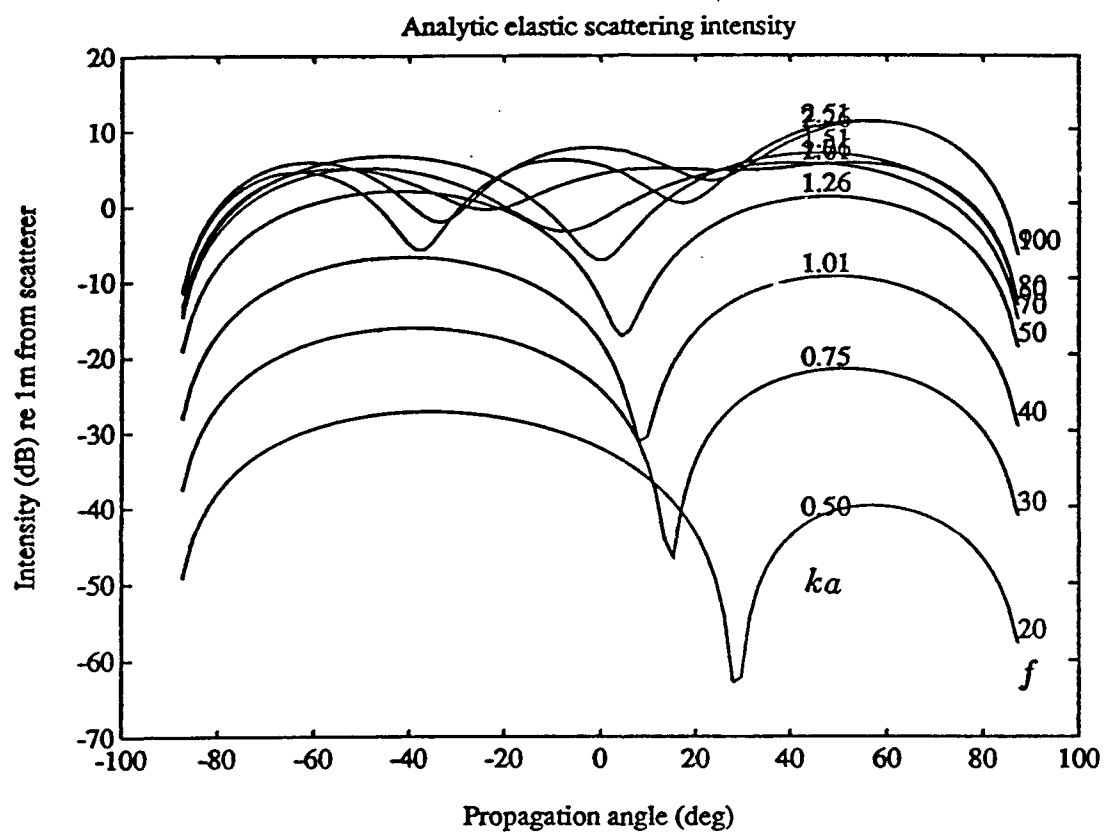
Figure 5.21: Analytic solution to the pseudo-floe problem. This solution is exact for an elastic cylinder insonified by a primary and a negative image source as shown in Figure 5.16 with $\gamma = 10°$. The problem is not identical to the elastic floe problem because the shear stress along the x-axis in not zero and does not match the free surface boundary condition required by the elastic floe. Nevertheless, the scattered field is qualitatively similar to that of the elastic floe showing a deep null at angles near $\Theta = 0$.

219
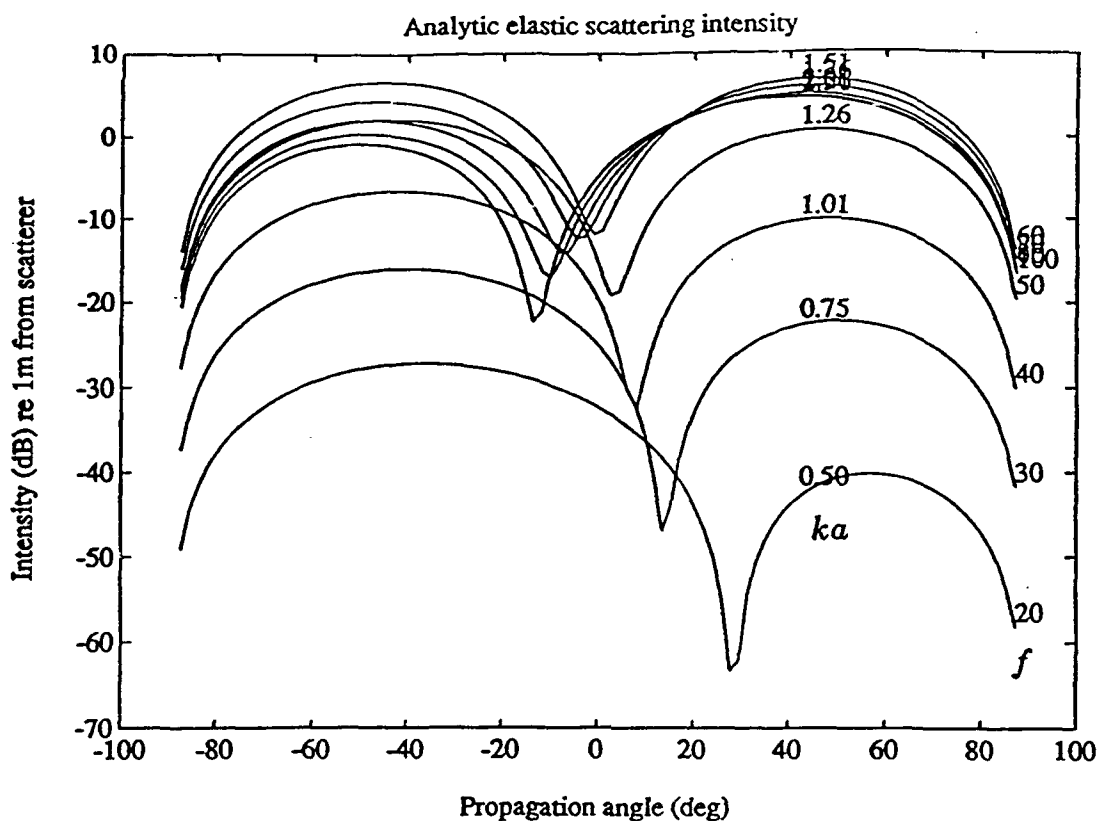
Figure 5.22: Scattered intensity for the pseudo-floe analytic problem computed using only the $m = 1, 2$ terms of the series in Equation (5.25). The deep null is clearly caused by the interaction of the dipole term, $m = 1$, and the quadrupole term, $m = 2$. Even for $ka = 0.5$ the strength of the quadrupole term is sufficient to cause the null.

the scattered intensity shown in Figure 5.21. The character of the scattered field for the pseudo-floe problem is similar to that of the elastic floe. Specifically, at low frequency there is a deep null in the intensity near the zero propagation angle. The low frequency null is caused by the interaction of the dipole and the quadrupole term as may be seen by the computation of the scattered intensity using only $m = 1, 2$ in Equation (5.25). This result is shown in Figure 5.22. Without going into the algebraic details, let me state that the

scattered intensity, Φ_s, may be written for small ka as

$$\Phi_s \sim \left| \underbrace{\sin\varphi\sin\gamma\left[\frac{\tan\eta_1}{1+\tan\eta_1^2}+\frac{i\tan\eta_1^2}{1+\tan\eta_1^2}\right]}_{\text{dipole}} + \underbrace{\sin(2\varphi)\sin(2\gamma)\left[\frac{\tan\eta_2}{1+\tan\eta_2^2}+\frac{i\tan\eta_2^2}{1+\tan\eta_2^2}\right]}_{\text{quadrupole}} \right|^2 ,$$

(5.26)

where $\tan\eta_1 \sim O([ka]^2)$ and $\tan\eta_2 \sim O([ka]^4)$. Only the leading order terms of the Bessel functions were kept in deriving this expression. In Φ_s the pure quadratic dipole term is $O([ka]^4)$, the cross term between the dipole and the quadrupole is $O([ka]^6)$, and the pure quadratic quadrupole term is $O([ka]^8)$. Clearly, for small ka the scattered intensity must be a dipole pattern. This is seen in Figure 5.23, where the values of ka span $0.03 < ka < 0.53$. For ka less than about 0.3 the field is dipolar, while for larger values the field is quadrupolar. The interaction of the dipole and the quadrupole to produce the null must involve higher order terms in the Bessel function series expansion. An analysis including these terms would be extremely tedious and I have not carried it out.

Another bit of analytical insight may be gained from the pseudo-floe problem. Specifically, what is the nature of the dipole to quadrupole transition with regard to shear modulus. From analytic analysis of the fluid floe, we know that for zero shear modulus the field is a dipole. When the shear modulus is high, as for the ice case, the field is a quadrupole. By varying the shear speed from $C_s = 0\,m/s$ up to $C_s = 1600\,m/s$, one finds that the scattered intensity abruptly changes character from dipolar to quadrupolar. The transition range for shear speed is $200 < C_s < 400\,m/s$, as shown in Figure 5.24. Thus, the character of the field is insensitive to the value of shear speed, except in the narrow transition region. This reinforces my decision to model only two types of ice: fluid ice, with $C_s = 0\,m/s$, and elastic ice, with $C_s = 1600\,m/s$. With this approach I capture the dominant character of the scattered field using only gross estimates of the shear speed for the two cases.

221
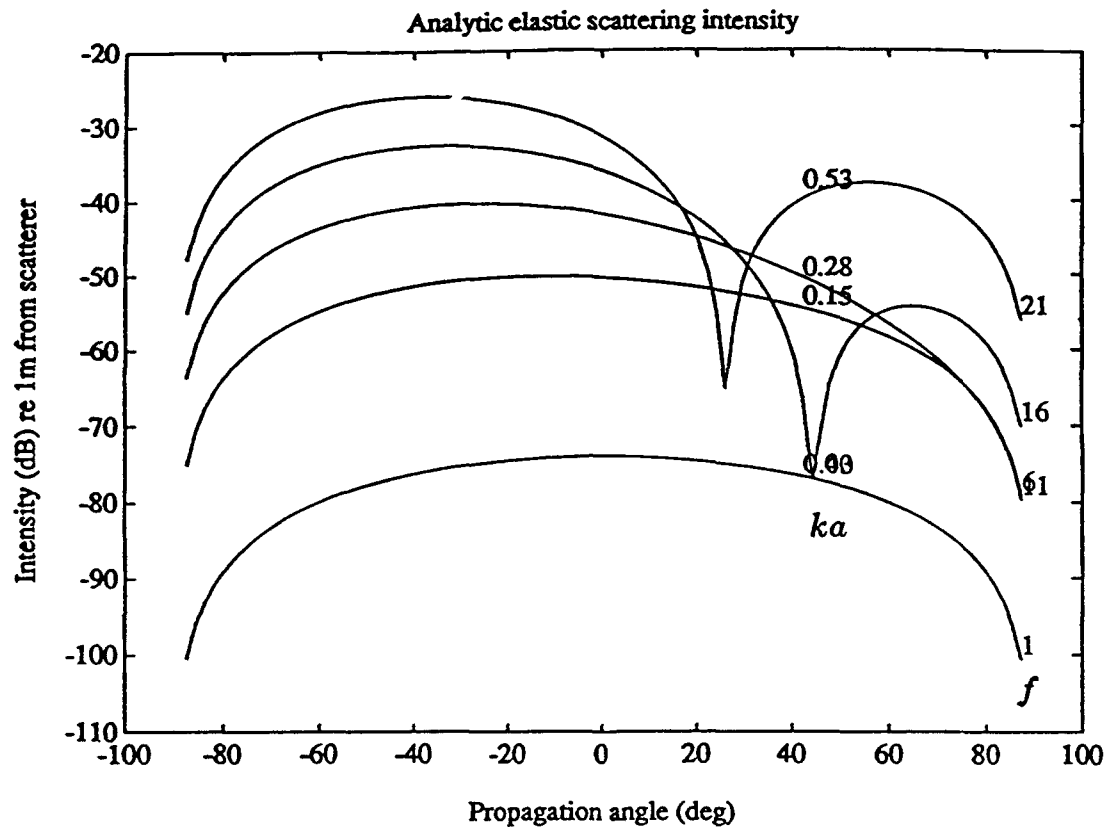
Figure 5.23: Scattered intensity of pseudo-floe problem for very low ka. Below $ka \sim 0.3$ the field is dipolar as predicted by the leading order analysis of Equation (5.26). For higher values of ka the quadrupole term in the series begins to have influence. This transition is not predicted by the leading order analysis.
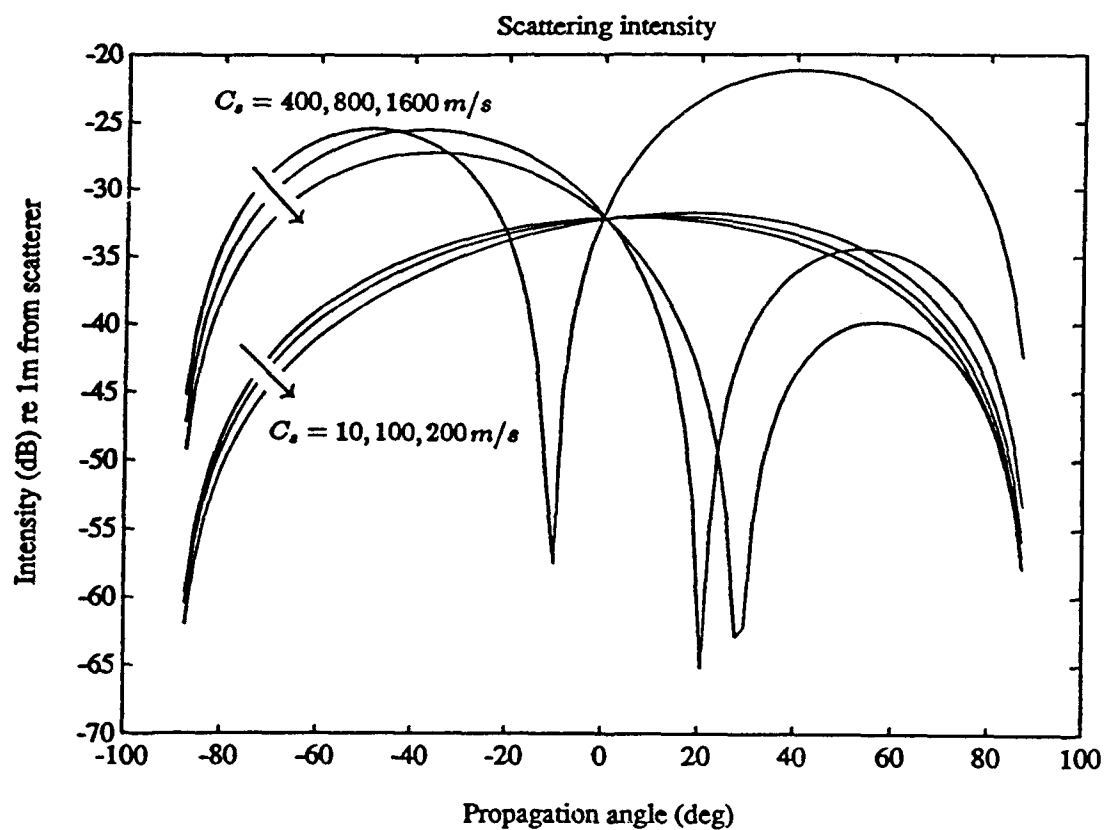
Figure 5.24: Scattered intensity for the pseudo-floe problem with $ka = 0.5$ for various shear speeds. Shear speed values less than $C_s = 200\,m/s$ produce a dipolar field, while values greater than $C_s = 400\,m/s$ produce a quadrupolar field. The transition takes place abruptly, with the character of the field on either side of the transition largely immune to variations of shear speed.

At this point I have described the quadrupolar field produced by an elastic floe phenomenologically and mathematically. What about the physical mechanism? For ease of illustration, this discussion is restricted to scatter from elastic cylinders. Though I didn't explain at the time, the dipole term in Equation (5.26) contains no shear effects in η_1. The shear terms are only present in the quadrupole term involving η_2. This leads to the conjecture for the physical mechanism shown in Figure 5.25. I suggest that the total field is the sum of a compressional mode, the dipole term, and a shear mode, the quadrupole term. The compressional mode corresponds to the cylinder oscillating back and forth, being forced by the incident plane wave. Shear modes in an elastic cylinder must be anti-symmetric with respect to the angular variable, φ. In particular, Faran shows the shear stress to be of the form $\sin(m\varphi)$ [16]. The quadrupole term corresponds to $m = 2$ and to the quadrilateral symmetry shown in Figure 5.25. In this mode there is zero shear stress along the diameters in line and perpendicular to the direction of the incident plane wave. The nulls in the scattered field are caused by an interaction of the normal particle velocities and stresses of the compressional and shear mode on the surface of the cylinder. Evidently, for large shear modulus, the strength of the shear mode is sufficient to create a quadrupolar scattered field. At low shear modulus the shear mode is too weak to have any effect. The question of why the scattered field changes so rapidly from dipolar to quadrupolar with respect to shear velocity remains unanswered.

Now, I return to the numerical experiments. The scattered intensity of the elastic keel, Experiment 38, is shown in Figure 5.26. Here again, as with the elastic floe, we see the fundamental quadrupolar nature of the field. Although the field is more complicated than that of the floe, the deep nulls near the zero propagation angle are clearly evident. The extra complexity is due to scattering of the source head wave as discussed earlier in Section 5.3.2.

224

Total Field = Dipole (Compressional mode) + Quadrupole (Shear mode)
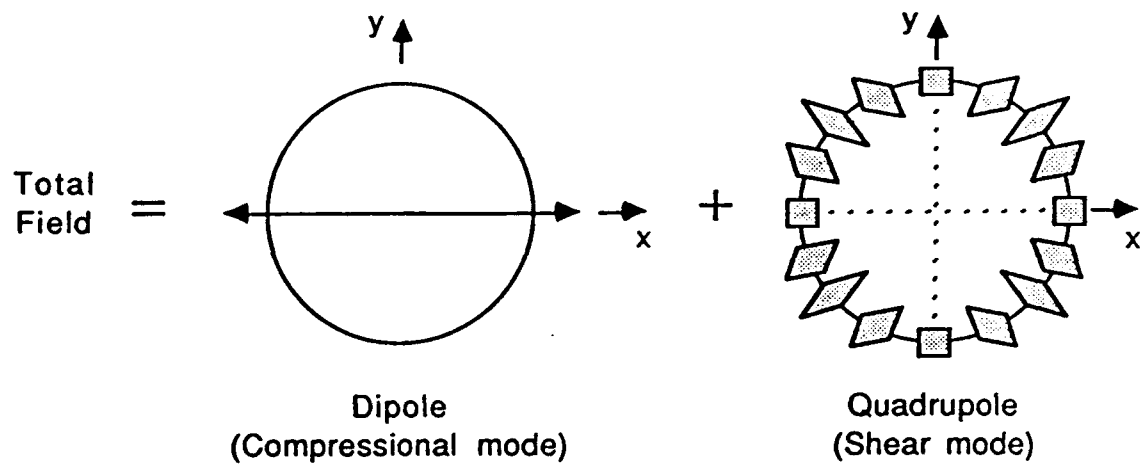
Figure 5.25: Physical mechanism conjecture explaining quadrupole scattered field for elastic cylinder. The total field scattered from an elastic cylinder excited by a plane wave propagating along the x-axis is the sum of two modes of oscillation. The first is a compressional mode and corresponds to the cylinder oscillating back and forth; it produces a dipolar field. The second is a shear mode and corresponds to balanced torsional oscillations; it produces a quadrupolar field.

Ice edge. The scattered intensity for the ice edge model in Experiment 36 is shown in Figure 5.27. Recall that the scattered field for the ice edge was computed using the response from a free surface as the coherent field. Again, we see higher amplitude in the forward direction with a null at low propagation angles, high grazing angles, indicating a quadrupolar field.

An approximate analytic solution for scatter from an ice edge is given by Dahl [11] but I have not compared his result with mine. I do, however, use his result to compare with my estimate of specular energy loss discussed later in Section 5.5.3.

Excitation of plate waves

Any roughness element acts as a transducer for the conversion of acoustic energy in the water into elastic plate wave energy. One can think of the roughness element as a window through which energy passes between the two media. For incidence angles away from the Mach angle

225

Scattering intensity
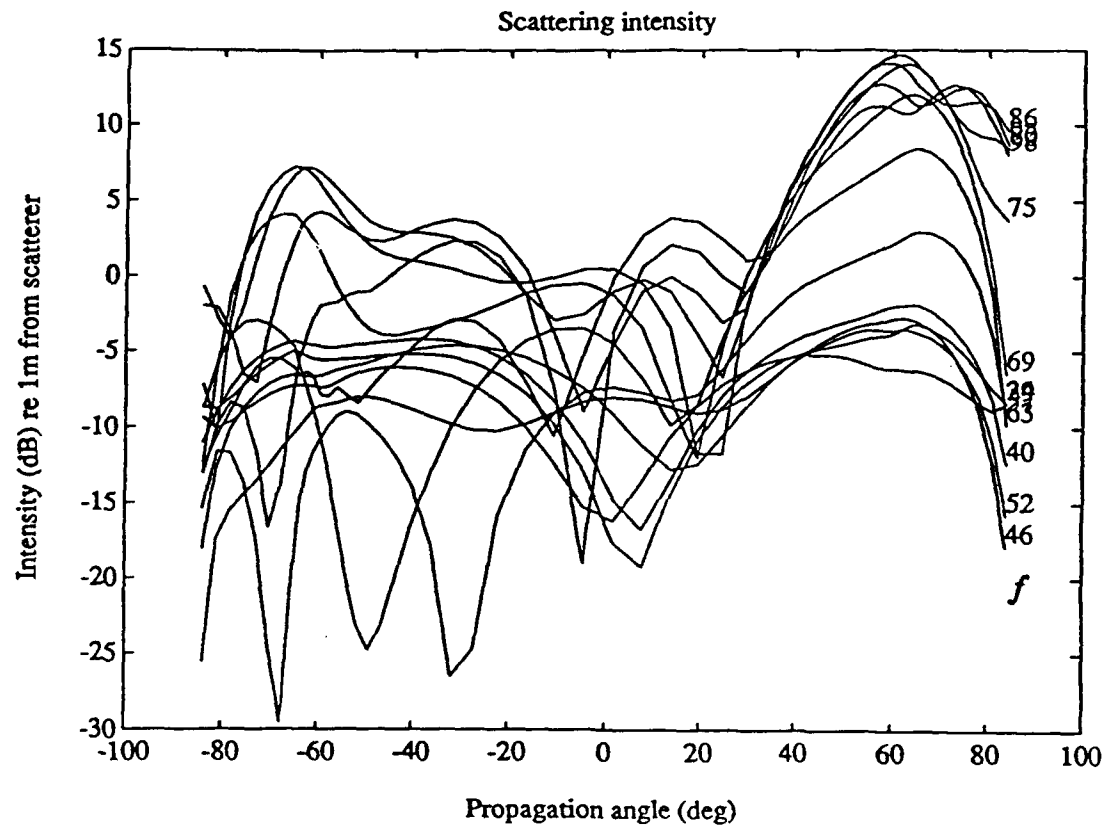
Figure 5.26: Scattered intensity for elastic keel, Experiment 38. The intensity is computed from the scattered pressure measurements shown in Figure 5.12. The field is quadrupolar with deep nulls near the zero propagation angle. The extra complexity of this field compared to that of the elastic floe is due to the scatter of the source head wave, which is generated by the isotropic line source.
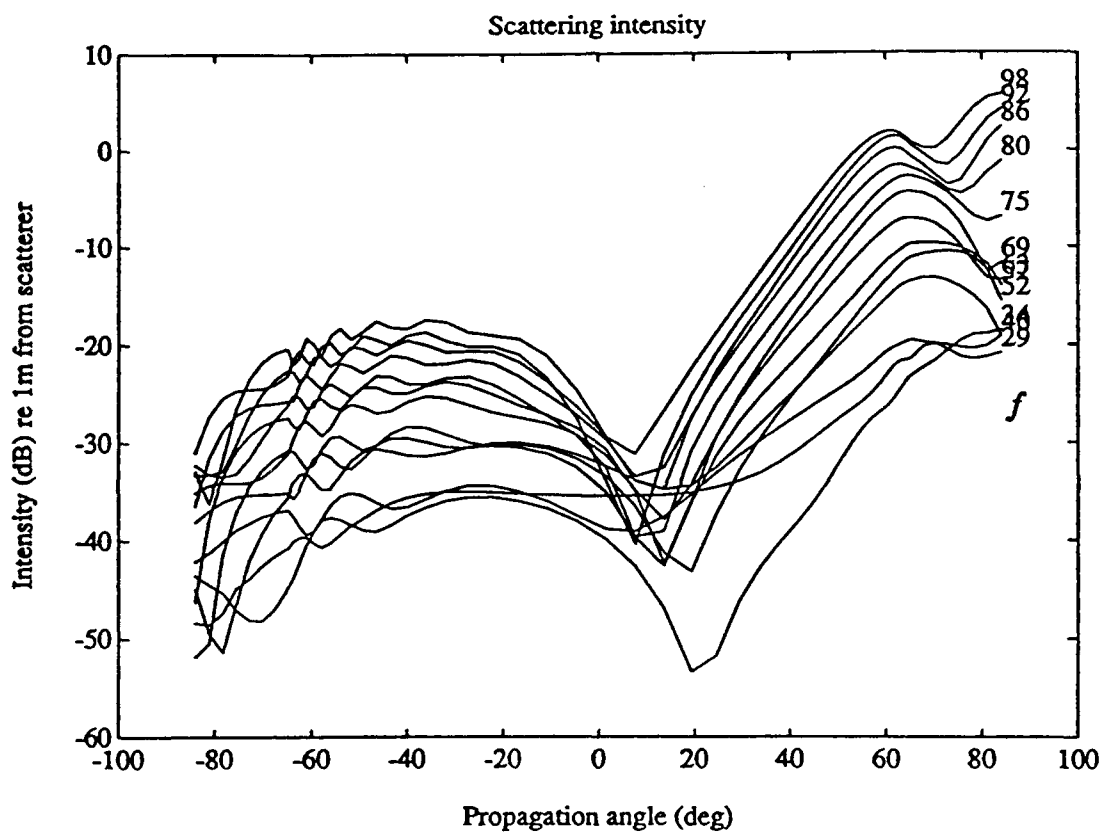
Figure 5.27: Scattered intensity for ice edge relative to a free surface, Experiment 36. The intensity is computed from the scattered pressure measurements shown in Figure 5.13. The field is quadrupolar with about 20 dB higher strength in the forward direction.

Exp. 1238; Total power flux for high shear keel model at t = 105.8 ms

Abs. Mx. = 287325
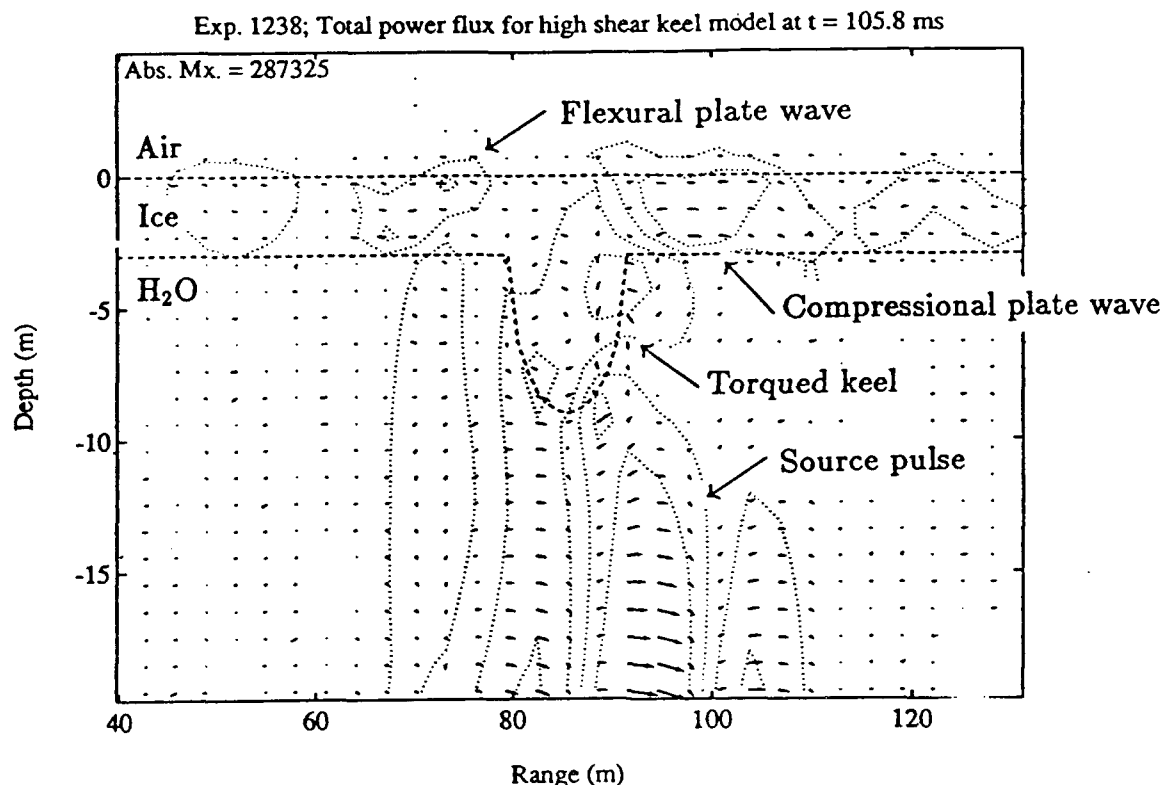
Figure 5.28: Excitation of plate waves at 106 ms for the elastic keel, Experiment 38. The arrows point in the direction of total power flux. Their length is a measure of the power flux magnitude. The dotted contours are normal stress in the water and horizontal normal stress in the ice. Labels indicate the passing source pulse, the torquing of the keel, and the presence of plate waves in the ice. Both compressional (symmetric) and flexural (anti-symmetric) components may be seen in the plate waves.

there is no energy conversion in the absence of the window. Ridges and the ice edge both transfer energy into the adjoining ice sheets. The best way to visualize this is with power flux snapshots taken during the passage of a sound pulse. Figure 5.28 shows the excitation of plate waves for the elastic keel model of Experiment 38. The power flux computations for this figure are based on Equation (4.30)[1] in Chapter 4, where $\phi_{T_s} = -\underline{\sigma}_{T_s}\underline{v}_{T_s}$.

Excitation of the plate wave is also seen in the scattered power flux time series computed from receivers in the ice and shown in Figure 5.29. The plate wave power flux is computed as described in Chapter 4, Equation (4.35). A negative value of power flux means that
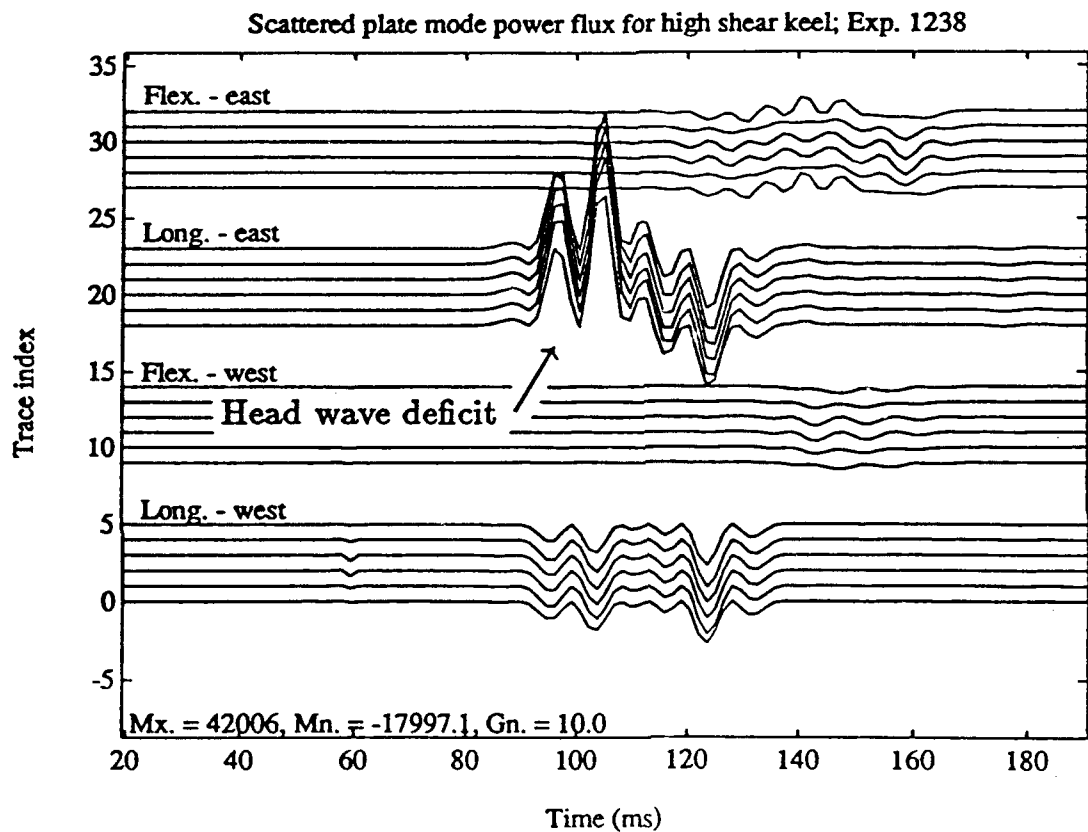
Figure 5.29: Plate wave scattered power flux for the elastic keel, Experiment 38. "Flex" means the flexural plate wave power flux, "Long" means the longitudinal plate wave power flux, and "east" and "west" designate the leg of the measurement array from which the power flux is computed. Except for the artifact of the source head wave (labeled), the longitudinal component appears to have slightly higher scatter in the forward direction and the flexural component has considerably more scatter in the forward direction.

power is leaving the control volume defined by the box array, while a positive value means power is entering the volume. If not for the source head wave, the scattered plate wave power flux would always be negative, that is power would always be moving away from the scatterer. With this interpretation in mind, consider the longitudinal mode on the east leg of the array. Here we see the scatterer creating a deficit in the source head wave that exists in the absence of the scatterer. A positive power flux means that the source head wave in the coherent model, flat ice, is supplying power to produce some of the scattered field in the scatter model.

The fraction of the total scattered energy captured in the ice plate is small: order 10% of the total energy that hits the ridge. The added dissipation used to stabilize the finite difference scheme, however, attenuates a large fraction of the plate wave energy injected into the ice and makes quantification of the plate wave energy impossible. Figure 5.30 shows a map of where the added dissipation has removed energy from the computational domain for the elastic keel in Experiment 38. No energy is dissipated in the water away from the ice. The plate waves and scattered elastic modes in the keel are the only waves affected by the added dissipation. As has been shown through comparisons with analytic solutions, the scattered field in the water is not greatly affected by the added dissipation. Despite this assertion, the added dissipation causes nagging problems, which have not yet been adequately addressed.

5.5.2 Plate wave scatter

For sound propagating in an ice plate there are two scattering mechanisms that occur when a roughness element is encountered. In the idealized scenario of an acoustic plane wave insonifying an elemental scatterer, these mechanisms do not occur since 1) no plate waves exist before the scatterer is insonified and 2) the plate waves generated at the scatterer
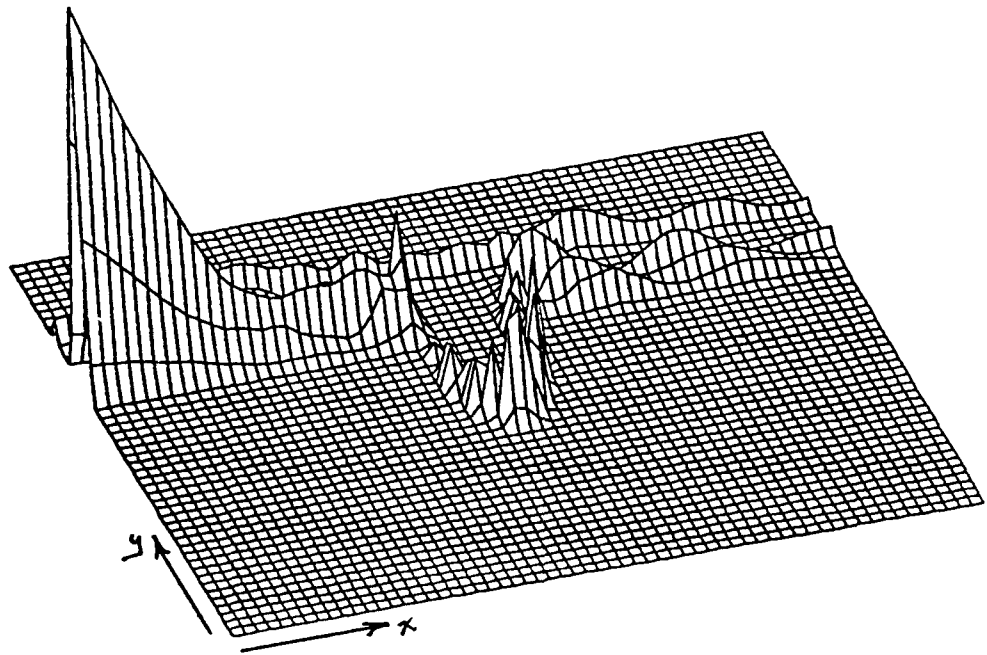
Figure 5.30: Map of energy density lost to added dissipation for the elastic keel, Experiment 38. The energy is lost primarily from plate waves, making a quantitative interpretation of the plate wave energy impossible.

never encounter another roughness element.

The experiments described in this chapter attempt to emulate the idealized scenario but fall short. Specifically, the isotropic line source injects energy into the ice plate in the form of the source head wave as described in Section 5.3.2. Because of this, the elemental scatterer is insonified first, by the head wave in the ice, and then, by the pseudo plane wave in the water. Thus, despite the troublesome presence of the source head wave, it is useful for showing scattering mechanisms that occur when a plate wave encounters a roughness element.

When sound traveling in a plate encounters a scattering element there is a change in impedance and scatter occurs. The scatter can be classified into one of two categories as shown in Figure 5.14(c) and (d): scatter of plate waves into plate waves and scatter of plate waves into acoustic waves.

I first demonstrate the scatter of plate waves into plate waves. Figure 5.31(a) shows a snapshot of the power flux of the compressional source head wave excited by the isotropic line source in flat ice. Note, especially, the strong compressional packet located at a range of 100 m. The source head wave has a velocity roughly twice that of the water wave and, hence, arrives at any given point along the ice sheet before the water wave. Figure 5.31(b) shows a snapshot at the same time as Figure 5.31(a) but for the case when the semi-circular keel of Experiment 38 is present. The water wave has not yet reached the keel, but the source head wave has already scattered from the impedance mismatch in the ice caused by the keel. In both the up and down range directions the plate wave now contains flexural, or anti-symmetric components, that are due to the scattered head wave. Again, note the wave packet at a range of 100 m. What was a compressional wave packet has been converted to a predominantly flexural wave packet through the influence of the scatterer.

Evidence for the second scattering mechanism, plate waves to acoustic waves, has already
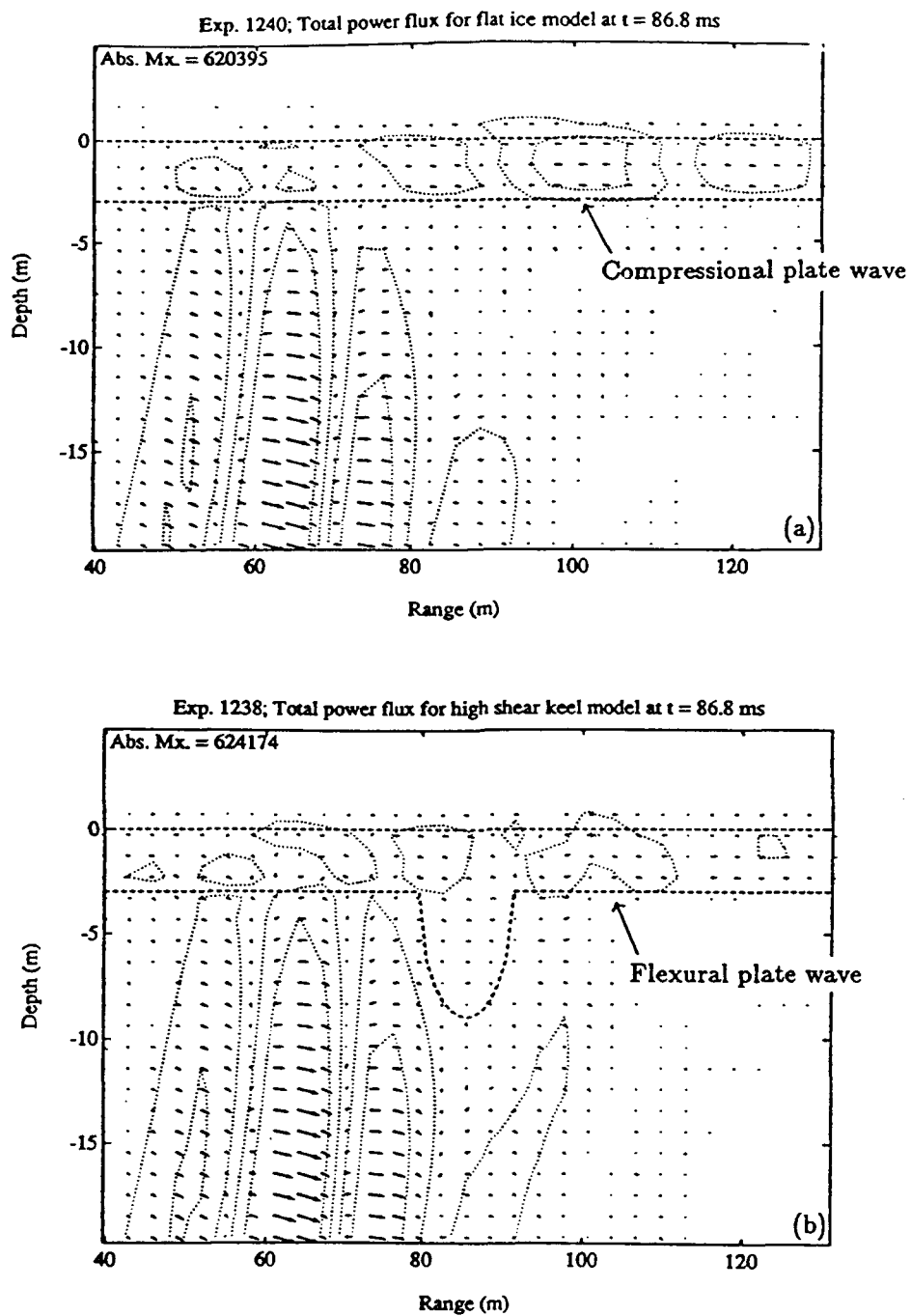
Figure 5.31: Power flux snapshots for (a) flat ice and (b) elastic keel, Experiment 38, at 87 *ms*. (a) The source head wave caused by the isotropic line source has moved out ahead of the water wave. Note especially the compressional wave packet at a range of 100 *m*. (b) The water wave has not yet reached the elastic keel but the source head wave has scattered from the impedance change in the ice plate due to the keel and scattered plate waves both up and down range. Note especially the flexural wave packet at a range of 100 *m*, which was a compressional wave packet in the flat ice experiment.

233

been shown in Figure 5.10 and 5.12. The former shows the scattered field for the elastic floe in Experiment 35, where no source head wave exists. The first arrival in the scattered time series is due to the direct acoustic scatter from the floe. By contrast, the scattered field in Figure 5.12 is from the elastic keel in Experiment 38 and the first arrival in the time series corresponds to the acoustic scatter of the source head wave.

In principle, neither the scatter of plate waves into plate waves nor the scatter of plate waves into acoustic waves occur for true plane wave excitation of an elemental scatterer. In reality, however, elemental scatterers never exist in nature, and plate wave scatter must occur often. In particular, the scatter induced injection of plate wave energy and the subsequent reconversion to acoustic energy by neighboring scatterers must play a part in increasing back ground noise. These are multiple scattering mechanisms, which are not studied in this thesis. The framework for such a study, however, is in place and future efforts will be made in this direction.

5.5.3 Specular energy loss

For plane waves incident on a scattering element there is a direct loss from the coherent field due to wide angle scatter and to the excitation of plate waves as discussed in Section 5.5.1. The loss from the coherent field and its dependence on frequency is the principle quantity of interest in understanding rough surface scatter in long-range propagation in the Arctic.

It is assumed that there is a power law relationship between specular energy loss, L_e, and frequency; the loss is of the form $L_e \propto f^\alpha$. On a log-log plot of loss versus frequency the power law becomes a straight line with a slope of α. This is how the specular loss curves are presented. Thus, α is both an exponent and a slope. The terms are used interchangeably. As we will see, the value of α depends on the scatterer type. For the elastic scatterer $\alpha \sim 4.5$, for the ice edge $\alpha \sim 2$, and for the fluid scatterer $\alpha \sim \frac{3}{2}$.

The other characteristic of the loss curve is its magnitude. As shown in Section 5.5.1, the specular loss is proportional to scatterer mass. In this section I show that the excitation of plate waves by elastic keels roughly doubles the loss relative to that of a floe with an identical shape. A fluid keel has roughly the same loss as that of a floe with an identical shape because of the poor coupling to the surrounding ice sheet.

Fluid inclusions

Using an analysis similar to that for the mass loading effect, the specular energy loss as a function of frequency can be shown to have a slope of $f^{\frac{3}{2}}$ for small ka. Refer back to Equations (5.12)-(5.16). Recall, particularly, the cross term $\Re(P_{coh}P^*_{scat}) \sim O(P_o^2(ka)^2\sqrt{\frac{2}{\pi kr}})$, which for fixed k reduced to $O([ka]^2)$. For fixed scatter size, a, however, the cross term is, from Equation (5.16)[1],

$$\Re(P_{coh}P^*_{scat}) \sim O([ka]^{\frac{3}{2}}). \tag{5.27}$$

Using this in Equation (5.13) yields the energy reflection coefficient

$$R_e \sim 1 + O([ka]^{\frac{3}{2}}) \tag{5.28}$$

for fixed a. Finally, this leads to a specular energy loss

$$L_s \sim -10\log_{10} R_e \sim O([ka]^{\frac{3}{2}}). \tag{5.29}$$

Thus, for fluid floe, we expect the specular loss to go as $f^{\frac{3}{2}}$. This power law, you may recall, is nearly the same as that estimated from the observed long-range propagation data in the Arctic, discussed in Chapter 1.

The numerical estimate of specular loss computed for the fluid floe in Experiment 37, using Equations (5.9) and (5.10), is shown in Figure 5.32. The fluid floe power law estimate from numerical data is $f^{1.4}$, which compares favorably with the analytic power law for small ka of $f^{1.5}$.

235
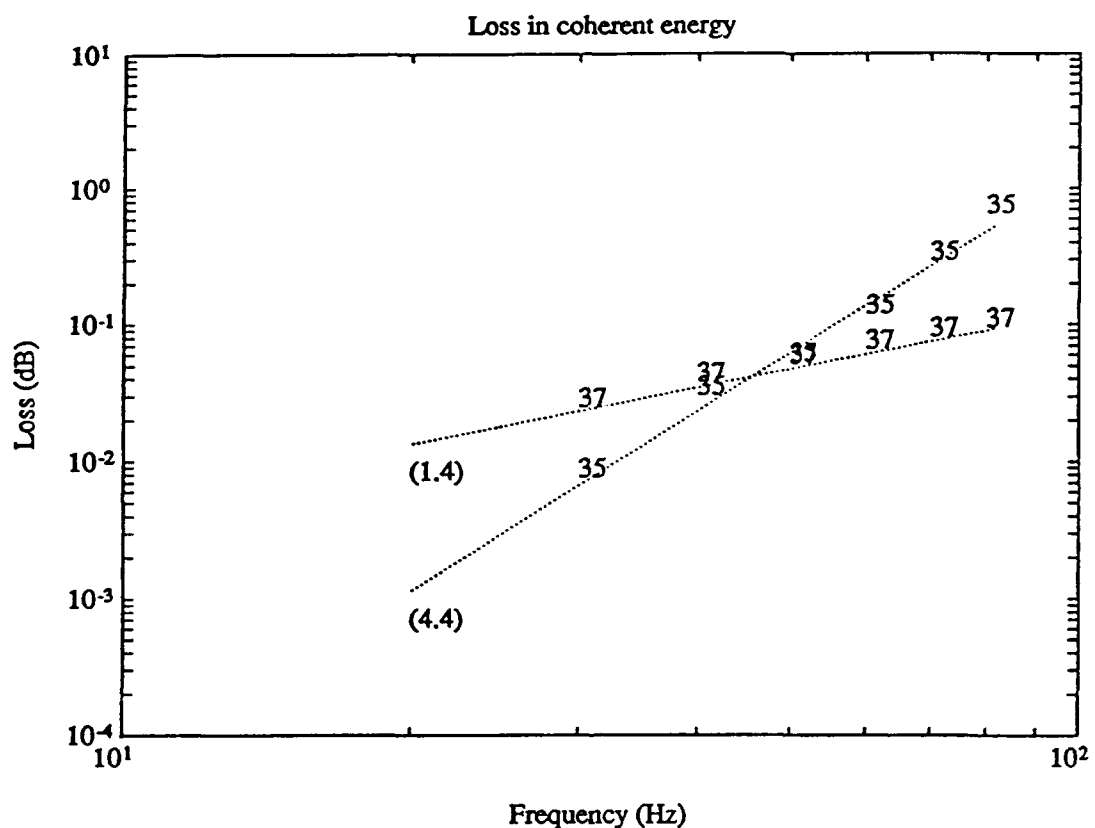
Figure 5.32: Specular energy loss for fluid (37) and elastic (35) floe. The slope of the energy loss for the fluid floe is 1.4, which compares to a slope of 1.5 computed for small ka using the analytic solution. The slope for the elastic floe is 4.4, three times greater than that of the fluid floe.
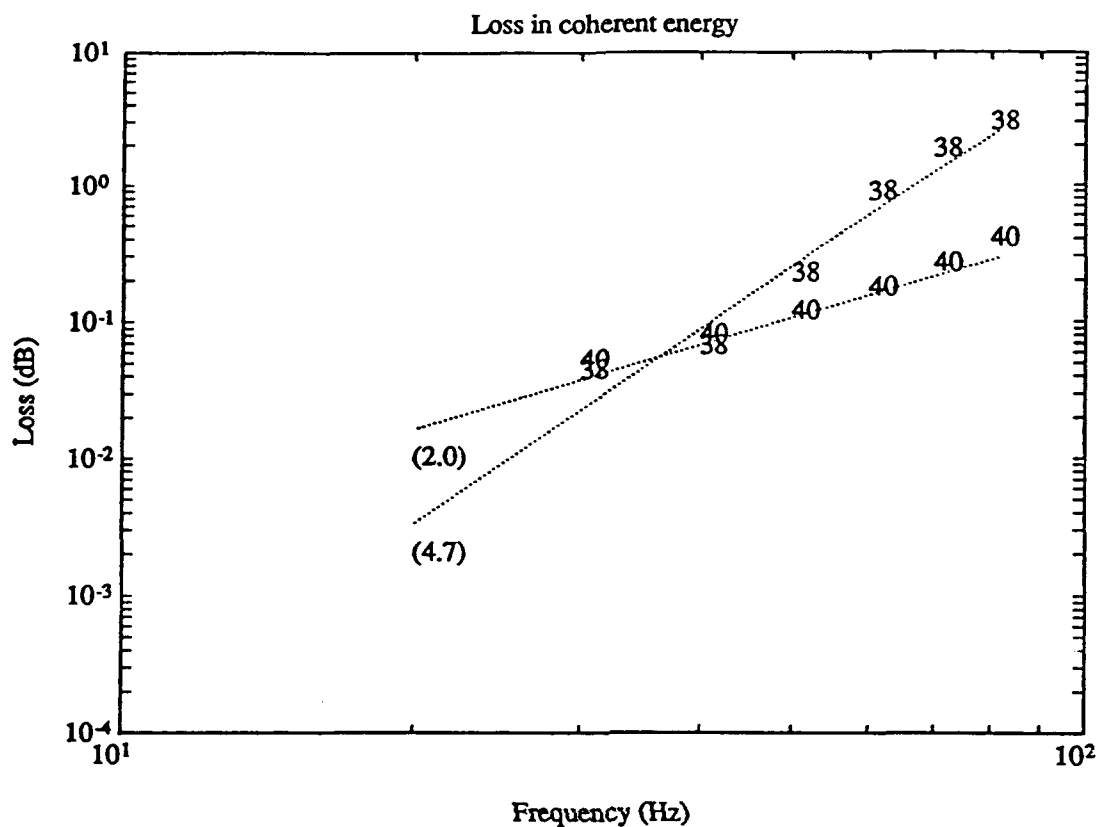
Figure 5.33: Specular energy loss for fluid (40) and elastic (38) keel. The slopes, as noted in the figure, are larger than those of the corresponding floe experiment. This is due to the scatter from the source head wave.

The specular energy loss for the fluid keel is shown in Figure 5.33 and has a power law of $f^{2.0}$, which is comparable to but larger than that of the fluid floe. The larger slope is evidently due to the effects of the source head wave scatter.

Plate waves are not strongly excited by a fluid keel due to the poor shear coupling between keel and the elastic ice plate. The specular loss comparison between the fluid floe of Experiment 37 and the fluid keel of Experiment 40 is shown in Figure 5.34. The mass of the fluid floe is $57\,m^2$, while that of the fluid keel is $93\,m^2$; the increase in loss would be about 1.7 for the keel relative to the floe, if loss were exactly proportional to mass. The data shows an increase of about 2.3 at $50\,Hz$ suggesting that mass loading is the dominant
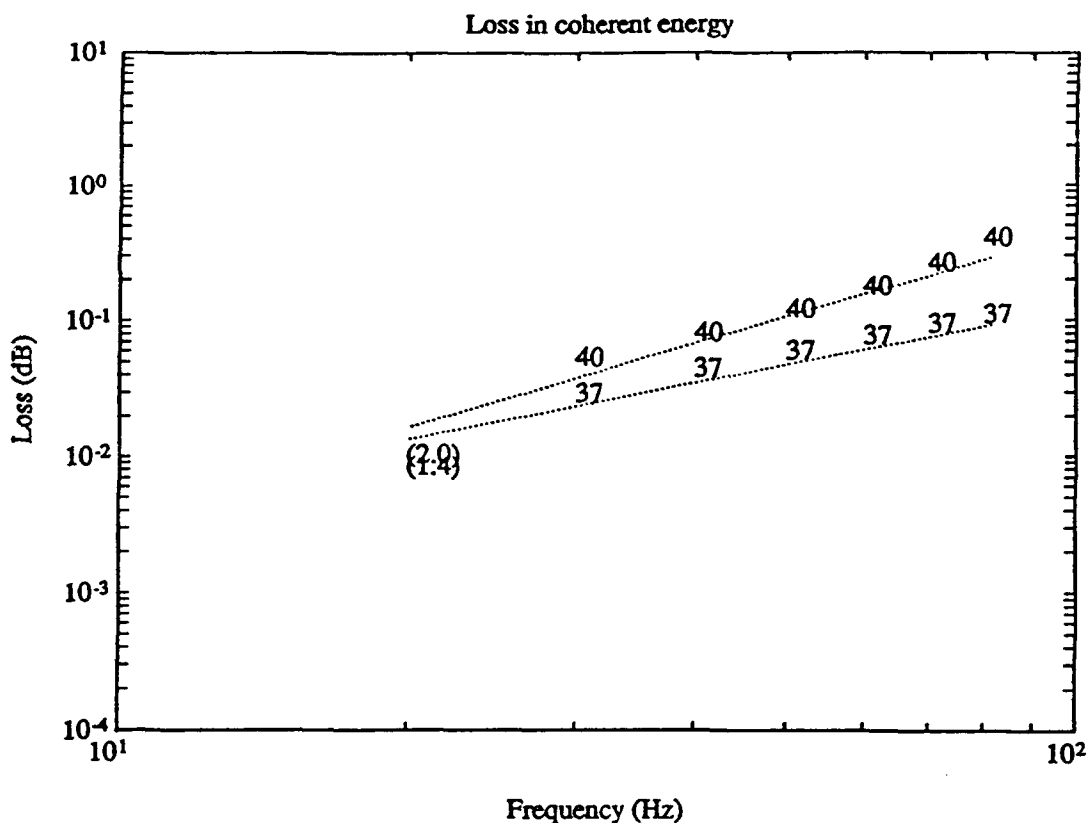
Figure 5.34: Specular loss of fluid floe (37) versus fluid keel (40). The increase in loss may be assigned almost entirely to the increase in mass for the keel relative to the floe. Excitation of plate waves by the fluid keel is not an important mechanism.

effect.

As described in Section 5.5.1, an absolute quantitative evaluation of plate wave energy cannot be made. Nevertheless, a relative comparison may be made for the plate wave excitation produced by the fluid keel in Experiment 40 versus the elastic keel in Experiment 38. Figure 5.35 shows the scattered plate wave power flux for the two experiments. The plot in (a) is for the fluid keel and shows essentially no excitation of plate waves. The two big events are due to the nearly total reflection of the source head wave when it encounters the transition point between the elastic ice sheet and the fluid keel. The longitudinal mode on the west leg shows negative power flux indicating that the reflected head wave is traveling

away from the scatterer, back toward the source. The positive longitudinal power flux on the east leg is the deficit of the compressional wave that was present in the flat ice but has been reflected by the presence of the fluid keel. A very small amount of flexural power flux is seen in the east leg. A fluid keel is not an efficient transducer of acoustic to plate wave energy.

Elastic inclusions

A leading order analysis of the specular energy loss slope for an elastic floe and for small ka produces a value of $\alpha = \frac{3}{2}$ because there is no shear influence in the lowest order terms. Hence, an analytic estimate of the frequency dependence for $ka \sim O(1)$ would require retaining higher order terms in the asymptotic series of the Bessel functions. This analysis has not been carried out. Instead, I present the numerical results alone.

The specular loss for the elastic floe of Experiment 35 is shown in Figure 5.32 along with the loss for the fluid floe of Experiment 37. Figure 5.33 shows a similar comparison for the elastic keel versus the fluid keel. In both cases, the elastic inclusion has a slope two to three times larger than the corresponding fluid inclusion.

The magnitude of the specular loss for an elastic keel is dependent on two mechanisms: mass loading, similar to the effect seen for fluid keels, and the excitation of plate waves, shown in Figure 5.35(b), an effect not seen in fluid keels. To get a feel for the effect of plate wave excitation on specular loss, consider three elastic inclusion experiments: the elastic floe in Experiment 35 and the two elastic keels in Experiments 38 and 42. The elastic keel in Experiment 42 is formed by connecting a $3\,m$ ice sheet onto either side of the elastic floe. The keel has the same mass as the floe; any additional specular loss must be ascribed entirely to plate wave excitation. The keel in Experiment 38 is formed by placing the floe beneath a $3\,m$ sheet of ice, increasing the mass, and hence, increasing the loss through both

Scattered plate mode power flux for low shear keel; Exp. 1240

Mx. = 55596, Mn. = -45311.1, Gn. = 10.0

(a)

Scattered plate mode power flux for high shear keel; Exp. 1238

Mx. = 42006, Mn. = -17997.1, Gn. = 10.0

(b)
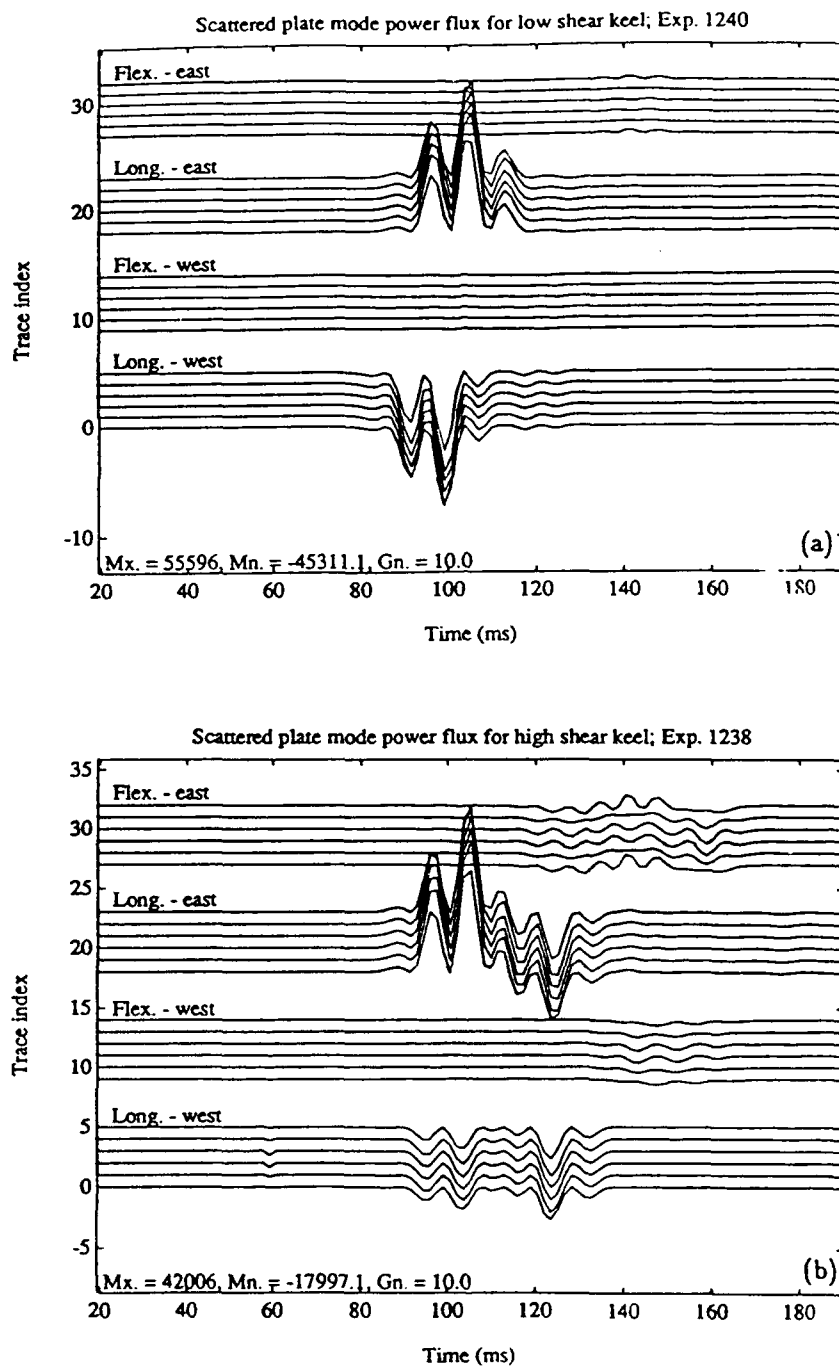
Figure 5.35: Comparison of plate wave excitation for fluid keel (a) versus elastic keel (b). These are plots of scattered plate wave power flux based on Equation (4.35). (a) Essentially no plate waves are excited by the fluid keel. The only events seen are the reflection of the source head wave on the west leg and the deficit of same in the east leg. (b) This is a repeat of Figure 5.29 showing the excitation of both types of plate waves in both directions due to an elastic keel. Clearly the elastic keel, in contrast to the fluid keel, is an efficient transducer of acoustic energy into plate wave energy.

240

mass loading and the excitation of plate waves.

The specular loss for the three cases is shown in Figure 5.36. The increase in loss between Experiment 35 and 42 is almost exactly a factor of 2. The increase is due entirely to the excitation of plate waves since the mass of the keel and that of the floe are virtually identical. In going from Experiment 42 to 38, there is an increase in loss of about 2.3. The extra loss is almost entirely due to an increase in mass. The excitation of plate waves roughly doubles specular energy loss for an ice plate thickness of 3 m. Other plate thicknesses have not been tested.

Ice edge

The specular loss due to an ice edge has an analytic power law with $\alpha = 2$ using the approximate analytic solution for scatter developed by Dahl [11]. In Figure 5.37 I show the numerical estimate for the specular energy loss due to an ice edge. The slope is $\alpha = 2.3$, which is in reasonable agreement with the analytic predictions. Presumably the magnitude of the loss is a function of the ice thickness, which for this study is fixed at 3 m, but I have not investigated this effect.

5.6 Summary

Analysis of the experimental results for a variety of elemental scatterers has produced a number of useful conclusions. I summarize these conclusions here for convenient reference.

- Specular energy loss is proportional to cross sectional area of the scattering object for floes and keels. Specifically,

$$L_e \propto A, \tag{5.30}$$
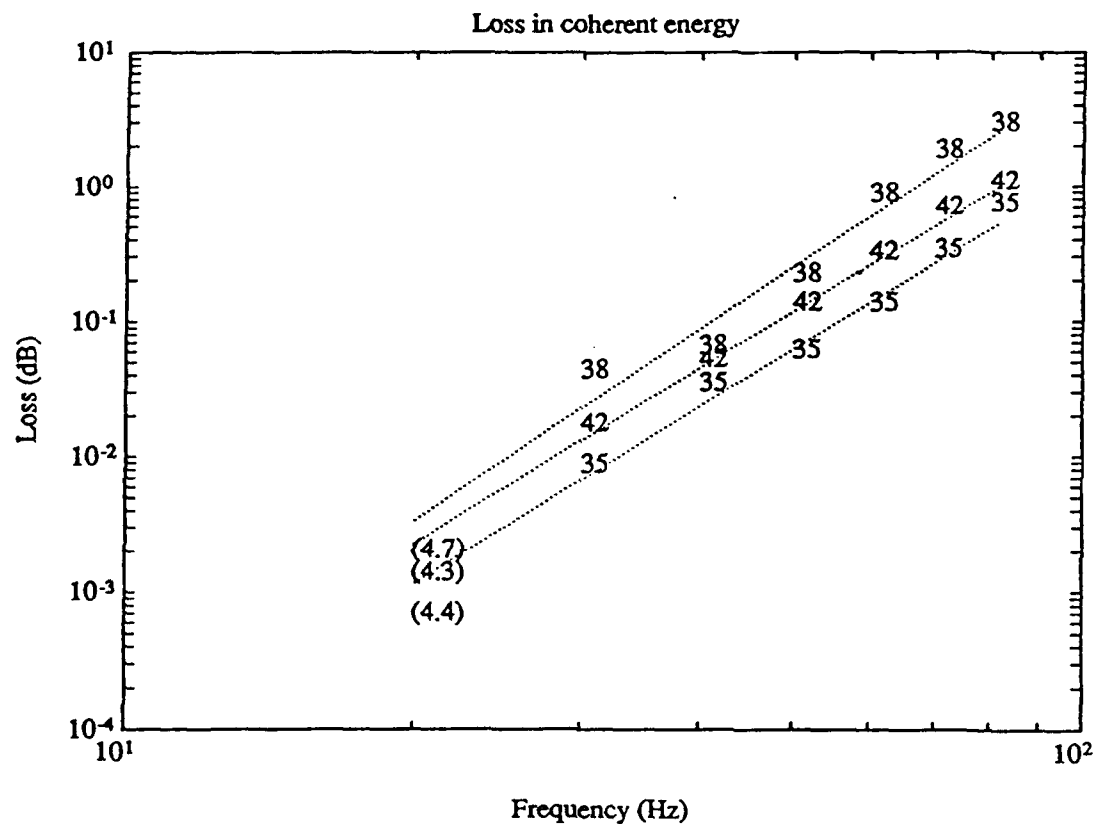
Figure 5.36: Specular energy loss for elastic inclusions. The specular loss for the elastic floe (35) is the least of the three. When the floe is converted to a keel (42) by bringing in a 3 m ice sheet on either side, the loss roughly doubles due to the excitation of plate waves. If the floe is converted to a keel (38) by placing it beneath a 3 m ice sheet, the loss increases by a factor of 4.6 or so: a factor of 2 for excitation of plate waves and another factor of about 2.3 for the increase in mass.
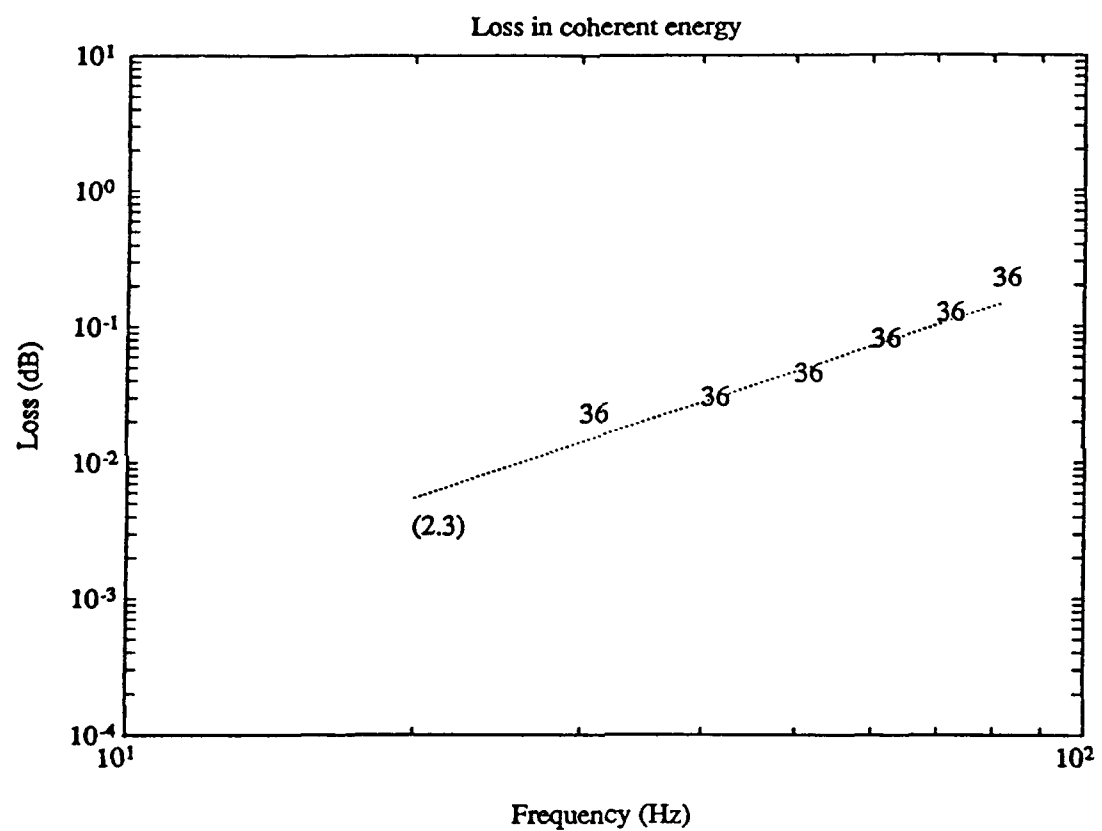
Figure 5.37: Specular energy loss of ice edge, Experiment 36. The slope of the loss is 2.3.

where A is the cross sectional area of the scatterer, which for fixed ice density, is proportional to mass per unit length.

- Fluid inclusions, that is floes and keels, have a wide angle scattering pattern, which is dipolar. The slope of the specular energy loss versus frequency is about $\alpha = \frac{3}{2}$.

- The scattering characteristics of elastic inclusions are different for different ranges of frequency.

  - When the value of ka is very small, say less than 0.1 or so, the scattered field is dipolar, as it is for the fluid case. In this low frequency range, shear effects are negligible and the specular energy loss versus frequency has a slope of $\alpha = \frac{3}{2}$. As an example, if we set a to be the average keel depth in the central Arctic, $9.6\,m$ [21], this low frequency limit applies to $f < 2.5\,Hz$ for $ka < 0.1$.

  - When the value of ka is modest, say $0.5 < ka < 2.5$ the scattered field is quadrupolar and the specular energy loss versus frequency has a slope of $\alpha \sim \frac{9}{2}$. This is the range of ka which is most important for long-range propagation experiments, corresponding to a frequency range of $10 < f < 100\,Hz$.

- For an ice edge the specular energy loss versus frequency has a slope of $\alpha = 2$.

- The excitation of plate waves roughly doubles the specular energy loss of an elastic keel relative to an elastic floe of the same size. Plate waves are not excited very efficiently by fluid keels; there is no additional specular loss for fluid keels relative to fluid floes of the same size.

These observations point to one overall conclusion that has not been adequately addressed in the literature. In terms of understanding and predicting scattering loss, the internal structure of a pressure ridge is just as important as the topographic roughness.

244

The former determines the slopes of the loss and the latter determines the amplitude. Historically, a great deal of attention has been paid to the topographic roughness of the under and upper surface of the ice. This, clearly, is part of the needed information, but the internal structure, at least in a bulk property sense, is needed as well if adequate loss predictions are to be made for long-range propagation. In Chapter 7 I outline the information needed in terms of conditional probabilities. This information must come from a census of ice characteristics in the Arctic.

Chapter 6

Scattering loss hypothesis

6.1 Overview

In the previous chapter I introduced the numerical scattering results for elemental ice features and compared the results with analytic solutions, where possible. In this chapter I compare the numerical results with the field data first introduced in Chapter 1. Specifically, I focus on the slope and magnitude of the specular loss to show that fluid ridges are the most likely candidates for explaining the observed excess loss in the field data.

6.2 Data comparison

In the last chapter I discussed the results of the numerical experiments with few references to field observations. This section brings the two data sets together for comparison: the objective being improved predictions of excess specular energy loss.

6.2.1 Field data

As shown in Chapter 1, Figure 1.2, the frequency dependence of the data is $\sim f^{\frac{3}{2}}$. In fact, a good fit to the data is given by $L_\epsilon = 3.0 f^{\frac{3}{2}}$ with f in kilohertz [46]. In this chapter, the phrase *observed loss* is reserved for the specular energy loss estimated from the field data. The observed loss is "true" in the sense that it is derived from field experiments [6] and provides a basis for comparison with the numerical results.

Analytic predictions of excess loss based on the method of small perturbations fall short by a large margin. The most accurate model, based on the impedance method, gives worse predictions than the less accurate free surface model in terms of both the slope and magnitude predictions [46]. The slope prediction using the impedance method is $\alpha \sim 3$ compared to $\alpha \sim \frac{3}{2}$ for the data. The magnitude of the loss is also too low, but this is less serious, for the moment, than the slope problem.

An analytic solution based on a rough free surface assumption is the best fit to the data and has a power law of $\alpha = \frac{3}{2}$. The good fit, however, makes no physical sense; the ice-water interface is not a free surface.

6.2.2 Numerical data

The numerical estimates of excess specular energy loss, computed in the last chapter, are expressed in terms of $dB/bounce$, while the field observations are expressed in terms of dB/Km. In converting the numerical results to dB/Km I make the assumption that the upward refracting sound channel is range independent with a constant skip distance, D_s. Using the sound speed at the surface, C_o, the grazing angle, γ, and the sound speed gradient, g, the skip distance is computed as $D_s = 2C_o \tan \gamma / g$ [46]. All the experiments in the last chapter were conducted with $\gamma = 10°$. A typical Arctic surface sound speed is $C_o = 1440\,m/s$, and a typical surface sound speed gradient is $g = 0.06\,s^{-1}$. These

values yield a skip distance of $D_s = 8.5 \, Km$. In the conversion of the numerical data from $dB/bounce$ to dB/Km, I also assume that every time a ray hits the ice it is hitting exactly the same kind of scatterer over and over again. With these two assumptions, I only have to divide the specular loss estimates from the last chapter by the skip distance of 8.5 Km to be able to compare with the field observations in dB/Km.

6.2.3 Specular energy loss

Slope

The wide range of power law exponents described in Section 5.5.3 suggests that matching the exponent estimated from field observations with that of a single scatter will indicate the dominant elemental scatterer influencing long-range propagation. Recognizing that the field observations have a slope of 1.2, as shown in Figure 1.2, points to the fluid inclusion as being the most likely candidate for the dominant scattering object. Estimated slopes for fluid inclusions range from $1.4 < \alpha < 2.0$. Scatter from ice edges is a second possibility, but the match is not as good as that for fluid inclusions. Scatter from elastic inclusions with $\alpha \sim 4.5$ is the worst match to the field observations.

Historically, attention has been focused on scatter from elastic inclusions as the most obvious mechanism to explain the observed specular energy loss. But given the results of the previous chapter, it is the least likely candidate. Results for the three types of scatterers are shown in Figure 6.1, where I have plotted the specular energy loss for the observed field data along with the loss computed from the numerical experiments.

Magnitude

In order to match the field data with the numerical results, it must be possible to adjust the magnitude of the specular loss shown in Figure 6.1 using physically reasonable arguments.

248
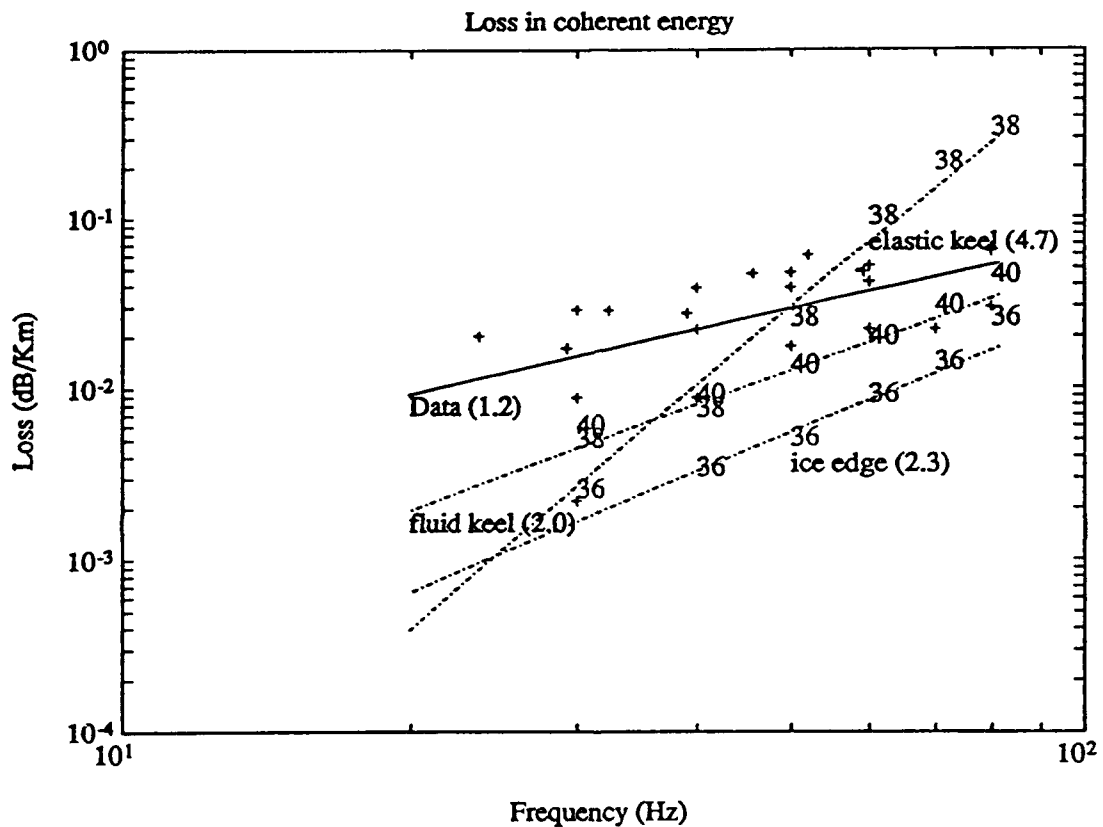
Figure 6.1: Specular energy loss versus frequency for field data and three different types of elemental scatterers. The '+' signs are data points derived from field observations [45,68], and the solid line is the linear regression through the data with an estimated slope of 1.2. The other three curves are numerical results for specular loss from the ice edge, Experiment 36, with a slope of 2.3, the fluid keel, Experiment 40, with a slope of 2.0, and the elastic keel, Experiment 38, with a slope of 4.7. The best match to the field data with respect to the frequency dependence is the fluid keel.

I focus on the ice edge and fluid inclusion models since they produce loss slopes that are close to that of the field data.

The magnitude of the specular loss due to ice edge scatter cannot be scaled since, for fixed ice thickness, ice edges are binary objects. They have no intrinsic length scale. Either an edge is present or it is not. The observed specular loss at $50\,Hz$ is about five times more than the estimated loss due to scatter from a truncated $3\,m$ ice sheet, the only thickness modeled. It is doubtful that any reasonable ice thickness would produce a loss five times greater than that of $3\,m$ ice. Because of this, it is unlikely that ice edges play a dominant role in long-range propagation loss in the central Arctic. In the marginal ice zone, however, where pressure ridges are uncommon, scatter from ice edges probably dominates.

In the last chapter we saw that specular energy loss due to a keel is proportional to the cross sectional area of the keel. The area of the keel in Experiment 40 is $93\,m^2$, based on a semi-circular floe with a radius of $6\,m$ beneath a $3\,m$ ice sheet. At $50\,Hz$ the estimated loss from this keel is about 2.2 times less than the loss observed in the field data. This difference can easily be accommodated by looking at estimates of average keel size in the Arctic.

Hibler et al. [21] report the average keel depth (of keels deeper than $6.1\,m$) in the central Arctic is $9.6\,m$ below the sea level datum. The average keel spacing is about $230\,m$. Their data is based on sonar measurements of the undersurface of the ice, covering a distance of about $1400\,Km$ and measuring a total of 5702 keels.

Suppose the average ridge, with a keel depth of $9.6\,m$, is shaped like the idealized model proposed by Diachok and shown in Figure 6.2 [12]. Further, suppose the average ridge is newly formed and, hence, is a fluid ridge. The ridge, then, has a cross sectional area of about $268\,m^2$, which is 2.7 times that of the keel in Experiment 40. Thus, the specular energy loss predicted for the average ridge is about 2.7 times larger than that of the keel in Experiment 40, which, in turn, is 2.2 times less than the observed loss from field data.
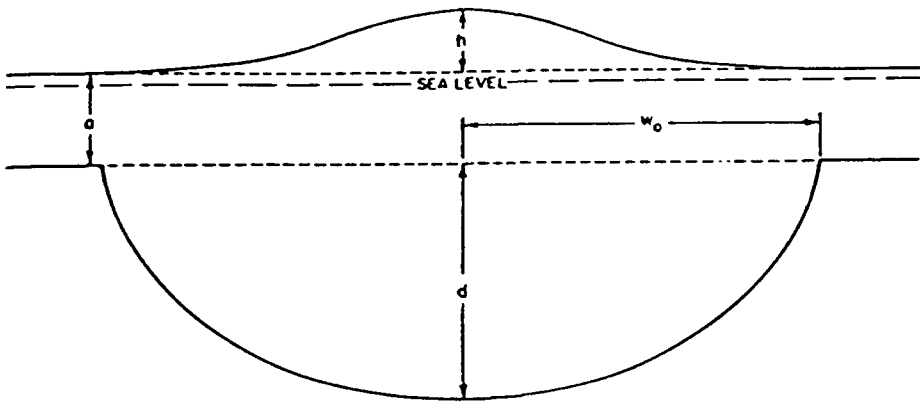
Figure 6.2: Idealized model of a pressure ridge taken from Diachok [12]. The keel depth is related to keel width and sail height by the ratios $d/h = 4.0$ and $w_o/d = 1.6$. Due to the random orientation of ridges, the effective ridge width, w, is assumed to be $w = \sqrt{2}w_o$. The keel is the shape of a semi-ellipse with area $\pi w d/2$ and the sail is the shape of a Gaussian distribution with area $\sqrt{2\pi}hw/3$. Using the given ratios the cross sectional area of the whole keel may be expressed as $A \simeq 4.1d^2 + 4.5ad$.

This illustration shows that the specular loss due to the average keel, if it is newly formed, has about the same slope and magnitude as the observed loss.

I am not arguing, by this illustration, that the observed scattering loss is completely explained by scatter from fluid ridges. Rather, I am arguing that this mechanism is a *plausible* explanation for the observed loss. The slope of the specular loss produced by elastic ridges is too high, and the magnitude of the specular loss produced by ice edges is too low. For fluid ridges, however, both the slope and the magnitude fall into a range comparable to that of the observed loss derived from field data.

6.3 Example from the literature

As another illustration of the assertion that scatter from fluid keels is the dominant loss mechanism, I now develop an example based on a keel measured by Rigby and Hanson [53].

The pressure ridge shown in Figure 6.3 was monitored for several months during the

251
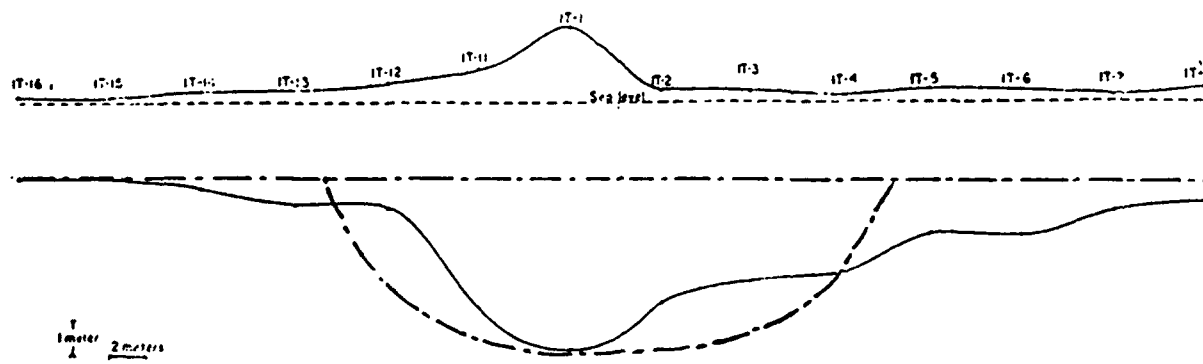
Figure 6.3: Profile of pressure ridge measured by Rigby and Hanson [53] on August 23, 1975. They estimated the pressure ridge to be about eight months old at the time of the measurement. The keel depth was about 4.4 m below the surrounding 2 m ice sheet, and the sail height was about 2 m above the ice surface. The dot-dash curves are the lines I use to estimate the cross sectional area of the pressure ridge with a semi-elliptical shape for the keel and a Gaussian distribution shape for the sail. My estimated half-width to depth ratio for the keel, when measured, is 3.3 (about twice the Diachok ratio [12]). I preserve this ratio for the newly formed and the year old ridge.

summer of 1975. The depth of the keel when measured on August 23, 1975 was about 4.4 m below the surrounding 2 m ice. The sail height was about 2 m above the ice surface. Rigby and Hanson estimate the keel was formed in mid-December of 1974, making it about eight months old at the time of the measurement.

Observed ablation rates for keels and sails indicate that pressure ridges loose about half their draft and height during their first year [53]. Based on these ablation rates, and assuming that depth and height loss is a linear function of time for the first year, I estimate the keel to have had a depth of 6.1 m below the surrounding ice and a sail height of 2.9 m when it was newly formed. At one year of age these values are halved to 3 m and 1.5 m, respectively. The keel area is estimated using a semi-ellipse, as indicated in Figure 6.3, and the sail area using a Gaussian distribution. A half-width-to-keel-depth ratio is maintained at 3.3 for both the newly formed pressure ridge and the year old ridge. The area for each part of the pressure ridge is computed as follows, using the notation of Figure 6.2. For the

252

keel

$$A_k = \frac{\pi w d}{2} \simeq 1.7\pi d^2.$$ (6.1)

For the sail

$$A_s = \frac{\sqrt{2\pi} w h}{3} \simeq 2.8 dh.$$ (6.2)

Finally, for the ice plate

$$A_p = 2aw = 6.6ad.$$ (6.3)

Using these formulas I estimate the newly formed ridge to have had an area of about 325 m^2, while the year old ridge had an area of about 100 m^2. Both the fluid keel in Experiment 40 and the elastic keel in Experiment 38 have an area of 93 m^2. Thus, multiplying the specular loss of the fluid keel in Experiment 40 by 325/93 $\simeq$ 3.5 estimates the specular loss due to the newly formed Rigby and Hanson pressure ridge. Similarly, multiplying the specular loss of the elastic keel in Experiment 38 by 100/9.3 $\simeq$ 1.1 estimates the specular loss due to the Rigby and Hanson ridge at an age of one year.

The results are plotted in Figure 6.4. These results reconfirm the plausibility of scatter from fluid keels as being the dominant scattering mechanism in long-range acoustic propagation. The slope is clearly better matched by the fluid keel and the magnitude is roughly correct. Still, there is a problem. The magnitude of the old, or elastic keel, is too large at high frequency, even though the old keel has been reduced in size. I submit, however, that the magnitude scaling is not a major issue for the following reason.

I have shown that the slope of the scattering loss is essentially binary, either $\alpha \sim \frac{3}{2}$ for fluid ridges or $\alpha \sim \frac{9}{2}$ for elastic ridges. The magnitude of the scattering loss, on the other hand, is a continuous function of the ridge cross sectional area. Thus, the first order of business is to match the slope of the observed loss using physically reasonable models, which I have done. The next order of business is to match the magnitude. Prediction of scattering loss magnitude requires a knowledge of the distribution of old versus new

pressures ridges and the distribution of their sizes and bulk material properties. Estimates of these distributions are not available, so quantitative predictions of scattering loss magnitude cannot be made. Nevertheless, using the measured ridge of Rigby and Hanson, I have demonstrated that the magnitude of scattering loss from fluid ridges can be adjusted using reasonable physical arguments to match the observed loss from field data.

6.4 Summary

This chapter compares the numerical scattering loss for a young and an old keel with the observed scattering loss from field data. A plausible explanation for the observed loss is suggested; specifically, based on comparisons of slope and magnitude, the loss is due to large, young pressure ridge formations. The older, smaller ridges have the wrong frequency dependence and evidently do not affect long-range acoustic loss significantly.

The slope of the specular loss for fluid ridges is $\alpha \sim \frac{3}{2}$, which is similar to that observed in field data. The magnitude may be adjusted by increasing the size of the ridge to match the numerical loss and the observed loss. An example of a measured ridge is used to confirm that scatter from a fluid ridge can be scaled within reasonable limits to match the observed loss from field data.
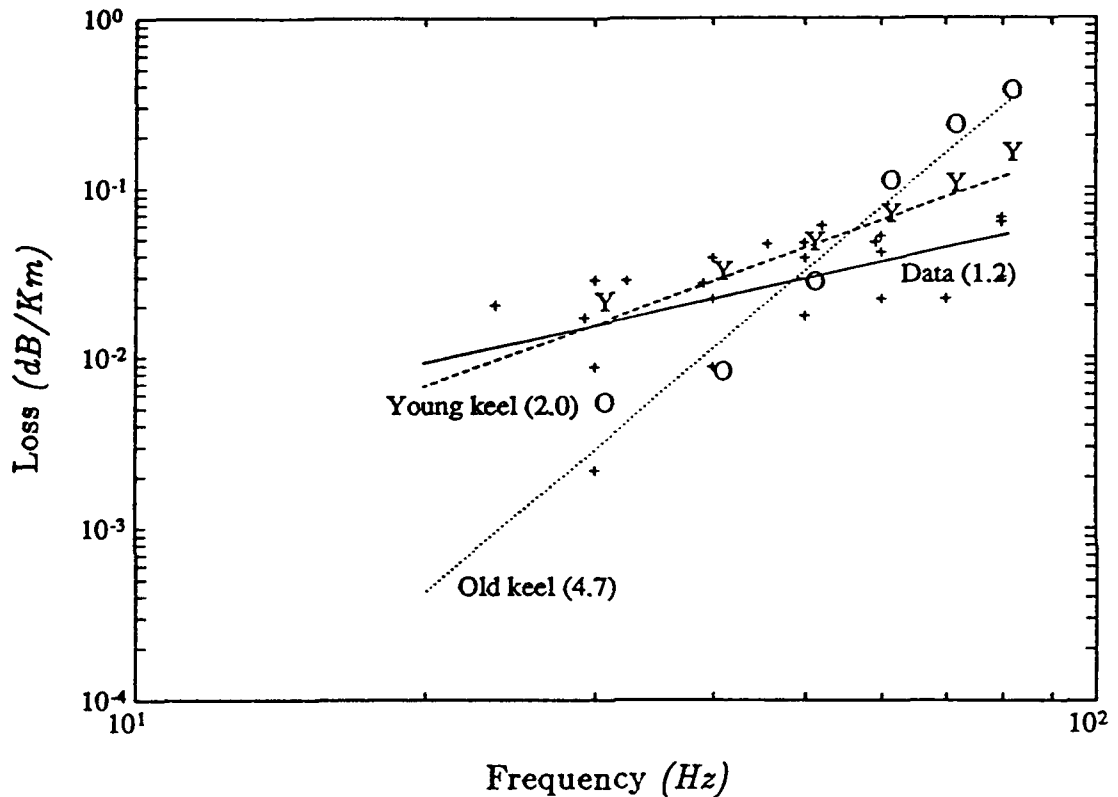
Figure 6.4: Specular scattering loss for young and old Rigby and Hanson [53] pressure ridge compared to measured data. As before, in Figure 6.1, the '+' are measured data with a linear regression marked by the solid line. The young ridge has a cross section of about 325 m^2 and is assumed to have the bulk properties of a fluid, hence, a low scattering loss slope. The old ridge has a cross section of 100 m^2 and is assumed to have the bulk properties of an elastic solid, hence, a large scattering loss slope. The young, fluid ridge matches the field data much better than the old, elastic ridge.

255

Chapter 7

Conclusion

7.1 Contributions

This thesis makes contributions to two rather disparate disciplines: numerical modeling and acoustic scattering in the Arctic. In so doing, the structure of the thesis has two parts. Chapters 2 and 3 provide the analytical and numerical development needed to model elastic wave propagation in a heterogeneous continuum with discrete internal boundaries. Chapter 4 covers the array processing needed to analyze the results from numerical scattering experiments; it acts as a transition chapter between the numerical modeling part of the thesis and the acoustic scattering part. Chapters 5 and 6 describe the numerical scattering experiments, which are conducted in an effort to explain the observed propagation loss over long ranges in the Arctic.

7.1.1 Numerical modeling

Chapters 2 and 3 provide the analytical and numerical development needed to model elastic wave propagation in a heterogeneous continuum with discrete internal boundaries. The boundaries may be fluid-fluid, fluid-solid, or solid-solid. Fluids are specified with two ma-

256

terial properties: density, ρ, and compressional sound speed, C_p. Solids are specified with three material properties: density, ρ, compressional sound speed, C_p, and shear sound speed, C_s. The material property transition across any boundary may be as large as desired, within the constraint that the medium continues to be adequately modeled by a continuum [10]. The elastodynamic equations developed in Chapter 2 cannot be solved analytically for arbitrary material geometry; hence, I proceed in Chapter 3 to investigate a numerical solution based on finite differences. The numerical solution must retain accuracy in the presence of the extreme contrasts in material properties that are allowed by the analytic system. This is a challenging problem, which is handled by drawing on the numerical methods used to solve nonlinear hydrodynamic equations wherein shocks may develop and propagate.

Extended PDE

The analytic system of equations developed in Chapter 2 is quasi-linear and may be written

$$
\begin{aligned}
\rho_{,t} &= -\nu_{i,i}, \\
\nu_{i,t} &= -\left(\frac{\nu_i \nu_j}{\rho}\right)_{,j} + \sigma_{ij,j}, \\
\sigma_{ij,t} &= \lambda \left(\frac{\nu_k}{\rho}\right)_{,k} \delta_{ij} + \mu \left[\left(\frac{\nu_i}{\rho}\right)_{,j} + \left(\frac{\nu_j}{\rho}\right)_{,i}\right],
\end{aligned}
\tag{7.1}
$$

where ρ is density, $\nu_i = \rho v_i$ is linear momentum, σ_{ij} is the symmetric stress tensor, and λ and μ are Lamé parameters, which may be spatially varying. The Lamé parameters are related to density and sound speed by the relations

$$
C_p = \sqrt{\frac{\lambda + 2\mu}{\rho}}, \quad C_s = \sqrt{\frac{\mu}{\rho}}.
\tag{7.2}
$$

These equations are analyzed dimensionally, and I show that the conservation of mass equation and the quasi-linear term in the momentum equation are unnecessary if $R_\Delta M \ll R$, where R_Δ is the change in density across a boundary, M is the Mach number, and

257

R is the local density. In smooth materials, R_Δ is always small, and hence, the linear elastodynamic equations may be used. If, however, a boundary exists between a gas and a solid, say ice and air, the density change is many orders of magnitude and the product $R_\Delta M$ may no longer be small on the gas side of the boundary. Thus, for generality I retain the mass equation and the quasi-linear term of the momentum equation.

Stable FD scheme

The quasi-linear elastodynamic equations cannot be solved for arbitrary arrangements of material properties. My interest, in particular, is the interaction of acoustic energy in the water with an arbitrarily rough elastic ice sheet. In Chapter 3 I analyze a technique based on the Lax-Wendroff finite difference scheme. For the model equation in conservation law form, $u_{,t} = f_{,x}$, the numerical solution may be found using the update equation

$$
\begin{aligned}
u^{l+\frac{1}{2}}_{m+\frac{1}{2}} &= \frac{1}{2}(u^l_{m+1} + u^l_m) + \frac{k}{2h}(f^l_{m+1} - f^l_m), \\
\tilde{u}^{l+1}_m &= u^l_m + \frac{k}{h}(f^{l+\frac{1}{2}}_{m+\frac{1}{2}} - f^{l+\frac{1}{2}}_{m-\frac{1}{2}}), \\
u^{l+1}_m &= \tilde{u}^{l+1}_m + \alpha h^2(u^l_{m-1} - 2u^l_m + u^l_{m+1}),
\end{aligned}
\tag{7.3}
$$

where $k = \Delta t$ is the time step, $h = \Delta x$ is the space step, and α is a dissipation constant. The third equation is only applied when the curvature of the field becomes large, which happens when high wavenumber components begin to grow. If the solution remains smooth then the diffusion equation $(7.3)^3$ is not used. The scheme is second order accurate except when the diffusion equation is invoked, in which case the accuracy is first order. When this scheme converges, the solution is guaranteed to be consistent with the quasi-linear elastodynamic equations it approximates.

7.1.2 Arctic scattering

The numerical modeling algorithm is used to conduct a variety of scattering experiments which simulate acoustic scattering from individual roughness features in an ice sheet. The purpose of these experiments is to determine the character of the scattering loss as a function of the scatterer size, shape, and composition. Several loss mechanisms are identified. Using field observations of long-range specular energy loss as a guide, scatter from fluid pressure ridges is determined to be the most likely dominant loss mechanism in the Arctic. Newly formed pressure ridges have low shear modulus since they are simply piles of loose ice blocks and it is conjectured that they behave acoustically like fluids. Also, newly formed ridges are large and diminish in size for the remainder of their existence. Ice edges produce a specular energy loss that is similar to that of fluid ridges, but the magnitude of the loss is much lower and cannot account for the observed loss.

Three mechanisms are observed and contribute to total specular energy loss: mass loading, plate wave excitation, and a frequency dependence dictated by material properties.

Mass loading

At low frequency the cross sectional area of a scattering element is linearly proportional to specular reflection loss. For a fixed ice density, cross sectional area is proportional to mass per unit length, hence the term *mass loading*. This phenomenon is shown analytically for the case of a fluid floe and is shown experimentally for elastic ridges using numerical data.

Excitation of plate waves

An elastic ridge may be formed from an elastic floe by bringing an ice sheet into welded contact on either side of the floe. The specular energy loss of the elastic ridge in decibels is twice the loss of the corresponding floe. Thus, coupling an ice sheet to an elastic floe has

the same effect on the specular energy loss as doubling the area of the floe. A fluid ridge does not behave this way. The surrounding ice sheet cannot be in welded contact because of the fluid-solid boundary and the specular loss from a fluid ridge is roughly the same as that from a fluid floe.

Frequency dependence

The specular energy loss, L_e, is a power law function of frequency, $L_e = f^\alpha$. When loss in decibels is plotted against frequency using a log-log scale, the power law exponent, α, becomes the slope of the loss curve. This slope varies, depending on the type of scattering object and its material properties. Three categories of scattering objects are identified: fluid inclusions, elastic inclusions, and ice edges. The term *inclusion* is used to group both floes and pressure ridges into a single category.

Fluid inclusions produce a specular loss slope of $\alpha \sim \frac{3}{2}$. I show analytically that for fluid floes with $ka \ll 1$, the slope is exactly $\frac{3}{2}$. For ka in the range $0.5 < ka < 2.5$, I show numerically that for fluid ridges, that is fluid floes connected to elastic ice sheets, the slope increases to $\alpha \sim 2$. Parenthetically, the specular loss observed for long-range propagation experiments has a slope $\alpha \sim \frac{3}{2}$. This suggests that fluid roughness elements are responsible for the observed scattering loss in the Arctic.

Results from numerical experiments show that elastic inclusions have a specular loss slope of $\alpha \sim 4.5$, which is much larger than that observed in long-range propagation experiments. Old pressure ridges are frozen solid and so may be modeled as elastic inclusions. In addition, old pressure ridges have lost a great deal of their original draft and height and so tend to be smaller than newly formed ridges. Because loss is proportional to cross sectional area, the magnitude of the specular loss for an old ridge should be less than that of a young ridge. This, again, suggests that scatter from young pressure ridges is the dominant

scattering mechanism in the Arctic.

Analytical work by Dahl [11] shows that the specular loss due to an ice edge has a slope of $\alpha = 2$ for small kH, where H is the thickness of the ice. My numerical experiments yield a slope of $\alpha \sim 2.3$ for a truncated $3\,m$ ice sheet. This slope, either the analytical or numerical value, is not too far from the observed slope in long-range propagation experiments. The magnitude of the predicted loss, however, is about five times less than the observed loss. Thus, it seems unlikely that scatter from ice edges plays a dominant role in the observed scattering loss for long-range propagation in the central Arctic.

7.2 Future work

As always, there are things left undone, improvements to be made, and extensions and implications for future work. The following summarizes my thoughts with regard to future work in numerical modeling, laboratory experiments, and field experiments. The numerical modeling algorithms will undergo evolutionary change to improve performance and add new capabilities. Laboratory experiments should be conducted to verify the findings of the numerical experiments. If the laboratory findings corroborate the numerical findings then a field effort is indicated to provide final confirmation.

7.2.1 Numerical modeling

While the numerical modeling algorithm as presented is adequate for the task of generating synthetic data, it is deficient in several ways. I had trouble with the added dissipation scheme, the absorbing boundary conditions, and the creation of a plane wave source. These three areas are candidates for improvement. Also, extensions to the algorithm are motivated by a desire to model three dimensional scatter.

Improvements

Added dissipation scheme. The Lax-Wendroff scheme, as implemented, is not unduly dissipative except in the regions where added dissipation is used to stabilize the solution. A better added dissipation algorithm or a better stabilization method should be developed. Work by Chang and Randall [7] indicates that a staggered grid, similar to that used by Virieux [69], with material averaging produces accurate results for cases of boundaries with large material contrasts. Another approach by McDonald [39] uses a flux-corrected monotone scheme in the vicinity of the boundary discontinuity, in contrast to my diffusive monotone scheme. These two new schemes should be investigated for improved performance.

Absorbing boundaries. Even with a sponge region width of two wavelengths in water, 2λ, and the one-way boundaries at the edges, my solutions are contaminated by spurious reflections. A better approach should be found, though this is a very difficult problem and there may be no completely satisfactory solution, especially at low frequency.

Pseudo plane wave source. The isotropic line source I used excites compressional plate waves in the ice. These plate waves complicate the interpretation of the scattered data. Of the three improvements suggested here, this is the easiest to deal with. A directional, pseudo plane wave source can easily be implemented by using an array of line sources. The beam pattern of the array of sources limits the energy injected into the head wave in the ice. Array weighting could also be used; this would further reduce the sidelobes. With such a source, the scattered field from an elemental roughness element would only have contributions from the direct acoustic scatter without the scatter from the source head wave seen in Chapter 5.

Extensions

The desire to accurately model scatter in three dimensions is one motivation for extending the the numerical algorithm. In particular, the question of scatter due to non-normal azimuthal incidence on a ridge or ice edge and the coupling to horizontal shear motion is not addressed by this thesis. Nor is the horizontal shear coupling due to scatter from two dimensionally rough surfaces. A full three dimensional formulation is required to investigate these problems

To achieve this goal, the 3-D development cannot be done with brute force. To as great an extent possible, the extensions must be done with efficiency in mind. One of the approaches that might be taken is to implement adaptive gridding techniques. The numerical development of Chapter 3 is based on a fixed, equally spaced grid throughout the computational domain. The ice sheet needs a small spatial sampling interval, but the water beneath, for example, does not. A variable gridding approach would improve the efficiency of the algorithm.

Another extension to the numerical algorithm deals with the material properties of the ice. The ice model assumed in this thesis is that of a simple material described by three material parameters, λ, μ, and ρ. A more complete description of the true composite nature of the ice should be considered. Specifically, the ice is porous, it is anisotropic, and there is a thin visco-elastic layer at the bottom interface. These characteristics may be important in the scattering process and, if so, should be included in the ice model.

7.2.2 Laboratory modeling

In Chapter 1, I stated that laboratory experiments did not make sense for the scattering study if many models are to be investigated. The numerical experiments of Chapter 5 have reduced the number of models to be investigated, and laboratory experiments should

be conducted to verify the numerical results. Scaled ultrasonic scattering measurements could be made, and the scattered pressure field could be estimated and compared with the numerical results.

Fluid versus elastic floe. The slope of the specular energy loss for a fluid floe versus an elastic floe should be demonstrated, as should the pattern of the scattered field, dipolar versus quadrupolar. This is the key to my hypothesis, that the dominant scattering mechanism is scatter from fluid roughness elements.

Loss versus area. Experiments with keels of various sizes should be conducted to verify the proportionality of specular energy loss versus cross sectional area. The frequency range should be selected to span $0.5 < ka < 2.5$, which corresponds, approximately, to the range of ka in long-range propagation experiments

7.2.3 Field research and experiments

Ultimately, the proof of my assertions are in the field, where experiments and research must be conducted to yield better scattering loss predictions. Two efforts are needed: 1) a census of pressure ridges and their characteristics such as age, and bulk material properties and 2) a number of controlled scattering experiments from well surveyed ridges.

Census. My analysis, comparing scatter from a single roughness element with long-range data, is based solely on one ridge at a time. The actual long-range experiment, of course, samples the ice many times and the net scattering loss is an ensemble average of all the ice sampled along the path. To develop better predictions, we need a better understanding of the distribution of ridges, their ages, and their bulk acoustic and elastic properties. I suggest that the following probability distributions are needed:

1. P{hitting a keel} (already have from submarine sonar transects),

2. P{keel age | hit a keel},

3. P{keel size | keel age},

4. P{keel $\overline{C_s}$ | keel age},

5. P{keel $\overline{C_p}$ | keel age}, and

6. P{keel $\bar{\rho}$ | keel age},

where the quantities $\bar{C}_s$, $\bar{C}_p$, and $\bar{\rho}$ are the bulk material properties of a keel. Using a technique similar to Langleben [33] these values may be estimated from acoustic data collected during the controlled experiments discussed below. With these probabilities and an understanding of the scattering process for each type roughness element, an estimate of the ensemble average of scattering loss over long ranges can be made.

Controlled experiment. Once the census is complete, a controlled experiment on several young and old ridges must be conducted. The experiment should include a thorough structural and acoustic survey. The structural survey would involve coring the ridge and mapping its profile and internal voids. A measure of the porosity of the ridge would be helpful in correlating with bulk shear modulus estimated from the acoustic data.

The acoustic survey should be done with as dense an array of receivers as possible using horizontal and vertical legs to surround the ridge. This would allow processing similar to that described in Chapter 4. A known newly formed ridge and a known multi-year ridge should be surveyed to confirm the frequency dependence of $\alpha \sim \frac{3}{2}$ versus $\alpha \sim \frac{9}{2}$. These two surveys should also confirm that a young ridge scatters in a dipolar pattern while an old ridge scatters in a quadrupolar pattern. Finally, the acoustic survey should confirm the proportionality of loss versus cross sectional area.

Bibliography

[1] M. Abramowitz and I. A. Stegun, ed., *Handbook of Mathematical Functions with Formulas, Graphs, and Mathematical Tables*, National Bureau of Standards: Applied Mathematics Series, issued June 1964; tenth printing Dec. 1972 with corrections.

[2] J. D. Achenbach, *Wave Propagation in Elastic Solids*, North-Holland Pub. Co., Amsterdam, 1973.

[3] Z. Alterman and F. C. Karal Jr., "Propagation of elastic waves in layered media by finite difference methods," *Bull., Seis. Soc. Am.*, 58, 367-398, 1968.

[4] G. K. Batchelor, *An Introduction to Fluid Dynamics*, Cambridge University Press, 1967, reprint 1985.

[5] L. M. Brekhovskikh, *Waves in Layered Media*, 2nd ed., Academic Press, 1980.

[6] B. M. Buck and C. R. Greene, "Arctic deep-water propagation and measurement," *J. Acoust. Soc. Am.*, 36, 1526-1533, 1964.

[7] H. W. Chang and C. J. Randall, "Finite-difference time-domain modeling of elastic wave propagation in the cylindrical coordinate system," *1988 IEEE Ultrasonics Symposium*, 397-402, 1988.

[8] C. H. Chapman, "Generalized Radon transforms and slant stacks," *Geophys. J. R. astr. Soc.*, **66**, 445-453, 1981.

[9] C. S. Clay, "Effect of a slightly irregular boundary on the coherence of waveguide propagation," *J. Acoust. Soc. Am.*, **36**, 833-837, 1964.

[10] A. H. Cottrell, *The Mechanical Properties of Matter*, Robert E. Krieger Pub. Co., Huntington, N.Y., 1981.

[11] P. H. Dahl, *Acoustic Diffraction from a Semi-Infinite Elastic Plate Under Arbitrary Fluid Loading with Application to Scattering from Arctic Ice Leads*, Ph.D. thesis, Massachusetts Institute of Technology and Woods Hole Oceanographic Institution, 1989.

[12] O. I. Diachok, "Effects of sea-ice ridges on sound propagation in the Arctic Ocean," *J. Acoust. Soc. Am.*, **59**, 1110-1120, 1976.

[13] F. DiNapoli and R. H. Mellen, "Low frequency attenuation in the Arctic Ocean," in *Ocean Seismo-acoustics*, ed. T. Akal and J. Berkson, Plenum, NY, 387-395, 1986.

[14] M. F. Dougherty and R. A. Stephen, "Geoacoustic scattering from seafloor features in the ROSE area," *J. Acoust. Soc. Am.*, **82**, 238-256, 1987.

[15] A. P. Dowling and J. E. Ffowcs-Williams, *Sound and Sources of Sound*, John Wiley & Sons, New York, 1983.

[16] J. J. Faran, Jr., "Sound scattering by solid cylinders and spheres," *J. Acoust. Soc. Am.*, **23**, 405-418, 1951.

[17] J. O. Fletcher, "Floating ice islands in the Arctic Ocean," *Tellus*, **2**, 323-324, 1950.

[18] D. Gottlieb, M. Gunzberger, and E. Turkel, "On numerical boundary treatment of hyperbolic systems for finite difference and finite element methods," *SIAM J. Num.*

Anal., **19**, 671-682, 1982.

[19] K. F. Graff, *Wave Motion in Elastic Solids*, Ohio State Univ. Press, 1975.

[20] A. Harten, J. M. Hyman, and P. D. Lax, "On finite-difference approximations and entropy conditions for shocks," *Comm. Pure and Appl. Math.*, **29**, 297-322, 1976.

[21] W. D. Hibler, III, W. F. Weeks, and S. J. Mock, "Statistical aspects of sea-ice ridge distributions," *J. Geophys. Res.*, **77**, 5954-5970, 1972.

[22] R. L. Higdon, "Initial-boundary value problems for linear hyperbolic systems," *SIAM Review*, **28**, 177-217, 1986.

[23] T. J. R. Hughes and J. E. Marsden, "Classical elastodynamics as a linear symmetric hyperbolic system," *J. of Elasticity*, **8**, 97-110, 1978.

[24] K. Hunkins, "Seismic studies of sea ice," *J. Geophys. Res.*, **65**, 3459-3472, 1960.

[25] K. C. Jezek, T. K. Stanton, A. J. Gow, and M. A. Lange, "Influence of environmental conditions on acoustic properties of sea ice," *J. Acoust. Soc. Am.*, **88**, 1903-1912, 1990.

[26] K. R. Kelly, R. W. Ward, S. Treitel, and R. M. Alford, "Synthetic seismograms: A finite-difference approach.", *Geophysics*, **41**, 2-27, 1976.

[27] R. Kosloff and D. Kosloff, "Absorbing boundaries for wave propagation problems," *J. Comp. Phys.*, **63**, 363-376, 1986.

[28] A. Kovacs and M. Mellor, "Sea ice morphology and ice as a geologic agent in the southern Beaufort Sea," *The Coast and Shelf of the Beaufort Sea*, J. C. Reed and J. E. Sater, eds., The Arctic Institute of North America, Arlington, VA, 113-161, 1974.

[29] W. A. Kuperman and F. Ingenito, "Attenuation of the coherent component of sound propagating in shallow water with rough boundaries," *J. Acoust. Soc. Am.*, **61**, 1178-1187, 1977.

[30] W. A. Kuperman and H. Schmidt, "Rough surface elastic wave scattering in a horizontally stratified ocean," *J. Acoust. Soc. Am.*, **79**, 1767-1777, 1986.

[31] H. Kutschale, "Arctic hydroacoustics," *Arctic*, **22**, 246-264, 1969.

[32] L. D. Landau and E. M. Lifshitz, *Theory of Elasticity, 2nd ed.*, trans. by J. B. Sykes and W. H. Reid, Pergamon Press, Oxford, England, 1970.

[33] M. P. Langleben, "Reflection of sound at the water-sea ice interface," *J. Geophy. Res.*, **75**, 5243-5246, 1970.

[34] A. J. Langley, "Acoustic emission from the Arctic ice sheet," *J. Acoust. Soc. Am.*, **85**, 692-701, 1989.

[35] P. D. Lax and B. Wendroff, "Systems of conservation laws," *Comm. Pure and App. Math.*, **13**, 217-237, 1960.

[36] F. K. Levin and D. J. Robinson, "Scattering by a random field of surface scatterers," *Geophysics*, **34**, 170-179, 1969.

[37] D. Loewenthal, L. Lu, R. Roberson, and J. W. C. Sherwood, "The wave equation applied to migration," *Geophys. Prosp.*, **24**, 380-399, 1976.

[38] R. T. Lowry and P. Wadhams, "On the statistical distribution of pressure ridges in sea ice," *J. Geophys. Res.*, **84**, 2487-2494, 1979.

[39] B. E. McDonald, "Flux-corrected pseudospectral method for scalar hyperbolic conservation laws," *J. Comput. Phys.*, **82**, 413-428, 1989.

[40] R. Madariaga, "Dynamics of an expanding circular fault," *Bull., Seism. Soc. Am.*, **66**, 639-666, 1976.

[41] H. W. Marsh, "Exact solution of wave scattering by irregular surfaces," *J. Acoust. Soc. Am.*, **33**, 330-333, 1961.

[42] H. W. Marsh and R. H. Mellen, "Underwater sound propagation in the Arctic Ocean," *J. Acoust. Soc. Am.*, **35**, 552-563, 1963.

[43] H. Medwin, M. J. Browne, K. R. Johnson, and P. L. Denny, "Low-frequency backscatter from Arctic leads," *J. Acoust. Soc. Am.*, **83**, 1794-1803, 1988.

[44] R. H. Mellen, A. H. Nuttall, R. L. Davenport, and F. R. DiNapoli, "Composite model for under-ice scattering," Paper Z6, 109th Acoustical Society of America meeting, Austin, TX, April 8-12, 1985.

[45] R. H. Mellen, *Underwater Acoustics in the Arctic Ocean: A Review of Sound Transmission, Scattering and Ambient Noise Under the Ice*, PSI Marine Sciences, New London, CT, 1985.

[46] R. H. Mellen and P. M. Scheifele, *Arctic Ice Attenuation Model Study: Final Report*, NUSC Technical Report 8089, September 1, 1987.

[47] D. H. Menzel, ed., *Fundamental Formulas of Physics*, in two volumes, Dover Publications, New York, 1960.

[48] J. Miklowitz, *The Theory of Elastic Waves and Waveguides*, North-Holland Pub., Amsterdam, 1978.

[49] P. M. Morse and H. Feshbach, *Methods of Theoretical Physics, Vol. 1,2*, McGraw-Hill, New York, 1953.

[50] J. Oliver, A. P. Crary, and R. Cottell, "Elastic waves in Arctic pack ice," *Trans. Am. Geophys. Union*, **35**, 282-292, 1954.

[51] A. Papoulis, *Probability, Random Variables, and Stochastic Processes*, 2nd Ed., McGraw-Hill, New York, 1984.

[52] W. H. Press, B. P. Flannery, S. A. Teukolsky, and W. T. Vetterling, *Numerical Recipes: The Art of Scientific Computing*, Cambridge Univ. Press, Cambridge, 1986.

[53] F. A. Rigby and A. Hanson, "Evolution of a large Arctic pressure ridge," AIDJEX Bull., No. 34, 46-71, December 1976.

[54] F. Santosa and Y. H. Pao, "Accuracy of a Lax-Wendroff scheme for the wave equation," *J. Acoust. Soc. Am.*, **80**, 1429-1439, 1986.

[55] R. C. Singleton, "An algorithm for computing the mixed radix fast fourier transform," *IEEE Tran. Audio Electroacoustics*, **AU-17**, 93-103, 1969.

[56] M. I. Skolnik, ed., *Radar Handbook*, McGraw-Hill Book Co., New York, 1970.

[57] G. A. Sod, *Numerical Methods in Fluid Dynamics: Initial and Initial Boundary-Value Problems*, Cambridge University Press, 1985.

[58] B. D. Steinberg, *Principles of Aperture and Array Design*, John Wiley and Sons, New York, 1976.

[59] J. W. Strutt, Baron Rayleigh, *The Theory of Sound* in two volumes, Dover Publications, New York, 1945.

[60] T. K. Stanton, K. C. Jezek, and A. J. Gow, "Acoustical reflection and scattering from the underside of laboratory grown sea ice: Measurements and predictions," *J. Acoust. Soc. Am.*, **80**, 1486-1494, 1986.

[61] T. K. Stanton, "Sound scattering by cylinders of finite length. I. Fluid cylinders," *J. Acoust. Soc. Am.*, **83**, 55-63, 1988.

[62] T. K. Stanton, "Sound scattering by cylinders of finite length. II. Elastic cylinders," *J. Acoust. Soc. Am.*, **83**, 64-67, 1988.

[63] R. A. Stephen, "A review of finite difference methods for seismo-acoustics problems at the seafloor," *Rev. of Geophys.*, V **26**, 445-458, 1988.

[64] G. Strang and G. J. Fix, *An Analysis of the Finite Element Method*, Prentice-Hall, Inc., Englewood Cliffs, NJ, 1973.

[65] L. N. Trefethen, "Group velocity in finite difference schemes," *SIAM Review*, **24**, 113-136, 1982.

[66] V. Twersky, "On scattering and reflection of sound by rough surfaces," *J. Acoust. Soc. Am.*, **29**, 209-225, 1957.

[67] R. J. Urick, *Principles of Underwater Sound*, McGraw-Hill Book Co., New York, 1975.

[68] R. J. Urick, *Sound Propagation in the Sea*, DARPA, Superintendent of Documents, U. S. Printing Office, Washington, D. C., 1979.

[69] J. Virieux, "P-SV wave propagation in heterogeneous media: Velocity-stress finite-difference method," *Geophysics*, V **51**, 889-901, 1986.

[70] P. Wadhams, 'Sea ice topography of the Arctic Ocean in the region $70°\,W$ to $25°\,E$," *Philos. Trans. Roy. Soc.*, **A 302**, 1464-1504, 1981.

[71] P. Wadhams, "The ice cover" in *The Nordic Seas*, B. G. Hurdle, ed., Springer-Verlag, New York, 20-85, 1986.

[72] W. F. Weeks, "Sea ice properties and geometry," AIDJEX Bull., No. 34, 152-171, December 1976.

[73] W. F. Weeks, "Sea ice conditions in the Arctic," AIDJEX Bull., No. 34, 173-205, December 1976.

[74] G. B. Witham, *Linear and Nonlinear Waves*, Wiley-Interscience, New York, 1974.

DOCUMENT LIBRARY

March 11, 1991

Distribution List for Technical Report Exchange

Attn: Stella Sanchez-Wade
Documents Section
Scripps Institution of Oceanography
Library, Mail Code C-075C
La Jolla, CA 92093

Hancock Library of Biology &
    Oceanography
Alan Hancock Laboratory
University of Southern California
University Park
Los Angeles, CA 90089-0371

Gifts & Exchanges
Library
Bedford Institute of Oceanography
P.O. Box 1006
Dartmouth, NS, B2Y 4A2, CANADA

Office of the International
    Ice Patrol
c/o Coast Guard R & D Center
Avery Point
Groton, CT 06340

NOAA/EDIS Miami Library Center
4301 Rickenbacker Causeway
Miami, FL 33149

Library
Skidaway Institute of Oceanography
P.O. Box 13687
Savannah, GA 31416

Institute of Geophysics
University of Hawaii
Library Room 252
2525 Correa Road
Honolulu, HI 96822

Marine Resources Information Center
Building E38-320
MIT
Cambridge, MA 02139

Library
Lamont-Doherty Geological
    Observatory
Colombia University
Palisades, NY 10964

Library
Serials Department
Oregon State University
Corvallis, OR 97331-5503

Pell Marine Science Library
University of Rhode Island
Narragansett Bay Campus
Narragansett, RI 02882

Working Collection
Texas A&M University
Dept. of Oceanography
College Station, TX 77843

Library
Virginia Institute of Marine Science
Gloucester Point, VA 23062

Fisheries-Oceanography Library
151 Oceanography Teaching Bldg.
University of Washington
Seattle, WA 98195

Library
R.S.M.A.S.
University of Miami
4600 Rickenbacker Causeway
Miami, FL 33149

Maury Oceanographic Library
Naval Oceanographic Office
Stennis Space Center
NSTL, MS 39522-5001

Marine Sciences Collection
Mayaguez Campus Library
University of Puerto Rico
Mayagues, Puerto Rico 00708

Library
Institute of Oceanographic Sciences
Deacon Laboratory
Wormley, Godalming
Surrey GU8 5UB
UNITED KINGDOM

The Librarian
CSIRO Marine Laboratories
G.P.O. Box 1538
Hobart, Tasmania
AUSTRALIA 7001

Library
Proudman Oceanographic Laboratory
Bidston Observatory
Birkenhead
Merseyside L43 7 RA
UNITED KINGDOM

50272-101

REPORT DOCUMENTATION PAGE	1. REPORT NO. WHOI-91-10	2.	3. Recipient's Accession No.
4. Title and Subtitle Acoustic Scattering from Elastic Ice: A Finite Difference Solution			5. Report Date June 1991
			6.
7. Author(s) J. Robert Fricke			8. Performing Organization Rept. No.
9. Performing Organization Name and Address Woods Hole Oceanographic Institution Woods Hole, Massachusetts 02543			10. Project/Task/Work Unit No. WHOI-91-10
			11. Contract(C) or Grant(G) No. (C) (G)
12. Sponsoring Organization Name and Address Funding was provided by the Office of Naval Research.			13. Type of Report & Period Covered Ph.D. Thesis
			14.

15. Supplementary Notes

This thesis should be cited as: J. Robert Fricke, 1991. Acoustic Scattering from Elastic Ice: A Finite Difference Solution. Ph.D. Thesis MIT/WHOI, WHOI-91-10.

16. Abstract (Limit: 200 words)

In this thesis I consider acoustic scattering from Arctic ice. No analytic scattering theories are able to explain the observed low frequency (10-100 Hz) loss measured in long-range propagation experiments.

Reasoning that a full-wave solution holds the key, I use the finite difference method to solve the elastodynamic equations. This technique allows arbitrary roughness, unrestricted in slope, displacement, or radius of curvature and provides direct, physical insight into the rough ice scattering mechanism. The underlying partial differential euqations treat the air-ice-water complex as a heterogeneous con' nuum in three dimensions. A plane strain approximation reduces the formulation to two dimensions, which limits the computational burden, while permitting the salient features of the scattering process to be studied.

Broadband numerical scattering experiments are conducted using two classes of roughness features: ice edges and pressure ridges. Specular loss due to an ice edge is found to be too low to explain the observed scattering loss in the central Arctic. The loss due to a ridge is affected by three phenomena: mass loading, excitation of plate waves, and a material dependent power law. The first two affect the magnitude of the loss, while the last affects the frequency dependence.

The observed loss is best explained by scatter from relatively young, large pressure ridges, which are modeled as fluid structures. The fluid model is appropriate because young ridges are loose aggregations of ice blocks and hence cannot support shear strain. Multi-year ridges, in contrast, are completely frozen and are better modeled as elastic structures. Scatter from multi-year ridges does not explain the observed data.

Future work with scale models at ultrasonic frequencies and full-scale field experiments are required before this hypothesis can be fully tested.

17. Document Analysis   a. Descriptors

scattering
finite difference
Arctic

b. Identifiers/Open-Ended Terms

c. COSATI Field/Group

18. Availability Statement Approved for publication; distribution unlimited.	19. Security Class (This Report)	21. No. of Pages 276
	20. Security Class (This Page)	22. Price

(See ANSI-Z39.18)   See Instructions on Reverse   OPTIONAL FORM 272 (4-77)
(Formerly NTIS-35)
Department of Commerce